15 Boundary Element Methods for Steady-State Unsaturated Fractured Media

Account Number: **As noted**
Collaborators: **As noted**
Directories: **$HOME2/Matlab/ExpToVG**

Objective: Develop methodology to examine steady-state flows in porous media using boundary integral techniques. Boundary integral methods have been used for saturated steady-state flows for decades; unsaturated steady-state flows have been considered for at least a decade using the quasilinear approximation. Variably saturated discrete-fracture networks were considered by Rasmussen (1987). To the best of my knowledge, unsaturated porous-medium flow simulations have been limited to homogeneous infinite or semi-infinite problems, perhaps interacting with saturated bulbs or with a finite-element mesh. Fracture simulations have been limited to saturated discrete fractures and to discrete-fracture networks in an impermeable matrix. It is of interest to develop methodology to relax the quasilinear assumption (i) to handle generic relative permeability functions, including fracture continua embedded in a porous matrix (i.e., the equivalent continuum approach); (ii) to handle multiple material zones (e.q., layering); and (iii) to handle discrete fractures in an unsaturated porous matrix. Such methodology would be useful for examining ambient-flow conditions at YM, including generating initial conditions for transient simulations. I expect the approach would be quite competitive for these applications; unfortunately, it is not clear how to extend the approach to coupled problems.

1/28/96 Multi-continuum boundary elements.

Steady-state unsaturated flow in a porous medium has been successfully simulated using boundary elements under the condition that the relative permeability is approximated using the exponential function, $K(P) = K_o \exp(\beta P)$ (note $P < 0$ when unsaturated). With this assumption, the Kirchhoff transform can be applied and the governing equation,

$$-\nabla \mathbf{q} = \nabla K(P)(\nabla P + \rho g \nabla z) = 0, \tag{15-1}$$

can be transformed to

$$\nabla^2 \Theta + \rho g \beta \frac{\partial \Theta}{\partial z} = 0. \tag{15-2}$$

There are Green's functions for this equation:

$$G_{3D} = \frac{1}{4\pi r}\exp[-\alpha(r-z)] \tag{15-3}$$

$$G_{2D} = \frac{1}{2\pi}\exp[\alpha(z-z_0)]\mathrm{K}_0(\alpha r), \tag{15-4}$$

where $\alpha = \rho g\beta/2$ and K_0 is the modified Bessel function of the second kind of order 0.

The Kirchhoff transform is

$$\Theta = \int_{-\infty}^{P} K(P)\,\mathrm{d}P \qquad \text{so that} \qquad \frac{\mathrm{d}\Theta}{\mathrm{d}P} = K(P). \tag{15-5}$$

With exponential relative permeability,

$$\Theta = K/\beta \tag{15-6}$$

$$\nabla\Theta = \frac{\mathrm{d}\Theta}{\mathrm{d}P}\nabla P = K(P)\nabla P \tag{15-7}$$

$$\begin{aligned}\nabla(K\nabla z) &= K\nabla^2 z + \nabla z\cdot\nabla K = \nabla z\cdot\nabla K \\ &= \frac{\partial K}{\partial z} = \frac{\mathrm{d}K}{\mathrm{d}P}\frac{\mathrm{d}P}{\mathrm{d}\Theta}\frac{\partial\Theta}{\partial z} = \frac{1}{K}\frac{\mathrm{d}K}{\mathrm{d}P}\frac{\partial\Theta}{\partial z} = \frac{\mathrm{d}\ln K}{\mathrm{d}P}\frac{\partial\Theta}{\partial z} = \beta\frac{\partial\Theta}{\partial z}.\end{aligned} \tag{15-8}$$

The difficulty with using the transform arises from the gravity term. A general relative permeability can easily be used when gravity is not present ($\partial K/\partial z \equiv 0$), but the need for $\mathrm{d}K/\mathrm{d}\Theta$ to be constant for the Green's function approach to work restricts the method in general.

In general, boundary element approaches are effective when material properties are piecewise constant. For saturated-flow problems, material discontinuities are readily treated by discretizing the discontinuity and enforcing pressure and normal-flux continuity to eliminate unknowns. For unsaturated-flow problems, the quasilinear approach imposes additional difficulty as the transform variable is not continuous. I have not seen material discontinuities handled for unsaturated problems, presumably because nonlinearity pops up along the discontinuity. Discrete-fracture problems could also be handled using the quasilinear approach, but would also be nonlinear.

My idea is that a possibly straightforward extension to the quasilinear approach can be imposed for a generic relative permeability function, by approximating the generic function as a sum of exponentials [$K(P) = \sum_i K_i(P) = \sum_i K_{oi}\exp(\beta_i P)$]. If the overall mass-balance equation can be solved by performing a set of integrals with different Green's functions for each of the K_i, the resulting set of linear equations should be determined by the number of elements. Equivalent-continuum approaches could be handled this way also. Two key questions arise: (i) can one approximate the generic function with a sum of exponentials, and (ii) can one use a sum of Green's functions to approximate a sum of quasilinear equations?

The quick answer to (i) is that to a certain degree of approximation, some van Genuchten (van Genuchten, 1980) functions can be handled over some range of (negative-only) pressures. Test *Matlab* files were created in ***$HOME2/Matlab/ExpToVar***, with a driver file of **show_kexp.m**. It appears that as the van Genuchten m parameter increases, the approximation deteriorates. As a reference, the m parameter becomes large for fractures.

The quick answer to (ii) is maybe one can avoid the process by noting that, as $\Theta = \sum_i K_i/\beta_i$, then $\mathrm{d}\Theta/\mathrm{d}K_i = 1/\beta_i$ and $\mathrm{d}K_i/\mathrm{d}\Theta = \beta_i$, and the transformed equation is actually

$$\nabla \sum_i K_i(P)(\nabla P + \rho g \nabla z) = \nabla^2 \Theta + \rho g \sum_i \beta_i \frac{\partial \Theta}{\partial z} = \nabla^2 \Theta + \rho g \beta \frac{\partial \Theta}{\partial z}, \tag{15-9}$$

where $\beta = \sum_i \beta_i$. If this is indeed correct, then the approach works essentially unchanged, which seems too good to be true. In fact, the generic transform could be used everywhere with the approximate Green's function only used for integration.

Boundary conditions are nonlinear, similar to the straight quasilinear approach. Generally, the boundary element approach requires that both Θ and $\partial\Theta/\partial n$ are defined along the boundary, and the work in the method is in determining the one of the two that is not specified by well-posed problem specifications. Pressure boundary conditions should not be a problem, since there must be a one-to-one relationship between P and Θ; however, since $\mathbf{q} = -K(\nabla P + \rho g \nabla z) = -\nabla\Theta - K(P)\rho g \nabla z$, there is a linkage between flux and pressure which must be resolved. I don't actually recollect seeing finite boundary conditions imposed when the quasilinear approximation was being used, probably due to the nonlinearity. The flux problem pops up with material discontinuities and fractures, while the ease of handling pressure disappears with material discontinuities since P is continuous, not $\Theta(P)$.

2/3/96 Boundary element solution procedure.

Assuming that there is indeed a Green's function for the problem, what is the procedure for solving the problem?

The first step in solving a generic boundary integral problem is to perform all integrals to result in a set of linearized simultaneous equations,

$$\mathbf{H} \cdot \boldsymbol{\Theta} = \mathbf{G} \cdot \boldsymbol{\Theta}_{,n}, \tag{15-10}$$

where $\mathbf{H}$ contains all of the Θ integrations, $\mathbf{G}$ contains all of the $\Theta_{,n}$ integrations, $\boldsymbol{\Theta}$ is the Θ vector, and $\boldsymbol{\Theta}_{,n}$ is the $\partial\Theta/\partial n$ vector. The process for creating $\mathbf{H}$ and $\mathbf{G}$ will be discussed elsewhere.

Rearranging to place all known values on the right-hand side,

$$\mathbf{A} \cdot \mathbf{u} = \mathbf{b}, \tag{15-11}$$

where $\mathbf{u}$ is the vector of unknowns and $\mathbf{b}$ is the vector of known values. Solving the resultant set of unknowns is sufficient to completely define the boundary values for linear problems. For unsaturated problems, however, where $\mathbf{A} = \mathbf{A}(\mathbf{u})$, iteration is required.

Two approaches are typically followed when solving nonlinear problems, Picard iteration and Newton-Raphson iteration. Picard iteration is linearly convergent, while Newton-Raphson iteration is quadratically convergent when the starting point is sufficiently close to the solution and divergent outside a convergence basin. Picard iteration is accomplished by rewriting equation 15-11 as

$$\mathbf{A}(\mathbf{u}^n) \cdot \mathbf{u}^{n+1} = \mathbf{b}^n, \tag{15-12}$$

where n is the iteration level, solving for $\mathbf{u}^{n+1}$ directly, and repeating until convergence. Newton-Raphson iteration is accomplished by defining a residual vector $f(\mathbf{u})$,

$$f(\mathbf{u}) = \mathbf{A}(\mathbf{u}) \cdot \mathbf{u} - \mathbf{b}, \tag{15-13}$$

expanding in a Taylor series and including only the first term, yielding

$$f(\mathbf{u}^m + \delta\mathbf{u}) = \mathbf{A}(\mathbf{u}^m) \cdot \mathbf{u}^m - \mathbf{b}^m + \delta\mathbf{u}\frac{\partial f(\mathbf{u}^m)}{\partial \mathbf{u}}, \tag{15-14}$$

setting $f(\mathbf{u}^m + \delta\mathbf{u})$ to zero, and solving for $\delta\mathbf{u}$. Finally, the unknowns are updated using $\mathbf{u}^{m+1} = \mathbf{u}^m + \delta\mathbf{u}$.

The efficiency of the linear-equation solution is dependent on two steps, the integration step and the matrix-solution step. The integration step is $O(N^2)$, while the matrix-solution step is $O(M^3)$, where N is the number of nodal values and M is the number of unknowns; however, due to the large number of operations for each integration, computational effort is roughly equivalent for moderately sized problems. Experience indicates that problems of hundreds to perhaps a thousand unknowns can be handled with direct Gaussian elimination. The Picard procedure is equivalent to solving a series of linear problems with N^2 integrations per iteration; however, the Newton-Raphson procedure is equivalent to performing N^4 integrations per iteration. Thus, it is extremely advantageous to be able to have separable $\mathbf{H}(\mathbf{u})$ and $\mathbf{G}(\mathbf{u})$ matrices, in the form $\mathbf{H}(\mathbf{u};\mathbf{x}) = \mathbf{H}_u(\mathbf{u}) \cdot \mathbf{H}_x(\mathbf{x})$ and $\mathbf{G}(\mathbf{u};\mathbf{x}) = \mathbf{G}_u(\mathbf{u}) \cdot \mathbf{G}_x(\mathbf{x})$, so that the computationally demanding spatial integrations can be done once and for all.

Now that solution ideas have been outlined, what do the $\mathbf{H}$ and $\mathbf{G}$ matrices consist of?

Pullan and Collins (1987) consider the boundary element solution of equation 15-9. Introducing a further transformation, $\Theta = H\exp(-sz)$ (note that the Pullan and Collins (1987) z is the negative of my z), the modified Helmholtz equation is derived,

$$\nabla^2 H = s^2 H, \tag{15-15}$$

where $s = \alpha/2$. Double-checking:

$$\frac{\partial H}{\partial x} = \frac{\partial}{\partial x}\left[\Theta\exp(sz)\right] = \exp(sz)\frac{\partial \Theta}{\partial x} \tag{15-16}$$

$$\frac{\partial H}{\partial z} = \frac{\partial}{\partial z}\left[\Theta\exp(sz)\right] = \exp(sz)\left(\frac{\partial \Theta}{\partial z} + s\Theta\right) \tag{15-17}$$

$$\frac{\partial^2 H}{\partial x^2} = \exp(sz)\frac{\partial^2 \Theta}{\partial x^2} \tag{15-18}$$

$$\frac{\partial^2 H}{\partial z^2} = \frac{\partial}{\partial z}\left(\frac{\partial H}{\partial z}\right) = \exp(sz)\left(\frac{\partial^2 \Theta}{\partial z^2} + 2s\frac{\partial \Theta}{\partial z} + s^2\Theta\right) \tag{15-19}$$

$$\nabla^2 H - s^2 H = \exp(sz)\left(\nabla^2\Theta + 2s\frac{\partial \Theta}{\partial z}\right) \tag{15-20}$$

The Green's function is given by Pullan and Collins (1987) as

$$G_{3D} = \exp(-sr)/r \tag{15-21}$$

$$G_{2D} = \mathrm{K}_0(sr). \tag{15-22}$$

From Green's theorem, the volume integral of any two sufficiently smooth functions G and H nonsingular in region Ω can be transformed to a surface integral along the boundary, σ,

$$\int_\Omega \left(G\nabla^2 H - H\nabla^2 G\right)\,\mathrm{d}\Omega = \int_\sigma \left(G\frac{\partial H}{\partial n} - H\frac{\partial G}{\partial n}\right)\,\mathrm{d}\sigma. \tag{15-23}$$

If G is the Green's function, $\int_\Omega H\nabla^2 G\,\mathrm{d}\Omega \equiv \alpha H(x)$ and since $\nabla^2 H \equiv 0$, only a surface integral remains:

$$\alpha H(x) = \int_\sigma \left(G\frac{\partial H}{\partial n} - H\frac{\partial G}{\partial n}\right)\,\mathrm{d}\sigma. \tag{15-24}$$

The new formulation presented in equation 15-9 seemed to be too good to be true. Double-checking the formulation:

$$\Theta = \sum_i K_{oi}\int_{-\infty}^{P}\exp(\beta_i P)\,\mathrm{d}P = \sum_i (K_{oi}/\beta_i)\exp(\beta_i P) \tag{15-25}$$

$$\frac{\mathrm{d}\Theta}{\mathrm{d}P} = \sum_i K_i(P) \tag{15-26}$$

$$\frac{\partial K}{\partial z} = \frac{\mathrm{d}K}{\mathrm{d}P}\frac{\mathrm{d}P}{\mathrm{d}\Theta}\frac{\partial \Theta}{\partial z} = \left[\frac{\sum_i(\beta_i K_{oi})\exp(\beta_i P)}{\sum_i K_{oi}\exp(\beta_i P)}\right]\frac{\partial \Theta}{\partial z} \tag{15-27}$$

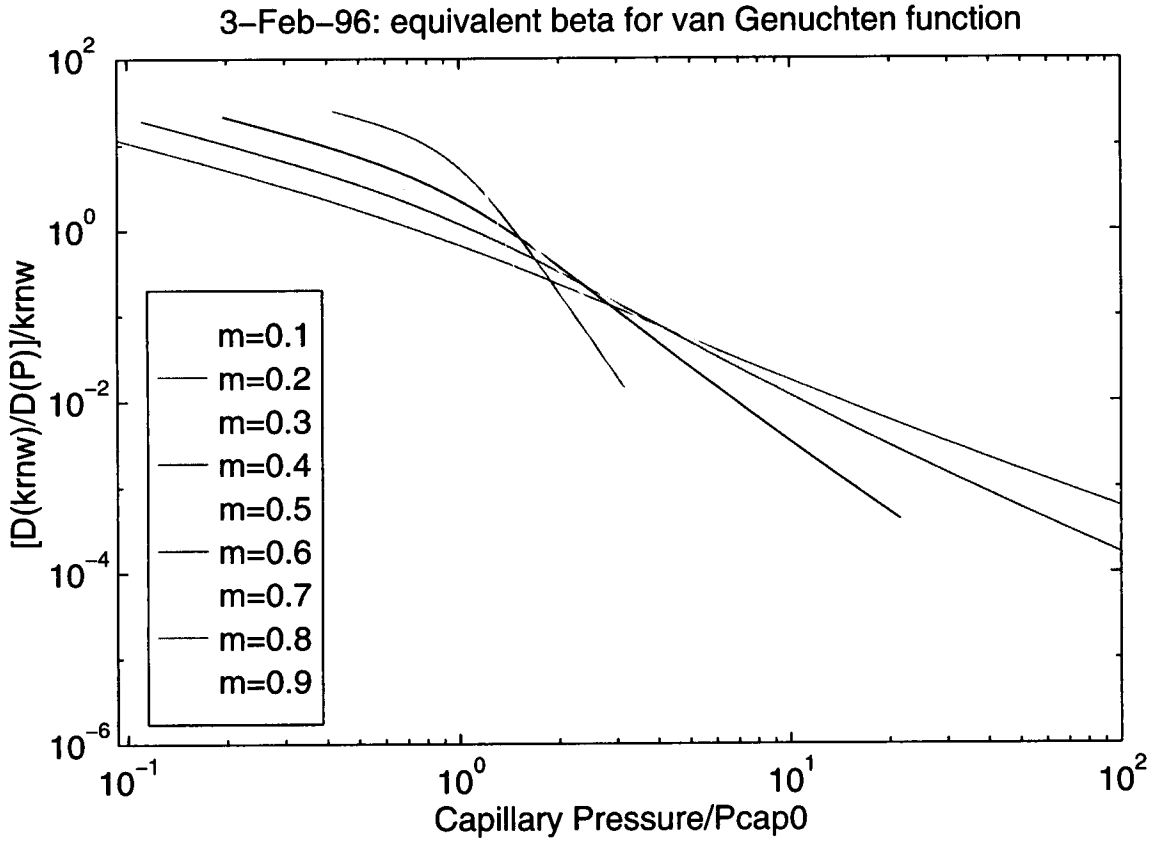

Figure 15-1: 2/3/96. Equivalent β for van Genuchten wetting relative permeability. Created by **$HOME2/Matlab/V4/make_DkDPrk.m**.

There we have the rub; $(\mathrm{d}K/\mathrm{d}P)/K$ is not constant with varying pressure as it is in the true quasilinear situation. In fact, as shown in Figure 15-1, the ratio is highly nonlinear; particularly for small m, a better argument could be made for $(\mathrm{d}K/\mathrm{d}\ln P)/K$ being a constant.

So what to do now? Ideas:

- Pick an equivalent s for some representative P for the Green's function. Based on Figure 15-1, this is pretty unpalatable.
- Think harder.

2/4/96 Return to previous idea.

The original idea was to break up the problem into parts by dividing up the relative permeability functions into exponential functions, so that

$$\nabla^2\Theta + \rho g\beta\frac{\partial\Theta}{\partial z} = \sum_{i=1}^{N}\left(\nabla^2\Theta_i + \alpha_i\frac{\partial\Theta_i}{\partial z}\right) = 0, \tag{15-28}$$

$$\Theta_i = \int_{-\infty}^{P} K_i(P)\,\mathrm{d}P. \tag{15-29}$$

Requiring that each exponential function is solved identically yields N equations solved independently but linked by the joint boundary conditions,

$$\nabla^2\Theta_i + \alpha_i\frac{\partial\Theta_i}{\partial z} = 0. \tag{15-30}$$

At each boundary, it is required that

$$\Theta_i = \Theta_i(P) \qquad \Leftrightarrow \qquad P = P(\Theta_i), \tag{15-31}$$

$$\mathbf{q} = \sum_{i=1}^{N}\mathbf{q}_i = -\sum_{i=1}^{N}\left[\frac{\partial\Theta_i}{\partial n} + K_i(P)\rho g\frac{\partial z}{\partial n}\right]. \tag{15-32}$$

Neither the pressure requirement nor the flux requirement is onerous for portions of the boundary where the pressure is specified and flux is unknown; there is a one-to-one relationship between Θ_i and P, and $\mathbf{q}$ is derived from calculated values of $\partial\Theta_i/\partial n$. On the other hand, where $\mathbf{q}$ is specified problems arise, since there is not a one-to-one correspondence between $\mathbf{q}$ and $\partial\Theta_i/\partial n$, and consistency between P values is not enforced.

What happens if it is required that $\partial P/\partial n$ be consistent for all boundaries?

$$\mathbf{q} = \sum_{i=1}^{N}\mathbf{q}_i = -\left(\sum_{i=1}^{N}\frac{\mathrm{d}\Theta_i}{\mathrm{d}P}\right)\frac{\partial P}{\partial n} - K(P)\rho g\frac{\partial z}{\partial n}, \tag{15-33}$$

$$\mathbf{q}_i = -\frac{\mathrm{d}\Theta_i}{\mathrm{d}P}\frac{\partial P}{\partial n} - K_i(P)\rho g\frac{\partial z}{\partial n} = -K_i(P)\left(\frac{\partial P}{\partial n} + \rho g\frac{\partial z}{\partial n}\right) = \frac{K_i(P)}{K(P)}\mathbf{q}. \tag{15-34}$$

It is obvious from this that if the materials are solved for independently, $\partial P/\partial n$ is a convenient variable of interest. However, writing the equations in fractional-flow form points out the basic difficulty; there is no reason that the $K_i(P)/K(P)$ ratio is going to be the same everywhere. In essence, there is transfer of flux from one continuum to the next. How can this be accommodated?

A quick check of the appropriateness of the assumptions can be done using an ODE solver in 1D. The check can be performed by picking a particular pressure, such as near the water table, and

a global flux, and integrating vertically. The key question is whether the pressure field is identical for each of the cases. Given zero fluxes, pressure must be hydrostatic and the various pressure fields are congruent; as fluxes increase, does this congruence hold?

2/5/96 New ideas.

How about a return to the dissertation idea of separate zones? With this approach, the generic relative permeability is approximated as a set of pressure zones, with each zone having an exponential relative permeability. A set of moving contours would be required; however, the pressure would be known on each contour and only the gradient would be needed, identical to the saturation contours in my dissertation. The advantage is that perhaps many fewer contours would be required and again each contour-bounded zone is independently solved for, so the global pressure matrix need not be formed. There is the advantage and disadvantage of transient stepping to a solution. Is this really much less work than a domain scheme?

Another wild idea. For a highly layered system, each interface gets discretized with fixed nodes and moving pressure contours skate along the interfaces. Perhaps the contours need some internal nodes as well.

2/9/96 Development in 1D.

Yesterday I found a Fall 1995 AGU talk that presents a methodology that is described schizophrenically but appears to be a combination of an approach discussed in my dissertation work but applied to the Richards equation and the multiple-Green's-function approach (Holt et al., 1995). I have been unable to get in touch with the authors as of yet. However, apparently they have had some success and have done some numerical comparisons.

The 1D Green's function approach for the potential-flow problem is as follows (abstracted from Chapter 2-4-1 of Banerjee and Butterfield (1981)). Given the governing equation with constant K coefficient,

$$\frac{\partial}{\partial x}\left(Kh_{,x}\right) + \psi(x) = 0 \qquad \Rightarrow \qquad h_{,xx} + \frac{\psi(x)}{K} = 0, \tag{15-35}$$

integration by parts yields

$$\begin{aligned}\int_a^b h_{,xx}G\,\mathrm{d}x &= [Gh_{,x}]_a^b - \int_a^b h_{,x}G_{,x}\,\mathrm{d}x \\ &= [Gh_{,x} - hG_{,x}]_a^b + \int_a^b hG_{,xx}\,\mathrm{d}x.\end{aligned} \tag{15-36}$$

If it is specified that

$$G_{,xx}(x,\xi) = -\delta(x-\xi), \tag{15-37}$$

a value at a base point ξ can be determined from the boundary values (neglecting the source term for clarity) using the equation

$$h(\xi) = [G(x,\xi)h_{,x}(x) - h(x)G_{,x}(x,\xi)]_{x=a}^{x=b}. \tag{15-38}$$

Note that G is continuous at $x=\xi$, but $\partial G/\partial x$ has a jump.

As a properly specified problem has only one of the boundary values available at either end, the other must be found. Writing the integral equation for each boundary yields

$$\begin{Bmatrix} h(b) \\ h(a) \end{Bmatrix} = \begin{bmatrix} G(b,b) & -G(a,b) \\ G(b,a) & -G(a,a) \end{bmatrix} \begin{Bmatrix} h_{,x}(b) \\ h_{,x}(a) \end{Bmatrix} - \begin{bmatrix} G_{,x}(b,b-\epsilon) & -G_{,x}(a,b) \\ G_{,x}(b,a) & -G_{,x}(a,a+\epsilon) \end{bmatrix} \begin{Bmatrix} h(b) \\ h(a) \end{Bmatrix}, \tag{15-39}$$

or, rearranging,

$$\begin{bmatrix} G_{,x}(b,b-\epsilon)+1 & -G_{,x}(a,b) \\ G_{,x}(b,a) & -G_{,x}(a,a+\epsilon)+1 \end{bmatrix} \begin{Bmatrix} h(b) \\ h(a) \end{Bmatrix} = \begin{bmatrix} G(b,b) & -G(a,b) \\ G(b,a) & -G(a,a) \end{bmatrix} \begin{Bmatrix} h_{,x}(b) \\ h_{,x}(a) \end{Bmatrix}. \tag{15-40}$$

The Green's function is found by integration.

$$G_{,x}(x,\xi) = -\frac{\operatorname{sgn}(x-\xi)}{2} \tag{15-41}$$

$$G(x,\xi) = \frac{1}{2}\begin{cases} C_1 + C_2(x-\xi) & x > \xi, \\ C_3 + C_4(x-\xi) & x < \xi, \end{cases} \tag{15-42}$$

$$G_{,x}(x,\xi) = \frac{1}{2}\begin{cases} C_2 & x > \xi, \\ C_4 & x < \xi. \end{cases} \tag{15-43}$$

Requiring that $G_{,x} = -1/2$ for $x > \xi$ and $G_{,x} = 1/2$ for $x < \xi$ specifies $C_2 = -1$ and $C_4 = 1$. Requiring that $G = 0$ at some distance L (which may be arbitrarily taken as $L = b - a$) and

requiring that G is continuous specifies $C_1 = C_3 = L$, yielding

$$G(x,\xi) = \frac{1}{2}\begin{cases} L-(x-\xi) & x > \xi, \\ L+(x-\xi) & x < \xi, \end{cases} \tag{15-44}$$

$$G_{,x}(x,\xi) = \frac{1}{2}\begin{cases} -1 & x > \xi, \\ +1 & x < \xi, \end{cases} \tag{15-45}$$

$$G'(x,\xi) = \frac{\mathrm{d}G}{\mathrm{d}\xi} = \frac{1}{2}\begin{cases} +1 & x > \xi, \\ -1 & x < \xi, \end{cases} \tag{15-46}$$

$$G'_{,x}(x,\xi) = \frac{\mathrm{d}G_{,x}}{\mathrm{d}\xi} = 0 \qquad x \neq \xi. \tag{15-47}$$

Plugging in the newly defined values for G,

$$\begin{bmatrix} -\frac{1}{2}+1 & -\frac{1}{2} \\ -\frac{1}{2} & -\frac{1}{2}+1 \end{bmatrix} \begin{Bmatrix} h(b) \\ h(a) \end{Bmatrix} = \begin{bmatrix} L/2 & 0 \\ 0 & -L/2 \end{bmatrix} \begin{Bmatrix} h_{,x}(b) \\ h_{,x}(a) \end{Bmatrix}$$

$$\frac{1}{2}\begin{bmatrix} 1 & -1 \\ -1 & 1 \end{bmatrix} \begin{Bmatrix} h(b) \\ h(a) \end{Bmatrix} = \frac{L}{2}\begin{bmatrix} 1 & 0 \\ 0 & -1 \end{bmatrix} \begin{Bmatrix} h_{,x}(b) \\ h_{,x}(a) \end{Bmatrix}. \tag{15-48}$$

At an interior point, h can be determined using

$$\begin{aligned} h(\xi) &= [G(b,\xi)h_{,x}(b) - G(a,\xi)h_{,x}(a)] - [G_{,x}(b,\xi)h(b) - G_{,x}(a,\xi)h(a)] \\ &= \tfrac{1}{2}[(L-b+\xi)h_{,x}(b) - (L+a-\xi)h_{,x}(a)] + \tfrac{1}{2}[h(b)+h(a)] \end{aligned} \tag{15-49}$$

and, assuming no internal sources so that $h_{,x}(a) = h_{,x}(b) = h_{,x}$,

$$= \tfrac{1}{2}[(L-b+\xi) - (L+a-\xi)]h_{,x} + \tfrac{1}{2}[h(b)+h(a)] \tag{15-50}$$

$$= \left[\xi - \frac{a+b}{2}\right] h_{,x} + \tfrac{1}{2}[h(b)+h(a)]. \tag{15-51}$$

The gradient of h at point ξ is obtained by taking the derivative with respect to ξ, yielding

$$\begin{aligned} h_{,\xi}(\xi) &= [G'(b,\xi)h_{,x}(b) - G'(a,\xi)h_{,x}(a)] - [G'_{,x}(b,\xi)h(b) - G'_{,x}(a,\xi)h(a)] \\ &= \frac{h_{,x}(b)+h_{,x}(a)}{2}, \end{aligned} \tag{15-52}$$

and the flux at point ξ is

$$\mathbf{q}(\xi) = -Kh_{,\xi}(\xi) = -K\frac{h_{,x}(b)+h_{,x}(a)}{2}. \tag{15-53}$$

The same procedure can be followed for the Richards equation with the quasilinear assumption (using h for Θ),

$$\nabla^2 h + \alpha \frac{\partial h}{\partial z} = 0. \tag{15-54}$$

Integration by parts yields

$$\begin{aligned} \int_a^b (h_{,xx} + \alpha h_{,x}) G \, \mathrm{d}x &= [G(h_{,x} + \alpha h)]_a^b - \int_a^b (h_{,x} + \alpha h) G_{,x} \, \mathrm{d}x \\ &= [G(h_{,x} + \alpha h) - h G_{,x}]_a^b + \int_a^b h(G_{,xx} - \alpha G_{,x}) \, \mathrm{d}x. \end{aligned} \tag{15-55}$$

If it is specified that

$$G_{,xx}(x,\xi) - \alpha G_{,x} = -\delta(x - \xi), \tag{15-56}$$

a value at a base point ξ can be determined from the boundary values (neglecting the source term for clarity) using the equation

$$h(\xi) = [G(x,\xi) h_{,x}(x) + h(x)(\alpha G(x,\xi) - G_{,x}(x,\xi))]_{x=a}^{x=b}. \tag{15-57}$$

Note that G is continuous at $x = \xi$, but $\partial G / \partial x$ has a jump.

As a properly specified problem has only one of the boundary values available at either end, the other must be found. Writing the integral equation for each boundary yields

$$\begin{aligned} \begin{Bmatrix} h(b) \\ h(a) \end{Bmatrix} &= \begin{bmatrix} G(b,b) & -G(a,b) \\ G(b,a) & -G(a,a) \end{bmatrix} \begin{Bmatrix} h_{,x}(b) \\ h_{,x}(a) \end{Bmatrix} \\ &\quad + \begin{bmatrix} \alpha G(b,b) - G_{,x}(b, b-\epsilon) & -\alpha G(a,b) + G_{,x}(a,b) \\ \alpha G(b,a) - G_{,x}(b,a) & -\alpha G(a,a) + G_{,x}(a, a+\epsilon) \end{bmatrix} \begin{Bmatrix} h(b) \\ h(a) \end{Bmatrix}, \end{aligned} \tag{15-58}$$

or, rearranging,

$$\begin{aligned} &\begin{bmatrix} G_{,x}(b, b-\epsilon) - \alpha G(b,b) + 1 & \alpha G(a,b) - G_{,x}(a,b) \\ G_{,x}(b,a) - \alpha G(b,a) & \alpha G(a,a) - G_{,x}(a, a+\epsilon) + 1 \end{bmatrix} \begin{Bmatrix} h(b) \\ h(a) \end{Bmatrix} \\ &\qquad = \begin{bmatrix} G(b,b) & -G(a,b) \\ G(b,a) & -G(a,a) \end{bmatrix} \begin{Bmatrix} h_{,x}(b) \\ h_{,x}(a) \end{Bmatrix}. \end{aligned} \tag{15-59}$$

The Green's function is found by integration.

$$G_{,x}(x,\xi) - \alpha G(x,\xi) = -\frac{1}{2}\operatorname{sgn}(x-\xi) \tag{15-60}$$

$$G(x,\xi) = \frac{1}{2}\begin{cases} C_1 + C_2\exp[\alpha(x-\xi)] & x > \xi, \\ C_3 + C_4\exp[\alpha(x-\xi)] & x < \xi, \end{cases} \tag{15-61}$$

$$G_{,x}(x,\xi) = \frac{1}{2}\begin{cases} \alpha C_2\exp[\alpha(x-\xi)] & x > \xi, \\ \alpha C_4\exp[\alpha(x-\xi)] & x < \xi. \end{cases} \tag{15-62}$$

Requiring that $G_{,x} - \alpha G = -1/2$ for $x > \xi$ and $G_{,x} - \alpha G = 1/2$ for $x < \xi$ specifies $C_1 = 1/\alpha$ and $C_3 = -1/\alpha$. Requiring that $G_{,x}$ approaches zero as $|x-\xi| \to \infty$ specifies $C_2 = 0$, while requiring that G is continuous at $x = \xi$ specifies $C_1 = C_3 + C_4$ so that $C_4 = 2/\alpha$, yielding

$$G(x,\xi) = \begin{cases} 1/2\alpha & x > \xi, \\ \{\exp[\alpha(x-\xi)] - 1/2\}/\alpha & x < \xi, \end{cases} \tag{15-63}$$

$$G_{,x}(x,\xi) = \begin{cases} 0 & x > \xi, \\ \exp[\alpha(x-\xi)] & x < \xi, \end{cases} \tag{15-64}$$

$$G_{,x}(x,\xi) - \alpha G(x,\xi) = \begin{cases} -1/2 & x > \xi, \\ +1/2 & x < \xi, \end{cases} \tag{15-65}$$

$$G'(x,\xi) = \begin{cases} 0 & x > \xi, \\ -\exp[\alpha(x-\xi)] & x < \xi, \end{cases} \tag{15-66}$$

$$G'_{,x}(x,\xi) = \begin{cases} 0 & x > \xi, \\ -\alpha\exp[\alpha(x-\xi)] & x < \xi, \end{cases} \tag{15-67}$$

$$G'_{,x}(x,\xi) - \alpha G'(x,\xi) = 0 \qquad x \neq \xi. \tag{15-68}$$

Plugging in the newly defined values for G,

$$\begin{bmatrix} -\frac{1}{2}+1 & -\frac{1}{2} \\ -\frac{1}{2} & -\frac{1}{2}+1 \end{bmatrix} \begin{Bmatrix} h(b) \\ h(a) \end{Bmatrix} = \frac{1}{2\alpha}\begin{bmatrix} 1\,[1-2\exp(-\alpha L)] \\ 1 \qquad\qquad -1 \end{bmatrix} \begin{Bmatrix} h_{,x}(b) \\ h_{,x}(a) \end{Bmatrix} \tag{15-69}$$

$$\frac{1}{2}\begin{bmatrix} 1 & -1 \\ -1 & 1 \end{bmatrix} \begin{Bmatrix} h(b) \\ h(a) \end{Bmatrix} = \frac{1}{2\alpha}\begin{bmatrix} 1\,[1-2\exp(-\alpha L)] \\ 1 \qquad\qquad -1 \end{bmatrix} \begin{Bmatrix} h_{,x}(b) \\ h_{,x}(a) \end{Bmatrix}. \tag{15-70}$$

At an interior point, h can be determined using

$$\begin{aligned} h(\xi) &= [G(x,\xi)h_{,x}(x) + h(x)(\alpha G(x,\xi) - G_{,x}(x,\xi))]_{x=a}^{x=b} \\ &= \frac{h(b)+h(a)}{2} + \frac{h_{,x}(b) + h_{,x}(a)\{1-2\exp[\alpha(a-\xi)]\}}{2\alpha}. \end{aligned} \tag{15-71}$$

The gradient of h at point ξ is obtained by taking the derivative with respect to ξ, yielding

$$h_{,\xi}(\xi) = h_{,x}(a)\exp[\alpha(a-\xi)]. \tag{15-72}$$

Returning from the transform variable to P [using the relationships $h = K/\beta$ and $K(P) = \exp(\beta P)$],

$$P(\xi) = \frac{\ln[\beta h(\xi)]}{\beta}, \tag{15-73}$$

and the flux at point ξ is

$$\begin{aligned}
\mathbf{q}(\xi) &= -K(P)(P_{,\xi} + \rho g z_{,\xi}) \\
&= -h_{,\xi}(\xi) - \beta\rho g z_{,\xi} h(\xi) = -h_{,\xi}(\xi) - \alpha h(\xi) \\
&= -h_{,x}(a)\exp[\alpha(a-\xi)] \\
&\quad - \alpha\left\{\frac{h(b)+h(a)}{2} + \frac{h_{,x}(b) + h_{,x}(a)\{1 - 2\exp[\alpha(a-\xi)]\}}{2\alpha}\right\} \\
&= -\left[\frac{\alpha[h(b)+h(a)]}{2} + \frac{h_{,x}(b)+h_{,x}(a)}{2}\right] \\
&= -\frac{h_{,x}(b) + \alpha h(b) + h_{,x}(a) + \alpha h(a)}{2} \\
&= \frac{\mathbf{q}(a) + \mathbf{q}(b)}{2}.
\end{aligned} \tag{15-74}$$

The result that $\mathbf{q}$ is independent of position is gratifying, since in the absence of sources (as was assumed) flux is constant throughout the domain.

2/10/96 Check of results.

A pair of *Matlab* files (saved as **make_bem_2pt.m.1**, **solve_bem_2pt.m.1**) were created in ***$HOME2/Matlab/ExpToVG*** to test the relationships presented above. A few tests were made to verify that solving for fluxes and plugging them back in to solve for pressure indeed works, and that fluxes are in the correct direction.

Extending the above approach to the idea of using a sum of Green's functions to approximate the generic Green's function,

$$G(x,\xi) \approx \sum_{i=1}^{N} w_i G_i(x,\xi), \tag{15-75}$$

yields

$$G(x,\xi) = \begin{cases} (1/2)(\sum_{i=1}^{N} w_i/\alpha_i) & x > \xi, \\ \sum_{i=1}^{N} w_i\{\exp[\alpha_i(x-\xi)] - 1/2\}/\alpha_i & x < \xi, \end{cases} \tag{15-76}$$

$$G_{,x}(x,\xi) = \begin{cases} 0 & x > \xi, \\ \sum_{i=1}^{N} w_i \exp[\alpha_i(x-\xi)] & x < \xi, \end{cases} \tag{15-77}$$

$$\sum_{i=1}^{N} w_i[G_{,x}(x,\xi) - \alpha_i G(x,\xi)] = \begin{cases} -1/2 & x > \xi, \\ +1/2 & x < \xi, \end{cases} \tag{15-78}$$

$$G'(x,\xi) = \begin{cases} 0 & x > \xi, \\ -\sum_{i=1}^{N} w_i \exp[\alpha_i(x-\xi)] & x < \xi, \end{cases} \tag{15-79}$$

$$G'_{,x}(x,\xi) = \begin{cases} 0 & x > \xi, \\ -\sum_{i=1}^{N} w_i\alpha_i \exp[\alpha_i(x-\xi)] & x < \xi, \end{cases} \tag{15-80}$$

$$\sum_{i=1}^{N} w_i[G'_{,x}(x,\xi) - \alpha_i G'(x,\xi)] = 0 \qquad x \neq \xi. \tag{15-81}$$

Plugging in the newly defined values for G,

$$\sum_{i=1}^{N} \frac{w_i}{2} \begin{bmatrix} 1 & -1 \\ -1 & 1 \end{bmatrix} \begin{Bmatrix} h(b) \\ h(a) \end{Bmatrix} = \sum_{i=1}^{N} \frac{w_i}{2\alpha_i} \begin{bmatrix} 1\,[1 - 2\exp(-\alpha_i L)] \\ 1 \qquad\qquad -1 \end{bmatrix} \begin{Bmatrix} h_{,x}(b) \\ h_{,x}(a) \end{Bmatrix}. \tag{15-82}$$

At an interior point ξ, h can be determined using

$$\sum_{i=1}^{N} w_i h(\xi) = [G(x,\xi)h_{,x}(x) + h(x)(\alpha G(x,\xi) - G_{,x}(x,\xi))]_{x=a}^{x=b} \tag{15-83}$$

$$h(\xi) = \frac{h(b) + h(a)}{2} + \frac{\sum_{i=1}^{N}(w_i/2\alpha_i)\,[h_{,x}(b) + h_{,x}(a)\{1 - 2\exp[\alpha_i(a-\xi)]\}]}{\sum_{i=1}^{N} w_i}. \tag{15-84}$$

The gradient of h at point ξ is obtained by taking the derivative with respect to ξ, yielding

$$h_{,\xi}(\xi) = h_{,x}(a)\frac{\sum_{i=1}^{N} w_i \exp[\alpha_i(a-\xi)]}{\sum_{i=1}^{N} w_i}. \tag{15-85}$$

Returning from h to P is best done with tables, since the relationships $K(P) = \sum_{i=1}^{N} w_i \exp(\beta_i P)$ and $h = \sum_{i=1}^{N} w_i \exp(\beta_i P)/\beta_i$ do not admit a straightforward inversion; however, reasoning by analogy, the flux at ξ is

$$\mathbf{q}(\xi) = \frac{\mathbf{q}(a) + \mathbf{q}(b)}{2}. \tag{15-86}$$

An interesting check to do will be to compare $\mathbf{q}(\xi) = -K(\xi)[h_{,\xi}(\xi)/(\mathrm{d}h(\xi)/\mathrm{d}P) + \rho g z_{,\xi}]$ with $\mathbf{q}(a)$ and $\mathbf{q}(b)$.

2/17/96 End of current look. SAS

In order to check whether the procedure shows promise despite the unpromising mathematics, a test problem was constructed more-or-less at random with two specified-pressure conditions of -1 and -0.1 gm/cm s^2. The van Genuchten parameters were $P_0 = 1$ gm/cm s^2 and $m = 0.7$, with $K_{sat} = 1$ cm/s, $g = 980$ cm/s^2, and total domain length of 1 mm. The problem is a balance between capillary effects and gravity drainage.

The van Genuchten relative permeability curve is approximated with ten exponential functions, using the routine **make_exp_vgwt.m** to approximate $K(P) = \sum_{i=1}^{N} w_i \exp(\beta_i P)$. The β_i values are evenly distributed between $1/\max|P|$ and $1/\min|P|$, and *Matlab*'s least-squares matrix division facility is used to ensure that relative permeability is well matched throughout the range. I found that 800 match points for each β_i works well. When the number of match points is N, it is better to have the match-point pressures evenly distributed, so **make_exp_vgwt.m** evenly distributes match-point pressures; however, it is critical to oversample, and I suspect that logarithmic variation would require far fewer match points for each β_i.

I found that excellent agreement can be found between the resultant approximated relative permeability curve and the original using the least-squares approach when the variation in relative permeability is less than 6 to 8 orders of magnitude. Relative permeabilities smaller than this are not matched, as roundoff error becomes significant, and negative relative permeabilities can occur. An alternate approach that minimizes the log of the error would be required for such cases. Quick informal tests were performed for m ranging from 0.1 to 0.7, and usually 10 to 40 exponential functions were required, depending on the pressure range and behavior of the relative permeability within the pressure range. It can be helpful to supply βs slightly outside the pressure range of the problem at hand.

The relative permeability match for the problem of interest is shown in Figure 15-2. Deviation between the two relative permeabilities is on the order of 10^{-6}. The true van Genuchten solution is created using the ODE procedure outlined in other parts of the notebook, using the solution routines starting with **solve_ODE_vg.m**. Since the ODE procedure requires a specified pressure and a specified flux, a bisection approach was used to find the flux that is compatible with both pressure boundary conditions. The solutions are shown in Figure 15-3; clearly there is no agreement between the two procedures. As a comparison, the set of pressures for each of the β_i, solved independently, is plotted against the van Genuchten solution in Figure 15-4. Again, there is little that leads one to suspect that a weighted sum of the exponential solutions would yield the van Genuchten solution.

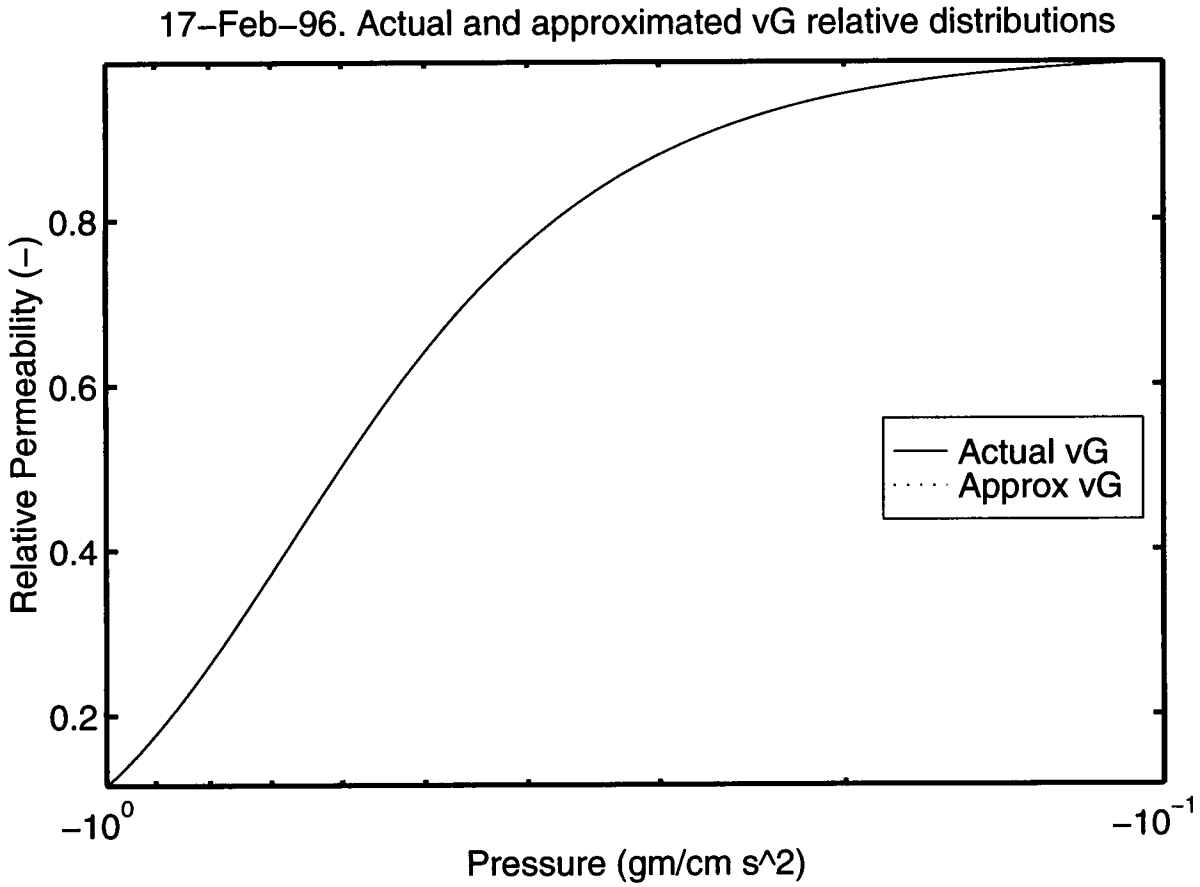

Figure 15-2: 2/17/96. expvg_rpmatch1.eps. Relative permeability for van Genuchten parameters $m = 0.7$ and $P_0 = 1$ gm/cm s^2. Actual and exponential-approximated relative permeabilities with 10 exponentials are shown.

Based on these results, the current look at the boundary integral approach is being tentatively closed out. I finally was able to discuss the Holt et al. (1995) abstract with John Wilson two days ago, and he will send a draft of a paper intended for WRR within a few weeks. The discussion revealed that their approach is not the same as my method-of-contours approach, involving implicit contours but not explicit contours. Perhaps if the approach seems workable at that time, the issue may be reopened at that time.

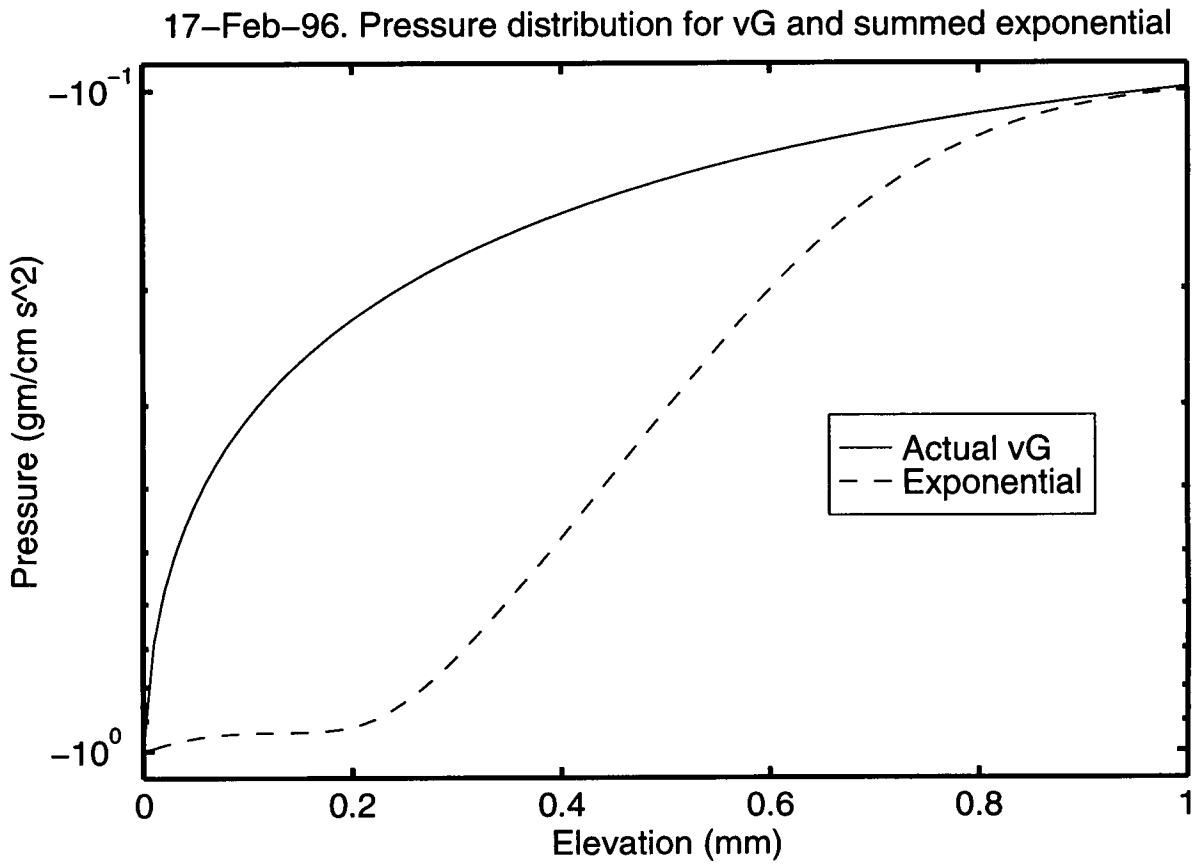

Figure 15-3: 2/17/96. expvg_soln1.eps. Pressure distribution for relative permeabilities shown in Figure 15-2.

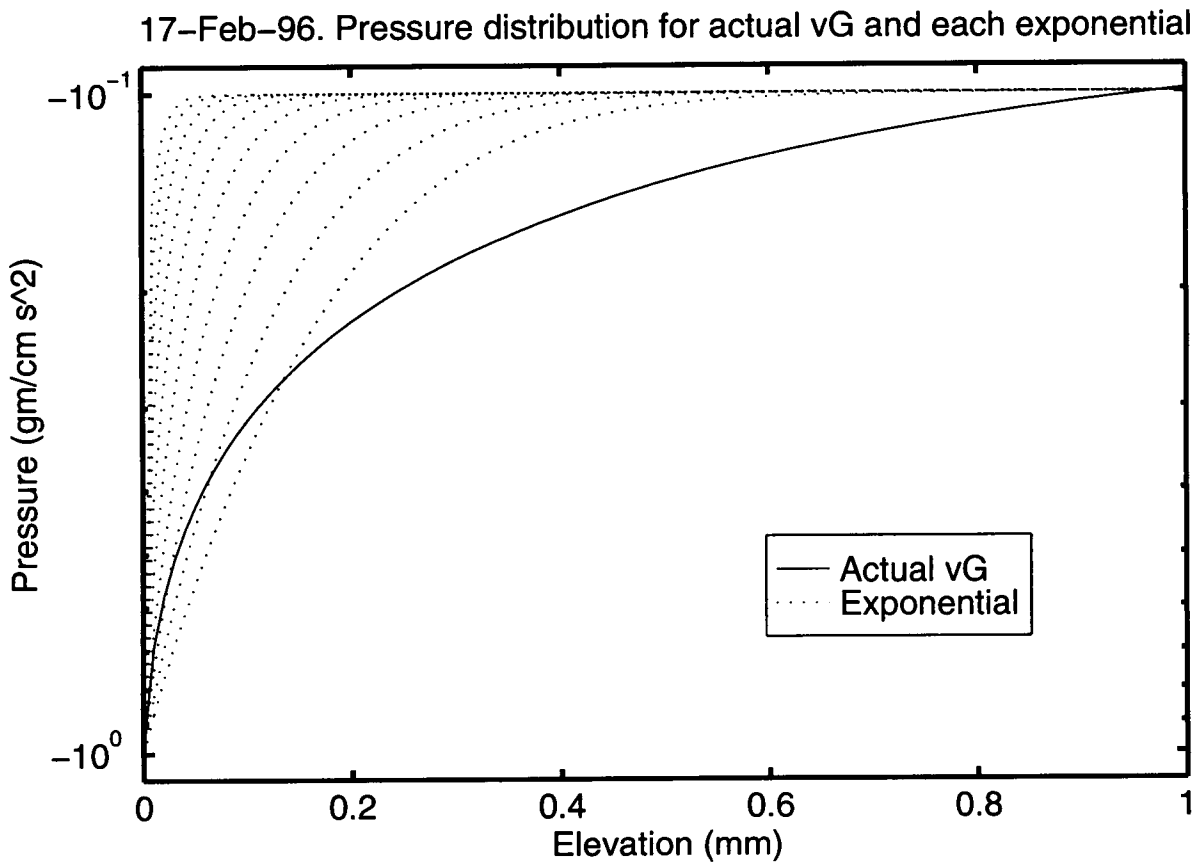

Figure 15-4: 2/17/96. expvg_press1.eps. Pressure distribution for each β_i in Figure 15-2 independently determined, compared with the true pressure distribution.

References

Banerjee, P. K. and R. Butterfield. 1981. *Boundary Element Methods in Engineering Science.* London, England: McGraw-Hill.

Holt, R. M., J. L. Wilson, and R. J. Glass. 1995. Approximate Solution of Steady Unsaturated Flow Equations using a Piecewise Hydraulic Conductivity Function. *Supplement to Eos, Transactions 76*(46), F262.

Pullan, A. J. and I. F. Collins. 1987. Two- and Three-Dimensional Steady Quasi-Linear Infiltration From Buried and Surface Cavities Using Boundary Element Techniques. *Water Resources Research 23*(8), 1633–1644.

Rasmussen, T. C. 1987. Computer Simulation Model of Steady Fluid Flow and Solute Transport Through Three-Dimensional Networks of Variably Saturated, Discrete Fractures. In D. D. Evans and T. J. Nicholson (Eds.), *Flow and Transport Through Unsaturated Fractured Rock*, Geophysical Monograph 42, pp. 107–114. Washington, DC: American Geophysical Union.

van Genuchten, M. T. 1980. A Closed-form Equation for Predicting the Hydraulic Conductivity of Unsaturated Soils. *Soil Science Society of America Journal 44*, 892–898.

16 Geomorphology of Mountain Erosion

Account Number: **20-5704-166 and 20-5704-174**
Collaborators: **David Farrell, Oliver Chadwick, Randy Fedors**
Directories: **$HOME2/Matlab/MassWaste → $MassWaste**

Objective: Build and use a relatively straightforward model for the redistribution of eroded material on a subregional to regional scale. The immediate application is to predict the slip rate of a fault based on the shape of alluvial fans.

12/20/95 Summary of previous work.

In the subregional flow and transport processes research project, I developed a simple finite difference (8/95) and slightly more sophisticated finite element (11/95) model based on using a DEM grid of elevations. See Stothoff and Bagtzoglou (1996) for a description of the FE application. The original YM work was done in ***$HOME2/Subreg/YMElev/MassWaste/MatMod.*** The object of the exercise was to predict the active depth of colluvium at Yucca Mountain. The model assumes quasi-steady state, with governing equations

$$\nabla q_{alluv} = Src, \tag{16-1}$$

$$q_{alluv} = -kb\nabla h, \tag{16-2}$$

$$Src = A\exp(-b/b_0)\exp(\alpha_1 \nabla h/\max(|\nabla h|))\exp(\alpha_2 radiation), \tag{16-3}$$

where q_{alluv} is the flux of alluvium/colluvium, k is a transport speed, b is the thickness of the flux zone, h is the elevation of the ground surface, A is a (material-dependent) erosion potential, b_0 is an extinction depth for erosion, α_1 and α_2 are coefficients, and *radiation* is solar radiation load (in winter?). The model was developed with no recourse to the literature. I expect this model to be appropriate for thin films, but flowing water is not considered; this is a serious weakness in washes and in deep alluvium.

In the subregional work, the elevation h is given; b is the unknown to be determined, and k is assumed spatially constant and subsumed into A. The FD model assumed $b_0 \to \infty$ and $\alpha_2 = 0$, which yielded very pixelly depths. The FE work suggested that the slope-dependent and radiation-dependent source-term modifiers do not have particularly significant impacts on colluvium distributions at YM, as long as b_0 is used. Values for b_0 were about 2 cm, and A/k were about

0.25. The implementation was crude, in the sense that the problem is hyperbolic and explicit flow-routing algorithms could be used to solve for b, rather than the brute-force Jacobi iteration I adopted. I expect a more appropriate algorithm could speed up calculations by one or two orders of magnitude. Nevertheless, usable approximations to colluvium depth were obtained.

Yesterday David Farrell pointed out an article which uses essentially the same model for q_{alluv} as a short-range transport mechanism, with the active diffusion depth constant, and uses a stormwater flow-routing scheme for long-range transport (Beaumont et al., 1992). The stormwater model drains orography-forced precipitation, and transports sediment according to

$$q_f^{eqb} = -K_f q_r \nabla h, \tag{16-4}$$

where q_f^{eqb} is the local-equilibrium sediment carrying capacity, K_f is a proportionality constant, and q_r is the runoff discharge.

12/21/95 Continued development.

In the Beaumont et al. (1992) paper, orography-forced precipitation for South Island, New Zealand, is assumed to be according to adiabatic decompression of moist air as it passes over the model topography. The simplest approach is taken, where air flux is normal to a grid boundary, steady, and uniform. Given $q_w(x = 0)$ is the flux of water vapor per unit length normal to the direction of flow, conversion of q_w to precipition rate $v_R(x)$ is given by

$$v_R(x) = -\frac{\mathrm{d}q_w(x)}{\mathrm{d}x} = \frac{h(x)}{h_R l_R} q_w(x) \tag{16-5}$$

where $a_R = h_R l_R$ is an extraction efficiency parameter governed by the topographic scale height, h_R, and the length scale, l_R, over which $1/e$ of the available precipitation would be extracted were $h(x) = h_R$.

In the work cited, h is the only dependent variable, all other flow parameters are constant except q_w, and q_w is adjusted according to the quasi-steady rainfall distribution.

An alluvium-flow model somewhat improved over the Beaumont et al. (1992) approach might also consider the colluvium layer (b) to be an unknown parameter. I propose a set of coupled equations:

$$\frac{\partial h}{\partial t} - \frac{\mathrm{d}z}{\mathrm{d}t} + Q_{weather} = 0, \tag{16-6}$$

$$\frac{\partial b}{\partial t} + \nabla q_{alluv} - \frac{V_{alluv}}{V_{rock}} Q_{weather} = 0, \tag{16-7}$$

$$q_{alluv} = -(kb + K_f q_r)\nabla(h + b), \tag{16-8}$$

where h is bedrock elevation, b is depth of colluvium/alluvium, $\mathrm{d}z/\mathrm{d}t$ represents change in elevation due to structural forces, V_{alluv}/V_{rock} represents volume expansion from bedrock to rubble, q_r is surface-water flux (episodic at Bare Mountain), and other parameters are as before. Adding 16-6 and 16-7 together,

$$\frac{\partial(h+b)}{\partial t} + \nabla q_{alluv} - \frac{\mathrm{d}z}{\mathrm{d}t} + \left(1 - \frac{V_{alluv}}{V_{rock}}\right) Q_{weather} = 0, \tag{16-9}$$

which is akin to the diffusion equation. It may be appropriate to solve 16-9 and 16-6 as the two equations. The source term $Q_{weather}$ might be $A\exp(-d/d_0)$, rather than $A\exp(-b/b_0)$, where d is thickness of cover normal to the surface rather than depth at the surface. The modification should not be numerically large unless there are steep slopes. I would expect A to be a function of rock type, solar radiation, slope, average temperature, and precipitation, so A would vary according to climatic influences.

Thoughts on modelling

The first-cut approach to modelling alluvium flow was to brute-force using Jacobi iteration to reach a steady state. Explicit time-stepping might not be too bad with this approach, but the river flow may be tricky. A second, implicit, tack might be to take advantage of the hyperbolic nature of the problem and integrate in shells from high elevation to low elevation. The scheme would be

1. Classify each face as a through-, convergence-, or divergence-face.
2. Find high points.
3. Start at highest point and create concentric layers that have completely outflowing faces at the downhill side.
4. Solve for unknowns at all nodes in the uppermost layer that have old values, using the newest uphill values as boundary conditions.
5. Repeat until all layers have been processed.

The advantage of this approach is that an efficient skyline solver could be used on systems with a relatively small bandwidth, and difficulties with allocating downhill flows for convergent/divergent faces are eased. Convergent/divergent faces might also be treated as a network of ridges/washes.

In fact, it might be a good idea to create a "potential wash" network, consisting of all edges and all cell diagonals, which would be activated at convergent faces and saddle or saddle-like cells. The trick would be in deciding when to turn on the wash behavior.

1/3/96 More thoughts on modelling.

The previous proposed model equations (16-6 and 16-9) have parameters k and K_f, as well as parameters associated with sources, and a currently unspecified surface-water flux q_r. The surface-water flux is simply overland flow, which is obviously highly transient. As a first cut, it may be acceptable to maintain a set of maximum flood depths corresponding to storms of various return periods (*i.e.*, 10-yr, 100-yr, 1000-yr) and calculate q_r as a weighted sum of the storm events, suitably averaged over time. Precipitation is plausibly elevation-dependent.

Additional thought: the alluvium/colluvium depth b should be broken into an "active" and an "inactive" zone, where the active zone consists of the top meter or so and the inactive zone is any remainder. The component of the q_{alluv} fluxes due to diffusion therefore is limited by a maximum depth.

As a quick and dirty test of the alluvium-fan idea, I propose that a rectangular region be considered. The initial condition for the region might be a set of small-amplitude sine waves, with a square-wave block uplift superimposed in the middle portion of the region ("Bare Mountain"). Along one side of the block there should be a hinge fault, with hinged uplift of "Bare Mountain" and "Amargosa Valley", and hinged downdrop of "Crater Flat". The surface should start out as bare rock. I predict that this test should generate steeper alluvial fans along the fault as the distance from the hinge increases, with larger and shallower fans on the opposite side of the block. As a rough start, perhaps 100 cells parallel to the fault, with the block consisting of 50–100 cells and the outwash areas consisting of 200-300 each? Perhaps ten sine waves perpendicular to the mountain to initiate washes.

1/4/96 Setup of test problems.

Created a project directory (***$HOME2/Matlab/MassWaste***) and copied the *Matlab* files for the YM work into the project directory. The quick and dirty test problem will be set up as defined above.

1/7/96 First examination of test problems.

Test problem is a halfsine mountain with normally distributed random noise superimposed, with initial conditions symmetric east and west of the mountain ridge. There is a fault at the base of E flank of mountain. Initial work quickly identified the need to ensure time scales are matched.

3/1/96 First entry for lahar examination.

Account Number: **20-5708-?**
Collaborators: **Chuck Connors**
Directories: **$HOME2/Matlab/Lahar → $Lahar**

Objective: Build and use a relatively straightforward model for the redistribution of gravity-driven flows on a subregional to regional scale. The immediate application is to predict the redistribution of potential lahars with various source magnitudes. The idea is that the probability of the event size together with the redistribution area of the event will provide an estimate of the risk. The initial project is a quick look to demonstrate methodology; this may be expanded in the future.

A set of files was obtained from Ron Martin, containing a digital elevation map (DEM) of a portion of the Kamchatka peninsula, southeast of Siberia and northeast of Japan. The files are in the .bil format. The ***$Lahar*** subdirectory was created on sierra, which will be the root directory for work on this project.

The overall DEM consists of 1209 rows and 1023 columns, with a grid spacing of 187.4725 m (all coordinates are in meters unless otherwise noted). Overall coordinates range from 5.0004×10^5 to 6.9164×10^5 in the east-west direction and 6.0949×10^6 to 6.3214×10^6 in the north-south direction. The region of interest is roughly 5.5×10^5 to 6.2×10^5 in the east-west direction and 6.15×10^6 to 6.21×10^6 in the north-south direction. The source for the lahar sequence is the volcano top located approximately 5.8×10^5 to 5.9×10^5 in the east-west direction and 6.185×10^6 to 6.19×10^6 in the north-south direction. As an approximation, the area with elevation above roughly 2750 m will serve as the source area, with the largest event considered completely removing the complete volume above that elevation.

The *Matlab* water-routing routines developed to simulate sediment transport will be modified to simulate the behavior of the lahar flows. Lahars are essentially mudflows with on the order of

30 percent moisture content, and behave in many ways like somewhat more viscous water flows. The probability calculations require only the area covered by any portion of a lahar flow, so these grid cells will be the end product for each event.

The modelling strategy that will be followed is extremely straightforward:

- Before running any flow simulations, calculate information that will be used for every simulation.
  - Infill depths required to assure outflow from each grid block.
  - Routing directions for the (infilled) DEM.
  - Routing weights for the (infilled) DEM.
  - Potential maximum final depth for each grid block, based on the slope of the (infilled) DEM and a minimum velocity below which flow will stop.
- Calculate the source volume and location.
- Route the flow downhill, removing a volume at each block corresponding to the final depth of lahar in the block *including infill depths calculated previously.*
- Find the grid cells with appreciable depths of lahar.
- Output.

Infill depths will be calculated by finding all grid blocks that do not have egress, and performing Laplace smoothing on the blocks and their neighbors until all blocks have egress. Infill depths are the difference between the smoothed and original depths, holding the boundaries fixed; expansion steps may be necessary if negative infill depths result from the procedure.

Flow velocity will loosely be modelled by

$$\mathbf{v} = -b\mathbf{K} \cdot (\nabla P + \rho g \nabla z) \approx -b\mathbf{K} \cdot (\rho g \nabla z). \tag{16-10}$$

The criterion for depth of lahar at stoppage will be $Ab\nabla z$, which has one global adjustable parameter (A). Potential final depth is easily calculated. The A parameter will be selected by requiring that a particular slope (say 15 degrees) yields a depth of 10 cm (say).

3/8/96 Summary of first lahar examination.

It turns out that removing hollows was quite important in creating successful footprints, and it was critical to use the same criterion for the hollow-removal algorithm as for the flow-routing algorithm; otherwise, the flow-routing found stray hollows and unrealistic flows resulted. It also turns out that 8-way routing is far superior to 4-way routing (*i.e.*, cells to the NE, NW, SW, and SE are available for flow as well as the cells to the E, N, W, and S). A C-language routine, **route_9waySink.cc**, did the routing; the routine was compiled into a *Matlab* mex file. The routing was defined using *Matlab* routine **make_route9way.m**. A set of seven initial lahar volumes ranging from 10^6 to 10^9 m^3 was routed, with routing driven by the **do_set.m** routine.

The resultant set of lahar footprints was handed off to Chuck Connor for his own needs.

4/14/96 First entry for re-examination of shallow colluvium flow.

Account Number: **20-5708-861**
Collaborators: **None**
Directories: **$HOME2/Matlab/ColluvWaste → $ColluvWaste**

Objective: Build and use a relatively straightforward model for the quasi-steady-state redistribution of gravity-driven shallow colluvium based on a DEM. A first numerical model for the process was developed under the now-discontinued Subregional Hydrology Research Project. The first model, a simplistic 4-way finite-difference model, suffers from slow convergence and is unrealistic in neglecting diagonal flow. Based on subsequent work, a much faster and more realistic model should be possible using flow routing ideas.

A 4-way flow-routing model was tried in the lahar work. The plausibility of the 4-way model was much lower than the 8-way model developed soon afterward. I propose here yet another 8-way flow-routing model for the colluvium flow, which should yield fast, unique, plausible solutions.

The original YM work was done in ***$HOME2/Subreg/YMElev/Mass Waste/MatMod.*** The object of the exercise was to predict the active depth of colluvium at Yucca Mountain. The model assumes quasi-steady state, with governing equations

$$\nabla q_{alluv} = Src, \tag{16-11}$$

$$q_{alluv} = -kb\nabla h, \tag{16-12}$$

$$Src = A\exp(-b/b_0)\exp(\alpha_1 \nabla h/\max(|\nabla h|))\exp(\alpha_2 radiation), \tag{16-13}$$

where q_{alluv} is the flux of alluvium/colluvium, k is a transport speed, b is the depth of the flux zone, h is the elevation of the ground surface, A is a (material-dependent) erosion potential, b_0 is an extinction depth for erosion, α_1 and α_2 are coefficients, and *radiation* is solar radiation load (in winter?). The model was developed with no recourse to the literature. I expect this model to be appropriate for thin films, but flowing water is not considered; this is a serious weakness in washes and in deep alluvium.

In the subregional work, the elevation h is given; b is the unknown to be determined, and k is assumed spatially constant and subsumed into A. The FD model assumed $b_0 \to \infty$ and $\alpha_2 = 0$, which yielded very pixelly depths. The FE work suggested that the slope-dependent and radiation-dependent source-term modifiers do not have particularly significant impacts on colluvium distributions at YM, as long as b_0 is used. Values for b_0 were about 2 cm, and A/k were about 0.25.

Several new approaches are to be implemented in the new model. The governing equation will be solved using upstream-weighted flow routing with finite-volume ideas to determine routing. Upstream weighting is to be performed only on the depth, so that the upstream depth is used and routing from highest to lowest node can be performed in one pass. In the pass from high to low elevation, a somewhat novel routing approach will be followed that assumes each of the eight directions from the current node are direct links. This routing approach is somewhat odd, insofar as adjacent nodes have diagonal connections that cross. Nevertheless, I expect the approach to be about the fastest 8-way routing algorithm around when implemented in C.

Eight connections are to be examined for the current node. Consider the four square elements surrounding the current node. Bisecting each of the eight element faces furthest from the current node forms eight partitions between connections. If the current node is the same elevation as the other node, the connection is ignored. Assuming that material properties are subsumed into the source term A as previously, an active connection from the current node, o, to another node, i, has a total flux of

$$Q_{oi} = b_{oi}\left(\frac{h_o - h_i}{\Delta_{oi}}\right) W|_{midpt}, \tag{16-14}$$

where b_{oi} is the colluvium depth at the higher node, h is the elevation of the ground surface, Δ_{oi} is the distance between the connected nodes, and $W|_{midpt}$ is the width of the connection at the midpoint between nodes. The following assumes that a regular DEM is used, with squares of side

length Δ. The four row and column connections have

$$\Delta_{oi} = \Delta \tag{16-15}$$

$$W|_{midpt} = \Delta/2 \tag{16-16}$$

$$Q_{oi} = b_{oi}(h_o - h_i)/2 \tag{16-17}$$

while the four diagonal connections have

$$\Delta_{oi} = \sqrt{2}\Delta \tag{16-18}$$

$$W|_{midpt} = \sqrt{2}\Delta/3 \tag{16-19}$$

$$Q_{oi} = b_{oi}(h_o - h_i)/3 \tag{16-20}$$

The second relationship follows from geometric considerations. The element diagonal has length $L = \sqrt{2}\Delta$. We wish to determine the length of the line, along the diagonal perpendicular to the connection, that lies between two partitions; a partition bisects the far element face. Similar triangles are used. The triangle formed by the perpendicular to the connection diagonal that intersects the partition bisection point has a long side of $3L/4$ and short side of $L/4$. For the similar triangle ending at the connection midpoint, the lengths are scaled by 2/3, yielding $\Delta_{oi} = L$ and $W = L/3$ (note two triangles form the entire width).

Given the connections, a mass balance is performed for the current node to determine colluvium depth.

$$\Delta^2 A \exp(-b_o/b_0) = \sum_{i=1}^{N} a_{oi} b_{oi}(h_o - h_i), \tag{16-21}$$

where a_{oi} is the area factor of the connection (1/2 for rows/columns and 1/3 for diagonals). Since sorting in order of elevation has been performed, each node equation reduces to the form

$$b_o = C_1 \exp(-b_o/b_0) + C_2, \tag{16-22}$$

where

$$C_1 = \frac{\Delta^2 A}{\sum_{i=1}^{N_{out}} a_{oi}(h_o - h_i)}, \tag{16-23}$$

$$C_2 = -\frac{\sum_{i=1}^{N_{in}} a_{oi} b_i (h_o - h_i)}{\sum_{i=1}^{N_{out}} a_{oi}(h_o - h_i)}. \tag{16-24}$$

An iterative approach, such as Newton's method or bisection, should be used to find b_o. Note that b_o should lie between C_2 and $C_1 + C_2$, so that bisection should be robust.

When there are no outgoing connections, the approach breaks down. For such cases, probably the best thing is to use a default value such as the maximum of the incoming connection depths.

4/15/96 More shallow colluvium flow.

SAS

I coded up the new algorithm in **$ColluvWaste/calc_9waySink_depth.cc**. The algorithm works like a champ, with similar but much less pixelly alluvium distributions than the old Jacobi four-way algorithm. Not only are the results more plausible, but the algorithm is blazing fast – it takes about 12 seconds for the entire YM area, whereas before I don't believe complete convergence occurred even in overnight runs. Note that there is no convergence question with the new algorithm, and it takes longer to plot than to calculate. With this approach, it may be feasible to test out adjustments to transport based on equivalent-steady-state sediment routing. Field data to match predictions is now desperately needed.

1/10/97 Part of software requirements for UZFLOW.

SAS

I developed a first-cut description of proposed software requirements for the UZFLOW module, documented in the section on IPA3. The description pertinant to geomorphic modeling is copied below in italics. The description was copied here on 8/18/98 for completeness.

Three equilibrium balance equations are solved to calculate the equilibrium depth of alluvium over the YM region; (i) an overall alluvium mass balance, (ii) a sediment mass balance, and (iii) a hydraulic mass balance or stream-flow model. The overall mass balance for alluvium, the first equation, is

$$\nabla \cdot \mathbf{q}_{alluv} + Q_{wea} + \overline{Q_{str}} = 0, \tag{16-25}$$

where $\mathbf{q}_{alluv}$ is the flux of alluvium, Q_{wea} is the source of alluvium due to weathering, and $\overline{Q_{str}}$ is the time-averaged flux due to stream action. The erosion-balance model assumes that all processes are at equilibrium. Thus, the stream-flow model assumes that a representative spatially uniform rainfall rate is applied over the entire mountain, and the resulting equilibrium hydraulic flux distribution is used to calculate equilibrium sediment transport. As streamflow is actually highly episodic at YM, the equilibrium sediment-transport velocities and erosion/deposition rates must be adjusted to account for the time with no streamflow. Time averaged stream-action flux is approximated here by

$$\overline{Q_{str}} \approx F_{str} Q_{str}, \tag{16-26}$$

where F_{str} is the fraction of time stream flow occurs. The procedure is likely to under-represent the time average in headwater and overland-flow areas, and over-represent the time average in deep washes and downstream areas.

Flux of alluvium, other than through sediment transport, is assumed to occur through creep and is gravity-driven,

$$\mathbf{q}_{alluv} = -Kb\nabla Z, \tag{16-27}$$

where b is the depth of alluvium, Z is the ground surface elevation, and K is a creep conductance (assumed spatially constant here). The alluvium-flux term is similar to the short-range transport model used by Beaumont et al. (1992), except that here b varies with time and Z is constant, while in the Beaumont et al. (1992) application, b is assumed constant and Z is allowed to vary over time.

A simple source term representing weathering is used here. It is assumed that alluvium protects the bedrock from weathering, so that weathering decreases exponentially with alluvial depth:

$$Q_{wea} = Q_0 \exp(-b/b_0) \tag{16-28}$$

where Q_0 is the source strength, and b_0 represents a weathering-protection alluvium depth. The weathering model has two fitting parameters, Q_0 and b_0, which can be used to match observed alluvium depths.

Erosion and deposition through stream action is calculated using the second equilibrium balance equation, a sediment-balance equation,

$$\nabla \cdot c_s \mathbf{q}_w - Q_{str} = 0, \tag{16-29}$$

where c_s is the concentration of the sediment in water and $\mathbf{q}_w$ is the flux of water. Following standard practices in the literature (e.g., Woolhiser et al. (1990)), a simple kinetic rate law is used to characterize erosion and deposition,

$$Q_{str} = C_g(c_s - c_{eq}), \tag{16-30}$$

where c_{eq} is the equilibrium sediment concentration for a reach along a stream bed and C_g is an equilibrium constant.

Numerous equilibrium sediment concentration capacity relationships exist in the literature (e.g., Yang (1973), Kilinc and Richardson (1973), Ackers and White (1973), Yalin (1963)). A particularly simple relationship is used herein (Meyer and Wischmeier, 1969), based on tractive force:

$$c_{eq} = C_s \frac{\mathbf{v}^4}{h}, \tag{16-31}$$

where C_s is a constant, $\mathbf{v}$ is water velocity, and h is hydraulic depth.

For erosion, C_g is a constant describing the erodibility of the alluvium or bedrock. For deposition ($c_s > c_{eq}$), C_g assumes that particles have fall velocities and drag characteristics similar to spheres (Fair and Geyer, 1954), and a coupled set of equations are used to calculate C_g:

$$v_s^2 = \frac{4}{3}\frac{g(S_s - 1)d}{C_D}, \tag{16-32}$$

$$C_D = \frac{24}{Re} + \frac{3}{\sqrt{Re}} + 0.34, \tag{16-33}$$

$$Re = v_s d/\nu, \tag{16-34}$$

$$C_g = \frac{v_s}{h}\left(1 - \frac{c_{eq}}{c_s}\right), \tag{16-35}$$

where v_s is the particle settling velocity, g is the acceleration due to gravity, S_s is the particle specific gravity, d is the particle diameter, C_D is the drag coefficient, Re is the Reynold's number, and ν is the kinematic viscosity.

The final equilibrium balance equation required to complete the alluvium-balance system is the water-balance equation,

$$\nabla \cdot \mathbf{q}_w + Q_{rain} = 0, \tag{16-36}$$

where Q_{rain} is the net rainfall. A standard practice in the literature is to use a kinematic-wave approximation for hydraulic flux in conjunction with the Manning hydraulic resistance law, so that (in metric units)

$$\mathbf{q}_w = \frac{S^{1/2}h^{5/3}}{n}, \tag{16-37}$$

where S is the slope and n is Manning's roughness coefficient.

Each of the three balance equations is solved using the same general finite-volume flow-routing approach. The DEM grid is discretized into square boxes, or nodes, with 1D connections to the nearest eight nodes. Taking advantage of the hyperbolic nature of the equations by assuming that upstream variables uniquely determine fluxes to downstream nodes, the nodes in the grid can be processed in order from highest to lowest elevation in one pass.

The water-balance equation is solved independently of the sediment- and alluvium-balance equations. In the water-balance equation, each node is processed using the algebraic equation,

$$A_i q_{rain} + \sum_{j=up} \frac{w_{ij}h_j^{5/3}}{n}\left(\frac{Z_j - Z_i}{\Delta_{ij}}\right)^{1/2} - \sum_{j=down} \frac{w_{ij}h_i^{5/3}}{n}\left(\frac{Z_i - Z_j}{\Delta_{ij}}\right)^{1/2} = 0, \tag{16-38}$$

where node i is the node being processed, node j is a neighboring node, A_i is the area associated with node i, q_{rain} is the rainfall rate minus infiltration, w_{ij} is the width of the 1D connection between

nodes i and j, and Δ_{ij} is the distance between nodes i and j. Summing over upstream nodes is denoted by $j = up$, and summing over downstream nodes is denoted by $j = down$. On a square grid with constant node spacing Δ, w_{ij} is $\Delta/2$ for nearest-neighbor connections and $\sqrt{2}\Delta/3$ for diagonal connections.

The sediment- and alluvium-balance equations are solved simultaneously, by requiring that each nodal alluvium depth and sediment concentration is compatible with outflow from the node. The algebraic balance equations are:

$$\sum_{j=up} c_{sj} Q_{wij} - \sum_{j=down} c_{si} Q_{wij} + \frac{A_i}{8} \sum_{j=down} \overline{C_{gij}(c_{eqij} - c_{si})} = 0, \tag{16-39}$$

$$\sum_{j=1}^{8} w_{ij} K_{ij} b_{up} \left(\frac{Z_j - Z_i}{\Delta_{ij}} \right) + A_i Q_0 \exp(-b_i/b_0) - \frac{A_i}{8} \sum_{j=down} \overline{C_{gij}(c_{eqij} - c_{si})} = 0, \tag{16-40}$$

where b_{up} is the upstream alluvium depth. Alluvium depths are solved by bisection between a minimum depth of 0 m and a maximum depth (arbitrarily assumed to be 20 m here). The equilibrium sediment concentration is found during each bisection step.

The flow-routing approach works well when there are no local minima in the domain, so that there is a route from every node to the boundary. A physical local minimum cannot exist at equilibrium unless there is a physical mechanism for removing alluvium (e.g., wind transport). Typically, however, local minima are artifacts of the DEM resolution, as elevations are only reported to the nearest meter. Also, narrow features such as upstream wash channels, which are on the order of a meter wide, cannot be resolved with the 30-m DEM grid. About 0.5 percent of the nodes in the DEM are local minima, almost all occurring in wash bottoms but a few occurring along ridgetops. For these minimum nodes, a preprocessing step is performed to eliminate artificial local minima, by artificially raising minima nodes at least 10 cm above the lowest of the surrounding nodes. A number of passes are required to eliminate multinode basins.

There are a total of 11 adjustable parameters in the set of coupled balance equations, The 11 parameters, and values found to result in reasonable predictions of colluvium depths, are shown in Table 16-1. As F_{str}, K, and Q_0 control the relative importance of stream processes, colluvial diffusion, and weathering, these three parameters are not completely independent, so scaling the three parameters by the same constant does not modify the predicted colluvium distribution.

Within the mapped alluvium outline, a post-processing step is performed to provide more realistic alluvium depths. An exponential relationship of alluvial depth to surface slope was determined by regression,

$$b = 47 \exp(-0.32 s) \tag{16-41}$$

Table 16-1: Adjustable parameters for creating colluvium distributions.

Name	Symbol	Base Value
Net rainfall rate	q_{rain}	5 cm/hr
Manning's roughness coefficient	n	0.1
Kinetic coefficient for alluvium scour	C_g	0.1 s^{-1}
Kinetic coefficient for bedrock scour	C_g	0.002 s^{-1}
Traction coefficient for sediment equilibrium	C_s	10^{-3}
Particle diameter	d	1 mm
Particle specific gravity	S_s	2.5
Alluvium creep conductance	K	10^{-12} m/s
Alluvium weathering rate	Q_0	10^{-9} m^3/m^2s
Alluvium weathering depth	b_0	1 cm
Fraction of time in streamflow	F_{str}	30 min/100 yr

where s is the slope, in degrees, of the ground surface at the nearest grid point in the DEM. The coefficient of determination is 0.61 for the relationship, using information from 56 of the boreholes discussed by Fernandez et al. (1994). Wherever the slope is less than 10 degrees within the Scott and Bonk (1984) alluvium outline, the alluvium depths are calculated using Equation 16-41; otherwise, the colluvium-routing model predictions are used. Note that in the near future Equation 16-41 will be replaced with a slightly better relationship of the form

$$b = as^{-c}, \tag{16-42}$$

where a and c are constants.

5/19/98 Equations for soil-genesis model.

Account Number: **20-5702-861**
Collaborators: **Oliver Chadwick, Randy Fedors**

During the trip to YM the past several days, Oliver Chadwick and I had several discussions regarding appropriate soil-genesis models for YM. We agreed that an attractive approach is to lay out a general formulation, then emphasize the aspects that are more appropriate for YM in particular.

The issue is of considerable importance, as soil depth and composition have a significant impact on MAI. For example, consider two representative hillslopes, representing typical YM and

Table 16-2: Representative soil properties for YM and Phinney Canyon.

Parameter	Yucca Mountain	Phinney Canyon
K_{sat} (cm/d)	106	10.8
k (cm^2)	1.3×10^{-8}	2.2×10^{-9}
α (cm^{-1})	0.075	0.02
P_0 (gm/cm-s^2)	1.3×10^{4}	4.9×10^{4}
n	1.89	1.41
m	0.47	0.29
θ_s	0.41	0.45
θ_r	0.065	0.067

typical Phinney Canyon hillslopes, with soil-filled fractured bedrock underlying a soil with rock fragments. The soil at YM is a sandy loam with roughly half rock fragments, while at Phinney Canyon the soil is a silty loam with about a third rock fragments and roughly twice the depth. Typical parameters for these soil types are in Table 16-2: Assume soil depth is 25 cm at YM and 50 cm at Phinney Canyon. Account for rock fragments by assuming that θ_s and θ_r are 0.205 and 0.0325 (YM) and 0.3015 and 0.449 (Phinney Canyon), yielding total pore space of 4.1 cm/cm^3 (YM) and 12.06 cm/cm^3 (Phinney Canyon).

Several simulations were presented in Table 2-10, with calcite- and soil-filled properties fairly similar in nature. With calcite-filled fractures, a base case of 25 cm cover and 0.2 porosity has MAI of 12 mm/yr, while 50 cm cover with 0.3 porosity has MAI of 4.9 mm/yr (approximate reduction of 0.4). A base case of 25 cm cover and P_0 of 10^4 has MAI of 18 mm/yr while 50 cm cover and P_0 of 5×10^4 gm/cm-s^2 has MAI of 0.13 mm/yr (approximate reduction of 0.0072). A base case of 25 cm cover and K_{sat} of 10^{-8} cm^2 has MAI of 8.6 mm/yr while 50 cm cover and K_{sat} of 10^{-9} cm^2 has MAI of 11 mm/yr (negligible increase expected if K_{sat} is 2×10^{-9} cm^2). Similarly, there is little impact due to van Genuchten m. If the effects of soil depth, porosity, and P_0 can be superimposed, the combination results in a decrease in MAI by about 2.5 orders of magnitude for the current climatic conditions.

The work will build upon the soil genesis model that I developed several years ago. That model was formulated before I had heard that most of the soil currently at YM is of æolian origin. The model assumes that soil is generated by weathering of the bedrock, with weathering exponentially decreasing with soil depth. Soil moves downslope according to creep, with rate of movement proportional to bedrock slope. Soil is also moved according to overland flow, characterized by one steady-state storm and one sediment grain size. As there is only overland flow for a very short

fraction of the time in the YM area, the sediment transport is time-weighted.

The structure and approach of the new model will be generally similar to the first model, only significantly more sophisticated in the physical processes considered. Instead of one generic soil, several size classes will be considered, each characterized by their respective mass fraction. Each size class will provide a source for every smaller size class as weathering occurs. Two types of external source material will be considered, æolian dust and rocks plucked from the bedrock. Downhill movement will occur through creep and overland flow, as before, but will also occur according to slump based on the critical angle. The soil profile may also be discretized into several computational layers.

Size classes

The preliminary discussion suggested that several size classes might be considered, including cobbles, gravel, coarse sand, fine sand and silt, clay (< 2 μm), and organic content. Dani suggested that it might be more attractive to use a particle-size distribution, characterized with perhaps a few means and standard deviations to capture modes. If weathering processes can be described as functionally dependent on particle size, the evolution of the statistical distribution can be recreated using a detailed histogram reconstructed from the statistics.

For example, assume that the particle-size distribution is lognormally distributed. Generating a histogram of perhaps a hundred bins, the weathering of the particles in each bin is straightforward, resulting in an output particle distribution for the bin. Each of the input bins creates an output distribution, which are accumulated into an overall output distribution. The statistics of the output distribution are then calculated and used for the next time step. The procedure is particularly useful if weathering-rate tables are formulated as a statistical description of the distribution of output particle sizes.

Weathering

The rates of the weathering and movement processes are typically dependent on temperature, moisture content, and perhaps organic content or vegetation density. The rate law for weathering will be of the standard exponential form,

$$\frac{\partial \chi_i}{\partial t} = \alpha_{ij} \chi_j, \tag{16-43}$$

where subscripts i and j represent the finer classes and the larger class, respectively, χ represents the mass fraction of the size class, and α_{ij} represents the rate constant. The rate constant is formed by adding physical weathering and chemical weathering rates. Physical weathering is most important for the large particles, scaling with the inverse of particle volume, while chemical weathering scales with particle surface area.

As the rates are dependent on the number of freeze-thaw cycles (for physical weathering) and on temperature, moisture content, and organic content (for chemical weathering), all of which vary rapidly relative to the anticipated time steps of at least centuries, it is necessary to use effective rates. The effective rates will be calculated by (i) forming a table of weathering rate (combined physical and chemical) as a function of freeze-thaw cycles, temperature, moisture content, and organic content; and (ii) calculating the fraction of the time step that each rate is active. The effective rate for each size breakdown is then

$$\alpha_{eff} = \sum_{i=1}^{N} \alpha_i \Delta t_i / \sum_{i=1}^{N} \Delta t_i, \tag{16-44}$$

where α_{eff} is the effective weathering rate, α_i is the weathering rate for bin i, and Δt_i is the time spent in bin i during the time step ($\sum_{i=1}^{N} \Delta t_i = \Delta t$).

It may be impractical to try to solve for soil moisture and temperature in each computational element for thousands of years, although perhaps a simple bucket model (as used by A. Flint of the United States Geological Survey (USGS)) might do the trick and could be explored in future work. Instead, the results from the many 1D simulations already performed will be used to estimate seasonal mean effective moisture and mean soil temperature as a function of MAP, MAT, hydraulic properties, and solar aspect. In order to use the simulations, the hydraulic characteristics and pore volume for the fine fraction (< 2 mm) will be used to translate between the 1D simulations and the soil column. The simulations may also be used to estimate the number of freeze-thaw cycles as a function of soil depth, MAP, and MAT, or an analytic expression may be used for temperature in a 1D column as a function of a sinusoidal forcing at one end. A synthetic history of MAP and MAT will be required, but not at a finer scale than a decade (all simulations are valid for a decade). The primary difficulty is that the simulations performed to date may be somewhat wetter than they would have been if vegetation was considered. As the rates are more sensitive to temperature than moisture (when sufficient moisture is present), the discrepancy may not have a great deal of impact on soil genesis. Greater impact would be expected under cooler and wetter conditions, where evaporation is less efficient at drying the soil.

Creep

Creep is dependent on soil-component fractions, moisture content, temperature, and vegetation density. Creep is relatively slow when large fragments are present with minimal fines, but as the fine component increases the large fragments are lubricated and creep accelerates. Similarly, soil moisture lubricates creep by decreasing effective pressure. On the other hand, creep decreases as vegetation increases, since roots are effective at holding together soil masses. Creep is drastically reduced when soil moisture is frozen, but freeze-thaw cycles enhance creep by jiggling soil particles.

As with weathering, resistance to creep may be highly time-dependent relative to the size of the time step. An effective resistance may be calculated using the same time-averaging approach as in Equation 16-44.

Slumping

One of the primary components of downhill mass wasting is through sudden slumping (*i.e.*, landslides). Obviously it is impractical to attempt to use a time step that resolves slumping. It is reasonable, however, to assume that the soil column saturates at least once during a time step of centuries. Accordingly, each time step the entire domain will be inspected for the critical angle under saturation and volumes where the critical angle is exceeded will be slumped. This approach succeeds when the time step is long relative to the intervals between saturation events. Assuming that saturation exists, soil composition is the primary determinant of critical angle.

One factor that may increase slumping is earthquakes during saturation conditions. Earthquakes are rare, as are saturation conditions (at least during current climatic conditions). Perhaps a small probability of having an earthquake could be factored in, which would result in a probability of having a decreased critical angle and slumping a somewhat greater proportion of the slopes.

Sources

Two soil-component sources will be considered, æolian dust and bedrock that physically weathers into soil components. The dust source has a regional component and a local component dependent on nearby playas. Dust input is dependent on climate, as cooler and moister conditions form lakes in playas, thereby decreasing dust production. Dust deposition is dependent on particle settling

rates and wind velocity, so that one would expect that dust accumulation might be greater in the relatively calm washes than on the windier ridgetops. As a first crack, a spatially uniform deposition will be considered.

The bedrock type will determine the generated particle-size distribution, with (i) the caprock forming a bimodal distribution (large boulders and lots of sands), (ii) non- to moderately welded units forming fines, (iii) nonlithophysal units forming large chunks, and (iv) lithophysal units forming smaller chunks. As discussed before, physical weathering depends on freezing and thawing. Accordingly, physical weathering decreases exponentially with depth, consistent with the exponential decrease in temperature variation with depth.

Overland flow and transport

The procedures followed in the first model, with one representative storm occurring for a representative length of time, may be modified to account for several storm sizes. Further, transport will be required to account for the range of particle sizes. Again, a time-weighting approach similar to Equation 16-44 will be used to create effective transport due to overland and stream flow. An estimate of storm frequency and flow duration will be required. It may be desirable to tap into Woolhiser's expertise here.

Carbonate modeling

Some of the discussion related to the deposition, dissolution, and redistribution of carbonates (caliche and fracture fillings). Carbonates strongly affect net infiltration. When carbonates or other fillings are present, simulations to date suggest that MAI is reduced in shallow soils but enhanced in deeper soils relative to the situation with unfilled fractures. Carbonates are present at many locations at YM but are lacking at others, and the team has not yet been able to develop a heuristic for predicting the carbonate level at any particular location. A predictive model may help to shed light on the issue.

This issue adds a significant level of complexity and would not be addressed until the soil model is fairly well developed. I suspect that it might be desirable to create a simple bucket model to handle the combination of soil moisture, temperature, wetting-pulse depth, soil carbon dioxide, and carbonate deposition.

Numerical issues

The first model used the 30 m by 30 m DEM that is standard for YM. This resolution is quite coarse, particularly in upper washes where the stream channel is only 1 m wide. It may be more appropriate to create a mesh with triangles, which can easily be done with *Matlab*, with a line along the channel bottom. Flow routing is less ambiguous with triangles than with squares, and node spacing can be adjusted to fit the slope and/or curvature.

Vertical resolution of the profile has not been completely decided on. It may be appropriate to have a uniformly mixed profile for first experiments, with perhaps a few computational layers in later work. The uniformly mixed profile fits better with the idea of using the 1D simulations already generated. Vertical variation does occur due to the natural buoyancy of large rocks in the presence of fines, as was observed in talus-slope dissections. Perhaps we could consider the possibility of characterizing vertical variability with a distribution of particle-size distributions. One might assume that there is a parabolic distribution for particle sizes in talus, for example, with the mode shifting from large particles at the top to smaller particles at the bottom.

8/17/98 Implementation of soil-genesis model.

There are any number of ways to implement the conceptual description of the soil-genesis model. Experience that I gained playing with various approaches before is not encouraging for using standard explicit methods to step through time, even though the approach taken for a quasisteady balance is quite robust. Accordingly, I propose to implement an operator-splitting scheme to handle the problem, with a quasisteady flux component and a composition balance component. The quasisteady flux component includes processes related to creep, overland flow, sediment transport, and dust accumulation. The composition balance component is responsible for updating the composition of the soil column at each node, including vegetation effects. A mixing step may also be incorporated, corresponding to landslides.

Conceptually, the soil column might be broken into layers. The layers might represent an active zone participating in sediment transport and several additional layers representing compositional processes. Under current conditions, all but the valleys might be represented by a single layer, but as climatic conditions change additional layers may be formed.

The computational procedure is as follows:

- Sort grid blocks by elevation plus soil thickness
- Perform a local mass balance proceeding from highest to lowest

The assumption is that flow processes are strongly dominated by elevation differences, so that all fluxes are fully upstream weighted. As will be shown below, flux from one block to the next is governed by soil thickness as well as elevation gradients. If the procedure is used in a quasisteady state manner, soil depth is uniquely determined by the depth required to achieve a flux balance. If the procedure is to be used in a time-dependent manner, however, it will be necessary to limit the time step so that the changes in soil depth are not too drastic in any one time step.

Creep will be considered a film-flow phenomenon. For a film on an incline (Bird et al., 1960),

$$\mathbf{v} = \frac{\rho g b^2 \cos\beta}{2\mu}\left[1 - \left(\frac{x}{b}\right)^2\right], \tag{16-45}$$

$$\bar{\mathbf{v}} = \frac{\rho g b^2 \cos\beta}{3\mu}, \tag{16-46}$$

$$\mathbf{q} = \frac{\rho g b^3 \cos\beta}{3\mu}, \tag{16-47}$$

where $\mathbf{v}$ is velocity tangential to the incline [L/T], $\bar{\mathbf{v}}$ is mean velocity tangential to the incline [L/T], $\mathbf{q}$ is volumetric flux tangential to the incline per unit width [L^3/LT], ρ is density [M/L^3], g is acceleration due to gravity [L/T^2], b is thickness of the layer [L], μ is viscosity of the layer [M/LT], and x is distance below the top of the layer [L]. In our simulations, there should be no reason for viscosity to be different for the various layers, as it will be strongly dependent on root retention. It should be acceptable to keep density constant as well, since it will vary much less than viscosity.

The other major transport component is related to sediment transport. This component is more complex than the creep component, since water moves different particle sizes at different rates.

Water flux is calculated using

$$\mathbf{v} = \frac{R_h^{2/3} S l^{1/2}}{n}, \tag{16-48}$$

$$\mathbf{q} = \mathbf{v} A_w, \tag{16-49}$$

where $\mathbf{v}$ is average fluid velocity [L/T], $R_h = A_w/P$ is hydraulic radius [L], A_w is wetted area [L^2], P is wetted perimeter [L], Sl is slope [–], and n is Manning's n [–]. For a rectangular channel, width is much larger than height so that

$$\mathbf{q} = \frac{W h^{5/3} S l^{1/2}}{n}, \tag{16-50}$$

where W is the width of the channel and h is the height of flow. Note that the total channel width is likely to be only a fraction of the potential surface area in a grid block. I believe that Woolhiser performs the calculations using a triangular channel in plane elements to account for this reduction.

The flow balance becomes

$$A_s Q_{rain} + \sum_{i=1}^{N} k_{io} Q_{wi} = 0, \tag{16-51}$$

where A_s is total surface area [L^2], Q_{rain} is rainfall rate [L/T], k_{io} is +1 if incoming and −1 if outgoing, and Q_{wi} is volumetric water flux [L^3/T]. Sorting from highest to lowest elevation, the flux balance always provides a unique flow depth (assuming an outflow exists for each node) by solving

$$h^{5/3} = \frac{A_s Q_{rain} + \sum Q_{in}}{\sum W_{out} S_{out}^{1/2}}, \tag{16-52}$$

where the *in* and *out* subscripts have self-evident meanings.

The sediment mass balance, for any particular particle size, is

$$\sum S_{in} \mathbf{q}_{in} - S_{out} \sum \mathbf{q}_{out} + (W/L) c_e (S_{out} - S_{eq}) = 0, \tag{16-53}$$

where S is sediment concentration, S_{eq} is equilibrium sediment concentration, W/L is travel width/travel length [–], and c_e is the (velocity-dependent) kinetic exchange coefficient [–]. Julien (1995) discusses other approaches for modeling sediment transport, including both bedload and suspended sediment. It may be desirable to investigate these more-physically based relationships in some greater detail. The equilibrium sediment concentration is a function of water velocity; the previously reported simple relationship (Meyer and Wischmeier, 1969), based on tractive force, will be used:

$$S_{eq} = C_s \frac{\mathbf{v}^4}{h}, \tag{16-54}$$

where C_s is a constant, $\mathbf{v}$ is water velocity, and h is hydraulic depth.

The exchange coefficient depends on whether deposition is occurring or scouring is occurring. If deposition is occurring,

$$c_e = \frac{\mathbf{v}_s}{h} \left(1 - \frac{S_{eq}}{S} \right), \tag{16-55}$$

where $\mathbf{v}_s$ is settling velocity [L/T] and h is water depth [L]. If scouring is occurring, a scouring coefficient is used (different coefficients for alluvium and exposed bedrock).

Julien (1995) discusses sediment transport processes. An approximate relationship for settling velocity, $\mathbf{v}_s$, is given by his equation 5.23c:

$$\mathbf{v}_s = \frac{8\mu_m}{\rho_m d_p}\left[\left(1 + 0.0139(G-1)\frac{g\rho_m^2}{\mu_m^2}\right)^{1/2} - 1\right], \tag{16-56}$$

where the m subscripts represent the mixture, d_p is the particle diameter [L], and G is ρ_p/ρ_m [-]. Julien (1995) suggests that this relationship is valid for a wide range of Reynolds numbers. The relationship replaces the previously used settling velocity formula.

Note that there will be several sediment sizes and perhaps several velocity distributions that will be considered during the simulations. These velocity distributions will be time-averaged.

The source terms for soil are a final component to be added to the transport equations. There are two basic sources, æolian and bedrock-derived. The æolian source will be applied in the top layer. As a first cut, dust will be applied uniformly; it may be appropriate to try a differential deposition based on topography. The bedrock source will be applied in the bottom layer. The source should decay with depth. The formulation used before has the right properties,

$$Src = A\exp(-b/b_0), \tag{16-57}$$

where the two coefficients may depend on climatic conditions.

Transport of all sediment size classes will be solved simultaneously, insofar as the creep component is dependent on the overall mass balance. I found that simultaneous solution provides much more stable results. The overall mass-balance equation becomes

$$\nabla \cdot \frac{W g b^3 \chi_i \rho_i}{3\mu} \nabla z \tag{16-58}$$

where χ_i is the fraction of column mass composed of grain size i, A is the area of a column [L^2], TF_j is the fraction of time that flow case j is active, Q_{dust} is the application rate for dust [L^3/T], A_i is the application rate for bedrock erosion [L^3/T], and b_{0i} is the extinction coefficient for bedrock erosion [L]. Note that iteration is required at each cell, particularly when steady-state simulations are being performed, because the source term for alluvium is dependent on the unknown value of alluvium depth.

The big challenge for modeling will be coming up with parameters and their relationship to climate. Parameters μ, TF, Q_{dust}, A_i, and b_0 should all be functions of climate, either directly (TF, Q_{dust}, A_i, b_0) or indirectly through biological activity related to climate (μ, A_i, b_0). Hopefully Oliver Chadwick will be able to help here.

Parenthetical note: previous simulations do not show a big difference between soil depths on north-facing and south-facing slopes at YM, even though field studies suggest that there are generally deeper soils on north-facing slopes. The difference between these cases was imposed through the source term. The inclusion of vegetation-dependent μ may have the desired effect, due to enhanced creep resistance.

11/20/98 Issues with implementation of soil-genesis model.

The soil-genesis model has the potential to be a memory hog. For example, if the soil grain size distribution is described with classes, each grid block will likely require at least a dozen values to describe soil composition in each computational layer. This resolution is difficult to handle with only one computational layer per grid block; with several layers, this resolution level may be intractable.

Dani Or suggested that characterizing the soil using a probability distribution for mass fraction may help out. The advantage is that an arbitrary number of classes can be accommodated with just a few parameters (*e.g.*, mean and standard deviation). There are many probability distributions that might be used, including lognormal, but the beta distribution is particularly attractive due to its great flexibility in shapes and boundedness. There is a possibility for limited bi-modality (at the endpoints), but in general bimodality would require multiple overlapping distributions.

Particle-mass redistribution occurs through addition of mass, from dust or bedrock, as well as weathering and particle breakup.

Particle breakup rates should be proportional to particle volume. Our working hypothesis is that freeze-thaw cycles (where moisture is available) are responsible for particle breakup, although heat stress may also play a role. The fraction of particles breaking up due to freeze-thaw per unit time is calculated by

$$f_{FT} = \mu_{FT} R^3 \sum_i N_{FTi} f_{MFTi}, \tag{16-59}$$

where f_{FT} is the fraction of particles breaking up, μ_{FT} is an efficiency coefficient, R is the effective radius of the particle size class, N_{FTi} is the mean number of freeze-thaw cycles per month, and f_{MFTi} is the fraction of the time that there is sufficient moisture to enable freeze-thaw cycles to be effective. The computational model for particle breakup accounts for freeze-thaw through a table lookup for number of cycles in individual months, with several depths, several mean air temperatures, and a full range of solar aspects. A similar table provides fraction of time that soil moisture is above a critical threshold, with additional table dimensions for total soil surface area

and mean annual precipitation.

Weathering is assumed to proceed through rind formation over the available surface area of the particles. The volume of a shell of weathering products is calculated by

$$V_w = \frac{4\pi}{3}(R^3 - (R-r)^3), \tag{16-60}$$

where V_w is the volume of weathering products and r is the thickness of the rind. Dividing by the original volume and assuming that the weathering products have the same density as the original particle, the fraction of the particle mass converted to weathering products given a rind thickness is

$$f_{pw} = 1 - \left(1 - \frac{r}{R}\right)^3. \tag{16-61}$$

The rind-thickness growth per unit time is

$$r = \mu_w \sum_i 2^{(T_i - T_o)/10} f_{MWi}, \tag{16-62}$$

where μ_w is the rind growth rate at temperature T_o, T_i is the mean temperature for month i, and f_{MWi} the mean fraction of time sufficient moisture exists in month i to enable weathering. The temperature-dependent and moisture-dependent functions are handled in the same type of table lookup used for the freeze-thaw calculations. Note that the power-law relationship for temperature means that using the mean temperature will underpredict the weathering rate; however, deeper than 10 cm or so temperature variability should be small enough to make it unnecessary to consider daily to weekly variability, so that only annual variability is considered.

The two mass conversion relationships are both proportional to R^3, with breakup increasing with increasing particle size and weathering decreasing with increasing particle size. Thus, it may be appropriate to calculate the rates for one particle size and scale it to all other sizes.

Multimodal distributions can be handled using a weighting scheme, such as the common finite element chapeau function, and using the probability distributions to describe mass fraction times the weight for that class. For example, if there were 10 classes and two functions, class weights for one function would go 0.05, 0.15, ..., 0.95; class weights for the other function would be reversed.

The mean and variance are calculated by

$$\bar{x} = \sum_i w_i x_i \tag{16-63}$$

$$\sigma_x^2 = \sum_i w_i \sum_{j=1}^{3} c_j (x_{ij} - \bar{x})^2 \tag{16-64}$$

where $\bar{x}$ and σ_x^2 are the mean and variance, respectively; x_i is the midpoint of histogram block i; w_i is the weight for histogram block i; c_j is 1/6, 4/6, and 1/6, respectively; and x_{ij} are the low endpoint, middle, and high endpoint of the histogram block, respectively.

A histogram block refers to the discretization of the grain-size distribution into bins, each with some mass associated. Each block has width of $(1/N_{bin})$, with a total range of 0 to 1. These would likely be best handled as uniform log-radius sections.

11/21/98 Implementation issues.

Limited experimentation with a beta distribution representation suggests that accurate reconstruction of a set of histograms requires that some care is necessary in order to calculate the appropriate standard deviation (there is no problem with the mean). Simpson's rule performs the integration admirably for a test problem with mean of 1/2 and variance of 1/12 (uniform distribution from 0 to 1), so that repeated cycles of beta-distribution parameterization and histogram construction does not cause the mean and standard deviation to drift significantly.

On slightly more complex cases, such as a simple triangular PDF, cycles of beta-distribution construction/histogram reconstruction yields drifting parameters. For this situation, it is possible to construct a linear approximation that should remain stable; however, the beta distribution can yield PDFs that go to infinity at endpoints (although histograms do not).

A reasonable method for handling the problem is to use the histograms to calculate changes in mean and variance, assuming that the change in the mean and variance used for the beta distribution is the same as the change in the mean and variance of the histogram distribution. This avoids the reconstruction issue entirely, while preserving the computational flexibility of the histogram approach with parameter parsimony of the beta distribution.

A test problem illuminates a difficulty with a single beta distribution. The problem is that of an initial triangular distribution subject to weathering and freeze-thaw breakup. The shift in mean and standard deviation to lower grain sizes tends to make the beta distribution create a bimodal distribution, ultimately with all mass concentrated in the two endpoint bins. This occurs whether the distribution starts with the bulk of the mass in the large or small grain sizes, and I believe that this is purely a numerical artifact.

2/22/99 Temperature distribution calculation.

I started a directory ***$HOME2/Matlab/Chadwick/SoilGen2*** for the next phase of modeling.

Weathering rates are temperature-dependent, and temperature variation is depth dependent. It is probably sufficient to use analytic solutions for temperature variation with depth, and to only consider annual variation (neglecting daily variation due to the shallow depth penetration of daily perturbations). The use of analytic solutions means that only a mean annual temperature and an amplitude are necessary to characturize the profile.

I resurrected a set of routines to calculate clear-sky shortwave radiation as a function of latitude, day, hour, and ground-surface rotation. The time history of clear-sky shortwave radiation over the year can be calculated.

An energy balance at the surface provides an estimate of soil temperature at the ground surface. The balance equation is

$$\sigma \sum_i \epsilon_a T_a^4 \Delta t - \sigma \sum_i \epsilon_s T_s^4 \Delta t + D_h \sum_i \Delta t (T_a - T_s) + \mathbf{q}_{sw} - \mathbf{q}_{geo} + \mathbf{q}_s = 0 \tag{16-65}$$

where σ is the Stefan-Boltzmann constant, ϵ is emissivity, T is temperature, D_h is the diffusion coefficient for heat, $\mathbf{q}$ is flux, and the a, s, sw, and geo subscripts refer to atmosphere, soil, net shortwave, and geothermal, respectively.

Characterizing T_s as

$$T_s = \bar{T}_s + A_0 \sin[\omega(J - t_0)] \tag{16-66}$$

where $\bar{T}_s$ is mean annual soil temperature, ΔT_s is soil temperature amplitude, ω is frequency ($\omega = 2\pi/365.25$), t_0 is a day shift, and J is julian day, yields an expression in three unknowns ($\bar{T}_s$, A_0, and t_0). The analytic solution for this problem is (Campbell, 1977)

$$T(z,t) = \bar{T}_s + A_0 \exp(-z/D) \sin[\omega(J - t_0) - z/D] \tag{16-67}$$

$$D = \left(\frac{2k_h}{\omega C_h}\right)^{1/2} \tag{16-68}$$

where z is depth, k_h is thermal conductivity, and C_h is thermal capacitance. The soil heat flux at the ground surface can be found by differentiating and rearranging, yielding

$$\mathbf{q}_s = A_0 \left(\frac{\omega C_h k_h}{2}\right)^{1/2} \{\sin[\omega(J - t_0)] + \cos[\omega(J - t_0)]\} . \tag{16-69}$$

The three unknown coefficients describing temperature can be solved for using standard least squares.

Generally it is necessary to break the day up into enough pieces to calculate the shortwave variation over the day. An hour or so is probably adequate for moderate ground-surface rotations, but for large north-south rotations (greater than 30 degrees) it is necessary to break up the day into 5-minute intervals or so for reasonably accurate calculations. Also note that the shortwave radiation loading starts significantly deviating from a sinusoid at such large rotations; for part of the year no sunlight may hit steep north-facing slopes. Accordingly, assumption of a sinusoidal temperature may not be totally valid.

3/1/99 Mean temperature distribution calculation.

A set of observations was performed by the USGS in Split Wash in 1997, with net radiation observed in the middle of the wash from days 50 through 212 (February 19 through July 31) and heat dissipation observed on north-facing (days 36 through 212) and south-facing slopes (days 17 through 212). Net radiation is calculated from four thermometers in the atmosphere (every 15 min), while heat dissipation is calculated from thermometers at two depths in the soil (every 6 hr). These data provide an opportunity to calibrate the temperature model.

Temperature is dependent on shortwave radiation, longwave radiation, dissipation into the subsurface, and sensible-heat diffusion across the boundary layer. Shortwave radiation is dependent on the path of the sun, the ground slope, and obscuration due to atmosphere and clouds. Longwave radiation is dependent on emissions from clouds, clear sky, and the ground surface, in turn dependent on cloudiness and atmospheric vapor density. Dissipation into the ground surface is dependent on the frequency of perturbations and material properties. Sensible-heat fluxes are dependent on the temperature difference across the boundary layer and the windspeed.

A fairly simple approach to predicting soil temperature relies on predicting the annual variation of the mean and superimposing perturbations on an hourly basis, decaying temperature appropriately with soil depth. In order to predict mean variation in soil temperature, the annual cycles of cloudiness, vapor density, and wind speed are useful. Mean values for all of these vary approximately sinusoidally over the year, as does atmospheric pressure. Each of these also have characteristic daily variations as well. Only cloudiness may require the daily variation to be taken into account, and only for shortwave contributions, as there is a peak in cloudiness during the most intense period of the midafternoon.

Hourly Desert Rock data is available for 1978 through 1994, of reasonable length for making calculations of annual atmospheric variation. These hourly data were aggregated into mean daily

values and a sine wave was fit to each resulting aggregate curve,

$$v = \bar{v} + A\sin[\omega(J - t_0)] \tag{16-70}$$

where v is the variable being fit and $\bar{v}$, A, and t_0 are fitting parameters. The match between data and model was made based on a least-squares fit, using a *Matlab* routine called fmins. The set of sinusoid fits are shown in Table 16-3, with plots of the data and matched curves shown in Figure 16-1.

Table 16-3: Parameters describing sinusoidal variation of atmospheric variables in form $v = \bar{v} + A\sin[\omega(J - t_0)]$.

Variable	$\bar{v}$	A	t_0
Windspeed (m/s)	4.07831	-0.441414	224.826
Relative Cloudiness	0.325176	-0.134497	136.154
Relative Humidity	0.331675	-0.134384	103.069
Temperature (C)	17.2165	12.1006	109.589
Pressure (mbar)	1136.81	-52.1159	87.7265

Note that vapor density is not fit well with a sinusoid (it depends on relative humidity and is exponentially dependent on temperature), but can be calculated from relative humidity and temperature (both of which are reasonably well captured). Even so, still not a particularly good fit, as hourly variations between these are inversely correlated. The inverse of vapor density is arguably fit the best using a sinusoidal functions among several options I tried. Perhaps a joint match of relative humidity, temperature, and vapor density would help. Fortunately, the sensitivity of soil temperature to vapor density is quite low.

3/2/99 Mean temperature distribution verification.

A comparison of the daily average incoming longwave and net shortwave components of atmospheric radiation are plotted in Figure 16-2, with a comparison to the comparable mean components calculated using the annual cycles of cloudiness, relative humidity, and vapor density. The daily average components are calculated using the average of the hourly readings for each day, and should account for fine-scale variability. The match is quite good.

Using the mean energy-balance components with an assumed boundary-layer sensible-heat diffusion coefficient, soil temperature can be estimated using a sinusoidal fitting function, as discussed two entries above.

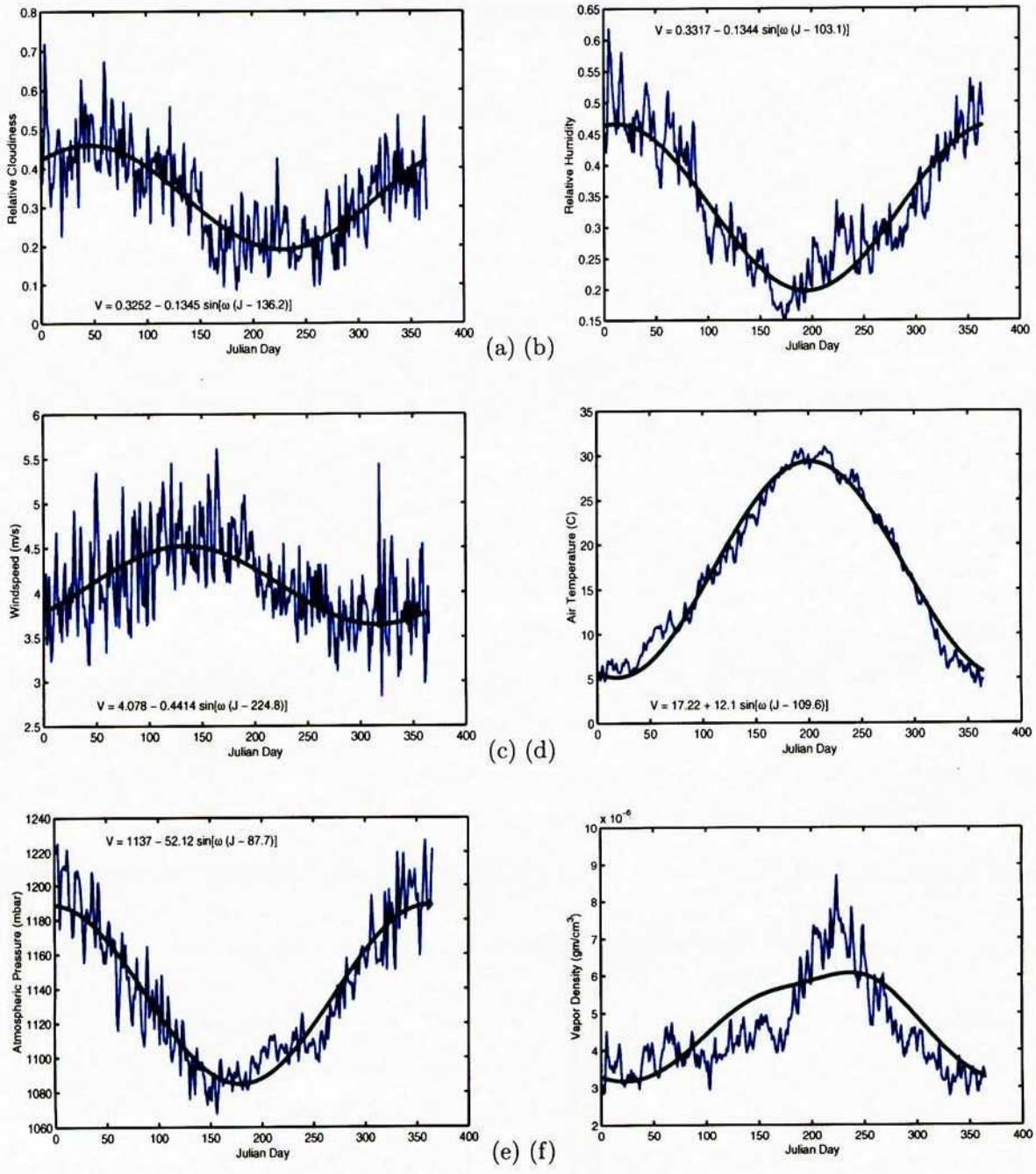

Figure 16-1: 3/1/99. Observed and predicted mean annual variation in (a) cloud cover, (b) relative humidity, (c) wind speed, (d) air temperature, (e) atmospheric pressure, and (f) vapor density.

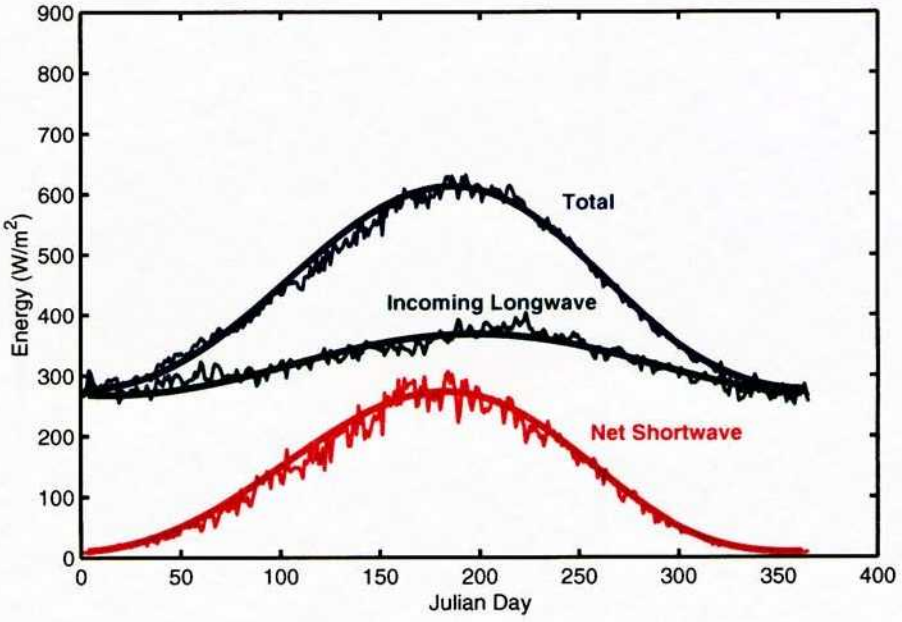

(a)

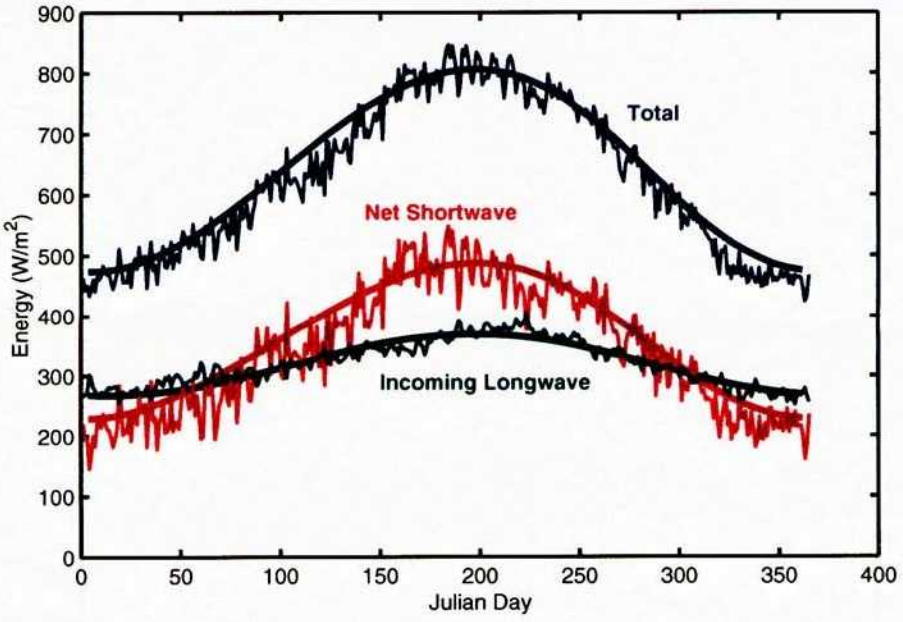

(b)

Figure 16-2: 3/2/99. Average daily and predicted mean annual values of radiation components for Split Wash slopes facing (a) south and (b) north with a slope of 25 degrees, using 1974 through 1994 Desert Rock observations. Albedo is assumed to be 0.1.

Measured soil and air temperatures are available for Split Wash, as discussed in the previous entry. The measured temperature profiles only cover part of a cycle and do not unambiguously contain either peak. However, it appears that the summer soil peak is roughly 29 and 32 degrees Celsius for north-facing and south-facing slopes (averaged over both depths), respectively, and the winter soil peak may be roughly 4 and 8 degrees Celsius, respectively. These are probably correct to within plus or minus 2 degrees.

Using the diffusion coefficient as a fitting parameter, reasonably good matches to the data are found, as shown in Figure 16-3. Reasonable matches were obtained for D_h in the range 5×10^{-3} to 10×10^{-3} J/s cm^{2}K, prior to checking plausible values. Note that D_h is dependent on the difference between soil and air temperatures, and requires an iterative process to estimate. Checking for plausible values of D_h with representative windspeeds and temperatures suggests that the lower two-thirds of this range are most reasonable.

A brief sensitivity test for input parameters suggests that:

- A thirty-percent change in cloudiness has minimal effect
- A fifty-percent change in atmospheric emissivity changes T by 2 degrees
- A fifty-percent change in vapor density has minimal effect
- A change in albedo from 0.1 to 0.4 drops mean temperatures by 0.6 and 1.6 degrees C for north-facing and south-facing slopes, respectively, with drops in summer larger than in winter
- Changes in air temperature are directly reflected in changes in soil temperature
- A change in soil emissivity from 0.9 to 0.95 drops mean temperatures by 0.3 degree C
- A change in soil diffusivity by a factor of two has minimal effect
- A change in D_h from 6.2×10^{-3} to 4.2×10^{-3} has a similar effect as changing albedo, with mean temperatures raising by 0.5 and 1.8 degree C for north- and south-facing slopes, respectively. Again the rise is larger in summer than winter.

For soil modeling purposes, the primary factors to capture are air temperature and slope, with less-important secondary factors of albedo and boundary-layer diffusion coefficient (windspeed).

Another factor to consider is what happens to the soil temperature over a daily cycle. This is important for freeze-thaw cycles, for example. In addition, since weathering is proportional to 2^{T-T_0}, perturbations about a mean yield a higher effective rate.

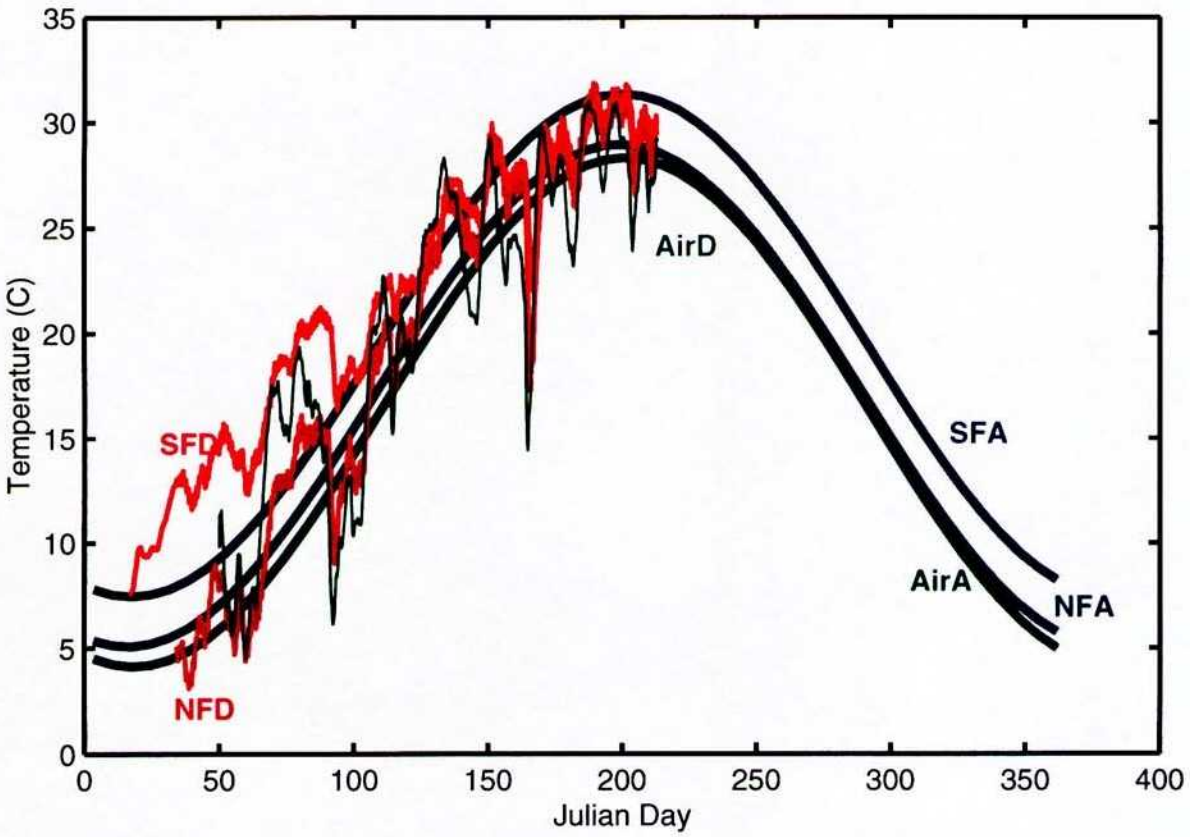

Figure 16-3: 3/2/99. Average daily and predicted mean annual temperatures for Split Wash north- and south-facing slopes and air temperatures. Temperatures increase from air to north-facing to south-facing. Temperature labels: AirA, analytic (sinusoidal) air; AirD, Split Wash daily average; NFA, north-facing soil analytic (30 cm deep); SFA, south-facing soil analytic (30 cm deep); NFD, north-facing soil data (29.2 cm deep); SFD, south-facing soil data (35.6 cm deep). Modeled albedo is 0.1 and boundary-layer diffusion is 7.2×10^{-3} J/s cm^2 K.

The Beatty data set provides minimum and maximum temperatures over the range from 1948 through 1994, with several missing intervals. The difference between maximum and minimum temperature varies slightly over the year, with the mean difference (all temperatures in Celsius) having the relationship $\bar{\Delta} = 18.3727 + 2.7465\sin[\omega(J - 113.2405)]$. A histogram of the deviation from the mean is slightly skewed, with a mean of -0.5636 and a standard deviation of 4.

The mean temperature (the mean of maximum and minimum), $T = 15.5172+10.7973\sin[\omega(J-$

112.1112)], is fairly similar to Desert Rock, with a mean 1.7 degrees cooler and an amplitude 1.3 degrees smaller. A histogram of the deviation from the mean is less skewed than the corresponding temperature-difference case, with a mean of -0.1821 and a standard deviation of 3.6179. The correlation between daily-mean deviation and temperature-range deviation is 0.241. From this information, assuming normality for both distributions should allow calculation of the number of freeze-thaw days and the fraction of time spent at various temperatures over the course of a year.

3/3/99 Perturbed temperature distribution.

The fraction of days with a freeze-thaw cycle can be calculated given the mean temperature, the variance of the daily average deviation from the mean, and the variance of the temperature range. Noting that the two variance variables are assumed normal and correlated, realizations are generated by first sampling one. The other is then created from the first using

$$m_{Y|X} = m_Y + \rho\frac{\sigma_Y}{\sigma_X}(x - m_X) \tag{16-71}$$

$$\sigma^2_{Y|X} = (1 - \rho^2)\sigma^2_Y \tag{16-72}$$

where m represents the mean, σ^2 is the variance, and ρ is the correlation coefficient. A table can be created for the temperatures with significant numbers of freeze-thaw cycles (generally in the range of $\pm 3(\sigma^2_X + \sigma^2_Y)^{1/2}$). The table should use roughly 1-degree steps within this range; it is reasonable to use at least 10^5 realizations per temperature for a smooth function. For each day of the year, given a mean temperature the expected number of freeze-thaw cycles can be calculated from the table; these can then be summed to yield an annual average.

The fraction of days with a freeze-thaw cycle is bell-shaped as a function of mean temperature, and is centered on 0 degrees C with no correlation. With a positive correlation the peak is shifted below 0, while with a negative correlation the peak is shifted above 0. For reasonable inputs the shifts are only a degree or so. Halving the standard deviation for daily temperature range halves the fraction of days with freeze-thaw cycles. Doubling the standard deviation for daily average deviation also halves peak, but doubles the spread of the curve and doubles the shift due to the correlation coefficient.

At a depth within the soil column, temperature perturbations decay, with effect of shrinking both standard deviations equally. The net effect would be to keep the same peak but decrease the spread of the curve.

The weathering rate (given sufficient moisture) is stated in the general form

$$R = A2^{\alpha(T-T_0)} \tag{16-73}$$

where T is temperature, R is the weathering rate, A and α are constants, and T_0 is a reference temperature. Note that $\alpha = 10$ (doubling in weathering for each 10 degree increase in temperature. Since temperature is essentially normally distributed, R has a larger mean than median. To handle this, note that the relationship can be rewritten as

$$R = A(2^{\Delta T})^{\alpha}2^{\alpha(\bar{T}-T_0)} \tag{16-74}$$

where $\bar{T}$ is a mean temperature and ΔT is the offset from the mean. Only the component with the ΔT need be calculated using realizations.

With a base case having standard deviations of 3.62 and 4 for daily mean deviation and daily range, respectively, $f = 2^{\alpha\Delta T}$ is about 1.5. Halving σ for the range drops f to 1.4, while doubling raises f to 1.9. Halving σ for the daily deviation drops f to 1.15, while doubling raises f to between 3 and 5. The correlation coefficient has no effect. As a practical matter, using 1.5 should be fine, particularly since A is a calibration coefficient anyway. One would expect that the variability would only decrease under wetter or cooler climates, since relative humidity should be larger and thereby buffer the temperature swings.

3/4/99 Annual freeze-thaw.

SAS

I wrote a *Matlab* routine called make_FT_table to drive the calculations of the freeze-thaw cycle as a function of the mean daily temperature. The base case uses the standard deviations and correlation for Beatty. A table is written out with the resulting fraction of the time a day with given mean temperature has a maximum greater than 0 degree C and a minimum less than 0 degree C, based on 10^6 realizations. The mean temperature is varied by 0.5 degree steps.

Another routine, test_get_annual_FT, plots the number of freeze-thaw cycles for various values of MAT and at various depths within the soil. It is assumed that the decay of the temperature amplitude with depth can be applied to the standard deviations for daily temperature range and daily-mean deviation. Thus, both standard deviations are multiplied by $\exp(-z/D)$, where z is depth below the soil surface, $D = (2k_h/\omega C_h)^{1/2}$, and $\omega = 2\pi/24$ (representing a daily cycle). For typical soils, D for daily perturbations might be about 15 cm. The resulting combination is implemented by scaling the mean temperatures corresponding to a given fraction, so that interpolation occurs using a table with entries based on $T\exp(-z/D)$. Typically an offset is needed in the scaling, but since freezing is based on 0 degree C the offset is zero.

Typical cases are shown in Figure 16-4, using the standard deviations, correlation coefficient, amplitudes, and offsets determined using the Beatty data set. Only MAT and depth are varied. Note the peaks in Figure 16-4 correspond to the cases where the peak of either summer or winter has an expected temperature of 0 degree C. The decay of the amplitude of the annual cycle with depth is also considered, tending to bring the peaks towards 0 degree C. Also note that freeze-thaw cycles are rare and shallow (less than 10 cm) with a ground-surface MAT corresponding to the atmospheric MAT at YM (17.2 degree C). If soil temperatures were 5 degree C cooler, however, there might be an annual average of 15 freeze-thaw cycles at the ground surface and several cycles even 50 cm deep within the soil profile.

For both north- and south-facing slopes, soil temperatures are higher than air temperatures; north-facing slopes are a few degrees warmer than air temperatures and south-facing slopes are at least four degrees warmer still. Even under glacial conditions it may be that south-facing YM slopes see minimal freeze-thaw activity.

The number of freeze-thaw cycles are only part of the story for weathering; moisture must also be available for weathering to occur. The appropriate assumption on moisture availability has yet to be confirmed. Options include: (i) the amount of moisture required is so minimal that it can always be assumed to be present, (ii) freeze-thaw has no effect unless at least 15 bar of suction exists, or (iii) some drier condition marks the activity threshold.

3/5/99 Probability of moisture above a threshold.

Quantifying the number of freeze-thaw cycles is the most straightforward component of the weathering problem, and the above work should be sufficient to handle it. The other component of weathering comes from weathering-rind formation.

Quantifying the expected rate of weathering-rind formation has with two subcomponents: (i) expected rate given moisture above a threshold, and (ii) probability that moisture is above or below the threshold. The first subcomponent has been discussed above, with the conclusion that the annual variation of temperature is probably all that needs to be accounted for (daily fluctuations are likely to cause a multiplier factor that is between 1 and 1.5, much smaller than the uncertainty in the weathering rate under base conditions). The second subcomponent is far more difficult to quantify, although the important simplification of temperature and moisture subcomponent independence is likely justified.

Probably the most satisfying approach for quantifying soil moisture frequency is to simply

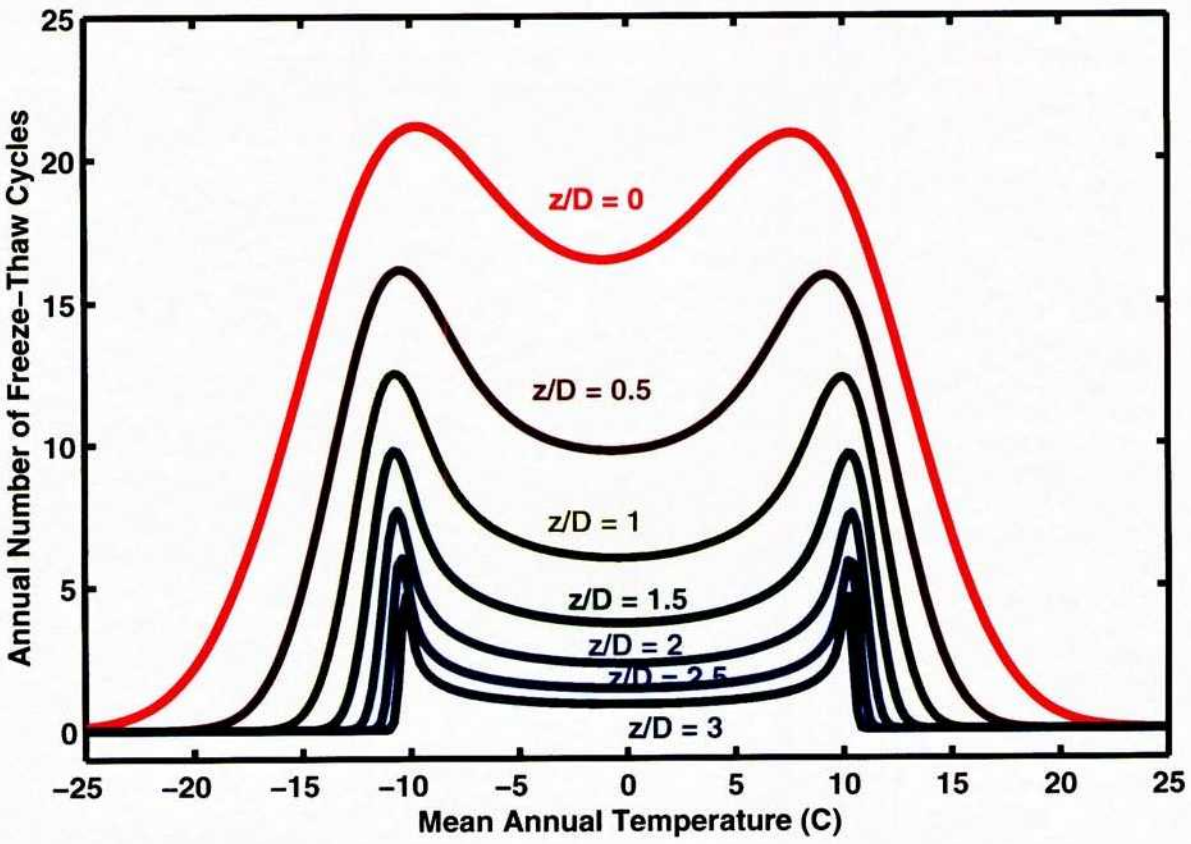

Figure 16-4: 3/4/99. Number of freeze-thaw cycles per year for various normalized soil depths and mean annual temperatures, using temperature statistics based on Beatty observations between 1948 and 1994. The z/D parameter is depth within the soil divided by a diffusion parameter (on the order of 15 cm for typical soils).

run several centuries of a model that accounts for precipitation, evapotranspiration, and net infiltration, using the sinusoidal climatic parameters except for precipitation. Precipitation would use appropriate generator statistics. The basic USGS approach of a bucket or cascading-bucket model would be an acceptable starting point, although adaptive vegetation would be highly desirable. Although this approach may be crude for estimating MAI, it may be quite reasonable for estimating the fraction of time that moisture is available above a threshold.

The shallow soils on YM allow the simplifying assumption that the soil column is divided into a dry-soil and an underlying wet-soil bucket lying above the bedrock. Within the wet bucket,

saturation and pressure is assumed uniform. The bucket model assumes that the losses due to infiltration into the bedrock are through gravity drainage; the conductivity of the underlying bedrock and fractures can be calculated with the bucket pressure. Gravity drainage rates in the soil place an upper limit on deliveries to the bedrock (in case of fractures).

Evaporation is calculated assuming that the soil in the dry zone is all at equilibrium with the vapor density at the annual average soil temperature. At the interface between the wet and dry zones, vapor density is calculated using the wet-zone pressure and an appropriate temperature. The velocity of the interface is calculated using

$$V_i = \frac{\mathbf{q}_v - \mathbf{q}_w}{\varepsilon(\theta_v - \theta_w)} \tag{16-75}$$

where V_i is the downward interface velocity, $\mathbf{q}_v$ is the downward vapor flux, $\mathbf{q}_w$ is the downward liquid flux (= 0), ε is porosity, θ_v is liquid saturation in the dry zone, and θ_w is liquid saturation in the wet zone.

Preliminary calculations suggest that the first two days after initial wetting should use time steps on the order of two to four hours; daily or larger time steps are acceptable after the drying zone develops appreciable thickness.

A mass balance is more convenient using soil water mass; however, the transfer function for change in pressure due to change in water mass is more easily determined by tabulating the mass in the column as a function of the pressure.

3/12/99 Testing code.

I performed a direct comparison of *breath* and the simplified infiltration model for a test case of soil over a fracture. The two models provide very similar results, in terms of total mass in the soil system, after the first 10 or 15 percent of the mass has evaporated. Both have total mass drop off as a power law. The volume of wetted soil is larger for the *breath* simulation, while the saturation of the wetted soil is larger for the simple model.

The discrepancy between the two predictions is due to the ability of the soil to deliver water to the ground surface through both vapor and liquid transport at early times in the *breath* simulations, while as soon as there is any air gap the simple model can only deliver water through the less-efficient mechanism of vapor transport.

Based on this test case, it appears that breaking the bucket into a few saturation contours

to describe the drying front would provide a significant improvement in predictions at relatively minimal computational cost, albeit with additional coding effort. This step would also tend to provide a better estimate of wetted volume. I would not use more than a few (*e.g.*, less than 6) saturation contours to describe the drying front. Perhaps they could be placed evenly according to conductivity.

Note, however, that simulations with only evaporation may be expected to have the largest discrepancy between detailed and simple simulations, while transpiration uptake may overwhelm the discrepancies. For example, roughly a quarter of plant-available storage is still available after a year of evaporation from a 50-cm column. I expect that the soil column would be essentially dry by late spring or early summer from a completely saturating winter rain.

One other approach may be fruitful as well. If there is assumed to be a hydrostatic capillary fringe, the equivalent conductance of the fringe can be taken into account. A table can be constructed of conductance for the fringe, with tabulated values corresponding to saturations relative to full saturation. Actual conductance is calculated by differencing.

4/11/99 Summary of meeting.

I presented current and ongoing work at a noontime seminar last week. There was a meeting between Randy Fedors, Oliver Chadwick, David Groeneveld, and myself built around the seminar, at which we fleshed out remaining details in infiltration and soil genesis modeling. David will provide typical ranges of values for transpiration and individual plant descriptions (*e.g.*, growth rates, sizes, shapes). Oliver will provide weathering rates, while looking out for information on roughnesses, dust deposition modeling, and creep. Randy will look into methods for translating soil particle-size distributions into van Genuchten retention parameters, and will ask Mike Miklas if he could look into some of the factors that Oliver is looking out for as well.

The soil genesis model clarified considerably in the discussions. The original model consisted of a particle-size distribution with uniform mineralogy (most importantly, weathering rates). The model now conceptually consists of up to five particle-size distributions: (i) native rock, (ii) fast-weathering, (iii) moderate-weathering, (iv) slow-weathering, and (v) carbonates.

The first distribution arises from bedrock entrainment. Our first inclination is to assume that the predominant weathering process is through mechanical weathering, although there is no particular reason that some type of chemical weathering might also take place. Either bedrock from all units weathers at the same rate or a mixture must be tracked.

The remaining distributions arise from dust deposition. Although in some cases an individual dust particle may be formed from a mixture of minerals (*e.g.*, welded-tuff source rock), the feeling from Randy and Oliver is that assuming single-mineral particles is not unreasonable. Certainly it is much easier to track separate distributions than it is to track particles composed of multiple minerals.

The carbonate class is a special case. Apparently the problem of caliche formation in desert soils has received a good deal of attention over the last 20 years, and neglecting caliche may raise eyebrows. Our observations suggest that caliche generally is not forming in the soil column, except in deeper soils, and rather is associated with soil/bedrock interfaces and bedrock fractures. Our model will likely deposit the carbonates within bedrock fractures, neglecting details of deposition mechanisms. Perhaps some analysis of wetting penetration depths will aid in justifying this assumption.

4/25/99 Updated approach.

The day-to-day programming of soil-genesis algorithms and modules is being documented in a Microsoft Word document with embedded *Matlab* commands and output. The notebook format is available on systems running Windows. The advantage of the notebook format is that the developed modules are documented and tested simultaneously. All of the *Matlab* code accessed by the notebook can be retested at will, enabling verification that code is not broken.

Unfortunately, there is no option for running either WordPerfect or LaTeX notebooks, although it should be possible to write macros for WordPerfect comparable to the macro package in Word. It would be much more difficult to implement such a notebook in LaTeX, unless it was modeled somehow on procedures for creating references.

Updated approaches to modeling soil genesis are being incorporated in the new code. The code will be run either in single-column mode or as a set of 1D columns linked with 2D sweeps at the ground surface. The 1D columns will account for creep, bedrock entrainment, and weathering; the 2D sweeps will account for dust and sediment balances at the ground surface.

The 1D column balances will include all but a top active layer. The sequence of steps will be:

- A bulk mass balance, providing bulk fluxes from column to column. This step does not need to consider texture or weathering.

- A particle mass balance, providing particle fluxes from column to column as well as weathering. The bulk fluxes from the first step will be used with the mass fraction corresponding to each particle bin.

Depending on the constitutive relationships, it may be necessary to iterate.

Bulk mass balance of the column will proceed element by element from bottom of the column to the top. The mass balance equation is

$$\frac{\partial M}{\partial t} + \sum_i Q_i = 0, \tag{16-76}$$

where M is mass in the element and Q_i is the ith flux into and out of the element. The variables in the equation are expanded in a finite-volume sense as

$$M = V\rho \tag{16-77}$$

$$V = Ab \tag{16-78}$$

$$Q = vA_c = vbw \tag{16-79}$$

where V is the volume of the element, A is the plan-view area of the element, A_c is the area of the connection between one element and the next, b is the thickness of the upstream element, w is the width of the connection between one element and the next, ρ is the mass density in the element, and q is the flux from one element to another.

Creeping flux is assumed to be governed by film flow, which is has a parabolic velocity distribution. For a constant-density film on an incline, the mean velocity $\bar{v}$ in an element with bottom and top elevations above bedrock of z_a and z_b, respectively, can be shown to be (adapting Bird et al. (1960))

$$\begin{aligned}
\bar{v} &= -\left(\frac{\rho g \nabla z}{6\mu}\right)\left(\frac{z_b^3 - z_a^3}{z_b - z_a}\right) \\
&= -\rho C\left(z_a^2 + z_a z_b + z_b^2\right) \\
&= -\rho C\left(z_a^2 + z_a(z_a + b) + (z_a + b)^2\right) \\
&= -\rho C\left(3z_a^2 + 3z_a b + b^2\right), \qquad (16\text{-}80)
\end{aligned}$$

$$C = \frac{g\nabla z}{6\mu}, \tag{16-81}$$

where g is the acceleration due to gravity, ∇z is the slope, and μ is the soil viscosity. With the assumption that the kinematic approach is valid, columns can be processed from top to bottom by elevation. Thus, fluxes can be classed as either incoming (known) or outgoing (unknown).

Substituting definitions into the mass balance equation yields

$$A[(b\rho)^{n+1} - (b\rho)^n] - \left(\sum Q_{in} - \sum Q_{out}\right)\Delta t = 0, \tag{16-82}$$

where n is the time step level. Assuming that the thickness of the element changes to accommodate mass balance changes, b^{n+1} can be isolated:

$$A(b\rho)^{n+1} + \Delta t\left(\sum (b\rho)^{n+1} w_i C_i\right)(3z_a^2 + 3z_a b + b^2)^{n+1} = A(b\rho)^n + \Delta t \sum Q_{in}, \tag{16-83}$$

yielding a cubic relationship for b^{n+1} even assuming that all else remains constant. It is easy enough to solve iteratively for $(b\rho)^{n+1}$ by rearranging,

$$(b\rho)^{n+1} = \frac{A(b\rho)^n + \Delta t \sum Q_{in}}{A + \Delta t(\sum w_i C_i)(3z_a^2 + 3z_a b + b^2)^{n+1}}, \tag{16-84}$$

where there is a quadratic expression including b^{n+1} in the denominator that forces the iteration. Presumably changes in b will be relatively small during a time step. It is possible to update ρ during the cycle if some reasonable method is found. Note that sources and sinks might be considered an incoming flux (*e.g.*, bedrock fluxes). Of course, if the thickness of the element is held constant, the change in density is calculated instead of the element thickness.

Physically one would expect that a mixing process takes place, so that not only the element thickness but the element density adjust over a time step. A mixing mass balance equation for density can be written

$$\frac{\partial \rho M}{\partial t} + \sum_i \rho_i Q_i = 0, \tag{16-85}$$

which, following the same steps, results in

$$A[(b\rho^2)^{n+1} - (b\rho^2)^n] - \left(\sum \rho_{in} Q_{in} - \rho \sum Q_{out}\right)\Delta t = 0, \tag{16-86}$$

and finally

$$(b\rho^2)^{n+1} = \frac{A(b\rho^2)^n + \Delta t \sum \rho_{in} Q_{in}}{A + \Delta t(\sum w_i C_i)(3z_a^2 + 3z_a b + b^2)^{n+1}}. \tag{16-87}$$

These two equations can be used to update $b\rho$ and $b\rho^2$. Simplifying the equations,

$$b\rho = \beta_1 \tag{16-88}$$

$$b\rho^2 = \beta_2 \tag{16-89}$$

yields solutions of

$$b = \frac{\beta_1^2}{\beta_2} \tag{16-90}$$

$$\rho = \frac{\beta_2}{\beta_1} \tag{16-91}$$

These still need iteration, due to the quadratic term with b. A simple test suggests that 5 iterations may be sufficient if the Courant number is less than 1 (incoming mass is less than the initial mass in the cell).

Once the bulk fluxes are obtained, then texture can be considered. The particle mass balance equation for a particle class is

$$\frac{\partial \chi M}{\partial t} - \sum \chi_{in} Q_{in} + \sum \chi Q_{out} - \sum_j S_j + \lambda \chi M = 0, \tag{16-92}$$

where χ is mass fraction, S is the particle mass created by weathering larger particles, and λ is the rate of loss of particle mass to smaller particles. Again external sources/sinks are treated as fluxes. Note that adding all of the particle mass balance equations together yields the bulk mass balance equation. Rearranging yields

$$(\chi M)^{n+1} + \Delta t \chi^{n+1} \left(\sum Q_{out} + \lambda M \right)^{n+1} = (\chi M)^n + \Delta t \left(\sum \chi_{in} Q_{in} + \sum_j S_j \right), \tag{16-93}$$

and finally the explicit relationship

$$\chi^{n+1} = \frac{(\chi M)^n + \Delta t \left(\sum \chi_{in} Q_{in} + \sum_j S_j \right)}{M^{n+1}(1 + \Delta t \lambda) + \Delta t \sum Q_{out}}. \tag{16-94}$$

It is best to not use the particle balance equation for one particle class, because the bulk equation has been used. Instead, it is better to subtract the mass in all particle classes from the total mass, thereby ensuring overall mass balance. Probably one of the clay bins would be a good candidate (maybe the fastest-weathering category).

4/27/99 Dispersion.

SAS

Preliminary tests of bulk mass balance in a 1D column seem to work pretty well. In the testing, I realized that the density balance calculation does not require iteration, as β_2/β_1 is completely known (the nonlinear denominator of both β_1 and β_2 is the same and cancels in the ratio, and the numerators are completely known *a priori*).

Vertical movement of particles must occur within a soil column: witness desert pavement, for example, where larger fragments float to the ground surface. Also, Oliver emphasized that a debris flow fully mixes the profile. These phenomena have not been included in our model to date, and I've been worried about how to do so. Today two approaches occurred to me that might help.

The mixing process due to creep and bulk flow is dispersive. In the porous-media transport literature, the dispersion coefficient is related to velocity. A similar relationship can be applied here, where vertical dispersion is due to slope-parallel fluxes. Such a relationship can be simply written in the form

$$D = \alpha V, \tag{16-95}$$

where D is the dispersion coefficient used for particle transport, α is dispersivity, and V is velocity. The velocity might be a flux-weighted average of all velocities in connections to a column. The dispersion coefficient will increase from the bottom of the column to the top, consistent with the parabolic velocity profile.

It occurs to me that the dispersivity should be proportional to the standard deviation of the particle-size distribution, and should be related to the nonuniformity of the larger particles. The reasoning is that an extremely uniform distribution with extremely spherical particles may move quite laminarly. Mixing should be enhanced by a wider particle-size distribution; just imagine the effect on smaller particles of rolling a cobble along. If the cobble is highly irregular, mixing should be even more enhanced.

The flotation process should also be enhanced by a wide distribution of particle sizes. Flotation occurs when the smaller grains are able to work their way under the larger particles, thereby switching elevations. If there is a narrow distribution, there is nothing to float. Flotation is enhanced by anything that causes grain movement, such as thermal expansion and vibrations. All of the movement-inducing processes active without bulk motion are dampened with depth below the surface.

One way to characterize the flotation process is by a body force on the particles. I imagine this force might have the form

$$f(z,r) = (a_1 \exp[(z - z_s)/D_z] + a_2 V_h)\left(\frac{r^2 - r_m^2}{r_m^2}\right), \tag{16-96}$$

where z is elevation, z_s is ground-surface elevation, r is particle radius, r_m is the mean particle radius, D_z is a damping depth (the diurnal thermal depth should be good), V_h is the horizontal velocity used to calculate dispersion, and a_1 and a_2 are scaling coefficients. The term with r yields an upward force for large particles and a downward force for small particles. I presume that the cross-sectional area of the particle should provide the proportionality, since force is pressure divided by area. The rationale for the exponential term is that surface-induced perturbations are exponentially dampened (such as thermal and pressure perturbations). The rationale for the velocity term is that bulk movement provides opportunity for particles to redistribute. Both terms decay with depth below ground surface.

4/29/99 More dispersion.

SAS

After further thought, the flotation flux should have the form

$$q(z,r) = (a_1 \exp[(z - z_s)/D_z] + a_2 V_h)(\pi \mathbf{g})(\langle \rho r^2 \rangle - \rho r^2) \tag{16-97}$$

$$\langle \rho r^2 \rangle = \frac{\sum_{i,j} \rho_{ij} r_{ij}^2 \chi_{ij}}{\sum_{i,j} \chi_{ij}} = \sum_{i,j} \rho_{ij} r_{ij}^2 \chi_{ij} \tag{16-98}$$

The summation is over the number of particle classes and bins. As before, the net flux is zero, but it also is dependent on particle density (both larger and lighter particles float better). Note that the gravity vector $\mathbf{g}$ points down and $\sum \chi = 1$.

A nice feature of the formulation is that net flux is inherently zero. However, a problem with this formulation is that all bins of all textures simultaneously participate in the summation. Aside from the flotation flux, the individual textures can be independently treated; each bin can be independently treated to boot (particle breakup cascades from larger to smaller particles). If not for dispersion, each element within a column could also be independently treated.

The overall particle balance equation for particle class k, with the newer thoughts, becomes

$$\frac{\partial M \chi_k}{\partial t} - \sum \chi_{in} Q_{in} + \sum \chi_k Q_{out} + M \chi_k \lambda_k - \sum_j \lambda_j \Xi_{jk} M_j \chi_j$$
$$- \sum_m D_m \nabla_m \chi_k + \sum Q_{float} - \sum Source = 0 \tag{16-99}$$

where λ is the decay rate from weathering, Ξ is the distribution function for weathering products into bins, $Source$ represents external sources/sinks (positive for sources), Q_{float} represents flotation fluxes, and the remainder are defined above.

Rigorous treatment of flotation generates a block-tridiagonal matrix if all textures are grouped by element. This structure is as compact as can be achieved. With the organization of the coefficient matrix by element at the coarsest level, the maximum width of active columns is $3 \times N_{\text{class}} \times N_{\text{bin}}$, where N_{class} is the number of particle classes and N_{bin} is the number of bins per particle class. For example, with 7 classes and 37 bins, the active width is 777. The dimension of the matrix is the active width times the number of elements.

The (reasonable) example might take a significant fraction of a minute to solve, which is much too slow for practical purposes. Replacing the direct solution with an iterative procedure, lagging the flotation component, reduces the coefficient matrix to a series of tridiagonals, one for each bin of each particle class. The example would produce 777 short tridiagonal matrices. The

flotation fluxes should be relatively small and consistent from beginning to end of a time step, so that iteration should be fast.

A rough estimate of solution effort for a banded matrix is NB^2. A tridiagonal matrix solves linearly with dimension. If N_t is the total number of particle-class bins, and N_e is the number of elements, an iterative step would take effort proportional to $N_t \times N_e$. The block-tridiagonal matrix would take effort proportional to $N_e \times N_t \times (N_t/2)^2$, simplifying to $N_e N_t^3$. Since N_e is generally going to be negligible compared to N_t, effort is approximately cubed for the block-tridiagonal relative to the multiple tridiagonal. This should mean a solution in several seconds rather than a minute for the example.

I would expect that it would be faster in *Matlab* to assemble and solve a triangular matrix than it would be to loop through the equivalent sequence directly, since the solution is hard-coded while looping is relatively inefficient. This matrix corresponds to the case with one element (no flotation). It is not clear whether a block-tridiagonal sequence with triangular blocks would be faster than looping over a sequence of tridiagonal matrices.

5/3/99 Timings.

A rough estimate of time required to perform various *Matlab* activities suggests that solving a lower-triangular system of equations (corresponding to the solution of a pure-advection system with weathering breakdown) is extremely fast if sparse storage is used. For example, a lower-triangular matrix of dimension 2000 takes about 7×10^{-4} sec. A symmetric tridiagonal matrix of the same dimension takes about 3.6×10^{-2} sec, while an unsymmetric tridiagonal matrix takes about 1.3 sec. A more typical size might be of dimension 800, yielding times of 2.8×10^{-4} sec, 1.4×10^{-2} sec, and 0.21 sec, respectively.

A block-tridiagonal matrix, with blocks of dimension 250, takes about 9 sec, while a block-tridiagonal matrix with lower triangular blocks takes about 2.4 sec.

The *Matlab* solvers have quirks. A matrix of dimension 1000 consisting of a lower triangular matrix with one additional diagonal just above the main diagonal takes 5.5 sec to solve if it is stored in sparse format, while it only takes 0.77 sec to solve if it is stored in full format. On the other hand, a lower triangular matrix of the same dimension uses 0.16 sec in full format and 3.3×10^{-4} sec in sparse format. There must be overhead involved in both formats, with additional checking in full format and indirect addressing in sparse format.

Correction dated 5/7/99: Matlab *support explained that the slowness of the sparse triangular matrix solution is due to a step that attempts to reorder the matrix to minimize fill-in (not necessary for my problem). They offer a procedure to turn on and off this reordering at will. The* Matlab *command* spparms('autommd',0) *turns off reordering and* spparms('autommd',1) *turns it back on. I would expect that my applications would not benefit significantly from reordering, since I am careful in maintaining matrix structure.* SAS

The form of the discretized full particle balance equation is

$$a_1\chi_i^{n+1} + \sum \chi_i^{n+1} q_{out} + \chi_i^{n+1}\lambda_i - \sum \chi_j^{n+1}\Xi_{ji} - \sum D\nabla_z\chi_i + \sum \chi_i q_{flot} = a_2\chi_i^n + \sum \chi_{in} q_{in} + \sum Source \tag{16-100}$$

Neglecting weathering (the λ and Ξ terms), dispersion (the D term), and flotation (the q_{flot} term) results in an explicit calculation. Adding just weathering yields a triangular matrix. Adding just dispersion yields a symmetric tridiagonal matrix. Adding just flotation yields a linear unsymmetric full matrix, or a nonlinear unsymmetric tridiagonal matrix.

The only hope for competitively fast solutions arises from using the triangular matrix with iteration to handle dispersion and flotation. Note that 50 solutions of the triangular matrix can occur in the same time that the equivalent symmetric tridiagonal can be solved (1850 solutions relative to the equivalent unsymmetric tridiagonal). Flotation clearly must be handled using iteration, while dispersion probably should as well (note that iteration will require reassembly of the right-hand side vector, so that matrix solution is not the only factor to be considered).

5/5/99 More timings and tests.

SAS

I finally got the bulk transport and differential transport modules working (without dispersive processes) and tested. I made up a nine-cell problem for which I could change the number of texture classes and the number of vertical elements. I tested two cases to examine mass balance: pure weathering (no sources) and pure transport (no weathering). Both cases identified bugs, but each one now has mass balance to within roundoff error (at least 14 decimal places), even with several elements, several texture classes, and numerous bins for each class.

Timings on the test problem suggest that 90 to 95 percent of the computational effort is in the beta transformation used to create the bins. This is the case with weathering but not vertical dispersion. The issues regarding matrix solution may be less important than I thought before, although a quick test is still in order. Overall time for a cell with 36 bins, 4 elements, and 2

textures is on the order of 4 seconds, of which at least 3.6 seconds go to the beta distributions. This gives 15 cells per minute; adding textures would reduce this. It appears that only hillslope simulations may be practical unless very coarse discretizations of the particle distribution are used. A factor of 10 speedup would result from not going through the statistical distribution, although memory would be a big problem. Probably 10^3 mass fractions per cell. Maybe for a problem with less than 10^3 cells (30×30), like a hillslope.

5/7/99 Revisions.

I've revised the coding to provide the option for carrying either a statistical representation (memory saving) or bin representation (memory intensive but faster and more accurate) for the particle-size distribution of each element. Inefficiency in the original coding was improved upon as well. As a comparison of relative speed, I have a problem with 2 texture components, 37 bins per texture, and 4 elements per column. The original coding with statistical representation ran one step of this problem 10 times in 37.6 sec, for an average of 3.76 sec/step (excluding setup costs). The updated coding ran one step of the same problem 100 times in 7.74 sec, for an average of 0.0774 sec/step (almost 50 times faster).

The updated code ran the statistical representation 10 times in 16.8 sec, for an average of 1.68 sec/step (2.2 times faster). Most of the speedup was accomplished by moving the evaluation of the breakdown transition matrix to a preprocessing step, halving the number of beta-distribution calls per time step. The remaining small speedup was likely gained by using global arrays rather than passing arguments.

In a mode with one element and four textures per column, and grain-size distribution characterized with 19 bins, representing a minimum resolution that might be used, one time step is roughly 0.0559 sec. This corresponds to about 1070 cells per minute. Converting the *Matlab* particle-update routine to a compiled version using the builtin *Matlab* converter realized a further speedup to a time step of 0.0395 sec, probably due to reduced looping overhead. Converting both the particle-update and the bulk flux driver routines resulted in a speed of 0.0367 sec/step, or about 1640 step/min (about 1.5 times faster). With 37 bins, the average rate is 0.597 sec/step (1.6 times slower); with 10 bins, 0.0375 sec/step (essentially the same).

The fastest rate would correspond to solving a 40×40 grid each minute for the subsurface particle transport. Note that additional processing (*e.g.*, sorting) would slow this down, and additional work is necessary for surface transport and sources. For comparison, the finest Split Wash

grid (1.875 m on a grid-block side) is 417 × 737 blocks for a total of 307,329 grid blocks; this would mean each time step takes more than 3 hours. Even though perhaps half of the grid blocks are not strictly necessary, a transient Split Wash simulation is still ambitious. A hillslope cross section at the same resolution would be only 200 blocks, so that several time steps could be accomplished per minute (much more practical).

5/8/99 Constitutive relationships.

Summarizing from previous entries, the sediment mass balance, for any particular particle size, is

$$\sum S_{in}\mathbf{q}_{in} - S\sum \mathbf{q}_{out} + (W/L)c_e(S - S_{eq}) = 0, \tag{16-101}$$

$$S_{eq} = C_s\frac{\mathbf{v}^4}{h}, \tag{16-102}$$

$$c_e = \begin{cases} \frac{\mathbf{v}_s}{h}\left(1 - \frac{S_{eq}}{S}\right) & \text{for deposition} \\ C_{scour} & \text{for detachment} \end{cases} \tag{16-103}$$

where

S is sediment concentration [M/L^3],
S_{eq} is equilibrium sediment concentration [M/L^3],
$\mathbf{q}$ is volumetric water flux [L^3/T],
$\mathbf{v}$ is water velocity [L/T],
$\mathbf{v}_s$ is particle settling velocity [L/T],
C_s is a coefficient [M T^4/L^6],
C_{scour} is a coefficient describing detachment [1/T],
$\mathbf{q}$ is volumetric water flux [L^3/T],
W/L is travel width/travel length [–], and
c_e is the kinetic exchange coefficient [–].

There are one-to-one relationships between velocity, flux, flow depth, and equilibrium sediment concentration, so that all can be calculated given one. Unfortunately, c_e is dependent on whether deposition or detachment is occurring.

The WEPP documentation (Flanagan and Nearing, 1995) has a similar but more complete approach to predicting erosion and detachment. In particular, detachment is much more physically based, considering shear stress and the effects of roughness. The WEPP approach partitions the system into rills (1D features) and delivery from interrill areas. Interrill areas are not explicitly treated, other than in the 1D features. Sediment transport is assumed steady state, with overland

flow assumed to occur at the peak rate for the length of time that produces the same total flux over the storm (*i.e.*, a equal-volume steady pulse).

The WEPP rill equation is

$$\frac{\partial G}{\partial x} = D_f + D_i \tag{16-104}$$

$$D_f = \begin{cases} \left(\frac{K_r}{T_c}\right)(\tau_f - \tau_c)(T_c - G) & \text{for detachment} \\ \left(\frac{\beta V_f}{q}\right)(T_c - G) & \text{for deposition} \\ D_i & = K_{iadj} I_e \sigma_{ir} SDR_{RR} \left(\frac{R_s}{w}\right) \end{cases} \tag{16-105}$$

where

G is sediment load [M/LT],
D_f is rill erosion rate [M/L^{2}T],
D_i is interrill sediment delivery rate [M/L^{2}T],
x is distance downstream [L],
K_r is a rill erodibility parameter [T/L],
τ_f is flow shear stress acting on the soil [M/LT^2],
τ_c is the critical flow shear stress for detachment [M/LT^2],
T_c is sediment transport capacity [M/LT],
β is a raindrop-induced turbulence coefficient (0.5 if raining, 1 if not) [–],
V_f is effective fall velocity for the sediment [L/T],
q is flow discharge per unit width [L^{2}T],
K_{iadj} is adjusted interrill erodibility [–],
I_e is effective rainfall intensity [L/T],
σ_{ir} is the interrill runoff rate [L/T],
R_s is the rill spacing [L], and
w is the rill width [L].

In order to translate the WEPP equation into the sediment concentration form, the following correspondences hold:

$$G = S\mathbf{v}w \tag{16-106}$$

$$T_c = S_{eq}\mathbf{v}w \tag{16-107}$$

$$q = \mathbf{v}w \tag{16-108}$$

Substituting into the WEPP and neglecting interrill delivery yields

$$\frac{\partial S\mathbf{v}w}{\partial x} = \begin{cases} \left(\frac{K_r}{S_{eq}\mathbf{v}w}\right)(\tau_f - \tau_c)(S_{eq} - S)\mathbf{v}w & \text{for detachment} \\ \left(\frac{\beta V_f}{\mathbf{v}w}\right)(S_{eq} - S)\mathbf{v}w & \text{for deposition} \end{cases} \tag{16-109}$$

Simplifying yields

$$\frac{\partial S\mathbf{v}w}{\partial x} = \begin{cases} \left(\frac{K_r}{S_{eq}}\right)(\tau_f - \tau_c)(S_{eq} - S) & \text{for detachment} \\ \beta V_f(S_{eq} - S) & \text{for deposition} \end{cases} \tag{16-110}$$

This can be written in the form

$$\sum(S\mathbf{v}) + \frac{L}{w}c_e(S - S_{eq}) = 0 \tag{16-111}$$

where c_e is extracted from the above relationships. The form in the WEPP documentation is the same as I used before, except for the length/width ratio. I think my previous documentation is in error, but the coding should be correct.

WEPP calculates the shear stress at the end of a segment, τ_{fe}, and the transport capacity as

$$\tau_{fe} = \gamma R \sin(\alpha)\left(\frac{f_s}{f_t}\right) \tag{16-112}$$

$$T_c = k_t \tau_f^{3/2} \tag{16-113}$$

where

- γ is the specific weight of water [M/L^{2}T^2],
- R is the hydraulic radius [L],
- α is the average slope angle [–],
- f_s is the friction factor for the soil [–],
- f_t is the total friction factor [–], and
- k_t is a transport coefficient [L$^{0.5}$ T^2/M$^{0.5}$].

In the WEPP documentation, regression relationships are given for K_r and τ_c for rangeland and cropland. The rangeland rill relationships, based on 18 rangeland soils, are

$$K_r = 0.0017 + 0.0024clay - 0.0088orgmat - \frac{0.00088\rho_d}{1000} - 0.00048ROOT_{10} \tag{16-114}$$

$$\tau_c = 3.23 - 5.6sand - 24.4orgmat + \frac{0.9\rho_d}{1000} \tag{16-115}$$

where

K_r has dimensions of [s/m],
τ_c has dimensions of [Pa],
$clay$ is the fraction of clay in the surface soil (0.033 to 0.422),
$sand$ is the fraction of sand in the surface soil (0.08 to 0.88),
$orgmat$ is the fraction of organic material in the surface soil (0.005 to 0.112),
ρ_d is the bulk density (1200 to 1800 kg/m^3), and
$ROOT_{10}$ is the total root mass in the top 10 cm of the soil (0.02 to 4.10 kg/m^2).

Adjustments in WEPP to the K_r and τ_c rill relationships are

$$K_{radj} = K_{rb} CK_{rbr} CK_{rdr} CK_{rlr} CK_{rsc} CK_{rft} \tag{16-116}$$

$$CK_{rbr} = \exp(-0.4br) \tag{16-117}$$

$$CK_{rdr} = \exp(-2.2dr) \tag{16-118}$$

$$CK_{rlr} = \exp(-3.5lr) \tag{16-119}$$

$$CK_{rsc} = \frac{K_{rcons}}{K_r} + \left(1 - \frac{K_{rcons}}{K_r}\right) \exp(-\rho_d daydis) \tag{16-120}$$

$$K_{rcons} = 0.00035 - 0.0014\theta_{cf} + 0.00068 silt + 0.0049 M_{cf} \tag{16-121}$$

$$CK_{rft} = 2.0(0.933)^{\Psi_{surf}} \tag{16-122}$$

$$\tau_{cadj} = \tau_{cb} C\tau_{rr} C\tau_{cons} C\tau_{sc} C\tau_{ft} \tag{16-123}$$

$$C\tau_{rr} = 1 + 8(RR_t - 0.006) \tag{16-124}$$

$$C\tau_{sc} = \frac{\tau_{rcons}}{\tau_r} + \left(1 - \frac{\tau_{rcons}}{\tau_r}\right) \exp(-\rho_d daydis) \tag{16-125}$$

$$\tau_{cons} = 8.37 - 11.8\theta_{fc} - 4.9 sand \tag{16-126}$$

$$C\tau_{ft} = 0.875 + 0.0543 \ln(Psi_{surf}) \tag{16-127}$$

where

K_{radj} is the adjusted value of K_r,
CK_{rbr} is the rill erodibility adjustment,
CK_{rdr} is the dead root adjustment,
CK_{rlr} is the live root adjustment,
CK_{rsc} is the sealing and crusting adjustment,
br is the mass of buried residue in the top 15 cm [kg/m^2],
dr is the mass of dead roots in the top 15 cm [kg/m^2],
lr is the mass of live roots in the top 15 cm [kg/m^2],
$daydis$ is the number of days since disturbance [day],
θ_{cf} is the volumetric water content at field capacity (1/3 bar) [m^3/m^3],
$silt$ is the fraction of silt in the surface soil [–],
RR_t is the random roughness of the surface soil [mm]

The adjustments for sealing and crusting are only made for cropland.

The interrill delivery rate, D_i, is

$$D_i = K_{iadj} I_e Q_r \tag{16-128}$$

where

K_{iadj} is the adjusted value of interrill erodibility [kg s/m^4],
I_e is the rainfall intensity [L/T],
Q_r is the runoff rate [L/T],

The relationships in WEPP for rangeland interrill erodibility are

$$K_{iadj} = K_{ib} RK_{icov} RK_{ift} \tag{16-129}$$

$$K_{ib} = 1.81 - 1.91 sand - 6.327 orgmat - 0.846\theta_{fc} \tag{16-130}$$

$$RK_{icov} = \exp[-7.0(inrcov + cancov)] \tag{16-131}$$

$$RK_{ift} = CK_{ift} \tag{16-132}$$

where

K_{ib} is the base value of interrill erodibility [kg s/m^4],
RK_{icov} is the adjustment for cover [–],
$inrcov$ is the interrill cover [0 to 1],
$cancov$ is the canopy cover [0 to 1].

5/9/99 Proposed revisions to constitutive theory.

These descriptions are somewhat unsatisfactory. There is always a deposition component, although it may be overcome by the detachment component. Partitioning c_e into either a deposition or a detachment mode loses this physical behavior. I would prefer to see something like the evaporation relationships in boundary layer theory, with a far-field concentration and a surface concentration based on the shear stress available for lifting particles.

Stress at the ground surface arising from fluid flow should be partitioned among all of the surface elements. I would expect that stress on a particular surface element (*e.g.*, a particular grain size) would be proportional to the exposed grain surface area relative to the total exposed surface area. This can be written

$$\tau_i = \tau_t \frac{SA_i}{\sum_j SA_j} \tag{16-133}$$

where τ_i is the stress over all surface elements of class i, τ_t is the total surface stress, SA represents the total exposed surface area, and the summation on the right-hand side is over all surface elements. Comparison of the stress relative to a critical stress for each surface element provides information on rates of detachment.

A development by Bird et al. (1960) suggests that the fall velocity, v_∞ of a particle in turbulent conditions is

$$v_\infty^2 = \frac{8gR}{3f}\left(\frac{\rho_s - \rho_f}{\rho_f}\right) \tag{16-134}$$

$$Re = \frac{2Rv_\infty\rho_f}{\mu} \tag{16-135}$$

$$f = \begin{cases} \frac{24}{Re} & Re < 2 \\ \frac{18.5}{Re^{3/5}} & 2 < Re < 500 \\ 0.44 & 500 < Re < 2 \times 10^5 \end{cases} \tag{16-136}$$

where

- g is the acceleration due to gravity [L/T^2],
- R is the particle radius [L],
- ρ_s is the sphere density [M/L^3],
- ρ_f is the fluid density [M/L^3], and
- μ is the fluid viscosity [M/LT].

A more recent analysis suggests that the friction factor should be

$$f = \frac{24}{Re} + 1.5 \tag{16-137}$$

for natural sands and gravels (Julien, 1995).

The same analysis might be adapted to calculate the forces on the particles given a fluid velocity. Such an analysis has been done by Einstein (1950) for particles in rivers, balancing stresses with gravity and incorporating a statistical distribution of angles.

5/10/99 Incorporating time-variable overland flow.

The approach for incorporating sediment transport in time-variable overland flow relies on steady-state sediment transport in time-averaged storms. The WEPP approach also uses steady-state transport for each storm, but here the mixture of storms is performed differently. The idea here is to run a sequence of storms representative of the natural distribution, accumulating the cumulative distribution of flow within each cell.

The cumulative distribution is broken into N bins for each cell. An equivalent set of storm fluxes arises from the N bins, in the form

$$\sum_i \left[\sum_j (S_{ij} f_{ij} \mathbf{v}_{ij}) + \frac{L}{w} f_i c_{ei} (S_i - S_{eqi}) \right] = 0 \tag{16-138}$$

where the i subscript represents a storm bin and f_i is the fraction of time that storm bin i is active. A subtlety of this approach is that f may not be the same for incoming and outgoing fluxes at a particular cell, meaning that there need not be continuity of water fluxes if there are losses due to infiltration or evaporation. Typically f would be lower for outgoing fluxes, which would yield additional deposition.

The coefficients used in the time-averaged storms should be appropriately time weighted as well. A particular flux may occur at any time of year, but may be more likely in some season. The coefficients should reflect this preferentiality.

In order to properly accumulate the storm statistics, I envision running numerous storms with numerous initial characteristics. Note that each storm should be quite fast to run (minutes or less). Some type of response surface could be built up, specific to the specific watershed. The factors in the response surface might include peak flow and the equivalent length of time for that flow. The factors that might be considered include:

- Initial moisture content
- Cover and canopy cover
- Surface soil texture
- Masses of live and dead roots and buried residue
- Random surface roughness
- Friction factors

Thus, each rainfall event might be rerun numerous times, although probably only a relatively few numbers of rainfall events would be necessary.

9/6/00 Simulation update.

Work estimating soil thicknesses since the last entry is reported in the chapter on the year-2000 milestone report. In this report, soil thicknesses are created using iterations for water, sediment, and alluvium all solved simultaneously. The elevation grid is dehollowed before the simulation start.

As a final stage in the section on soil thicknesses, I have started comparing the USGS estimates of soil thickness with the mass-balance results. There is some difficulty because the two grids are at different scales and are offset. They may be in different coordinate systems as well (NAD27 versus NAD83) but both are supposed to be in NAD27. Grid verification remains to be done.

The USGS approach maps the domain into *a priori* domains of 0 to 0.5, 0.5 to 3, 3 to 6, and $>$ 6 m soil thicknesses. Within each class, soil thickness is based on slope with a different relationship for each class. In my approach, I also use a slope-dependent regression in areas with deep alluvium but the regression is approximately inversely dependent on slope instead of the linear relationships favored by USGS.

In comparing the maps, the mass-balance results are aggregated to the coarser USGS grid. Disturbingly, my results and the USGS don't really correspond for each depth class, implying that the grids are misaligned or at least one of the two approaches is totally off-base.

Inspired by the comparison, I revisited the idea of a regression-based approach to soil thickness. The $\log(A/\tan\beta)$ similarity index is commonly used in watershed studies to estimate satu-

rated zone thickness in shallow soils above bedrock, where A is upstream area and β is local slope. Reasoning that soil may behave similarly (pun intended) I started looking at the mass balance results.

The simulations never estimated upslope area or local slope, so I've post-processed estimates for these values. Since no losses to soil is allowed in estimating water depth, A is estimated for each cell from the depth in the cell and the local slope using the Manning equation.

I find that regression results are almost identical when I use β, $\tan\beta$, or $\sin\beta$, perhaps a miniscule edge going to using β.

I find that there is a strikingly good similarity parameter for the mass balance results:

$$H = \frac{D\beta^{1/2}}{A} \tag{16-139}$$

where D is the local soil thickness. Excellent results are obtained if I use a local 3-by-3 moving average of thickness, area, and slope to account for post-processing errors. Plotting D/A versus β on a log-log plot results in almost all pixels lying very close to a single line.

I've tried using borehole data in the same relationship, since I have soil thickness for almost all neutron probe boreholes and many of the other boreholes about the site. The 75 boreholes within the area of the 7.5-m grid were assigned to the nearest cell to get upslope area and slope. There is quite a bit of scatter but again a D/A versus β relationship can be found. In this case, the exponent for β is much larger (about 1.4). The result is shaky, however, since I think that the boreholes are in UTM NAD86 while the grid is UTM NAD27, which can result in a 200-m north-south offset (channel versus ridge in the repository footprint). Randy is going to convert the borehole data to NAD27 for a better comparison.

I'd like to nail down the relationships between soil thickness, area, and slope for different scenarios (dust-, bedrock-, water-, or creep-dominated conditions). The mass balance approach has a soft spot insofar as hollows are badly handled in the equations. Cells that have no outlets are treated like sinks that suck up all incoming stuff. The dehollowing preprocessing step is only partially successful, since somehow hollows may appear during subsequent calculations.

I've implemented a heuristic approach that iterates on water and soil equations and multiplies the depths in hollows by a factor, but this does not eliminate all hollows even after 300 iterations. Less than 0.1 percent of pixels are flagged as hollows after only a few iterations, but improvement slows rapidly. Although there is minimal impact on scatterplots for comparison of mass-balance pixels, the field situation does not have such sinks to suck up flow. A direct result

is that comparisons of borehole data with mass-balance estimates are damaged by not eliminating hollows. In order to get polished results, it is imperative to account for hollows in an efficient manner.

The routing approach for water and soil is very successful in areas where the ground slope dominates transport. The energy slope in this domain is readily estimated from the ground slope, so that few iterations are required to polish the water/soil thicknesses. Because the routing approach is explicit, however, it performs poorly when the energy slope depends strongly on the solution itself. In this case, an implicit approach is indicated. I'd like to implement a hybrid approach, where the implicit approach is only used for restricted areas and the routing approach is used elsewhere. I envision using the routing approach with implicit zones around each hollow studding the domain like raisins in pudding.

The main objection to using the implicit approach on the full domain is the size of the resulting coefficient array. The large 7.5-m grid is on the order of 1200 by 800, which means that there are about a million linear equations to solve simultaneously, and the bandwidth is about 1600. Even with sparse storage, this may be demanding to solve.

The diffusion equation for shallow-water flow is written in finite-volume form as

$$A_e \frac{\partial H}{\partial t} + \sum_{i=1}^{N} C_i K (H_{i1} - H_{i2}) - A_e S = 0 \tag{16-140}$$

where K is conductivity [L/T], H is elevation of the free surface [L], A_e is cell area [L^2], C_i is cross-sectional length of the connection between cells (width times height) divided by distance between cells [L], and S is internal source flux rate. In SI units,

$$K = \frac{b_w^{5/3}}{n\sqrt{S_n}} \tag{16-141}$$

$$S_n = \left[\left(\frac{\partial H}{\partial x} \right)^2 + \left(\frac{\partial H}{\partial y} \right)^2 \right]^{1/2} \tag{16-142}$$

where b_w is thickness of the surface water, n is Manning's n, and S_n is the friction slope [–].

Within each hollow, the diffusion equation should provide an effective simulation approach. Note that even a steady flow (no time derivative) requires iteration, since K depends on both water thickness and water slope.

The effectiveness of a combined approach depends on identifying the regions that are considered implicit. The overall solution strategy will be

- Perform explicit routing from high to low until a hollow is encountered
- Cycle until convergence occurs for the hollow
  - Route fluxes for the range of explicit cells between highest inlet and lowest outlet
  - Solve the hollow using latest explicit boundary fluxes
- Continue explicit routing until next hollow
- Iterate the entire cycle to polish

Note that hollows may overlap in an elevation range, so provision will be necessary to separate these cases.

The strategy for identifying implicit zones should work down from the highest elevation until a hollow is identified, then expand the perimeter until an outlet cell is found. An outlet cell has outflow that doesn't go to an interior or perimeter cell. When working outwards, the lowest perimeter cell is checked for outlets, and if none the perimeter is expanded to include all adjacent cells that aren't already either interior or perimeter cells. This procedure guarantees that no interior cells are higher than any perimeter cell.

If an existing hollow is found during the expansion, the existing hollow should be merged with the new one (perimeters merged). if the existing hollow has an outlet that doesn't drain into the new hollow, the job is done for the new hollow. Otherwise, expansion should go on as before for the merged hollow. Since processing is performed from high to low, this should guarantee that an outlet is found for all hollows.

9/11/00 Routing model update.

SAS

I've coded up a trial version of the hollow-detection code and tested it on the 7.5-m 1200-by-800-pixel grid for the YM area. The code identifies nearly 800 initial hollows (cells with no outlet) for the current surface topography, all or essentially all lying in channels or ridgelines. Since hollows may join with nearby hollows, particularly in channels, expanding hollows to find outlets reduces the total to about 640 hollows after processing. Each processed hollow has between 9 and 44 cells including perimeter cells. The processed hollows are collected into about 150 hollow zones, where hollows with overlapping elevation ranges are included in each zone. Non-hollow cells between the lowest outlet in each pair of zones are identified for each hollow zone as well. The complete routing for the grid takes about a minute.

Two sets of routing arrays need be created, one for water (updated after every alluvium iteration) and one for alluvium (created once at the start of simulation). Since bedrock is fixed, alluvium routing is fixed. However, since the top of alluvium is not fixed, water routing may shift about.

9/18/00 Routing model update.

The revised version of the implicit/explicit water routing code is operational enough to run through most of the domain. There were several bugs primarily related to indexing that took some work to stamp out, but I've been able to complete a pass with a reduced domain of 100 by 100 cells.

I selected an 800 by 800 block to process but I had problems with out-of-memory messages about 2/3 of the way through the first pass. Windows did not handle this situation well, crashing the computer. It's taken several days to get the computer back up and operational. I took steps to clear memory usage in the code but it turns out that there is a memory leak in one of *Matlab*'s routines used by the compiler. The first index operation into a global array grabs memory each time the compiled routine executes, but does not release it until *Matlab* quits operation. The memory grab is significant over the hundreds of calls needed for processing. I've created a demo problem and sent it to the Mathworks, but will probably need to create a C routine to eliminate the problem. Luckily I have a template already coded from earlier routing versions that should be readily adaptable, although it is not as convenient.

One problem has repeatedly arisen with the implicit/explicit routing algorithm that did not seem to pop up in the purely explicit routing. In channels downstream of hollows, sometimes the water level required to push water out results in a mound within the cell. This mound appears to create large nonphysical fluxes that propagate downstream, resulting in infinite depths within a few dozen cells. The problem doesn't manifest for low rainfall rates (two orders of magnitude smaller than used before). I suspect that it didn't manifest during the purely explicit routing because hollows acted as sinks that sucked up excess fluxes, while the hollow-handling algorithm allows the fluxes to pass through.

A possible solution to the cell-mounding problem is to increase the number of channel cells that are implicitly handled. Currently cells are identified as hollows if they have no outlet. Hopefully it may be sufficient to modify this criterion to identify additional cells as hollows when the maximum outlet slope is flatter than some criterion. If this doesn't work, perhaps marking cells as implicit with upstream area (based on low rainfall rates) greater than some criterion would

work. The latter solution is not attractive since it requires additional (expensive) solutions to be obtained.

Parenthetically, part of the problem with hollows continually being created before was due to making routing decisions according to the latest water level instead of soil surface elevation. Keeping routing directions (but not flux magnitude) from soil elevation may not be completely consistent but at least allows iteration without new hollows.

9/17/02 Update from work for others.

I developed a simulator for the Everglades National Park that is based on the simulator used here. That code, called *SEDFLOW*, is a 3D simulator to consider overland flow, subsurface flow, and sediment mass balance. The water column is vertically integrated (hence uses a 2D grid), but sediment can be transported using a 3D grid. The water is much deeper and slower than at YM, and the sediment is organic rather than inorganic. However, much of the insights gained from that work are directly applicable to YM.

The Everglades code underwent a significant amount of testing and revealed some features of the approach that suggest using a revised scheme. In particular, the link-based finite-volume approach is not able to handle dispersion properly, since dispersion requires cross derivatives that are not calculated for typical link-based finite volume methods.

The method was shown to be reasonably accurate with the flows were aligned with the grid. However, comparisons of the method with a 1D PDE solver provided with *Matlab* showed that the *Matlab* routine converged faster under grid refinement with essentially the same number of unknowns. I think that this is due to the subtle inconsistencies that can occur unless careful when the problem has advective components. This observation spurred the implementation of the staggered-grid algorithm described below. Staggered-grid algorithms are used in the literature; presumably they are based on the same integrations although I couldn't locate details without a trip to the library.

I maintained a scientific notebook for the Everglades project. The following is copied essentially verbatim from that other notebook to provide guidance for the YM work. The 2D integrations reported are directly applicable, form the basis for a fully implicit code for YM, and have been implemented and tested on example problems. The 3D integrations have not been implemented or tested and thus are more likely to have errors; the 3D work is only included for completeness.

ENP Entry 8/4/01: Grid scheme

The scheme for performing flux calculations is specialized for a regular rectangular grid. All internal cells have the same dimensions, with a single layer of zero-width boundary cells to handle boundary conditions.

Several options are provided to create links between cells. The straightforward ones are x1d, y1d, and cross (cross is a 4-way pattern linking adjacent cells in both of the x and y directions). In these patterns, total flux between cells is

$$Q = K\frac{L}{\Delta}(H_1 - H_2) \tag{16-143}$$

where Q is flux, K is vertically integrated conductivity (not averaged over depth), L is width of the interface between cells, Δ is distance between cell centroids, and H is a field value whose gradient drives flux (*e.g.*, energy surface). The L/Δ term is simply the ratio of cell dimensions, depending on the direction of the connection. The zero thickness of the boundary layer means that the local value of L/Δ is 0 along the boundary layer and 2 perpendicular to the boundary (since Δ is half its normal value).

The star option allows diagonal connections between cells as well, which is a diffusive approach that is handy for heterogeneity. Instead of flux across an interface arising from only perpendicular cells, 3 adjacent cells on the exterior of the cell (1 perpendicular and 2 diagonal) contribute to perpendicular flux. The scheme is

$$\hat{Q}_{21} = wQ_{21} + \frac{(1-w)}{2}[Q_{11} + Q_{31}] \tag{16-144}$$

where $\hat{Q}$ is total perpendicular flux, Q_{21} is flux between perpendicular cells, Q_{11} and Q_{31} is the perpendicular component of flux between diagonal cells, and w is the weighting between perpendicular and diagonal components. When $w = 1$, the cross scheme is obtained; when $w = 0$, only diagonal flow is used. Typically one might use $w = 1/2$.

The L/Δ factor is stored for each link. A perfect mass balance occurs for a constant K and planar H when

$$\frac{L}{\Delta} = \begin{cases} w\frac{\Delta_2}{\Delta_1} & \text{in the } x_1 \text{ direction} \\ w\frac{\Delta_1}{\Delta_2} & \text{in the } x_2 \text{ direction} \\ \frac{(1-w)}{2}\left(\frac{\Delta_1}{\Delta_2} + \frac{\Delta_2}{\Delta_1}\right) & \text{in the diagonal directions} \end{cases}$$

where Δ_i is the grid spacing in the ith direction. Perpendicular and diagonal links contacting a boundary cell have L/Δ multiplied by 2; boundary-boundary links have $L/\Delta = 0$, and diagonal links contacting a corner cell are multiplied by 4.

I tested the scheme with uniform water and layer thicknesses and consistent boundary conditions, but with different orientations of the bottom-elevation plane. The scheme resulted in unchanged water elevations, which is the analytic solution. Numerous other schemes were tried with the same type of test case, all with spurious sources and sinks (especially near the corners).

One would expect that the star scheme is about 4 times slower than the cross scheme, since the matrix bandwidth is twice as large and matrix solution is roughly proportional to the square of bandwidth. For a case with a 42 by 42 grid, a random field for the thickness of the second porous medium layer, and the water table near the mean interface between porous medium and surface water, the cross scheme was about 3.2 times slower (674 seconds versus 209 seconds). Matrix solution is only part of the computational burden, and the star scheme is less than twice the computational effort otherwise.

Estimating the interface K value for diffusive flux is another computational issue. For the flow equation, upstream weighting adds robustness, thus is used exclusively.

A mass balance equation is generically written

$$V_c \frac{\partial M}{\partial t} + \sum_{i=1}^{N} A_i q_i = 0 \tag{16-145}$$

where V_c is cell volume, A_i is interface area, M is mass, and q_i is flux per area across interface i. The increment approach to the mass balance equation is

$$\frac{V_c}{\Delta t}\left[M^{n+1} - M^n + \sum_{j=1}^{M} \frac{\mathrm{d}M}{\mathrm{d}u_j}\delta_j\right] + \sum_{i=1}^{N} A_i \left(q_i^n + \sum_{j=1}^{M} \frac{\mathrm{d}q_i}{\mathrm{d}u_j}\delta_j\right) = 0 \tag{16-146}$$

where superscripts n and $n+1$ denote time levels, superscripts m and $m+1$ denote iterations within a time step, u is a state variable, and $\delta = u^{n+1,m+1} - u^{n+1,m}$. Instead of solving for $u^{n+1,m+1}$ directly, δ is solved for.

Zhang and Ewen (2000) present an approach for simulating gravity-dominated flow in unsaturated porous media that recognizes that $K(u)\nabla z$ can be treated implicitly, essentially by $\mathrm{d}K/\mathrm{d}u\delta\nabla z$. Normally this term is thrown on the right-hand side of the equation, but noting that ∇z is a constant makes it attractive to keep this term as part of the matrix equation.

Since I had had some difficulty with convergence in previous versions of the surface water equations, I implemented this implicit approach in the code to examine if it might be helpful. A preliminary case used a formulation for surface flow that is the vegetation formulation with the same drag at all depths. For low slopes such as in the Everglades, the approach does not

appreciably aid convergence and adds overhead. For more strongly gravity-driven flows, however, the approach works like a champ. Convergence is amazingly rapid for free-surface problems even with slopes greater than 1, or 45° (note that Everglades has a regional slope of 2.5×10^{-5}). A simple 1D free-surface problem with a slope of 2.5 that is limited to time steps of 0.005 or so without the implicit approach converged to steady state (say time 1) in about ten time steps using the implicit approach. Both cases used fully upstream values of K (arithmetic averages caused severe numerical oscillations).

The additional expense is offset by convergence with perhaps less than an order of magnitude increase in regional slope compared to the Everglades, based on one simple 1D test. A second test using a drag that exponentially decreases with water depth showed marked improvement with the implicit approach even at the Everglades slope. A slight nonlinearity is all that it takes to make the approach a no-brainer.

When I tried a case where there was random noise in the interface between soil and water on a 40 by 40 DEM, performance deteriorated for the implicit K scheme. I traced this to considering the sensitivity of K to energy slope. I had implemented a minimum value for slope because K gets very large (K goes to infinity if slope is zero). Apparently this threshold messes up the sensitivity calculation. Comparing identical cases with and without considering slope sensitivity, I found that considering slope sensitivity is not warranted. For moderate slopes, there is minimal impact but for the very low Everglades slopes there is drastic deterioration. I conclude that the slope factor should be assumed constant when calculating sensitivities.

I also ran a few tests for the averaging scheme (upstream versus arithmetic average). Arithmetic averaging worked several times better than upstream averaging for Everglades slopes; however, for greater slopes the downstream boundary condition polluted the solution and amplifying numerical oscillations could drag it to a halt. The solution is to create an adaptive weighting so that outflow boundaries are always upstream weighted.

ENP Entry 8/6/01: Constitutive relations for surface water

The equations for vertically integrated surface water flow start in the 3D form

$$V_c\frac{\partial M}{\partial t} - \sum_{i=1}^{N} A_i \left[\frac{1}{h}\int_0^h K\,\mathrm{d}z\right]\nabla H = 0 \qquad (16\text{-}147)$$

which is converted into the 2D form

$$A_c \frac{\mathrm{d}}{\mathrm{d}H}\left(\int_0^h M\,\mathrm{d}z\right)\frac{\partial H}{\partial t} + \sum_{i=1}^{N}\frac{L_i}{\Delta}\left[\int_0^h K\,\mathrm{d}z\right](H_i - H_j) = 0 \tag{16-148}$$

where

- A_c cell area [L^2]
- V_c cell volume [L^3]
- L_i interface length [L]
- A_i interface area [L^2]
- M mass density [M/L^3]
- K diffusion coefficient [$M/T\ L^2$]
- h thickness of the water layer [L]
- H elevation of the water surface [L]

Mass density

The mass density M is always in the form

$$M = \epsilon\rho \tag{16-149}$$

where ϵ is volume fraction of water [–] and ρ is the mass density of surface water [M/L^3]. The derivative is in the form

$$\frac{\mathrm{d}}{\mathrm{d}H}\left(\int_0^h M\,\mathrm{d}z\right) = M|_h \tag{16-150}$$

where $M|_h$ is M evaluated at the top of the water column.

Relationships for K

Different constitutive relationships for K exist, depending on the physical problem of interest. Vertical integration may be done in layers, each with a different form for K. In all cases, the derivative of the integral of K is in the form

$$\frac{\mathrm{d}}{\mathrm{d}H}\left(\int_0^h K\,\mathrm{d}z\right) = K|_h \tag{16-151}$$

where $K|_h$ is K evaluated at the top of the water column.

Porous medium

The relationship for K in a porous medium is

$$K = \frac{\epsilon \rho^2 g k k_r}{\mu} \tag{16-152}$$

$$\int_0^B K \, \mathrm{d}z = \frac{\epsilon \rho^2 g k k_r}{\mu} B \tag{16-153}$$

where

- ϵ volume fraction of porous medium [–]
- k intrinsic permeability [L^2]
- k_r relative permeability [–]
- ρ density [M/L^3]
- μ viscosity [M/L T]
- g gravitational acceleration [L/T^2]

For the simulator, it is assumed that the water table is a sharp interface with no contribution to flow in the tension zone. Thus, k_r is 1 below the water table and 0 above it.

Manning flow

The Manning relationship only provides the depth-averaged velocity, rather than a full velocity distribution. When just the vertically averaged velocity is needed, it is sufficient to assume that the velocity distribution is constant with depth, so that the relationship for K with Manning flow is

$$K = \frac{\epsilon \rho B^{2/3}}{n\sqrt{S_o}} \tag{16-154}$$

$$\int_0^B K \, \mathrm{d}z = \frac{\epsilon \rho B^{2/3}}{n\sqrt{S_o}} B \tag{16-155}$$

$$S_o = \left[\left(\frac{\partial H}{\partial x} \right)^2 + \left(\frac{\partial H}{\partial y} \right)^2 \right]^{1/2} \tag{16-156}$$

where

- B total thickness of water column [L]
- n Manning's resistance parameter [$T/L^{1/3}$]

The Manning relationship only provides the depth-averaged velocity, rather than a full velocity distribution. When just the vertically averaged velocity is needed, it is sufficient to assume that the velocity distribution is constant with depth. Modifications must be made if the vertical profile is needed for transport, such as assuming a logarithmic profile. Use of the vertically averaged velocity is likely to overpredict dense sediment transport and underpredict transport of floating matter. The simulator only considers depth-averaged Manning velocity at present.

Note that the effects of fluid viscosity and gravitational acceleration are bound into the Manning n, which makes the equation less appealing for considering water/sediment mixtures.

Piecewise constant vegetative resistance

The relationship for K in a piecewise-constant resistant medium in a turbulent flow field is

$$K = \epsilon\rho\left(\frac{2g\mu}{S_o A_f C_D \mu_o}\right)^{1/2} \tag{16-157}$$

$$\int_0^B K\,\mathrm{d}z = \epsilon\rho\left(\frac{2g\mu}{S_o A_f C_D \mu_o}\right)^{1/2} B \tag{16-158}$$

where

- ϵ volume fraction of porous medium [–]
- ρ density [M/L^3]
- μ mixture viscosity [M/L T]
- μ_o clear water viscosity [M/L T]
- g gravitational acceleration [L/T^2]
- A_f area of resistance elements per volume [L^2/L^3]
- C_D coefficient of drag [–]
- S_o energy slope [–]

This relationship assumes that drag force on the vegetation, D_f, is expressed as

$$D_f = \frac{A_f C_D \rho}{2}\bar{u}^2 \tag{16-159}$$

where $\bar{u}$ is time-averaged fluid velocity. For flume experiments with dense sawgrass, flow transitions from laminar to turbulent at about 3 mm/s. In laminar flow, drag increases dramatically and the turbulent relationship is not appropriate.

Although S_o is a function of H, numerical experiments suggest that better computational results are obtained by neglecting the dependence when calculating the derivative of the integral.

Piecewise exponential vegetative resistance

The relationship for K in a piecewise-exponential resistant medium in a turbulent flow field is

$$K = K_{vc} \exp(h/\beta) \tag{16-160}$$

$$\int_0^B K \, \mathrm{d}z = \beta K_{vc} \left[\exp(B/\beta) - 1\right] \tag{16-161}$$

where

K_{vc} K for piecewise constant resistance [M/T L^2]
h height above bottom [L]
β resistance extinction depth [L]

Note that $A_f C_D$ is defined for the bottom of the region.

Laminar film flow

The relationship for K with laminar film flow is

$$K = \frac{\epsilon \rho^2 g h^2}{\mu} \tag{16-162}$$

$$\int_0^B K \, \mathrm{d}z = \frac{\epsilon \rho^2 g B^3}{2\mu} \tag{16-163}$$

where

h height above bottom [L]

ENP Entry 8/19/01: Handling slope and dispersion

I figured out last week how to properly handle local energy slope. The definition of the local energy slope is

$$S_o = \left[\left(\frac{\partial H_e}{\partial x}\right)^2 + \left(\frac{\partial H_e}{\partial y}\right)^2\right]^{1/2} \tag{16-164}$$

I had originally been calculating S_o for each link, which can give zero slopes perpendicular to the flow direction. Thus diagonals in the star scheme were inconsistent with perpendicular elements

causing spurious sources. The key insight is to define S_o for each cell rather than for each link. This is just as easy and takes care of the spurious source terms.

The four neighbors are used to calculate S_o for each cell, averaging each pair of opposing sides in a second-order accurate centered difference scheme. For boundary cells, the first-order accurate one-sided value is used in the direction normal to the boundary.

I have also been pondering how to handle standard dispersive fluxes in the form

$$\mathbf{q}_j = \sum_{i=1}^{N} D_{ij} \cdot \nabla C \tag{16-165}$$

with the dispersion tensor D_{ij}

$$D_{ij} = \delta_{ij}\alpha_T|\mathbf{q}| + (\alpha_L - \alpha_T)\frac{\mathbf{q}_i\mathbf{q}_j}{|\mathbf{q}|} \tag{16-166}$$

where δ_{ij} is the Dirac delta function, α_T and α_L are tangential and longitudinal dispersivities, and $\mathbf{q}_j$ is flux in the j direction. Actually there should be a vertical term as well, which is 20 percent or so of the horizontal tangential value, which in turn is about 1/3 of the horizontal longitudinal value (Chien and Wan, 1998). The same type of thinking as for slope should yield velocities and thus D_{ij} by cell, and the individual links could pick a weighted value of several D_{ij} based on the link direction. The cross scheme is trivial to implement, but the star scheme will need a weighting scheme to obtain the coordinate-direction fluxes.

ENP Entry 8/16/02: Revision to computational scheme

I performed a number of tests on *SEDFLOW* over the last month to test the flow and transport algorithms. After stamping out a few bugs, the simulator works well for flow. The simulator also works well for transport as long as flow is aligned with the grid, but only a minor deviation causes significant numerical dispersion. This is largely because the cross-derivative dispersion terms are not considered in *SEDFLOW*. These tests are documented in a report to Everglades National Park (ENP).

During the testing process, several options for improving the code were encountered.

- Testing for flow validity was performed against the pdepe routine in *Matlab*, which is a 1D simulator based on the method of lines for time stepping. Spatial discretization uses a finite-element approach, with the approximation being that unknowns are located at mesh

points but fluxes are evaluated at cell centroids assuming linear interpolation of the unknowns. This discretization scheme converged with a coarser grid than the *SEDFLOW* scheme. The method-of-lines scheme is provided as a *Matlab* routine, and is attractive as a robust and efficient time-stepping scheme.

- It turns out that transport simulation accuracy is dependent on the Courant number, which requires quite small time steps for our typical grids and flows. The Courant restriction can be removed for linear transport and steady flow by using a Laplace-transform technique (Sudicky, 1989), which has a side benefit of not requiring as fine of a grid as well. I think that the equations can be cast in an appropriate form, with the primary difficulty lying in the scour term. As a benefit, cumulative fluxes can easily be obtained. The approach requires complex mathematics to invert. My estimate is that the number of grid cells that can be considered is lowered by about a factor of 8, and computational cost breaks even if 30 to 100 time steps are eliminated.
- A highly accurate scheme has been proposed in 2D based on the method of characteristics and the Laplace-transform approach. The equations appear to be fairly complex, and the extension to 3D is worse.

I think that it is wise to recast the *SEDFLOW* equations into an approach philosophically identical to the pdepe spatial discretization, and provide the option of stepping in time using the method of lines. Much of the original scheme and data structure would remain the same. The transport algorithm should also provide the option of using the Laplace-transform approach. Necessary information is documented here.

Interpolation strategies

Consider the typical conservation equation

$$\frac{\partial M}{\partial t} + \nabla \cdot \mathbf{q} = Src \tag{16-167}$$

The *SEDFLOW* approach recasts this in the form of

$$V_c \frac{\partial M}{\partial t} - \sum_{i=1}^{N} A_i \mathbf{q}_i = V_c Src \tag{16-168}$$

where

A_c cell area [L^2]
V_c cell volume [L^3]
L_i interface length [L]
A_i interface area [L^2]
M mass density [M/L^3]
$\mathbf{q}$ mass flux [$M/T\ L^2$]

The revised formulation is in the form

$$\int_{\Omega_c} w\frac{\partial M}{\partial t}\,\mathrm{d}\Omega_c + \int_{\sigma_c} \mathbf{n}\cdot\mathbf{q}\,\mathrm{d}\sigma_c = \int_{\Omega_c} wSrc\,\mathrm{d}\Omega_c \tag{16-169}$$

where

Ω_c domain subregion [L^3]
σ_c domain subregion boundary [L^2]
w weighting function for domain integration [–]

For a rectilinear brick cell, local coordinates ξ, η, and ζ are defined

$$\frac{\xi-\xi_0}{\xi_1-\xi_0} = \frac{x-x_0}{x_1-x_0} \tag{16-170}$$

$$\frac{\eta-\eta_0}{\eta_1-\eta_0} = \frac{y-y_0}{y_1-y_0} \tag{16-171}$$

$$\frac{\zeta-\zeta_0}{\zeta_1-\zeta_0} = \frac{z-z_0}{z_1-z_0} \tag{16-172}$$

where $\xi_0 = \eta_0 = \zeta_0 = -1$ and $\xi_1 = \eta_1 = \zeta_1 = 1$. For each node i defining a brick corner, a nodal value ξ_i is defined as ξ_0 or ξ_1 to make $\xi + \xi_i = 0$ at the opposite end of the domain. A similar assignment provides η_i and ζ_i. Note that the local coordinates would be more complex for deformed bricks.

An integral over an x range is transformed to an integral over the corresponding ξ range using

$$\int_{x_a}^{x_b} (\cdot)\,\mathrm{d}x = \int_{\xi_a}^{\xi_b} (\cdot)x_{,\xi}\,\mathrm{d}\xi \tag{16-173}$$

A corresponding transformation using η and ζ is used for integrals over y and z. Derivatives of the

local coordinates with respect to the global coordinates are

$$\xi_{,x} = \frac{\partial \xi}{\partial x} = \frac{2}{x_1 - x_0} = \frac{1}{x_{,\xi}} \tag{16-174}$$

$$\eta_{,y} = \frac{2}{y_1 - y_0} = \frac{1}{y_{,\eta}} \tag{16-175}$$

$$\zeta_{,z} = \frac{2}{z_1 - z_0} = \frac{1}{z_{,\zeta}} \tag{16-176}$$

where the comma subscript notation denotes a derivative. In the constant-size grid used in *SEDFLOW*, these derivatives are identical for all cells.

The coordinate transformation is straightforward to evaluate since the cells are rectilinear. If the cells were deformed, analytical integration would be much harder since the coordinate transformation is not invariant within the cell. Numeric integration is generally used for deformed finite-element cells.

The formulation consistent with the pdepe spatial discretization uses unknown dependent variables defined at nodes, parameters defined as constant over cells, and two different weighting functions.

For domain integrals, the weighting function for an unknown defined at node i is

$$w_i = \begin{cases} 1 & \xi + \xi_i \le 1/2 \text{ and } \eta + \eta_i \le 1/2 \text{ and } \zeta + \zeta_i \le 1/2 \\ 0 & \text{otherwise} \end{cases} \tag{16-177}$$

This is a subdomain weighting function and is identical to the finite-volume weighting function (except that it straddles 4 adjacent cells in 2D and 8 in 3D).

For 3D contour integrals, the corresponding node-i weighting function within a cell is

$$w_i = c_i(\xi + \xi_i)(\eta + \eta_i)(\zeta + \zeta_i) \tag{16-178}$$

The values of the coefficients are defined in Table 16-4.

The weighting functions provide trilinear interpolation within the cell, where

$$u = \sum_{i=1}^{N} w_i u_i \tag{16-179}$$

Table 16-4: Coefficients for local coordinates in a 3D cell. Numbering runs counter-clockwise from the (x_0, y_0, z_0) corner in the $z = z_0$ plane, then moves to the $z = z_1$ plane.

Node	c_i	ξ_i	η_i	ζ_i
1	$-1/8$	-1	-1	-1
2	$1/8$	1	-1	-1
3	$-1/8$	1	1	-1
4	$1/8$	-1	1	-1
5	$1/8$	-1	-1	1
6	$-1/8$	1	-1	1
7	$1/8$	1	1	1
8	$-1/8$	-1	1	1

The values of derivatives of the weighting functions are

$$\frac{\partial w_i}{\partial x} = c_i(\eta + \eta_i)(\zeta + \zeta_i)\xi_{,x} \tag{16-180}$$

$$\frac{\partial w_i}{\partial y} = c_i(\xi + \xi_i)(\zeta + \zeta_i)\eta_{,y} \tag{16-181}$$

$$\frac{\partial w_i}{\partial z} = c_i(\xi + \xi_i)(\eta + \eta_i)\zeta_{,z} \tag{16-182}$$

and the corresponding spatial derivatives of u are

$$\frac{\partial u}{\partial x} = \sum_{i=1}^{N} u_i \frac{\partial w_i}{\partial x} \tag{16-183}$$

$$\frac{\partial u}{\partial y} = \sum_{i=1}^{N} u_i \frac{\partial w_i}{\partial y} \tag{16-184}$$

$$\frac{\partial u}{\partial z} = \sum_{i=1}^{N} u_i \frac{\partial w_i}{\partial z} \tag{16-185}$$

It is useful to write u as a function of ξ, η, and ζ, in the form

$$\begin{aligned} u &= \sum_{i=1}^{N} c_i(\xi + \xi_i)(\eta + \eta_i)(\zeta + \zeta_i)u_i \\ &= C_{u1} + C_{u2}\xi + C_{u3}\eta + C_{u4}\zeta + C_{u5}\xi\eta + C_{u6}\xi\zeta + C_{u7}\eta\zeta + C_{u8}\xi\eta\zeta \\ &= [\mathbf{v}_{u1} + \mathbf{v}_{u2}\xi + \mathbf{v}_{u3}\eta + \mathbf{v}_{u4}\zeta + \mathbf{v}_{u5}\xi\eta + \mathbf{v}_{u6}\xi\zeta + \mathbf{v}_{u7}\eta\zeta + \mathbf{v}_{u8}\xi\eta\zeta] \cdot \mathbf{u} \end{aligned} \tag{16-186}$$

Each term in the sum arises from a product of c_i, ξ or ξ_i, η or η_i, ζ or ζ_i, and u_i. For example,

$C_{u5} = \sum_{i=1}^{N} c_i \zeta_i u_i$; ξ_i and η_i are missing since C_{u5} multiplies ξ and η. The vector form is also convenient, where $C_{uj} = \mathbf{v}_{uj} \cdot \mathbf{u}$ and $\mathbf{u}$ is the vector of u_i values.

The derivatives of the unknowns can be rearranged into functions of ξ, η, and ζ as follows

$$\begin{aligned} u_{,x} &= \sum_{i=1}^{N} c_i \xi_{,x}(\eta + \eta_i)(\zeta + \zeta_i) u_i \\ &= \xi_{,x}(C_{x1} + C_{x2}\eta + C_{x3}\zeta + C_{x4}\eta\zeta) \\ &= \xi_{,x}(\mathbf{v}_{u2} + \mathbf{v}_{u5}\eta + \mathbf{v}_{u6}\zeta + \mathbf{v}_{u8}\eta\zeta) \cdot \mathbf{u} \end{aligned} \tag{16-187}$$

$$\begin{aligned} u_{,y} &= \sum_{i=1}^{N} c_i \eta_{,y}(\xi + \xi_i)(\zeta + \zeta_i) u_i \\ &= \eta_{,y}(C_{y1} + C_{y2}\xi + C_{y3}\zeta + C_{y4}\xi\zeta) \\ &= \eta_{,y}(\mathbf{v}_{u3} + \mathbf{v}_{u5}\xi + \mathbf{v}_{u7}\zeta + \mathbf{v}_{u8}\xi\zeta) \cdot \mathbf{u} \end{aligned} \tag{16-188}$$

$$\begin{aligned} u_{,z} &= \sum_{i=1}^{N} c_i \zeta_{,z}(\xi + \xi_i)(\eta + \eta_i) u_i \\ &= \zeta_{,z}(C_{z1} + C_{z2}\xi + C_{z3}\eta + C_{z4}\xi\eta) \\ &= \zeta_{,z}(\mathbf{v}_{u4} + \mathbf{v}_{u6}\xi + \mathbf{v}_{u7}\eta + \mathbf{v}_{u8}\xi\eta) \cdot \mathbf{u} \end{aligned} \tag{16-189}$$

The 2D form has bilinear interpolation in the form

$$w_i = c_i(\xi + \xi_i)(\eta + \eta_i) \tag{16-190}$$

Coefficients correspond to nodes 5 through 8 in Table 16-4, except that the c_i values are doubled. Corresponding spatial derivatives are

$$\frac{\partial w_i}{\partial x} = c_i(\eta + \eta_i)\xi_{,x} \tag{16-191}$$

$$\frac{\partial w_i}{\partial y} = c_i(\xi + \xi_i)\eta_{,y} \tag{16-192}$$

Writing u as a function of ξ and η,

$$\begin{aligned} u &= \sum_{i=1}^{N} c_i(\xi + \xi_i)(\eta + \eta_i) u_i \\ &= C_{u1} + C_{u2}\xi + C_{u3}\eta + C_{u4}\xi\eta \\ &= [\mathbf{v}_{u1} + \mathbf{v}_{u2}\xi + \mathbf{v}_{u3}\eta + \mathbf{v}_{u4}\xi\eta] \cdot \mathbf{u} \end{aligned} \tag{16-193}$$

The derivatives of the unknowns can be rearranged into functions of ξ and η as follows

$$\begin{aligned} u_{,x} &= \sum_{i=1}^{N} c_i \xi_{,x}(\eta + \eta_i) u_i \\ &= \xi_{,x}(C_{x1} + C_{x2}\eta) \\ &= \xi_{,x}(\mathbf{v}_{u2} + \mathbf{v}_{u4}\eta) \cdot \mathbf{u} \end{aligned} \tag{16-194}$$

$$\begin{aligned} u_{,y} &= \sum_{i=1}^{N} c_i \eta_{,y}(\xi + \xi_i) u_i \\ &= \eta_{,y}(C_{y1} + C_{y2}\xi) \\ &= \eta_{,y}(\mathbf{v}_{u3} + \mathbf{v}_{u4}\xi) \cdot \mathbf{u} \end{aligned} \tag{16-195}$$

Domain integrals

Domain integrals are extremely straightforward to evaluate. A typical 3D integral in the region within a cell where $w = 1$ is in the form

$$\begin{aligned} \int_{\Omega_c} w_i C u_i \, \mathrm{d}\Omega_c &= \int_{z_0}^{z_1} \int_{y_0}^{y_1} \int_{x_0}^{x_1} w_i C_c u_i \, \mathrm{d}x \, \mathrm{d}y \, \mathrm{d}z \\ &= \int_{\zeta_0}^{\zeta_1} \int_{\eta_0}^{\eta_1} \int_{\xi_0}^{\xi_1} w_i C_c u_i x_{,\xi} y_{,\eta} z_{,\zeta} \, \mathrm{d}\xi \, \mathrm{d}\eta \, \mathrm{d}\zeta \\ &= \int_{\zeta_0}^{\zeta_1} \int_{\eta_0}^{\eta_1} \int_{\xi_0}^{\xi_1} w_i C_c u_i \frac{\Delta x}{2} \frac{\Delta y}{2} \frac{\Delta z}{2} \, \mathrm{d}\xi \, \mathrm{d}\eta \, \mathrm{d}\zeta \\ &= \frac{V_c C_c u_i}{8} \end{aligned} \tag{16-196}$$

where

- C_c coefficient that is constant in cell c
- u_i unknown defined for node i

The total 3D integral over the domain is

$$\int_{\Omega} w_i C u_i \, \mathrm{d}\Omega = \sum_{j=1}^{M} \frac{V_j C_j u_i}{8} \tag{16-197}$$

where there are M cells that node i belongs to ($M = 8$ for interior cells). The 2D integrals are exactly analogous, except they are divided by 4 instead of 8.

Contour integrals

Contour integrals are somewhat more complex to evaluate, particularly for transport. The integrals are simplified somewhat by their location along constant planes of ξ, η, and ζ, each passing through the cell centroids.

The following shorthand notation is used for definite integrals from this point on:

$$\langle \sigma \rangle = [\sigma]_{\sigma_a}^{\sigma_b} \tag{16-198}$$

$$\langle \sigma^2 \rangle = \left[\frac{\sigma^2}{2}\right]_{\sigma_a}^{\sigma_b} \tag{16-199}$$

$$\langle \sigma^3 \rangle = \left[\frac{\sigma^3}{3}\right]_{\sigma_a}^{\sigma_b} \tag{16-200}$$

where σ is any local coordinate.

Diffusive flow contour integrals

Flow contour integrals are all in 2D. For generality, the anisotropic case is derived, although this is not necessarily going to be implemented for flow. Diffusive flux $\mathbf{q}$ is defined by

$$\mathbf{q} = -\mathbf{K} \cdot \nabla H \tag{16-201}$$

with components

$$\mathbf{q}_x = -K_{xx}\frac{\partial H}{\partial x} - K_{xy}\frac{\partial H}{\partial y} \tag{16-202}$$

$$\mathbf{q}_y = -K_{yx}\frac{\partial H}{\partial x} - K_{yy}\frac{\partial H}{\partial y} \tag{16-203}$$

Remember, K values are vertically integrated. Insofar as the parameters are constant within a cell, only the derivatives are integrated (the parameters multiply the integrals). For the isotropic case, $K_{xy} = K_{yx} = 0$ and $K_{xx} = K_{yy} = K$.

Integrating derivatives of u along $\eta = 0$ yields

$$\int_{\xi_a}^{\xi_b} u_{,x} x_{,\xi}\, \mathrm{d}\xi = x_{,\xi}\xi_{,x}(\mathbf{v}_{u2}\langle\xi\rangle) \cdot \mathbf{u} = \mathbf{I}_1 \cdot \mathbf{u} \tag{16-204}$$

$$\int_{\xi_a}^{\xi_b} u_{,y} x_{,\xi}\, \mathrm{d}\xi = x_{,\xi}\eta_{,y}(\mathbf{v}_{u3}\langle\xi\rangle + \mathbf{v}_{u4}\langle\xi^2\rangle) \cdot \mathbf{u} = \frac{\Delta x}{\Delta y}\mathbf{I}_4 \cdot \mathbf{u} \tag{16-205}$$

Table 16-5: Invariant coefficients from diffusive-flux integrals for flow equation. When referring to the specific range, $\mathbf{I}_{1i}$ is the first integral set and $\mathbf{I}_{2i}$ is the second set.

Name	From	Coef	$\int_{-1}^{0}(\cdot)\,dx$				$\int_{0}^{1}(\cdot)\,dx$			
			u_1	u_2	u_3	u_4	u_1	u_2	u_3	u_4
$\mathbf{I}_1$	$\mathbf{v}_{u2}\langle\xi\rangle$	1/4	-1	1	1	-1	-1	1	1	-1
$\mathbf{I}_2$	$\mathbf{v}_{u3}\langle\eta\rangle$	1/4	-1	-1	1	1	-1	-1	1	1
$\mathbf{I}_3$	$\mathbf{v}_{u2}\langle\eta\rangle + \mathbf{v}_{u4}\langle\eta^2\rangle$	1/8	-3	3	1	-1	-1	1	3	-3
$\mathbf{I}_4$	$\mathbf{v}_{u3}\langle\xi\rangle + \mathbf{v}_{u4}\langle\xi^2\rangle$	1/8	-3	-1	1	3	-1	-3	3	1

and similarly integrating along $\xi = 0$ yields

$$\int_{\eta_a}^{\eta_b} u_{,x} y_{,\eta}\,d\eta = y_{,\eta}\xi_{,x}(\mathbf{v}_{u2}\langle\eta\rangle + \mathbf{v}_{u4}\langle\eta^2\rangle)\cdot\mathbf{u} = \frac{\Delta y}{\Delta x}\mathbf{I}_3\cdot\mathbf{u} \tag{16-206}$$

$$\int_{\eta_a}^{\eta_b} u_{,y} y_{,\eta}\,d\eta = y_{,\eta}\eta_{,y}(\mathbf{v}_{u3}\langle\eta\rangle)\cdot\mathbf{u} = \mathbf{I}_2\cdot\mathbf{u} \tag{16-207}$$

Using the integrals and evaluating the invariant coefficients arising from the basis functions yields the coefficients defined in Table 16-5.

Let's use the convention of nodes locally numbered 1, 2, 3, and 4 counterclockwise around a cell, starting in the (x_{min}, y_{min}) corner. The normal is defined positive outwards. Flux contour integrals within a cell for each corner are

$$\int_{\sigma_1}\mathbf{n}\cdot\mathbf{q}\,d\sigma = \int_{-1}^{0}\mathbf{q}_x y_{,\eta}\,d\eta + \int_{-1}^{0}\mathbf{q}_y x_{,\xi}\,d\xi \tag{16-208}$$

$$\int_{\sigma_2}\mathbf{n}\cdot\mathbf{q}\,d\sigma = -\int_{-1}^{0}\mathbf{q}_x y_{,\eta}\,d\eta + \int_{0}^{1}\mathbf{q}_y x_{,\xi}\,d\xi \tag{16-209}$$

$$\int_{\sigma_3}\mathbf{n}\cdot\mathbf{q}\,d\sigma = -\int_{0}^{1}\mathbf{q}_x y_{,\eta}\,d\eta - \int_{0}^{1}\mathbf{q}_y x_{,\xi}\,d\xi \tag{16-210}$$

$$\int_{\sigma_4}\mathbf{n}\cdot\mathbf{q}\,d\sigma = \int_{0}^{1}\mathbf{q}_x y_{,\eta}\,d\eta - \int_{-1}^{0}\mathbf{q}_y x_{,\xi}\,d\xi \tag{16-211}$$

Table 16-6: Assignment of invariant integrals to each coefficient for 2D diffusion with constant coefficients.

Node	$K_{xx}\frac{\Delta y}{\Delta x}$	K_{xy}	K_{yx}	$K_{yy}\frac{\Delta x}{\Delta y}$
1	$-\mathbf{I}_{13}$	$-\mathbf{I}_{12}$	$-\mathbf{I}_{11}$	$-\mathbf{I}_{14}$
2	$\mathbf{I}_{13}$	$\mathbf{I}_{12}$	$-\mathbf{I}_{21}$	$-\mathbf{I}_{24}$
3	$\mathbf{I}_{23}$	$\mathbf{I}_{22}$	$\mathbf{I}_{21}$	$\mathbf{I}_{24}$
4	$-\mathbf{I}_{23}$	$-\mathbf{I}_{22}$	$\mathbf{I}_{11}$	$\mathbf{I}_{14}$

where the subscript on σ denotes the corner, $\mathbf{q}_x$ is evaluated at $\xi = 0$, and $\mathbf{q}_y$ is evaluated at $\eta = 0$. The definitions of $\mathbf{q}_x$ and $\mathbf{q}_y$ are combined with the integrals listed in Table 16-5 to yield the values tabulated in Table 16-6. When K is isotropic, the equations simplify to

$$\int_{\sigma_1} \mathbf{n}\cdot\mathbf{q}\,d\sigma = K\left[-\frac{\Delta y}{\Delta x}\mathbf{I}_{13} - \frac{\Delta x}{\Delta y}\mathbf{I}_{14}\right]\cdot\mathbf{u} \tag{16-212}$$

$$\int_{\sigma_2} \mathbf{n}\cdot\mathbf{q}\,d\sigma = K\left[\frac{\Delta y}{\Delta x}\mathbf{I}_{13} - \frac{\Delta x}{\Delta y}\mathbf{I}_{24}\right]\cdot\mathbf{u} \tag{16-213}$$

$$\int_{\sigma_3} \mathbf{n}\cdot\mathbf{q}\,d\sigma = K\left[\frac{\Delta y}{\Delta x}\mathbf{I}_{23} + \frac{\Delta x}{\Delta y}\mathbf{I}_{24}\right]\cdot\mathbf{u} \tag{16-214}$$

$$\int_{\sigma_4} \mathbf{n}\cdot\mathbf{q}\,d\sigma = K\left[-\frac{\Delta y}{\Delta x}\mathbf{I}_{23} + \frac{\Delta x}{\Delta y}\mathbf{I}_{14}\right]\cdot\mathbf{u} \tag{16-215}$$

Advective flow contour integrals

The same weighting functions can be integrated for advective fluxes. In the transport equation, mass flux is simply the concentration times the liquid flux. The flow equation has advective components arising from implicitly considering conductivity advected by gravity.

For generality, let's consider the same anisotropic dispersive phase flux in the context of transport. The advective-flux components of transport are now

$$\mathbf{q}_x = u\left(-K_{xx}\frac{\partial H}{\partial x} - K_{xy}\frac{\partial H}{\partial y}\right) \tag{16-216}$$

$$\mathbf{q}_y = u\left(-K_{yx}\frac{\partial H}{\partial x} - K_{yy}\frac{\partial H}{\partial y}\right) \tag{16-217}$$

while for flow they are

$$\mathbf{q}_x = \delta\left(-\frac{\mathrm{d}K_{xx}}{\mathrm{d}h}\frac{\partial a}{\partial x} - \frac{\mathrm{d}K_{xy}}{\mathrm{d}h}\frac{\partial a}{\partial y}\right) \tag{16-218}$$

$$\mathbf{q}_y = \delta\left(-\frac{\mathrm{d}K_{yx}}{\mathrm{d}h}\frac{\partial a}{\partial x} - \frac{\mathrm{d}K_{yy}}{\mathrm{d}h}\frac{\partial a}{\partial y}\right) \tag{16-219}$$

where a is the elevation of the bottom of the domain. In these cases, H or a is already known, and u or δ is sought.

Let's define the components of the integrals in the form

$$a_{,x} = \xi_{,x}(\mathbf{v}_{u2} + \mathbf{v}_{u4}\eta)\cdot\mathbf{a} = \xi_{,x}(C_{a2} + C_{a4}\eta) \tag{16-220}$$

$$a_{,y} = \eta_{,y}(\mathbf{v}_{u3} + \mathbf{v}_{u4}\xi)\cdot\mathbf{a} = \eta_{,y}(C_{a3} + C_{a4}\xi) \tag{16-221}$$

The following line integrals of weighting functions are also needed:

$$\begin{aligned}\int_{\xi_0}^{\xi_1}[a_{,x}u]_{\eta=0}x_{,\xi}\,\mathrm{d}\xi &= \int_{\xi_0}^{\xi_1} C_{a2}(\mathbf{v}_{u1} + \mathbf{v}_{u2}\xi)\cdot\mathbf{u}\xi_{,x}x_{,\xi}\,\mathrm{d}\xi \\ &= C_{a2}\left(\mathbf{v}_{u1}\langle\xi\rangle + \mathbf{v}_{u2}\langle\xi^2\rangle\right)\cdot\mathbf{u} = C_{a2}\mathbf{J}_1\cdot\mathbf{u}\end{aligned} \tag{16-222}$$

$$\begin{aligned}\int_{\eta_0}^{\eta_1}[a_{,y}u]_{\xi=0}y_{,\eta}\,\mathrm{d}\eta &= \int_{\eta_0}^{\eta_1} C_{a3}(\mathbf{v}_{u1} + \mathbf{v}_{u3}\eta)\cdot\mathbf{u}\eta_{,y}y_{,\eta}\,\mathrm{d}\eta \\ &= C_{a3}\left(\mathbf{v}_{u1}\langle\eta\rangle + \mathbf{v}_{u3}\langle\eta^2\rangle\right)\cdot\mathbf{u} = C_{a3}\mathbf{J}_2\cdot\mathbf{u}\end{aligned} \tag{16-223}$$

$$\begin{aligned}\int_{\xi_0}^{\xi_1}[a_{,y}u]_{\eta=0}x_{,\xi}\,\mathrm{d}\xi &= \int_{\xi_0}^{\xi_1}(C_{a3} + C_{a4}\xi)(\mathbf{v}_{u1} + \mathbf{v}_{u2}\xi)\cdot\mathbf{u}\eta_{,y}x_{,\xi}\,\mathrm{d}\xi \\ &= \eta_{,y}x_{,\xi}\left[C_{a3}(\mathbf{v}_{u1}\langle\xi\rangle + \mathbf{v}_{u2}\langle\xi^2\rangle) + C_{a4}(\mathbf{v}_{u1}\langle\xi^2\rangle + \mathbf{v}_{u2}\langle\xi^3\rangle)\right]\cdot\mathbf{u} \\ &= \frac{\Delta x}{\Delta y}(C_{a3}\mathbf{J}_1 + C_{a4}\mathbf{J}_3)\cdot\mathbf{u}\end{aligned} \tag{16-224}$$

$$\begin{aligned}\int_{\eta_0}^{\eta_1}[a_{,x}u]_{\xi=0}y_{,\eta}\,\mathrm{d}\eta &= \int_{\eta_0}^{\eta_1}(C_{a2} + C_{a4}\eta)(\mathbf{v}_{u1} + \mathbf{v}_{u3}\eta)\cdot\mathbf{u}\xi_{,x}y_{,\eta}\,\mathrm{d}\eta \\ &= \xi_{,x}y_{,\eta}\left[C_{a2}(\mathbf{v}_{u1}\langle\eta\rangle + \mathbf{v}_{u3}\langle\eta^2\rangle) + C_{a4}(\mathbf{v}_{u1}\langle\eta^2\rangle + \mathbf{v}_{u3}\langle\eta^3\rangle)\right]\cdot\mathbf{u} \\ &= \frac{\Delta y}{\Delta x}(C_{a2}\mathbf{J}_2 + C_{a4}\mathbf{J}_4)\cdot\mathbf{u}\end{aligned} \tag{16-225}$$

Performing the individual integrals yields invariant components, denoted $\mathbf{J}$, that arise from integrating the basis functions. The $\mathbf{J}$ coefficients are defined in Table 16-7. Flux contour integrals within a cell for each corner are the same for advection and diffusion; the values multiplying each

Table 16-7: Invariant coefficients from advective-flux integrals for flow equation. When referring to the specific range, $\mathbf{J}_{1i}$ is the first integral set and $\mathbf{J}_{2i}$ is the second set.

Name	Factor	Coef	$\int_{-1}^{0}(\cdot)\,dx$				$\int_{0}^{1}(\cdot)\,dx$			
			u_1	u_2	u_3	u_4	u_1	u_2	u_3	u_4
$\mathbf{J}_1$	$\mathbf{v}_{u1}\langle\xi\rangle + \mathbf{v}_{u2}\langle\xi^2\rangle$	1/8	3	1	1	3	1	3	3	1
$\mathbf{J}_2$	$\mathbf{v}_{u1}\langle\eta\rangle + \mathbf{v}_{u3}\langle\eta^2\rangle$	1/8	3	3	1	1	1	1	3	3
$\mathbf{J}_3$	$\mathbf{v}_{u1}\langle\xi^2\rangle + \mathbf{v}_{u2}\langle\xi^3\rangle$	1/24	-5	-1	-1	-5	1	5	5	1
$\mathbf{J}_4$	$\mathbf{v}_{u1}\langle\eta^2\rangle + \mathbf{v}_{u3}\langle\eta^3\rangle$	1/24	-5	-5	-1	-1	1	1	5	5

Table 16-8: Assignment of invariant integrals to each coefficient for 2D advection with constant coefficients.

Node	$K_{xx}\frac{\Delta y}{\Delta x}$	K_{xy}	K_{yx}	$K_{yy}\frac{\Delta x}{\Delta y}$
1	$-(C_{a2}\mathbf{J}_{12} + C_{a4}\mathbf{J}_{14})$	$-C_{a3}\mathbf{J}_{12}$	$-C_{a2}\mathbf{J}_{11}$	$-(C_{a3}\mathbf{J}_{11} + C_{a4}\mathbf{J}_{13})$
2	$(C_{a2}\mathbf{J}_{12} + C_{a4}\mathbf{J}_{14})$	$C_{a3}\mathbf{J}_{12}$	$-C_{a2}\mathbf{J}_{21}$	$-(C_{a3}\mathbf{J}_{21} + C_{a4}\mathbf{J}_{23})$
3	$(C_{a2}\mathbf{J}_{22} + C_{a4}\mathbf{J}_{24})$	$C_{a3}\mathbf{J}_{22}$	$C_{a2}\mathbf{J}_{21}$	$(C_{a3}\mathbf{J}_{21} + C_{a4}\mathbf{J}_{23})$
4	$-(C_{a2}\mathbf{J}_{22} + C_{a4}\mathbf{J}_{24})$	$-C_{a3}\mathbf{J}_{22}$	$C_{a2}\mathbf{J}_{11}$	$(C_{a3}\mathbf{J}_{11} + C_{a4}\mathbf{J}_{13})$

parameter are shown in Table 16-8 (the entire group of coefficients is dotted with $\mathbf{u}$). For isotropic media, the equations reduce to

$$\int_{\sigma_1} \mathbf{n}\cdot\mathbf{q}\,d\sigma = K[-C_{a2}\mathbf{J}_{12} - C_{a4}\mathbf{J}_{14} - C_{a3}\mathbf{J}_{11} - C_{a4}\mathbf{J}_{13}]\cdot\mathbf{u} \tag{16-226}$$

$$\int_{\sigma_2} \mathbf{n}\cdot\mathbf{q}\,d\sigma = K[C_{a2}\mathbf{J}_{12} + C_{a4}\mathbf{J}_{14} - C_{a3}\mathbf{J}_{21} - C_{a4}\mathbf{J}_{23}]\cdot\mathbf{u} \tag{16-227}$$

$$\int_{\sigma_3} \mathbf{n}\cdot\mathbf{q}\,d\sigma = K[C_{a2}\mathbf{J}_{22} + C_{a4}\mathbf{J}_{24} + C_{a3}\mathbf{J}_{21} + C_{a4}\mathbf{J}_{23}]\cdot\mathbf{u} \tag{16-228}$$

$$\int_{\sigma_4} \mathbf{n}\cdot\mathbf{q}\,d\sigma = K[-C_{a2}\mathbf{J}_{22} - C_{a4}\mathbf{J}_{24} + C_{a3}\mathbf{J}_{11} + C_{a4}\mathbf{J}_{13}]\cdot\mathbf{u} \tag{16-229}$$

Diffusive constant-coefficient transport contour integrals

Transport integrals are all 3D and anisotropic, as the dispersion coefficients are obtained from the velocity field.

Diffusive flux $\mathbf{q}$ is defined by

$$\mathbf{q} = -\mathbf{K} \cdot \nabla u \tag{16-230}$$

with components

$$\mathbf{q}_x = -K_{xx}\frac{\partial u}{\partial x} - K_{xy}\frac{\partial u}{\partial y} - K_{xz}\frac{\partial u}{\partial z} \tag{16-231}$$

$$\mathbf{q}_y = -K_{yx}\frac{\partial u}{\partial x} - K_{yy}\frac{\partial u}{\partial y} - K_{yz}\frac{\partial u}{\partial z} \tag{16-232}$$

$$\mathbf{q}_z = -K_{zx}\frac{\partial u}{\partial x} - K_{zy}\frac{\partial u}{\partial y} - K_{zz}\frac{\partial u}{\partial z} \tag{16-233}$$

Insofar as the parameters are constant within a cell, only the derivatives are integrated (the parameters multiply the integrals).

The derivatives of the unknowns can be rearranged into functions of ξ, η, and ζ as follows

$$\begin{aligned} u_{,x} &= \sum_{i=1}^{N} c_i \xi_{,x}(\eta + \eta_i)(\zeta + \zeta_i)u_i \\ &= \xi_{,x}(\mathbf{v}_{u2} + \mathbf{v}_{u5}\eta + \mathbf{v}_{u6}\zeta + \mathbf{v}_{u8}\eta\zeta) \cdot \mathbf{u} \end{aligned} \tag{16-234}$$

$$\begin{aligned} u_{,y} &= \sum_{i=1}^{N} c_i \eta_{,y}(\xi + \xi_i)(\zeta + \zeta_i)u_i \\ &= \eta_{,y}(\mathbf{v}_{u3} + \mathbf{v}_{u5}\xi + \mathbf{v}_{u7}\zeta + \mathbf{v}_{u8}\xi\zeta) \cdot \mathbf{u} \end{aligned} \tag{16-235}$$

$$\begin{aligned} u_{,z} &= \sum_{i=1}^{N} c_i \zeta_{,z}(\xi + \xi_i)(\eta + \eta_i)u_i \\ &= \zeta_{,z}(\mathbf{v}_{u4} + \mathbf{v}_{u6}\xi + \mathbf{v}_{u7}\eta + \mathbf{v}_{u8}\xi\eta) \cdot \mathbf{u} \end{aligned} \tag{16-236}$$

The constant coefficients are defined by inserting the values of c_i, ξ_i, η_i, and ζ_i, just as in 2D.

Integrating along $\zeta = 0$ yields

$$\iint u_{,x}x_{,\xi}y_{,\eta}\,\mathrm{d}\eta\,\mathrm{d}\xi = x_{,\xi}y_{,\eta}\xi_{,x}(\mathbf{v}_{u2}\langle\xi\rangle\langle\eta\rangle + \mathbf{v}_{u5}\langle\xi\rangle\langle\eta^2\rangle) \cdot \mathbf{u} = \Delta y \mathbf{L}_{x\zeta} \cdot \mathbf{u} \tag{16-237}$$

$$\iint u_{,y}x_{,\xi}y_{,\eta}\,\mathrm{d}\eta\,\mathrm{d}\xi = x_{,\xi}y_{,\eta}\eta_{,y}(\mathbf{v}_{u3}\langle\xi\rangle\langle\eta\rangle + \mathbf{v}_{u5}\langle\xi^2\rangle\langle\eta\rangle) \cdot \mathbf{u} = \Delta x \mathbf{L}_{y\zeta} \cdot \mathbf{u} \tag{16-238}$$

$$\begin{aligned} \iint u_{,z}x_{,\xi}y_{,\eta}\,\mathrm{d}\eta\,\mathrm{d}\xi &= x_{,\xi}y_{,\eta}\zeta_{,z}(\mathbf{v}_{u4}\langle\xi\rangle\langle\eta\rangle + \mathbf{v}_{u6}\langle\xi^2\rangle\langle\eta\rangle + \mathbf{v}_{u7}\langle\xi\rangle\langle\eta^2\rangle + \mathbf{v}_{u8}\langle\xi^2\rangle\langle\eta^2\rangle) \cdot \mathbf{u} \\ &= \frac{\Delta x \Delta y}{\Delta z}\mathbf{L}_{z\zeta} \cdot \mathbf{u} \end{aligned} \tag{16-239}$$

Similarly, integrating along $\xi = 0$ yields

$$\iint u_{,x} y_{,\eta} z_{,\zeta} \, d\eta \, d\zeta = y_{,\eta} z_{,\zeta} \xi_{,x} (\mathbf{v}_{u2} \langle \eta \rangle \langle \zeta \rangle + \mathbf{v}_{u5} \langle \eta^2 \rangle \langle \zeta \rangle + \mathbf{v}_{u6} \langle \eta \rangle \langle \zeta^2 \rangle + \mathbf{v}_{u8} \langle \eta^2 \rangle \langle \zeta^2 \rangle) \cdot \mathbf{u}$$

$$= \frac{\Delta y \Delta z}{\Delta x} \mathbf{L}_{x\xi} \cdot \mathbf{u} \tag{16-240}$$

$$\iint u_{,y} y_{,\eta} z_{,\zeta} \, d\eta \, d\zeta = y_{,\eta} z_{,\zeta} \eta_{,y} (\mathbf{v}_{u3} \langle \eta \rangle \langle \zeta \rangle + \mathbf{v}_{u7} \langle \eta \rangle \langle \zeta^2 \rangle) \cdot \mathbf{u} = \Delta z \mathbf{L}_{y\xi} \cdot \mathbf{u} \tag{16-241}$$

$$\iint u_{,z} y_{,\eta} z_{,\zeta} \, d\eta \, d\zeta = y_{,\eta} z_{,\zeta} \zeta_{,z} (\mathbf{v}_{u4} \langle \eta \rangle \langle \zeta \rangle + \mathbf{v}_{u7} \langle \eta^2 \rangle \langle \zeta \rangle) \cdot \mathbf{u} = \Delta y \mathbf{L}_{z\xi} \cdot \mathbf{u} \tag{16-242}$$

and integrating along $\eta = 0$ yields

$$\iint u_{,x} x_{,\xi} z_{,\zeta} \, d\xi \, d\zeta = x_{,\xi} z_{,\zeta} \xi_{,x} (\mathbf{v}_{u2} \langle \xi \rangle \langle \zeta \rangle + \mathbf{v}_{u6} \langle \xi \rangle \langle \zeta^2 \rangle) \cdot \mathbf{u} = \Delta z \mathbf{L}_{x\eta} \cdot \mathbf{u} \tag{16-243}$$

$$\iint u_{,y} x_{,\xi} z_{,\zeta} \, d\xi \, d\zeta = x_{,\xi} z_{,\zeta} \eta_{,y} (\mathbf{v}_{u3} \langle \xi \rangle \langle \zeta \rangle + \mathbf{v}_{u5} \langle \xi^2 \rangle \langle \zeta \rangle + \mathbf{v}_{u7} \langle \xi \rangle \langle \zeta^2 \rangle + \mathbf{v}_{u8} \langle \xi^2 \rangle \langle \zeta^2 \rangle) \cdot \mathbf{u}$$

$$= \frac{\Delta x \Delta z}{\Delta y} \mathbf{L}_{y\eta} \cdot \mathbf{u} \tag{16-244}$$

$$\iint u_{,z} x_{,\xi} z_{,\zeta} \, d\xi \, d\zeta = x_{,\xi} z_{,\zeta} \zeta_{,z} (\mathbf{v}_{u4} \langle \xi \rangle \langle \zeta \rangle + \mathbf{v}_{u6} \langle \xi^2 \rangle \langle \zeta \rangle) \cdot \mathbf{u} = \Delta x \mathbf{L}_{z\eta} \cdot \mathbf{u} \tag{16-245}$$

There are 3 coefficients, each with 8 corner values, and 12 internal faces to evaluate these integrals over. The integrals are readily evaluated with these formulae. The integrals for each face are presented in Table 16-9, Table 16-10, and Table 16-11. The tables show integrals for all faces in a plane with a specified zero coordinate. Remember, it is assumed that the nodes are locally numbered counter-clockwise from (x_{min}, y_{min}), with the upper nodes numbered after all bottom nodes, as shown in Table 16-4.

The flux relationships for each corner is summarized in Table 16-12. Notice that fluxes across each face appear twice, once with a minus sign and once positive. Accordingly, fluxes are conserved. The assignment of invariant coefficients to diffusion parameters for the flux relationships in Table 16-12 is shown in Table 16-13. In the assembly of matrix equations, it will be more efficient to make a vector from contributions for a node for all parameters, then assemble the vector to the array, rather than assemble the array by contributing parameter.

Table 16-9: Invariant coefficients from diffusive-flux integrals in the plane of $\xi = 0$.

Name	Coef	u_1	u_2	u_3	u_4	u_5	u_6	u_7	u_8
$\xi = 0, \eta \leq 0, \zeta \leq 0$									
$\mathbf{L}_{1x\xi}$	1/64	-9	9	3	-3	-3	3	1	-1
$\mathbf{L}_{1y\xi}$	1/32	-3	-3	3	3	-1	-1	1	1
$\mathbf{L}_{1z\xi}$	1/32	-3	-3	-1	-1	3	3	1	1
$\xi = 0, \eta \leq 0, \zeta \geq 0$									
$\mathbf{L}_{2x\xi}$	1/64	-3	3	1	-1	-9	9	3	-3
$\mathbf{L}_{2y\xi}$	1/32	-1	-1	1	1	-3	-3	3	3
$\mathbf{L}_{2z\xi}$	1/32	-1	-1	-3	-3	1	1	3	3
$\xi = 0, \eta \geq 0, \zeta \leq 0$									
$\mathbf{L}_{3x\xi}$	1/64	-1	1	3	-3	-3	3	9	-9
$\mathbf{L}_{3y\xi}$	1/32	-1	-1	1	1	-3	-3	3	3
$\mathbf{L}_{3z\xi}$	1/32	-1	-1	-3	-3	1	1	3	3
$\xi = 0, \eta \geq 0, \zeta \geq 0$									
$\mathbf{L}_{4x\xi}$	1/64	-3	3	9	-9	-1	1	3	-3
$\mathbf{L}_{4y\xi}$	1/32	-3	-3	3	3	-1	-1	1	1
$\mathbf{L}_{4z\xi}$	1/32	-3	-3	-1	-1	3	3	1	1

Table 16-10: Invariant coefficients from diffusive-flux integrals in the plane of $\eta = 0$.

Name	Coef	u_1	u_2	u_3	u_4	u_5	u_6	u_7	u_8
$\xi \leq 0, \eta = 0, \zeta \leq 0$									
$\mathbf{L}_{1x\eta}$	1/32	-3	3	3	-3	-1	1	1	-1
$\mathbf{L}_{1y\eta}$	1/64	-9	-3	3	9	-3	-1	1	3
$\mathbf{L}_{1z\eta}$	1/32	-3	-1	-1	-3	3	1	1	3
$\xi \leq 0, \eta = 0, \zeta \geq 0$									
$\mathbf{L}_{2x\eta}$	1/32	-1	1	1	-1	-3	3	3	-3
$\mathbf{L}_{2y\eta}$	1/64	-3	-1	1	3	-9	-3	3	9
$\mathbf{L}_{2z\eta}$	1/32	-1	-3	-3	-1	1	3	3	1
$\xi \geq 0, \eta = 0, \zeta \geq 0$									
$\mathbf{L}_{3x\eta}$	1/32	-1	1	1	-1	-3	3	3	-3
$\mathbf{L}_{3y\eta}$	1/64	-1	-3	3	1	-3	-9	9	3
$\mathbf{L}_{3z\eta}$	1/32	-1	-3	-3	-1	1	3	3	1
$\xi \geq 0, \eta = 0, \zeta \leq 0$									
$\mathbf{L}_{4x\eta}$	1/32	-3	3	3	-3	-1	1	1	-1
$\mathbf{L}_{4y\eta}$	1/64	-3	-9	9	3	-1	-3	3	1
$\mathbf{L}_{4z\eta}$	1/32	-3	-1	-1	-3	3	1	1	3

Table 16-11: Invariant coefficients from diffusive-flux integrals in the plane of $\zeta = 0$.

Name	Coef	u_1	u_2	u_3	u_4	u_5	u_6	u_7	u_8
$\xi \leq 0, \eta \leq 0, \zeta = 0$									
$\mathbf{L}_{1x\zeta}$	1/32	-3	3	1	-1	-3	3	1	-1
$\mathbf{L}_{1y\zeta}$	1/32	-3	-1	1	3	-3	-1	1	3
$\mathbf{L}_{1z\zeta}$	1/64	-9	-3	-1	-3	9	3	1	3
$\xi \leq 0, \eta \geq 0, \zeta = 0$									
$\mathbf{L}_{2x\zeta}$	1/32	-1	1	3	-3	-1	1	3	-3
$\mathbf{L}_{2y\zeta}$	1/32	-1	-3	3	1	-1	-3	3	1
$\mathbf{L}_{2z\zeta}$	1/64	-3	-1	-3	-9	3	1	3	9
$\xi \geq 0, \eta \geq 0, \zeta = 0$									
$\mathbf{L}_{3x\zeta}$	1/32	-1	1	3	-3	-1	1	3	-3
$\mathbf{L}_{3y\zeta}$	1/32	-1	-3	3	1	-1	-3	3	1
$\mathbf{L}_{3z\zeta}$	1/64	-1	-3	-9	-3	1	3	9	3
$\xi \geq 0, \eta \leq 0, \zeta = 0$									
$\mathbf{L}_{4x\zeta}$	1/32	-3	3	1	-1	-3	3	1	-1
$\mathbf{L}_{4y\zeta}$	1/32	-3	-1	1	3	-3	-1	1	3
$\mathbf{L}_{4z\zeta}$	1/64	-3	-9	-3	-1	3	9	3	1

Table 16-12: Integration limits for each flux component for each corner.

Node	$\mathbf{q}_x$							$\mathbf{q}_y$							$\mathbf{q}_z$						
	Sign	ξ_a	ξ_b	η_a	η_b	ζ_a	ζ_b	Sign	ξ_a	ξ_b	η_a	η_b	ζ_a	ζ_b	Sign	ξ_a	ξ_b	η_a	η_b	ζ_a	ζ_b
1	+	0	0	−1	0	−1	0	+	−1	0	0	0	−1	0	+	−1	0	−1	0	0	0
2	−	0	0	−1	0	−1	0	+	0	1	0	0	−1	0	+	0	1	−1	0	0	0
3	−	0	0	0	1	−1	0	−	0	1	0	0	−1	0	+	0	1	0	1	0	0
4	+	0	0	0	1	−1	0	−	−1	0	0	0	−1	0	+	−1	0	0	1	0	0
5	+	0	0	−1	0	0	1	+	−1	0	0	0	0	1	−	−1	0	−1	0	0	0
6	−	0	0	−1	0	0	1	+	0	1	0	0	0	1	−	0	1	−1	0	0	0
7	−	0	0	0	1	0	1	−	0	1	0	0	0	1	−	0	1	0	1	0	0
8	+	0	0	0	1	0	1	−	−1	0	0	0	0	1	−	−1	0	0	1	0	0

Table 16-13: Assignment of invariant integrals to each coefficient for diffusion with constant coefficients.

Node	$\frac{\Delta y \Delta z}{\Delta x} K_{xx}$	$\Delta z K_{xy}$	$\Delta y K_{xz}$	$\Delta z K_{yx}$	$\frac{\Delta x \Delta z}{\Delta y} K_{yy}$	$\Delta x K_{zy}$	$\Delta y K_{zx}$	$\Delta x K_{zy}$	$\frac{\Delta x \Delta y}{\Delta z} K_{zz}$
1	$-\mathbf{L}_{1x\xi}$	$-\mathbf{L}_{1y\xi}$	$-\mathbf{L}_{1z\xi}$	$-\mathbf{L}_{1x\eta}$	$-\mathbf{L}_{1y\eta}$	$-\mathbf{L}_{1z\eta}$	$-\mathbf{L}_{1x\zeta}$	$-\mathbf{L}_{1y\zeta}$	$-\mathbf{L}_{1z\zeta}$
2	$\mathbf{L}_{1x\xi}$	$\mathbf{L}_{1y\xi}$	$\mathbf{L}_{1z\xi}$	$-\mathbf{L}_{4x\eta}$	$-\mathbf{L}_{4y\eta}$	$-\mathbf{L}_{4z\eta}$	$-\mathbf{L}_{4x\zeta}$	$-\mathbf{L}_{4y\zeta}$	$-\mathbf{L}_{4z\zeta}$
3	$\mathbf{L}_{4x\xi}$	$\mathbf{L}_{4y\xi}$	$\mathbf{L}_{4z\xi}$	$\mathbf{L}_{4x\eta}$	$\mathbf{L}_{4y\eta}$	$\mathbf{L}_{4z\eta}$	$-\mathbf{L}_{3x\zeta}$	$-\mathbf{L}_{3y\zeta}$	$-\mathbf{L}_{3z\zeta}$
4	$-\mathbf{L}_{4x\xi}$	$-\mathbf{L}_{4y\xi}$	$-\mathbf{L}_{4z\xi}$	$\mathbf{L}_{1x\eta}$	$\mathbf{L}_{1y\eta}$	$\mathbf{L}_{1z\eta}$	$-\mathbf{L}_{2x\zeta}$	$-\mathbf{L}_{2y\zeta}$	$-\mathbf{L}_{2z\zeta}$
5	$-\mathbf{L}_{2x\xi}$	$-\mathbf{L}_{2y\xi}$	$-\mathbf{L}_{2z\xi}$	$-\mathbf{L}_{2x\eta}$	$-\mathbf{L}_{2y\eta}$	$-\mathbf{L}_{2z\eta}$	$\mathbf{L}_{1x\zeta}$	$\mathbf{L}_{1y\zeta}$	$\mathbf{L}_{1z\zeta}$
6	$\mathbf{L}_{2x\xi}$	$\mathbf{L}_{2y\xi}$	$\mathbf{L}_{2z\xi}$	$-\mathbf{L}_{3x\eta}$	$-\mathbf{L}_{3y\eta}$	$-\mathbf{L}_{3z\eta}$	$\mathbf{L}_{4x\zeta}$	$\mathbf{L}_{4y\zeta}$	$\mathbf{L}_{4z\zeta}$
7	$\mathbf{L}_{3x\xi}$	$\mathbf{L}_{3y\xi}$	$\mathbf{L}_{3z\xi}$	$\mathbf{L}_{3x\eta}$	$\mathbf{L}_{3y\eta}$	$\mathbf{L}_{3z\eta}$	$\mathbf{L}_{3x\zeta}$	$\mathbf{L}_{3y\zeta}$	$\mathbf{L}_{3z\zeta}$
8	$-\mathbf{L}_{3x\xi}$	$-\mathbf{L}_{3y\xi}$	$-\mathbf{L}_{3z\xi}$	$\mathbf{L}_{2x\eta}$	$\mathbf{L}_{2y\eta}$	$\mathbf{L}_{2z\eta}$	$\mathbf{L}_{2x\zeta}$	$\mathbf{L}_{2y\zeta}$	$\mathbf{L}_{2z\zeta}$

Advective constant-coefficient transport contour integrals

As with 2D transport, advection is obtained by multiplying concentration by phase flux. The flow field for *SEDFLOW* is not described by a fully 3D interpolation of corner values, so the analogy is not complete.

Advective flux $\mathbf{q}$ is defined by components

$$\mathbf{q}_x = u\mathbf{q}_{px} = u\left(-K_{xx}\frac{\partial H}{\partial x} - K_{xy}\frac{\partial H}{\partial y}\right) \tag{16-246}$$

$$\mathbf{q}_y = u\mathbf{q}_{py} = u\left(-K_{yx}\frac{\partial H}{\partial x} - K_{yy}\frac{\partial H}{\partial y}\right) \tag{16-247}$$

$$\mathbf{q}_z = u\mathbf{q}_{pz} \tag{16-248}$$

where $\mathbf{q}_p$ represents the phase flux. Assuming that $\mathbf{K}$ is constant within the cell and there are no internal phase sources, $\mathbf{q}_{px}$ and $\mathbf{q}_{py}$ are constant in the vertical; $\mathbf{q}_{pz}$ linearly varies in the vertical (is constant across horizontal planes). Linear vertical variation of $\mathbf{q}_{pz}$ is not required in the integrations below. Insofar as the parameters are constant within a cell, only the derivatives are integrated (the parameters multiply the integrals).

Concentration is described by

$$\begin{aligned} u &= \sum_{i=1}^{N} c_i(\xi+\xi_i)(\eta+\eta_i)(\zeta+\zeta_i)u_i \\ &= C_{u1} + C_{u2}\xi + C_{u3}\eta + C_{u4}\zeta + C_{u5}\xi\eta + C_{u6}\xi\zeta + C_{u7}\eta\zeta + C_{u8}\xi\eta\zeta \end{aligned} \tag{16-249}$$

The derivatives can be rearranged into functions of ξ and η as follows

$$H_{,x} = \sum_{i=1}^{N} c_i\xi_{,x}(\eta+\eta_i)H_i = \xi_{,x}(C_{x1} + C_{x2}\eta) \tag{16-250}$$

$$H_{,y} = \sum_{i=1}^{N} c_i\eta_{,y}(\xi+\xi_i)H_i = \eta_{,y}(C_{y1} + C_{y2}\xi) \tag{16-251}$$

The constant coefficients are defined by inserting the values of c_i, ξ_i, and η_i.

Integrating u along $\zeta = 0$ (phase flux is a constant) yields

$$\begin{aligned} \iint u x_{,\xi} y_{,\eta}\,\mathrm{d}\eta\,\mathrm{d}\xi &= \iint (C_{u1} + C_{u2}\xi + C_{u3}\eta + C_{u5}\xi\eta) x_{,\xi} y_{,\eta}\,\mathrm{d}\eta\,\mathrm{d}\xi \\ &= x_{,\xi} y_{,\eta}(C_{u1}\langle\xi\rangle\langle\eta\rangle + C_{u2}\langle\xi^2\rangle\langle\eta\rangle + C_{u3}\langle\xi\rangle\langle\eta^2\rangle + C_{u5}\langle\xi^2\rangle\langle\eta^2\rangle) \\ &= \Delta x\Delta y \mathbf{M}_\zeta \cdot \mathbf{u} \end{aligned} \tag{16-252}$$

Integrating along $\xi = 0$ yields

$$\begin{aligned}\iint uH_{,x}y_{,\eta}z_{,\zeta}\,\mathrm{d}\eta\,\mathrm{d}\zeta &= \iint (C_{u1}+C_{u3}\eta+C_{u4}\zeta+C_{u7}\eta\zeta)\xi_{,x}(C_{x1}+C_{x2}\eta)y_{,\eta}z_{,\zeta}\,\mathrm{d}\eta\,\mathrm{d}\zeta \\ &= y_{,\eta}z_{,\zeta}\xi_{,x}[C_{x1}(C_{u1}\langle\eta\rangle\langle\zeta\rangle + C_{u3}\langle\eta^2\rangle\langle\zeta\rangle + C_{u4}\langle\eta\rangle\langle\zeta^2\rangle + C_{u7}\langle\eta^2\rangle\langle\zeta^2\rangle) \\ &\quad + C_{x2}(C_{u1}\langle\eta^2\rangle\langle\zeta\rangle + C_{u3}\langle\eta^3\rangle\langle\zeta\rangle + C_{u4}\langle\eta^2\rangle\langle\zeta^2\rangle + C_{u7}\langle\eta^3\rangle\langle\zeta^2\rangle)] \\ &= \frac{\Delta y\Delta z}{\Delta x}(C_{x1}\mathbf{M}_{\xi 1}+C_{x2}\mathbf{M}_{\xi 2})\cdot\mathbf{u} \qquad (16\text{-}253)\end{aligned}$$

$$\begin{aligned}\iint uH_{,y}y_{,\eta}z_{,\zeta}\,\mathrm{d}\eta\,\mathrm{d}\zeta &= \iint (C_{u1}+C_{u3}\eta+C_{u4}\zeta+C_{u7}\eta\zeta)\eta_{,y}C_{y1}y_{,\eta}z_{,\zeta}\,\mathrm{d}\eta\,\mathrm{d}\zeta \\ &= \Delta z C_{y1}\mathbf{M}_{\xi 1}\cdot\mathbf{u} \qquad (16\text{-}254)\end{aligned}$$

Integrating along $\eta = 0$ yields

$$\begin{aligned}\iint uH_{,x}x_{,\xi}z_{,\zeta}\,\mathrm{d}\xi\,\mathrm{d}\zeta &= \iint (C_{u1}+C_{u2}\xi+C_{u4}\zeta+C_{u5}\xi\zeta)\xi_{,x}C_{x1}x_{,\xi}z_{,\zeta}\,\mathrm{d}\xi\,\mathrm{d}\zeta \\ &= \Delta z C_{x1}\mathbf{M}_{\eta 1}\cdot\mathbf{u} \qquad (16\text{-}255)\end{aligned}$$

$$\begin{aligned}\iint uH_{,y}x_{,\xi}z_{,\zeta}\,\mathrm{d}\xi\,\mathrm{d}\zeta &= \iint (C_{u1}+C_{u2}\xi+C_{u4}\zeta+C_{u5}\xi\zeta)\xi_{,x}(C_{y1}+C_{y2}\xi)x_{,\xi}z_{,\zeta}\,\mathrm{d}\xi\,\mathrm{d}\zeta \\ &= x_{,\xi}z_{,\zeta}\eta_{,y}[C_{y1}(C_{u1}\langle\xi\rangle\langle\zeta\rangle + C_{u2}\langle\xi^2\rangle\langle\zeta\rangle + C_{u4}\langle\xi\rangle\langle\zeta^2\rangle + C_{u5}\langle\xi^2\rangle\langle\zeta^2\rangle) \\ &\quad + C_{y2}(C_{u1}\langle\xi^2\rangle\langle\zeta\rangle + C_{u2}\langle\xi^3\rangle\langle\zeta\rangle + C_{u4}\langle\xi^2\rangle\langle\zeta^2\rangle + C_{u5}\langle\xi^3\rangle\langle\zeta^2\rangle)] \\ &= \frac{\Delta x\Delta z}{\Delta y}(C_{y1}\mathbf{M}_{\eta 1}+C_{y2}\mathbf{M}_{\eta 2})\cdot\mathbf{u} \qquad (16\text{-}256)\end{aligned}$$

Note that the flux in the $\zeta = 0$ integral is multiplied by area ($\Delta x\Delta y$), while the flux in the other integrals is multiplied by area divided by a spatial length. This is because there is a spatial derivative considered in the horizontal cases but not in the vertical.

The **M** integrals for each face are presented in Table 16-14. Using the corner-flux specifications in Table 16-12, fluxes for each corner are defined in Table 16-15.

Advective exponential-coefficient transport contour integrals

For some of the flow cases, it is not appropriate to consider **K** constant within a cell, as it varies vertically. This occurs with the exponential-drag flow model, for example. Modifications to the integrals for the case where **K** varies exponentially are presented here. Only the integrals on vertical faces change, as the vertical fluxes are handled identically regardless of the vertical variation of **K**.

Table 16-14: Invariant coefficients from integrals for 3D advection with constant coefficients.

Range															
ξ_a	ξ_b	η_a	η_b	ζ_a	ζ_b	Name	Coef	u_1	u_2	u_3	u_4	u_5	u_6	u_7	u_8
0	0	−1	0	−1	0	$\mathbf{M}_{1\xi 1}$	1/64	9	7	5	3	5	3	1	-1
						$\mathbf{M}_{1\xi 2}$	1/192	-15	-11	-7	-3	-9	-5	-1	3
0	0	−1	0	0	1	$\mathbf{M}_{2\xi 1}$	1/64	3	5	-1	1	7	9	3	5
						$\mathbf{M}_{2\xi 2}$	1/192	-5	-9	3	-1	-11	-15	-3	-7
0	0	0	1	−1	0	$\mathbf{M}_{3\xi 1}$	1/64	1	-1	5	3	5	3	9	7
						$\mathbf{M}_{3\xi 2}$	1/192	1	-3	9	5	7	3	15	11
0	0	0	1	0	1	$\mathbf{M}_{4\xi 1}$	1/64	3	5	7	9	-1	1	3	5
						$\mathbf{M}_{4\xi 2}$	1/192	3	7	11	15	-3	1	5	9
−1	0	0	0	−1	0	$\mathbf{M}_{1\eta 1}$	1/64	9	3	3	9	3	1	1	3
						$\mathbf{M}_{1\eta 2}$	1/192	-15	-3	-3	-15	-5	-1	-1	-5
0	1	0	0	−1	0	$\mathbf{M}_{2\eta 1}$	1/64	3	1	1	3	9	3	3	9
						$\mathbf{M}_{2\eta 2}$	1/192	-5	-1	-1	-5	-15	-3	-3	-15
−1	0	0	0	0	1	$\mathbf{M}_{3\eta 1}$	1/64	1	3	3	1	3	9	9	3
						$\mathbf{M}_{3\eta 2}$	1/192	1	5	5	1	3	15	15	3
0	1	0	0	0	1	$\mathbf{M}_{4\eta 1}$	1/64	3	9	9	3	1	3	3	1
						$\mathbf{M}_{4\eta 2}$	1/192	3	15	15	3	1	5	5	1
−1	0	−1	0	0	0	$\mathbf{M}_{1\zeta}$	1/128	9	5	-1	3	7	3	1	5
0	1	−1	0	0	0	$\mathbf{M}_{2\zeta}$	1/128	3	-1	5	9	5	1	3	7
−1	0	0	1	0	0	$\mathbf{M}_{3\zeta}$	1/128	1	5	7	3	-1	3	9	5
0	1	0	1	0	0	$\mathbf{M}_{4\zeta}$	1/128	3	7	5	1	5	9	3	-1

The model for each component of $\mathbf{K}$ is

$$\begin{aligned}\mathbf{K} &= \mathbf{K}_0\gamma^w \\ &= \mathbf{K}_0\lambda^{2w} \\ &= \mathbf{K}_0\lambda^{\zeta+1} \\ &= \mathbf{K}_m\lambda^{\zeta} = \mathbf{K}_0 k(\zeta) \qquad (16\text{-}257)\end{aligned}$$

$$\mathbf{K}_m = \mathbf{K}|_{\zeta=0} = \mathbf{K}_0\lambda$$

$$w = \frac{\zeta-\zeta_0}{\zeta_1-\zeta_0} = \frac{\zeta+1}{2} \qquad (16\text{-}258)$$

where subscripts 0 and 1 represent the bottom and top of the cell and γ provides the ratio of top

Table 16-15: Assignment of invariant integrals to each coefficient for 3D advection with constant coefficients.

Node	$K_{xx}\frac{\Delta y\Delta z}{\Delta x}$	$K_{xy}\Delta z$	$K_{yx}\Delta z$	$K_{yy}\frac{\Delta x\Delta z}{\Delta y}$	$\mathbf{q}_{pz}\Delta x\Delta y$
1	$-(C_{x1}\mathbf{M}_{1\xi1}+C_{x2}\mathbf{M}_{1\xi2})$	$-C_{y1}\mathbf{M}_{1\xi1}$	$-C_{x1}\mathbf{M}_{1\eta1}$	$-(C_{y1}\mathbf{M}_{1\eta1}+C_{y2}\mathbf{M}_{1\eta2})$	$\mathbf{M}_\zeta$
2	$(C_{x1}\mathbf{M}_{1\xi1}+C_{x2}\mathbf{M}_{1\xi2})$	$C_{y1}\mathbf{M}_{1\xi1}$	$-C_{x1}\mathbf{M}_{2\eta1}$	$-(C_{y1}\mathbf{M}_{2\eta1}+C_{y2}\mathbf{M}_{2\eta2})$	$\mathbf{M}_\zeta$
3	$(C_{x1}\mathbf{M}_{3\xi1}+C_{x2}\mathbf{M}_{3\xi2})$	$C_{y1}\mathbf{M}_{3\xi1}$	$C_{x1}\mathbf{M}_{1\eta1}$	$(C_{y1}\mathbf{M}_{1\eta1}+C_{y2}\mathbf{M}_{1\eta2})$	$\mathbf{M}_\zeta$
4	$-(C_{x1}\mathbf{M}_{3\xi1}+C_{x2}\mathbf{M}_{3\xi2})$	$-C_{y1}\mathbf{M}_{3\xi1}$	$C_{x1}\mathbf{M}_{2\eta1}$	$(C_{y1}\mathbf{M}_{2\eta1}+C_{y2}\mathbf{M}_{2\eta2})$	$\mathbf{M}_\zeta$
5	$-(C_{x1}\mathbf{M}_{2\xi1}+C_{x2}\mathbf{M}_{2\xi2})$	$-C_{y1}\mathbf{M}_{2\xi1}$	$-C_{x1}\mathbf{M}_{3\eta1}$	$-(C_{y1}\mathbf{M}_{3\eta1}+C_{y2}\mathbf{M}_{3\eta2})$	$-\mathbf{M}_\zeta$
6	$(C_{x1}\mathbf{M}_{2\xi1}+C_{x2}\mathbf{M}_{2\xi2})$	$C_{y1}\mathbf{M}_{2\xi1}$	$-C_{x1}\mathbf{M}_{4\eta1}$	$-(C_{y1}\mathbf{M}_{4\eta1}+C_{y2}\mathbf{M}_{4\eta2})$	$-\mathbf{M}_\zeta$
7	$(C_{x1}\mathbf{M}_{4\xi1}+C_{x2}\mathbf{M}_{4\xi2})$	$C_{y1}\mathbf{M}_{4\xi1}$	$C_{x1}\mathbf{M}_{3\eta1}$	$(C_{y1}\mathbf{M}_{3\eta1}+C_{y2}\mathbf{M}_{3\eta2})$	$-\mathbf{M}_\zeta$
8	$-(C_{x1}\mathbf{M}_{4\xi1}+C_{x2}\mathbf{M}_{4\xi2})$	$-C_{y1}\mathbf{M}_{4\xi1}$	$C_{x1}\mathbf{M}_{4\eta1}$	$(C_{y1}\mathbf{M}_{4\eta1}+C_{y2}\mathbf{M}_{4\eta2})$	$-\mathbf{M}_\zeta$

to bottom magnitudes for $\mathbf{K}$. The use of $\mathbf{K}_m$ is consistent with evaluating quantities at the cell midpoint wherever possible.

It is now necessary to include λ components in the integrals, due to the vertical variation, thus the integrals are slightly more complex. The following are useful identities

$$\lambda^\zeta = \exp[\zeta \ln\lambda] = \exp(\beta\zeta) \tag{16-259}$$

$$\int_{\zeta_a}^{\zeta_b} \lambda^\zeta \,\mathrm{d}\zeta = \left[\frac{\lambda^\zeta}{\ln\lambda}\right]_{\zeta_a}^{\zeta_b} = \lceil\zeta\rceil \tag{16-260}$$

$$\begin{aligned}\int_{\zeta_a}^{\zeta_b} \zeta\lambda^{\zeta+1}\,\mathrm{d}\zeta &= \int_{\zeta_a}^{\zeta_b} \zeta\exp(\beta\zeta)\,\mathrm{d}\zeta \\ &= \left[\frac{\exp(\beta\zeta)}{\beta^2}(\beta\zeta-1)\right]_{\zeta_a}^{\zeta_b} \\ &= \left[\lambda^\zeta\frac{\zeta\ln\lambda-1}{(\ln\lambda)^2}\right]_{\zeta_a}^{\zeta_b} \\ &= \lceil\!\lceil\zeta\rceil\!\rceil\end{aligned} \tag{16-261}$$

Note that $\lambda > 0$ and $\lambda \neq 1$; if $\lambda = 1$, $\mathbf{K}$ is constant and the constant-coefficient derivation holds. The special brackets are shorthand to denote the exponential included in the exponential.

The procedure for evaluating the integrals is identical to the constant-coefficient case, al-

though rearrangement would increase computational efficiency, since the exponential term will vary as the water surface rises and falls.

Integrating along $\xi = 0$ yields

$$\begin{aligned}\iint k(\zeta)uH_{,x}y_{,\eta}z_{,\zeta}\,\mathrm{d}\eta\,\mathrm{d}\zeta &= y_{,\eta}z_{,\zeta}\xi_{,x}[C_{x1}([C_{u1}\langle\eta\rangle + C_{u3}\langle\eta^2\rangle]\lceil\zeta\rceil + [C_{u4}\langle\eta\rangle + C_{u7}\langle\eta^2\rangle]\lceil\!\lceil\zeta\rceil\!\rceil) \\ &\quad + C_{x2}([C_{u1}\langle\eta^2\rangle + C_{u3}\langle\eta^3\rangle]\lceil\zeta\rceil + [C_{u4}\langle\eta^2\rangle + C_{u7}\langle\eta^3\rangle]\lceil\!\lceil\zeta\rceil\!\rceil] \\ &= \frac{\Delta y\Delta z}{\Delta x}[C_{x1}(\lceil\zeta\rceil\mathbf{M}_{\xi1} + \lceil\!\lceil\zeta\rceil\!\rceil\mathbf{M}_{\xi2}) \\ &\quad + C_{x2}(\lceil\zeta\rceil\mathbf{M}_{\xi3} + \lceil\!\lceil\zeta\rceil\!\rceil\mathbf{M}_{\xi4})]\cdot\mathbf{u} \end{aligned} \tag{16-262}$$

$$\iint k(\zeta)uH_{,y}y_{,\eta}z_{,\zeta}\,\mathrm{d}\eta\,\mathrm{d}\zeta = \Delta z C_{y1}(\lceil\zeta\rceil\mathbf{M}_{\xi1} + \lceil\!\lceil\zeta\rceil\!\rceil\mathbf{M}_{\xi2})\cdot\mathbf{u} \tag{16-263}$$

Integrating along $\eta = 0$ yields

$$\iint k(\zeta)uH_{,x}x_{,\xi}z_{,\zeta}\,\mathrm{d}\xi\,\mathrm{d}\zeta = \Delta z C_{x1}(\lceil\zeta\rceil\mathbf{M}_{\eta1} + \lceil\!\lceil\zeta\rceil\!\rceil\mathbf{M}_{\eta2})\cdot\mathbf{u} \tag{16-264}$$

$$\begin{aligned}\iint k(\zeta)uH_{,y}x_{,\xi}z_{,\zeta}\,\mathrm{d}\xi\,\mathrm{d}\zeta &= x_{,\xi}z_{,\zeta}\eta_{,y}[C_{y1}([C_{u1}\langle\xi\rangle + C_{u2}\langle\xi^2\rangle]\lceil\zeta\rceil + (C_{u4}\langle\xi\rangle + C_{u5}\langle\xi^2\rangle]\lceil\!\lceil\zeta\rceil\!\rceil) \\ &\quad + C_{y2}([C_{u1}\langle\xi^2\rangle + C_{u2}\langle\xi^3\rangle]\lceil\zeta\rceil + (C_{u4}\langle\xi^2\rangle + C_{u5}\langle\xi^3\rangle]\lceil\!\lceil\zeta\rceil\!\rceil)] \\ &= \frac{\Delta x\Delta z}{\Delta y}[C_{y1}(\lceil\zeta\rceil\mathbf{M}_{\eta1} + \lceil\!\lceil\zeta\rceil\!\rceil\mathbf{M}_{\eta2}) \\ &\quad + C_{y2}(\lceil\zeta\rceil\mathbf{M}_{\eta3} + \lceil\!\lceil\zeta\rceil\!\rceil\mathbf{M}_{\eta4})]\cdot\mathbf{u} \end{aligned} \tag{16-265}$$

The invariant **M** vectors here are different than for the constant-coefficient case. However, the constant-coefficient ones are recovered by replacing $\lceil\zeta\rceil$ with $\langle\zeta\rangle$, $\lceil\!\lceil\zeta\rceil\!\rceil$ with $\langle\zeta^2\rangle$, and adding terms appropriately.

Fluxes are evaluated in just the same way as for the constant-coefficient case. Note that the exponential terms will need to be recalculated if the flow domain changes.

Dispersive exponential-coefficient transport contour integrals

Dispersion is a function of velocity in *SEDFLOW*, although diffusion is not. In the approximation used in *SEDFLOW*, direction cosines are vertically invariant for horizontal flow and are approximately vertically invariant for all practical purposes. Accordingly, dispersion coefficients are linearly proportional to velocity; in turn, dispersion coefficients are linearly dependent on the vertical distribution of the flow conductivity. This functionality can be explicitly accounted for in the integrations.

Assuming that the primary source of velocity-magnitude variation is due to vertical variation in flow conductivity, it is reasonable to use the same model for dispersion coefficient variation as for velocity variation,

$$D = D_0 \gamma^w = D_m \lambda^\zeta \tag{16-266}$$

where

D dispersion coefficient component
D_0 dispersion coefficient component at the cell bottom
D_m dispersion coefficient component at the cell centroid

The integrals along the $\zeta = 0$ plane are unchanged by the exponential variation in D, but the other integrals require modification just as in the advective case. All of the integrals should substitute $\lceil \zeta \rceil$ for $\langle \zeta \rangle$ and $\lceil\lceil \zeta \rceil\rceil$ with $\langle \zeta^2 \rangle$; again, rearrangement of the components will yield additional invariant vectors based on fewer components. Otherwise, fluxes are evaluated identically.

ENP Entry 8/27/02: Boundary conditions/stresses

Stresses

There are several boundary conditions and stresses that are typically used for flow and transport. These include

- Specified nodal values
- Specified cell fluxes
- Specified edge fluxes
- Specified gradients at edges

Specified nodal values

A very common case is for specific nodes to have specified values. The balance equation is simply replaced with the corresponding equation

$$u = u_s(\mathbf{x}, \mathbf{y}) \tag{16-267}$$

which, in the matrix equation, becomes

$$\delta = 0 \tag{16-268}$$

Now that I think of it, since the multiplier on δ is arbitrary, it would likely help scaling if the equation was

$$\frac{V_c}{\Delta t}\delta = 0 \tag{16-269}$$

The $(\mathbf{x}, \mathbf{y})$ pair refers to the nodal locations.

Specified volumetric fluxes

This was already discussed. The cell volumetric flux is simply divided by the number of nodes per cell and added to each of the nodal balance equations.

Typically cell values are specified cell-by-cell. The $(\mathbf{x}, \mathbf{y})$ pair in functional specification refers to the cell centroid locations.

Specified edge fluxes

Edge fluxes represent lateral inflows. Once total flux is calculated, edge fluxes are evenly added to all nodes connected to the edge. Typically edge values are specified edge-by-edge. The $(\mathbf{x}, \mathbf{y})$ pair in functional specification refers to the edge centroid locations.

Three types of fluxes are convenient to use:

- Flux per area. This is multiplied by edge area before being added to the balance equations.
- Flux per edge cell. This is added to the balance equations directly.
- Total flux over all found edge cells. This is scaled by the fraction of total area for each cell before being added to the balance equations.

Note that any edge, either at the boundary or internally between cells, can have a flux. Accordingly, these need not be restricted to the boundary edges.

Specified gradients at edges

The idea is to specify flux at an edge in the form

$$\mathbf{q}_n = \mathbf{n} \cdot (-\mathbf{K} \cdot \nabla u) \tag{16-270}$$

where $\mathbf{q}_n$ is the flux normal to the edge, Generally one specifies $\mathrm{d}u/\mathrm{d}n$ and uses the adjacent cell $\mathbf{K}$. When $\mathbf{K}$ is isotropic

$$\mathbf{q}_n = -Ku_n \tag{16-271}$$

Otherwise, the flux normal to a cell interface, $\mathbf{q}_n$, is obtained by taking the dot product of dispersive flux with the normal vector to the cell interface $\mathbf{n}$, inserting an identity ($\mathbf{n}^T \cdot \mathbf{n} = 1$, where the superscript T denotes a transpose), and rearranging

$$\begin{aligned}
\mathbf{q}_n = \mathbf{q}_n\mathbf{n} &= -\mathbf{n}^T \cdot \mathbf{K} \cdot \nabla u \\
&= -\mathbf{n}^T \cdot \mathbf{K} \cdot (\mathbf{n} \cdot \mathbf{n}^T) \cdot \nabla u \\
&= -(\mathbf{n}^T \cdot \mathbf{K} \cdot \mathbf{n}) \cdot (\mathbf{n}^T \cdot \nabla u) \\
&= -(\mathbf{n}^T \cdot \mathbf{K} \cdot \mathbf{n}) \frac{\partial u}{\partial n} \\
&= -K_n \frac{\partial u}{\partial n} \qquad (16\text{-}272)
\end{aligned}$$

$$\begin{aligned}
K_n = {} & n_1(n_1K_{11} + n_2K_{12} + n_3K_{13}) \\
& + n_2(n_1K_{21} + n_2K_{22} + n_3K_{23}) \\
& + n_3(n_1K_{31} + n_2K_{32} + n_3K_{33}) \qquad (16\text{-}273)
\end{aligned}$$

where $\partial u/\partial n$ denotes the gradient of u normal to the boundary and n_i is the ith component of $\mathbf{n}$. For boundaries aligned with the principal direction, K_n will be K_{11}, K_{22}, or K_{33}, depending on which direction the cell boundary is normal to.

As a practical matter, in a simulator one could specify u_n at either interior edges or exterior boundaries. For interior edges, specified u_n would be relative to the local cell edge, thus the flux would be in the opposite direction for the two adjoining cells.

A complication arises when flux is in the form

$$\mathbf{q} = -\mathbf{K} \cdot \nabla(u + a) \tag{16-274}$$

where a is specified. In this case,

$$\mathbf{q}_n = -K_n \left(\frac{\partial u}{\partial n} + \frac{\partial a}{\partial n} \right) \tag{16-275}$$

and it becomes necessary to evaluate $\partial a/\partial n$ along the edge. When the edges are along axis directions, only terms corresponding to K_{xx}, K_{yy}, and K_{zz} are needed. In 2D,

$$a_{,x} = \xi_{,x}(\mathbf{v}_{u2} + \mathbf{v}_{u4}\eta) \cdot \mathbf{a} \tag{16-276}$$

$$a_{,y} = \eta_{,y}(\mathbf{v}_{u3} + \mathbf{v}_{u4}\xi) \cdot \mathbf{a} \tag{16-277}$$

Since $a_{,i}$ is not a function of coordinate direction i, the same integrals used before for the principal components of the $\mathbf{K}$ array can be used here as well. This is true in 3D also.

Another complication arises when flux is in the form

$$\mathbf{q} = -\mathbf{D} \cdot \nabla u - (\mathbf{K} \cdot \nabla a)u \tag{16-278}$$

where a is specified. In this case,

$$\mathbf{q}_n = -D_n \frac{\partial u}{\partial n} - \left(K_n \frac{\partial a}{\partial n}\right) u \tag{16-279}$$

and both $\partial u/\partial n$ and u are needed along the edge (as well as $\partial a/\partial n$, which is evaluated as described above). The usual case has zero diffusive flux ($\partial u/\partial n = 0$), thus leaving advective flux to be evaluated. This boils down to evaluating u along the edge.

The value for u that is used for advective flux depends on the direction of advection. If fluxes are entering, an external value for u must be specified, which for simplicity is assumed constant over the edge. In this case, the integrals

$$\begin{aligned}\int_{\eta_0}^{\eta_1} [a_{,x}u_e]_{\xi=\xi_j} y_{,\eta}\, \mathrm{d}\eta &= u_e \int_{\eta_0}^{\eta_1} (C_{a2} + C_{a4}\eta)\xi_{,x} y_{,\eta}\, \mathrm{d}\eta \\ &= u_e \frac{\Delta y}{\Delta x}(C_{a2}\langle\eta\rangle + C_{a4}\langle\eta^2\rangle)\end{aligned} \tag{16-280}$$

$$\begin{aligned}\int_{\xi_0}^{\xi_1} [a_{,y}u_e]_{\eta=\eta_j} x_{,\xi}\, \mathrm{d}\xi &= u_e \int_{\xi_0}^{\xi_1} (C_{a3} + C_{a4}\xi)\eta_{,y} x_{,\xi}\, \mathrm{d}\xi \\ &= u_e \frac{\Delta x}{\Delta y}(C_{a3}\langle\xi\rangle + C_{a4}\langle\xi^2\rangle)\end{aligned} \tag{16-281}$$

are used.

If fluxes are leaving, the internal value is used. Writing u as a function of ξ and η in 2D,

$$u = [\mathbf{v}_{u1} + \mathbf{v}_{u2}\xi + \mathbf{v}_{u3}\eta + \mathbf{v}_{u4}\xi\eta] \cdot \mathbf{u} \tag{16-282}$$

The following line integrals of weighting functions are needed:

$$\begin{aligned}\int_{\eta_0}^{\eta_1}[a_{,x}u]_{\xi=\xi_j}y_{,\eta}\,\mathrm{d}\eta &= \int_{\eta_0}^{\eta_1}(C_{a2}+C_{a4}\eta)\left[\mathbf{v}_{u1}+\mathbf{v}_{u2}\xi_j+(\mathbf{v}_{u3}+\mathbf{v}_{u4}\xi_j)\eta\right]\cdot\mathbf{u}\xi_{,x}y_{,\eta}\,\mathrm{d}\eta\\ &= \xi_{,x}y_{,\eta}\left[C_{a2}\left((\mathbf{v}_{u1}+\mathbf{v}_{u2}\xi_j)\langle\eta\rangle+(\mathbf{v}_{u3}+\mathbf{v}_{u4}\xi_j)\langle\eta^2\rangle\right)\right.\\ &\qquad \left.+C_{a4}\left((\mathbf{v}_{u1}+\mathbf{v}_{u2}\xi_j)\langle\eta^2\rangle+(\mathbf{v}_{u3}+\mathbf{v}_{u4}\xi_j)\langle\eta^3\rangle\right)\right]\cdot\mathbf{u}\\ &= \frac{\Delta y}{\Delta x}(C_{a2}\mathbf{J}_{1j}+C_{a4}\mathbf{J}_{2j})\cdot\mathbf{u}\end{aligned}\tag{16-283}$$

$$\begin{aligned}\int_{\xi_0}^{\xi_1}[a_{,y}u]_{\eta=\eta_j}x_{,\xi}\,\mathrm{d}\xi &= \int_{\xi_0}^{\xi_1}(C_{a3}+C_{a4}\xi)\left[\mathbf{v}_{u1}+\mathbf{v}_{u3}\eta_j+(\mathbf{v}_{u2}+\mathbf{v}_{u4}\eta_j)\xi\right]\cdot\mathbf{u}\eta_{,y}x_{,\xi}\,\mathrm{d}\xi\\ &= \eta_{,y}x_{,\xi}\left[C_{a3}\left((\mathbf{v}_{u1}+\mathbf{v}_{u3}\eta_j)\langle\xi\rangle+(\mathbf{v}_{u2}+\mathbf{v}_{u4}\eta_j)\langle\xi^2\rangle\right)\right.\\ &\qquad \left.+C_{a4}\left((\mathbf{v}_{u1}+\mathbf{v}_{u3}\eta_j)\langle\xi^2\rangle+(\mathbf{v}_{u2}+\mathbf{v}_{u4}\eta_j)\langle\xi^3\rangle\right)\right]\cdot\mathbf{u}\\ &= \frac{\Delta x}{\Delta y}(C_{a3}\mathbf{J}_{3j}+C_{a4}\mathbf{J}_{4j})\cdot\mathbf{u}\end{aligned}\tag{16-284}$$

Performing the individual integrals yields the invariant components multiplying C_{a2}, C_{a3}, and C_{a4}. Note that since u is bilinearly interpolated, half of the nodes in the cell do not contribute and the corresponding entries in the $\mathbf{J}_{ij}$ vectors are zero.

Selecting the convention that the normal direction is out of the cell, positive outwards flux is obtained when

$$-\left(K_n\frac{\partial a}{\partial n}\right)_{\xi=\xi_0} = K_{xx}a_{,x}\tag{16-285}$$

$$-\left(K_n\frac{\partial a}{\partial n}\right)_{\xi=\xi_1} = -K_{xx}a_{,x}\tag{16-286}$$

$$-\left(K_n\frac{\partial a}{\partial n}\right)_{\eta=\eta_0} = K_{yy}a_{,y}\tag{16-287}$$

$$-\left(K_n\frac{\partial a}{\partial n}\right)_{\eta=\eta_1} = -K_{yy}a_{,y}\tag{16-288}$$

Using this convention with the integrals results in

$$\int_{-1}^{0} \mathbf{q}_n|_{\xi=\xi_0} y_{,\eta}\, \mathrm{d}\eta = \frac{\Delta y}{\Delta x} K_{xx}(C_{a2}\mathbf{J}_{111} + C_{a4}\mathbf{J}_{211}) \cdot \mathbf{u} \tag{16-289}$$

$$\int_{0}^{1} \mathbf{q}_n|_{\xi=\xi_0} y_{,\eta}\, \mathrm{d}\eta = \frac{\Delta y}{\Delta x} K_{xx}(C_{a2}\mathbf{J}_{121} + C_{a4}\mathbf{J}_{221}) \cdot \mathbf{u} \tag{16-290}$$

$$\int_{-1}^{0} \mathbf{q}_n|_{\xi=\xi_1} y_{,\eta}\, \mathrm{d}\eta = -\frac{\Delta y}{\Delta x} K_{xx}(C_{a2}\mathbf{J}_{112} + C_{a4}\mathbf{J}_{212}) \cdot \mathbf{u} \tag{16-291}$$

$$\int_{0}^{1} \mathbf{q}_n|_{\xi=\xi_1} y_{,\eta}\, \mathrm{d}\eta = -\frac{\Delta y}{\Delta x} K_{xx}(C_{a2}\mathbf{J}_{122} + C_{a4}\mathbf{J}_{222}) \cdot \mathbf{u} \tag{16-292}$$

Similarly,

$$\int_{-1}^{0} \mathbf{q}_n|_{\eta=\eta_0} x_{,\xi}\, \mathrm{d}\xi = \frac{\Delta x}{\Delta y} K_{yy}(C_{a3}\mathbf{J}_{311} + C_{a4}\mathbf{J}_{411}) \cdot \mathbf{u} \tag{16-293}$$

$$\int_{0}^{1} \mathbf{q}_n|_{\eta=\eta_0} x_{,\xi}\, \mathrm{d}\xi = \frac{\Delta x}{\Delta y} K_{yy}(C_{a3}\mathbf{J}_{321} + C_{a4}\mathbf{J}_{421}) \cdot \mathbf{u} \tag{16-294}$$

$$\int_{-1}^{0} \mathbf{q}_n|_{\eta=\eta_1} x_{,\xi}\, \mathrm{d}\xi = -\frac{\Delta x}{\Delta y} K_{yy}(C_{a3}\mathbf{J}_{312} + C_{a4}\mathbf{J}_{412}) \cdot \mathbf{u} \tag{16-295}$$

$$\int_{0}^{1} \mathbf{q}_n|_{\eta=\eta_1} x_{,\xi}\, \mathrm{d}\xi = -\frac{\Delta x}{\Delta y} K_{yy}(C_{a3}\mathbf{J}_{322} + C_{a4}\mathbf{J}_{422}) \cdot \mathbf{u} \tag{16-296}$$

One can be more generic by using a relationship in the form

$$\int_{\sigma_0}^{\sigma_1} \mathbf{q}_n|_{\sigma=\sigma_0} \frac{\mathrm{d}x_i}{\mathrm{d}\sigma}\, \mathrm{d}\sigma = \left[C_{mx} \frac{\Delta y}{\Delta x} K_{xx}(C_{a2}\mathbf{J}_{1jk} + C_{a4}\mathbf{J}_{2jk}) + C_{my} \frac{\Delta x}{\Delta y} K_{yy}(C_{a3}\mathbf{J}_{3jk} + C_{a4}\mathbf{J}_{4jk}) \right] \cdot \mathbf{u} \tag{16-297}$$

where C_{mx} and C_{my} are -1, 0, or 1 depending on the sign of the flux integrals after they've been evaluated (0 is used on edges where K_{xx} or K_{yy} are not used).

Unfortunately, it is possible for fluxes to be in over part of a cell edge and out over the remainder. For example, if two adjacent nodes have the same H value, while one other is greater

than H and the other is less than H, the gradient of H changes across the edge. The change in gradient is linear along the edge (remember, for example, $a_{,x} = \xi_{,x}(\mathbf{v}_{u2} + \mathbf{v}_{u4}\eta) \cdot \mathbf{a}$). This situation is likely to be rare, but may adversely affect mass balance when encountered.

Ideally one would do the integrations with limits set by the crossing point where flux changes from entry to exit. A criterion proportional to exit flux can be evaluated at the endpoints

$$g_{-1} = [C_{mx}(\mathbf{v}_{u2} - \mathbf{v}_{u4}) + C_{my}(\mathbf{v}_{u3} - \mathbf{v}_{u4})] \cdot \mathbf{a} \tag{16-298}$$

$$g_{+1} = [C_{mx}(\mathbf{v}_{u2} + \mathbf{v}_{u4}) + C_{my}(\mathbf{v}_{u3} + \mathbf{v}_{u4})] \cdot \mathbf{a} \tag{16-299}$$

Since g is linearly varying along the edge,

$$g = g_{-1} + w(g_{+1} - g_{-1}) \tag{16-300}$$

where g is the criterion and $0 \leq w \leq 1$. The crossover point where $g = 0$ is

$$w = \frac{g_{-1}}{g_{-1} - g_{+1}} \tag{16-301}$$

The integrations can be performed with w in mind.

Performing the integrations with variable endpoints is not particularly efficient, although probably the overhead will be quite small. A simpler approach is to evaluate the integral of g over a segment and use the integral for the criterion, making a decision for the entire segment. The same decision is made using the midpoint values

$$g_{-1/2} = \left[C_{mx}(\mathbf{v}_{u2} - \frac{\mathbf{v}_{u4}}{2}) + C_{my}(\mathbf{v}_{u3} - \frac{\mathbf{v}_{u4}2}{)}\right] \cdot \mathbf{a} \tag{16-302}$$

$$g_{+1/2} = \left[C_{mx}(\mathbf{v}_{u2} + \frac{\mathbf{v}_{u4}2}{)} + C_{my}(\mathbf{v}_{u3} + \frac{\mathbf{v}_{u4}2}{)}\right] \cdot \mathbf{a} \tag{16-303}$$

Yet another approach is to use the average segment phase flux over edge segments containing crossover points. All one needs to do is an evaluation at the segment midpoint and multiply it by the segment length.

It should be recognized that for 2D integrations it is possible to reduce the work to a line integral. The integrands are all linearly varying along the edge. For advection without thickness dependence,

$$\begin{aligned}\int_0^1 gu\,\mathrm{d}w &= g_0u_0 + (u_0\Delta g + g_0\Delta u)\langle w\rangle + \Delta g\Delta u\langle w^2\rangle \\ &= g_0u_0 + u_0\Delta g + g_0\Delta u + \Delta g\Delta u\frac{1}{2}\end{aligned} \tag{16-304}$$

where the 0 subscript represents the value at the start of the integration path and the Δ represents the change along the path. Similarly, with thickness dependence

$$\begin{aligned}\int_0^1 hgu\,\mathrm{d}w &= h_0g_0u_0 + (g_0u_0\Delta h + h_0u_0\Delta g + h_0g_0\Delta u)\langle w\rangle \\ &\quad + (u_0\Delta h\Delta g + h_0\Delta g\Delta u + g_0\Delta h\Delta u)\langle w^2\rangle + \Delta h\Delta g\Delta u\langle w^3\rangle \\ &= h_0g_0u_0 + g_0u_0\Delta h + h_0u_0\Delta g + h_0g_0\Delta u \\ &\quad + (u_0\Delta h\Delta g + h_0\Delta g\Delta u + g_0\Delta h\Delta u)\frac{1}{2} + \Delta h\Delta g\Delta u\frac{1}{3} \qquad (16\text{-}305)\end{aligned}$$

Of course there are some coordinate changes involved as well.

9/18/02 Testing *SOILFLOW* algorithms.

A fully implicit test version of the soil code is called *SOILFLOW*, and is implemented fully within *Matlab*. At this time it includes the staggered-grid 2D algorithms for surface-water flow and a conservative species. Flow options include

- Linear steady flow
- Linear unsteady flow with constant stepsize multiplier
- Nonlinear steady flow

Transport options include

- Linear steady flow
- Linear unsteady flow with constant stepsize multiplier
- Linear unsteady flow with constant step (single LU decomposition for multiple steps)

The idea behind the test code is to examine strategies for implementing an implicit code on a very large grid. The routing scheme used to date can perform, in a reasonable wall-clock time, iterations on a 7.5-m YM grid with 800 by 1205 cells (almost 10^6 cells), although it does not successfully handle local hollows. It would be desirable to use the implicit scheme with a grid that approaches this resolution, but such a large grid requires special handling techniques.

In the last several days, I've been testing the algorithms on a simple problem. The domain is rectangular, with uniform properties aside from 3 inclusions. Two inclusions are much lower permeability than the main domain, while 1 is much higher permeability. The domain is steeply tilted (although this is immaterial for some of the tests). Different problems are obtained from the base case by changing the number of cells used to discretize the domain. The idea is to identify how many cells can be considered with the implicit scheme.

Solver options

The first consideration is replacing the direct solver applicable for smaller grids (say less than 10^4 cells) with an iterative solver. *Matlab* provides several options for solvers (which need to handle unsymmetric matrices), including

- Biconjugate gradients (BICG)
- Biconjugate gradients – stabilized (BICGSTAB)
- Conjugate gradient squared (CGS)
- Quasi-minimal residual (QMR)
- Conjugate gradients on the normal equations (LSQR)

I tested all of these on several smaller problems, and found that all of them needed a preconditioner. The two recommended preconditioners were partial LU decomposition and Cholesky decomposition, and each had an option regarding the allowable sparse-matrix fill-in. The LU decomposition seemed to work much better than the Cholesky decomposition on the few tests I ran, and the bicgstab and cgs solvers seemed to be comparable, and considerably better than the other solvers. Over several discretizations and preconditioner options, the total time for the bicgstab solver was marginally faster than the total time for the cgs solver, even though for any particular case either could be faster.

The option for fill-in for the LU decomposition routine, called the drop criterion, had a significant impact on speed as well. Entries that are less in magnitude than the drop criterion times the magnitude of the main diagonal are dropped, increasing matrix sparsity. The larger the criterion, the less memory needed but the more iterations required for convergence. For the cases I considered, a drop criterion of 10^{-4} was usually the fastest option. As the drop criterion

reduced, solution times slowed significantly even though total iterations reduced. Increasing the drop criterion by an order of magnitude made the solver not converge.

The convergence criterion for the iterative solvers also made a difference in overall solution time. I tried values of 10^{-6}, 10^{-10}, and 10^{-15}. The solvers always worked for the first two criteria, but never achieved the tightest criterion. For the tight criterion, stagnation generally occurred between 10^{-11} to 10^{-13}.

I tried several ranges of problem size, including 44x45, 84x85, 124x125, 164x165, 224x225, and 524x525. I did not use the direct solver as a comparison on the largest problems, but on the other problems the best combination of drop and convergence criteria generally sped up solution times by roughly a factor of 2. Poor selection of a drop criterion could make the direct and iterative methods comparable in overall solution time.

The largest grid took 11 minutes to solve with a drop criterion of 10^{-4}, but ran out of memory with a drop criterion of 10^{-5}. It would not likely be practical to try using a problem with more than about 3×10^5 cells. A 15-m pixel grid for the YM area should be doable, although only for steady problems that run for an hour or two.

The overall best approach seems to be to use the bicgstab solver with LU decomposition. The drop criterion should be about 10^{-4}, while the convergence criterion should be about 10^{-10}.

Matlab factors

There are other factors inherent in *Matlab* that strongly affect performance with large grids. Initialization of sparse arrays (used for iterative solvers) incurs overhead to keep track of the nonzero entries. Typically I have preallocated storage to the array, then added entries to it. The overhead becomes noticable on problems as small as 5000 unknowns, and slower than a matrix solution for 15000 unknowns. I've noticed this problem before, and have implemented a strategy of reinitializing the coefficient matrix with 10^{-64} in every location with an entry to avoid incurring the overhead. Still, the trend is unacceptable for our larger problems.

A second problem arose when there were more than 2^{31} entries in a matrix (corresponding to about 215x215 grid cells). It becomes impossible to add vectors to the matrix, since the pointers in the matrix are 32 bits long. This is a very serious problem, since one cannot build linear equations in the way one typically would.

Both problems can be straightforwardly resolved for a DEM-based grid. In this case, the coefficient matrix is banded with nine diagonals. As it turns out, there is little overhead involved in making a sparse matrix from array columns representing diagonals, and is negligible relative to matrix solution time. This procedure is also not limited by matrix size.

The revised procedure for the DEM-based grid uses a full 9-column array to store the coefficients. Each row corresponds to an equation. When building the coefficient array used in the solver, each column is shifted up or down to accommodate the peculiarities of the routine converting the diagonals to the sparse array. The 9-column array is not sparse, so it is simply cleared before rebuilding the matrix.

I would be interested to see if the *Matlab* developers have done anything fancy for the pdetool triangle-based finite element solver they provide. They should run into the same issues for large problems. I suppose that one of the remedies is to do element-level matrix-vector operations for the iterative solver and thus avoid building the coefficient matrix altogether.

Multizone algorithmic improvement

Insofar as it does not appear possible to handle the very large grids that we want to, even with iterative methods, it will likely be necessary to resort to a multizone approach. In the multizone approach, the domain is broken into subdomains. Each subdomain is solved implicitly, with adjacent subdomains stitched together with compatibility boundary conditions. A variation that might be interesting to explore is to overlap adjacent subdomains, using interior conditions from one subdomain as boundary conditions for another.

The subdomain approach for YM would likely be best implemented as east-west strips extending across the entire domain. This would tend to keep the washes aligned with the strips, although Solitario Canyon would cross the strips perpendicularly. Note that the matrix solution time in direct solvers is proportional to the square of the bandwidth, so long skinny strips would solve faster than square patches even with the same number of unknowns.

Some quick tests suggest that the bicgstab routine is significantly better than the cgs for certain grid ratios, and that a smaller drop criterion for the LU decomposition may pay increasing dividends for skinny domains. The drop criterion of 10^{-6} is about 3 times faster than the drop criterion of 10^{-4} when the aspect ratio is 32, and the smaller drop criterion is also more accurate. As a compromise, perhaps a criterion of 10^{-5} would be best.

The biggest issues with the multizone approach involve boundary conditions, which need to be made compatible between subdomains. I favor the approach of overlapping subdomains to take out the internal (non-physical) boundary conditions imposed on each sweep. Two general approaches suggest themselves with overlapping subdomains: (i) parallel strips that are offset by half the width of a strip, and (ii) orthogonal strips. In both cases, one would solve one set of independent subdomains in a sweep, then use the updated solution for boundary conditions in the other set of independent subdomains.

Without actually testing the methods, I would favor the parallel-strip approach over the orthogonal-strip approach. The parallel-strip approach should relatively quickly remove internal boundary conditions by alternation. Even though the orthogonal-strip approach might be able to propagate information better in both directions, the internal boundary conditions will tend to provide a checkerboard pattern with unchanging corners where the edges of the strips intersect. Perhaps the fastest overall approach is to alternate directions but use the parallel-strip approach in both directions.

9/26/02 Update.

I've been working with the test code to modify it into a proper simulator for YM problems. At this time there are modules for water flow, alluvium thickness, and the outlines of one for sediment transport. I've maintained two versions so far, one that solves for all cells simultaneously and one that partitions the domain into overlapping strips (the multizone approach). I'm keeping two versions for now as milestones, but the multizone version can solve for the entire domain simultaneously.

The multizone simulator is a wrapper around the single-domain routines. Each multizone strip has exactly the same size and shape, so all of the pointers and invariant information can be calculated for one strip and used for all zones. The wrapper is responsible for maintaining global arrays for the entire domain (*e.g.*, for state variables, sources, etc.) and transferring global information to and from the local single-domain arrays. So far I've only implemented the strips in one direction (the user can choose the direction), but it should be straightforward to use alternating strips (at the cost of two sets of local arrays). Perhaps the local arrays could be swapped to the hard drive as the strips alternate.

The user selects the strip width and the multizone wrapper selects beginning node indices evenly spaced between the start boundary and one strip width from the end boundary. Actually the

indices are rounded to the nearest row/column. This provides a set of strips that may or may not overlap slightly. An additional set of strips is positioned to straddle the sutures between the first set of strips. Where strip boundaries lie along the edges of the big domain, the actual boundary conditions are used; otherwise, the state variable is held fixed. The second set of overlapping strips serve to "erase" the fixed condition.

I've been testing the multizone algorithm on several problems to shake out bugs and examine convergence. The tests are performed exclusively on the alluvium-thickness portion of the code, using the laminar film-flow option for creep. This is the option where flux is proportional to thickness cubed. I only have transfer routines for specified-thickness boundary conditions so far (although the single-zone components can consider flux and gradient conditions).

Before running any multizone simulations, I tested the single-zone algorithms. As the primary focus is YM, the 7.5-m YM grid was used for simulations, with various resolutions achieved by selecting every 1, 2, or 4 cells. I kept getting results with nonlinear flow and a uniform source (both for water flow and soil creep) that broke out into checkerboard noise patterns. After playing with a large number of combinations, including several tricks used in nonlinear flow problems such as slowing down the update rate, several observations became clear.

- Starting with the thickness larger than the true solution and allowing it to deflate appears to converge faster and reduce numerical problems relative to starting with a thickness smaller than the true solution and allowing it to inflate. This is particularly true with a uniformly distributed source term.
- Inappropriate boundary conditions can propagate severe 2-Δx oscillations upstream several wavelengths. The gentlest exit boundary condition is the parallel-gradient condition, where the free surface is parallel to the bottom. Explicitly including this equation in the matrix appears to work well. Forcing the exterior nodes to artificially be exit nodes allows the condition to be used on all boundaries if there are internal sources.
- Grid resolution/smoothness has a great deal to do with checkerboard noise and local "hollow" pits/towers. It appears that the bedrock must be locally fairly smooth at the grid-cell scale, and as the grid becomes coarser it also becomes rougher (unless some smoothing is performed). For the finer resolutions, the main oscillation problems seem to be on hillslopes and narrow channels. Thus, it appears important to try to run simulations on very fine grids (even the 7.5-m grid has hillslope problems).

The first set of simulations using the multigrid algorithm was for a parabolic domain

$$Z = 1000\left(f_x - \frac{1}{2}\right)^3 \tag{16-306}$$

where Z is bedrock elevation [m] and f_x is the fraction of the distance from minimum to maximum x coordinate. The domain size is on the order of several kilometers across, with the y direction 1.5 times longer than the x direction. Another set of simulations tilted this parabola in the y direction,

$$Z = 1000\left[\left(f_x - \frac{1}{2}\right)^3 + 2f_y\right] \tag{16-307}$$

where f_y is the y correspondent to f_x. Note that there is flow in both the x and y direction for both cases, due to the fixed-thickness boundaries.

It quickly became obvious that one should do several iterations for each strip to minimize the overhead of transferring to and from the global array. This strategy appeared to speed up overall convergence rate per clock time, even though each zone took several times longer. Near global convergence, convergence within a zone may occur before all of the iterations were done, thus the zone can terminate early and the work per global iteration drops significantly.

Several generalizations immediately became apparent.

When the flow was primarily in the x direction, x-oriented strips converged quicker than y-oriented strips, although the work involved in one iteration of an x strip is slightly larger. This is because work for a single sweep is proportional to the length of the strip times the number of strips. For a domain of 150 by 100 cells and a strip width of 25 cells, there are 7 y-oriented strips and 11 x-oriented sweeps, so overall work is about 10.5 to 11 assuming that the orientation of the strip does not affect the solver. Generally the work per iteration is close regardless of the sweep direction and the choice of sweep direction should be based on convergence per iteration.

When the flow was strongly in the y direction, y-oriented strips converged far faster than the x-oriented strips. Here y convergence was essentially complete after 4 or 5 global iterations, while x convergence took several times as many iterations. One could watch a very distinct bulge in the solution propagate from upstream strip to downstream strip. Thus, the more of the strips perpendicular to flow, the more iterations required to propagate the solution from upstream to downstream.

The slanted problem provided an opportunity to examine how the converged solutions differ in the two directions. The solution is a pair of mounds starting in the upstream corners and deepening parabolically towards the center of the downstream boundary. The x strips tended to

provide solutions that were dispersed in the x direction relative to the full-domain solution (*i.e.*, the mounds are wider than the full-domain solution). The y strips tended to provide mounds narrower than the full-domain solution, and not propagated quite as far in the x direction. As the strip width decreased, the discrepancy increased. The maximum relative error was about 2 percent for y-oriented strips 25 cells wide (1/4 of the domain width).

Returning to the YM problem with the multizone algorithm, it quickly became clear that one should use the widest strips possible to aid in channel convergence. Often edges between zones become very distinct due to altered flow patterns as a channel crosses an edge. Convergence in channels is usually the slowest component (I include artificial channels caused by DEM seams in this category) and hammering it with discontinuities does not help. With narrow y strips, one can watch the solution propagate downstream from strip to strip, just as in the parabola example.

When considering just the area of YM near the repository footprint, x-oriented strips appear to converge faster than y strips, although channels encountering edges are a problem. However, with wide strips the solutions become similar after 5 or 6 iterations and overall convergence is not greatly different. If the area considered quadruples, strip edges are more significant at slowing convergence. The large washes in particular, which are not oriented east-west, can be strongly affected by x strips. However, work per iteration does not increase as N^3. Moving from a 300 by 200 grid to a 600 by 400 grid increases work per global iteration by only 5 to 6 times (from about 1.6 min to 8 or 9 min). Note that there are 4 iterations within each zone for these quotes.

Quadrupling the grid size again increases solver work per iteration to about 45 min per global iteration (roughly 5 times as long for 4 times the unknowns). Note that the solver effort is the majority of the total computational burden (*e.g.*, one profiled example had the solver using 80 percent of the total burden). Since all of the components of the simulator should scale linearly with the number of unknowns except the solver, it is gratifying that the overall computational effort increases linearly with the number of unknowns, given a fixed strip width.

The notion of effort scaling linearly with the number of unknowns is perhaps a little misleading, since as the number of unknowns increases each strip is a smaller fraction of the overall problem. Generally more iterations are necessary for convergence, and it becomes more necessary to have alternating direction strips.

9/28/02 More observations on overland flow.

I've been playing with the overland-flow simulator to get a feel for the strengths and weaknesses. In particular, I've been trying to merge subsurface and overland flow to avoid handling wet and dry cells, although it appears to be very hard to get the combination to converge.

One thing that struck me is how inappropriate boundary conditions can destroy the solution with oscillations. The second thing I noticed is that sometimes simply refining the grid will help the boundary-condition induced oscillations. I realized that the grid Peclet number is at work here, where the grid Peclet is defined as

$$\mathrm{Pe} = \frac{|\nabla a|}{|\nabla h|}\Delta x \tag{16-308}$$

and where a is bottom elevation, h is flow thickness, and Δx is grid spacing. According to this, areas where flows are changing thickness are vulnerable to oscillations. This explains the hillslope oscillations I observed in YM tests, where the oscillations appear to be caused by the channels.

Planning to incorporate a water sink into the equations got me thinking. Typically the fraction of area that is wetted in shallow overland flow is less than one through microtopography effects. Also, flow typically tends to be localized. This handled in KINEROS as a triangular wedges (hillslopes) and prisms (channels), while (Defina, 2000) assumes a normal distribution. The general way of handling areally integrated parameters is to perform an integration in the form

$$\int_A F(b)\,\mathrm{d}A = \int_{b_1}^{b_2} F(b)\frac{\mathrm{d}A}{\mathrm{d}b}\,\mathrm{d}b \tag{16-309}$$

where

- b is local thickness [L],
- A is integration area [L^2], and
- $F(b)$ is a function of b.

The functional form of $\mathrm{d}A/\mathrm{d}b$ used by KINEROS is to use shallow triangular channels on hillslopes. Channels are allowed to have more detailed topology, since they are treated as linear features. Assuming that triangular channels are used and a constant local water elevation applies, local b varies linearly from mid-channel to the edge of the wetted area. In this case,

$$\frac{\mathrm{d}A}{\mathrm{d}b} = -\frac{A}{\Delta b} \tag{16-310}$$

where Δb is the local microtopography relief ($h_{top} - h_{chan}$), where h_{top} is the local topmost elevation and h_{chan} is the channel-bottom elevation.

Integration limits are another consideration. Integrating from deepest to shallowest, $b_1 = H - h_{chan}$, where H is local water elevation, and $b_2 = \max(0, H - h_{top})$.

As an example, assume $F(b) = Kb$. The areal integration is

$$\int_A F(b)\,\mathrm{d}A = -\frac{AK}{\Delta b}\int_{b_1}^{b_2} b\,\mathrm{d}b = -\frac{AK}{2\Delta b}(b_2^2 - b_1^2) \tag{16-311}$$

Note that in the limit,

$$\left[-\frac{(b-\delta)^2 - b^2}{2\delta}\right]_{\delta\to 0} = \left[\frac{2b\delta - \delta^2}{2\delta}\right]_{\delta\to 0} = b \tag{16-312}$$

and the form without microtopography applies in the limit.

Losses from overland flow are significantly affected by wetted fraction. Net mass source/sink terms are

$$\rho S_{net} = \rho(Q_{rain} - Q_{soil}) \tag{16-313}$$

where

S_{net} is volumetric source per area [L^3/T L^2],
Q_{rain} is rainfall rate [L/T], and
Q_{soil} is rate of loss to soil (out bottom of domain) [L/T].

Typically Q_{soil} would be gravity drainage under steady conditions. Where soil is wetted (overland flow is occurring), $Q_{soil} = K_{sat}$, where K_{sat} is saturated soil conductivity. Where overland flow is not occurring, $Q_{soil} = \min(Q_{rain}, K_{sat})$. Thus, the net source/sink terms are

$$\rho S_{net} = \rho\left[Q_{rain} - f_w K_{sat} - (1 - f_w)\min(Q_{rain}, K_{sat})\right] \tag{16-314}$$

where

$$f_w = \begin{cases} 0 & H \le h_{chan} \\ b_1/\Delta b & h_{chan} \le H \le h_{top} \\ 1 & H \ge h_{top} \end{cases} \tag{16-315}$$

To write the integration cases in a form that works for $\Delta \ge 0$ without dividing by zero, let's consider the generic form

$$B(n) = \frac{A}{\Delta}\int_{b_1}^{b_2} b^n\,\mathrm{d}b \tag{16-316}$$

where

$$b_1 = \max(H - h_{top}, 0) \tag{16-317}$$

$$b_2 = \max(H - h_{chan}, 0) = b_1 + \delta = b_1 + w\Delta \tag{16-318}$$

The generic answer is

$$B(n) = \frac{A}{(n+1)\Delta}(b_2^{n+1} - b_1^{n+1}) \tag{16-319}$$

The integral is sensitive to changes in free surface elevation, so it is of interest to calculate the derivative. The values of b_1 and b_2 depend on H, but not the integrand. Thus, taking into account Leibnitz's rule,

$$\frac{\mathrm{d}B(n)}{\mathrm{d}H} = \frac{A}{\Delta}\left[b_2^n \frac{\partial b_2}{\partial H} - b_1^n \frac{\partial b_1}{\partial H}\right] \tag{16-320}$$

It is also necessary to consider cases with an exponential,

$$\begin{aligned} E(\beta) &= \frac{A}{\Delta}\int_{b_1}^{b_2} \exp(\beta b)\,\mathrm{d}b \\ &= \frac{1}{\beta}[\exp(\beta b_2) - \exp(\beta b_1)] \end{aligned} \tag{16-321}$$

$$\frac{\mathrm{d}E(\beta)}{\mathrm{d}H} = \frac{A}{\Delta}\left[\exp(\beta b_2)\frac{\partial b_2}{\partial H} - \exp(\beta b_1)\frac{\partial b_1}{\partial H}\right] \tag{16-322}$$

The w weighting parameter is $(b_2 - b_1)/\Delta$ if $\Delta > 0$. Otherwise, $w = 0$ if $b_2 = 0$ and $w = 1$ if $b_2 > 0$. The following avoid the division by Δ (except to evaluate w).

$$B(0) = wA \tag{16-323}$$

$$B(1) = wA_i(1) = wA\left(b + \frac{\delta}{2}\right) \tag{16-324}$$

$$B(2) = wA_i(2) = wA\left(b^2 + b\delta + \frac{\delta^2}{3}\right) \tag{16-325}$$

$$B(3) = wA_i(3) = wA\left(b^3 + \frac{3}{2}b^2\delta + b\delta^2 + \frac{\delta^3}{4}\right) \tag{16-326}$$

The corresponding derivatives for $\mathrm{d}B(n)/\mathrm{d}h$ are

$$\frac{\mathrm{d}B(0)}{\mathrm{d}H} = \frac{\mathrm{d}w}{\mathrm{d}H}A \tag{16-327}$$

$$\frac{\mathrm{d}B(1)}{\mathrm{d}H} = wA + \frac{\mathrm{d}w}{\mathrm{d}H}A_i(1) \tag{16-328}$$

$$\frac{\mathrm{d}B(2)}{\mathrm{d}H} = wA\left(2b+\delta\right) + \frac{\mathrm{d}w}{\mathrm{d}H}A_i(1) \tag{16-329}$$

$$\frac{\mathrm{d}B(3)}{\mathrm{d}H} = wA\left(3b^2+3b\delta+\delta^2\right) + \frac{\mathrm{d}w}{\mathrm{d}H}A_i(3) \tag{16-330}$$

$$\frac{\mathrm{d}w}{\mathrm{d}H} = \begin{cases} 0 & b<0 \text{ or } b-\delta>0 \\ 1/\Delta & \text{otherwise} \end{cases} \tag{16-331}$$

9/30/02 Observations on stairstep microtopography.

The consideration of microtopography is probably not terribly important for water flow resistance calculations, although perhaps convergence would be improved since a greater change in flow height is required to affect a given change in flow. Strictly speaking, the formulation as developed is appropriate when the microchannels are oriented in the direction of flow, which is generally the case for water. Soil is more likely to encounter a stairstepping bedrock pattern, however, due to stratified layers.

I ran quite a few 1D simulations of soil moving downslope with varying degrees of stairstepping. Physically what I would expect under steady state without water reworking the soil profile is for one of three regimes to occur.

- Small protuberances form a bump in the surface profile.
- Large protuberances on slopes well below the angle of repose form a continuous profile, albeit bumpy.
- Large protuberances on slopes above a critical threshold trap soil with a discontinuous slope. Within the pocket the soil is at the angle of repose.

My concern is with relating soil depths calculated assuming a smooth bedrock microtopography to soil depths accounting for stairstepping.

I used the laminar-flow model for all of the cases, since this is what I propose using for the distributed simulations. For ease of comparison, the upslope incoming flux is specified and the

downslope condition is that the gradient of the soil top is parallel to the the mean bedrock gradient. To generate bumps, I use a sine wave in the form

$$S = A|S_o|^n \operatorname{sign}(S_o) \tag{16-332}$$

$$S_o = \max[M, sin(2\pi r f)] \tag{16-333}$$

$$f = \frac{x - x_0}{x_1 - x_0} \tag{16-334}$$

where

- S is the perturbation applied to the base slope,
- S_0 is the base perturbation,
- r is recurrence rate over the interval,
- f is fraction of distance from top to bottom, and
- A is amplitude.

It turns out that large, closely spaced protuberances generate a series of "waterfalls", with flatlying pools in between. Thin films coat the downstream edge of the protuberance. Qualitatively this is not what I expect, since the angle of repose is essentially zero rather than the 10 to 30 degrees that might be expected. Making the soil more viscous makes the soil layer thicker, making the protuberances smaller relative to soil thickness. Soils at the peak of the protuberances are generally somewhat thicker than the corresponding smooth-slope soil depth.

The smooth-bedrock and perturbed-bedrock solutions yield comparable results for long-wavelength sinusoidal perturbations ($A(x_1 - x_0)/r << 1$) when the average depth corresponds to the average of the channel and peak perturbation depths. Both flux and mean depth are predicted well. This correspondance holds up for symmetric perturbations such as clipped sines, but does not hold up for asymmetric perturbations. The problem seems to be that the bedrock surface is more erratic than the soil surface. Large offsetting perturbations cancel so the means are nearly identical. Actually, the correspondance in long-wavelength cases is best midway between perturbations.

As a side note for possible investigation, the laminar film model is clearly not correct for short wavelength large perturbations. Another resistance model is needed. Often a Bingham model is considered appropriate for debris flows, where the top rides as a plug flow (no shear) and the edges undergo viscous shear. The Bingham model is broken into two ranges (Bird et al., 1960) for film flow, one (at the top of the flow) where horizontal velocity is vertically uniform

$$\frac{\partial v_x}{\partial y} = 0 \qquad |\tau_{yx}| < \tau_0 \tag{16-335}$$

and another (at the bottom of the flow) where velocity is Newtonian with an offset

$$\tau_{yx} = \tau_0 + \mu_0 \frac{\partial \mathbf{v}_x}{\partial y} \qquad |\tau_{yx}| > \tau_0 \tag{16-336}$$

Here the x coordinate is along flow and y is from the free surface towards the bottom. For film flow,

$$\tau_{yx} = \rho g \nabla H \tag{16-337}$$

The μ_0 and τ_0 parameters correspond to viscosity and offset stress, where

$$\tau_0 = y_0 \rho g \nabla H \tag{16-338}$$

Since the integrals are separable, one finds in the shear zone

$$\mathbf{v}_x = (B^2 - y^2)\frac{\rho g}{2\mu_0}\nabla H - (B - y)\frac{\tau_0}{\mu_0} \tag{16-339}$$

and in the plug-flow zone

$$\mathbf{v}_x = (B - y_0)^2 \frac{\rho g}{2\mu_0}\nabla H \tag{16-340}$$

Substituting for τ_0, in the shear zone

$$\mathbf{v}_x = [B^2 - y^2 - 2y_0(B - y)]\frac{\rho g}{2\mu_0}\nabla H \tag{16-341}$$

Vertical integrals yield

$$\int_{y_0}^{B} \mathbf{v}_x \, \mathrm{d}y = (B - y_0)^3 \frac{\rho g}{3\mu_0}\nabla H \tag{16-342}$$

$$\int_{0}^{y_0} \mathbf{v}_x \, \mathrm{d}y = y_0(B - y_0)^2 \frac{\rho g}{2\mu_0}\nabla H \tag{16-343}$$

$$\int_{0}^{B} \mathbf{v}_x \, \mathrm{d}y = (B - y_0)^2(2B + y_0)\frac{\rho g}{6\mu_0}\nabla H \tag{16-344}$$

Of course, if $y_0 > B$,

$$\int_{0}^{B} \mathbf{v}_x \, \mathrm{d}y = 0 \tag{16-345}$$

The sensitivity of flux to velocity is easily done under the integral, noting that

$$\frac{\mathrm{d}B}{\mathrm{d}H} = 1 \tag{16-346}$$

It turns out that the same expression is valid for both the plug-flow and shear zones,

$$\frac{\mathrm{d}\mathbf{v}_x}{\mathrm{d}B} = (B - y_0)\frac{\rho g}{\mu_0}\nabla H \tag{16-347}$$

Integrating then yields

$$\int_0^B \frac{\mathrm{d}\mathbf{v}_x}{\mathrm{d}H}\,\mathrm{d}y = (B - y_0)^2\frac{\rho g}{2\mu_0}\nabla H = \mathbf{v}_x|_{y=0} \tag{16-348}$$

10/02/02 Flow elevation-change limiters.

I've noticed that mixing overland and subsurface flow tends to be very difficult to control when the free surface crosses the air/soil interface. The change in flow for a given change in head is vastly larger in overland flow than in subsurface flow, thus water rising across the interface during an iteration will far overshoot the interface. Also, overland flow is quite nonlinear so there is a tendency for the free surface to overshoot during an iteration. Because of this, it is important to limit the change permitted for each state variable during an iteration. The limits can be thought of as a type of crude line search.

There are several conditions to handle.

- The free surface is above-ground and thick. It should be constrained to change no more than a fraction of the above-ground thickness.
- The free surface is above-ground and thick. It should be constrained to drop no more than the larger of an "interface-crossing" step and the thickness fraction.
- The free surface is below-ground. It should be constrained to rise no more than the larger of an "interface-crossing" step and a fraction of the porous-medium layer thickness. It should also be constrained to drop no more than the larger of a fraction of the water thickness and a fraction of the porous-medium layer thickness (constrained to always have positive thickness).

These conditions are imposed with the following parameters: (i) maximum change in relative surface-water thickness, (ii) maximum fraction of porous medium layer to change, (iii) minimum surface-water downward limiter, and (iv) minimum porous-medium upward limiter. The minimum limiters restrict the limit placed on a step to some minimum value, allowing the free surface to cross the interface, and probably one value could be used for both.

I tried these on a simple problem where the solution had a free surface entirely in the surface-water zone, but started entirely in the porous medium, and another with the opposite characteristics. The limiters seemed to work well enough for these cases.

10/04/02 Flow routing.

The implicit numerical scheme for calculating flow thickness works reasonably well for soil thickness, but appears to be unstable (or at least slowly convergent) for many water-flow problems on steep natural slopes. The problem seems to be for thin films of overland flow, where small undulations are large relative to the film thickness. Deeper flows tend to be more able to control themselves. Soil tends to be thick enough that small undulations cause only a small change in cell conductivity, thus converge well.

As flow routing seemed to work well on steep hillslopes without hollows, it may be desirable to implement a routing scheme in combination with the implicit scheme. Let's look at this in the context of the staggered-grid scheme, especially the characteristics that make it attractive.

Flux is represented as

$$\mathbf{q} = -\left(\int_a^H K(z, \nabla H)\, \mathrm{d}z\right) \nabla H \tag{16-349}$$

where

- $\mathbf{q}$ is flux [M/T],
- a is lowest elevation of the film [L],
- H is free-surface elevation [L], and
- K is mass hydraulic conductivity [M/T L^2]

Let's first consider the case where the porous-medium component is negligible (film-flow only). In this case, only overland flow contributes and a represents the soil top. When $h << L|\nabla a|$, one can make the following approximations

$$\nabla H \approx \nabla a \tag{16-350}$$

$$\mathbf{q} = -\left(\int_a^H K(z, \nabla a)\, \mathrm{d}z\right) \nabla a \tag{16-351}$$

In the fully implicit scheme, K for each cell is evaluated using all four corner h values to evaluate h_c. A further approximation can be made to use the upstream h instead, at the cost of

additional numerical dispersion. The upstream h could be evaluated as a weighted sum of h for the nodes attached to the upstream face of the cell, with the upstream face evaluated using the flux vector evaluated at the centroid. The upstream h could also be evaluated as the largest of the surrounding nodes, which would be necessary for explicit routing.

If an explicit flow routing scheme were adopted, the analogous approach to what was implemented before would be to

- Sort the nodes from highest to lowest.
- Process from highest to lowest nodes
- For each node, construct a balance equation using the surrounding cells to calculate the node h.
  - For a cell with a defined centroid h_c, fluxes on internal partition faces are pre-calculated using h_c and ∇a.
  - For all other cells, fluxes on the internal partition faces are sought so that the sum of the undetermined (outlet) faces balances the inflows. All undetermined h_c values are assumed identical to the unknown h at the node being processed.
  - Iteration is needed if the source/sink terms are dependent on h_c, otherwise a single calculation is sufficient.
- Continue until all nodes are processed.

The explicit routing approach for the staggered grid will likely share the strengths and weaknesses of the 9-way scheme used before, although it should be less dispersive since the computational scheme is inherently less dispersive. However, simply using h from the highest node to evaluate h_c will run into problems for channels that run diagonally across a cell, since the channel h will probably be much different from bank h. Considering subsurface flow as well as surface flow will complicate matters further.

Perhaps the simplest and most robust approach is to keep the implicit scheme, but use the upstream h to evaluate K. The sensitivity term $(\mathrm{d}K_c/\mathrm{d}h_c \mathrm{d}h_c/\mathrm{d}h_i \delta_i)\nabla a$ will only involve nodes defining the upstream face, which will help considerably to tame oscillations.

10/09/02 Gravity on steep slopes.

Gravity is a driving force for flow. I noticed in Bird et al. (1960) that volume rate of 1D film flow per unit width is described by

$$Q = \frac{\rho g B^3 \cos\beta}{3\mu} \tag{16-352}$$

where β is the angle between the gravity vector and the normal to the surface (0 for a horizontal surface, 1 for vertical). However, this is implemented as

$$Q = \frac{\rho g B^3}{3\mu} \nabla H \tag{16-353}$$

Letting a be the elevation of the bottom,

$$\nabla a = \cot\beta = \frac{\cos\beta}{\sin\beta} \tag{16-354}$$

For relatively horizontal planes, $\sin\beta \approx 1$, but for steeper inclines this is not true. Just take the example of the vertical, where $\nabla a \to \infty$ but $\cos\beta = 1$. Clearly we prefer to have a correct form for gravitational acceleration.

Let's look at the formal implementation. We want to have $\mathbf{g} \cdot \mathbf{t}$, where $\mathbf{t}$ is the tangent to the flow bottom pointing downhill. This can be achieved using

$$\mathbf{g} \cdot \mathbf{t} = g\mathbf{z} \cdot \mathbf{n} \nabla a = g \frac{x}{L} \frac{y}{x} = g \frac{y}{L} = g \cos\beta \tag{16-355}$$

where a right triangle is used with components x, y, and L for x leg, y leg, and along-flow leg. Accordingly, we need to add a factor of $\mathbf{z} \cdot \mathbf{n}$ to our equations.

For our 2D cells, elevation is described by

$$Z_a = [\mathbf{v}_{u1} + \mathbf{v}_{u2}\xi + \mathbf{v}_{u3}\eta + \mathbf{v}_{u4}\xi\eta] \cdot \mathbf{a} \tag{16-356}$$

and the function describing the soil surface is

$$f = z - Z_a = 0 \tag{16-357}$$

A vector normal to the surface evaluated at the cell centroid is

$$\begin{aligned} \mathbf{v} &= \left[\frac{\partial f}{\partial x} \frac{\partial f}{\partial y} \frac{\partial f}{\partial z}\right] \\ &= [-\xi_{,x}\mathbf{v}_{u2} \cdot \mathbf{u} - \eta_{,y}\mathbf{v}_{u3} \cdot \mathbf{u}1] \end{aligned} \tag{16-358}$$

and the unit normal vector is

$$\mathbf{n} = \frac{\mathbf{v}}{|\mathbf{v}|} \tag{16-359}$$

The correction factor multiplying the equation is

$$\mathbf{z} \cdot \mathbf{n} = \frac{1}{\left(v_1^2 + v_2^2 + 1\right)^{1/2}} \tag{16-360}$$

For the 7.5-m pixel grid I've been using for Split Wash (which runs from slightly above the Solitario Canyon channel on the west flank of Yucca Crest through most of Split Wash), the steepest gradient in a cell is about 50 degrees, although less than 1 percent are steeper than about 33 degrees. The correction factor ranges from 1 through 0.85 for all but the few very steep cells, with the steepest cell having a correction of about 0.65.

Note: this correction is correct for film flow and porous-medium flow, but is it correct for the other resistance forms? The square root should be appropriate for vegetative resistance, since the square root of gravity is in the resistance. And Manning resistance doesn't have gravity explicitly included (although through analogy with Chezy resistance it too has a square-root dependence). Square roots of the factor are 0.92 and 0.8 for the Split Wash cells, making it perhaps a second-order correction in these cases.

10/10/02 Scaling tricks.

I've noticed that simulating thick films tends to be much more robust than simulating thin films on irregular terrain. I attribute this to the lesser importance of topographic protuberances. My experiments on stair-stepped topography demonstrate this feature. Let's see if we can transform the equations so that we can lessen the effect of minor topographic irregularities.

The governing equation for overland flow with power-law resistance is

$$\frac{\partial \rho \epsilon b}{\partial t} - \nabla \cdot \left(\rho \epsilon K b^m \nabla H\right) = S \tag{16-361}$$

where

- ρ is density [M/L^3],
- ϵ is volume-fraction occupied by fluid [L^3/L^3],
- b is film thickness [L],
- H is free-surface elevation [L], and
- K is hydraulic conductivity [L/T].

We wish to maintain the following relationships

$$\epsilon_s b_s = \epsilon_o b_o \tag{16-362}$$

$$\epsilon_s K_s b_s^m = \epsilon_o K_o b_o^m \tag{16-363}$$

where s and o represent scaled and old values. Rearranging,

$$\frac{\epsilon_s}{\epsilon_o} = \frac{b_o}{b_s} \tag{16-364}$$

$$\frac{K_s}{K_o} = \frac{\epsilon_o}{\epsilon_s}\left(\frac{b_o}{b_s}\right)^m \tag{16-365}$$

Letting V_r, K_r, and B_r be the ratios of ϵ, K, and b, respectively,

$$V_r = B_r^{-1} \tag{16-366}$$

$$K_r = V_r^{-1} B_r^{-m} = B_r^{1-m} \tag{16-367}$$

Thus, a scaled b results in scaled ϵ and K. It is necessary to use the same scale factor everywhere, which means that one should be careful about channels. One doesn't want channel flow to be so deep that an entire wash is flooded halfway to the ridges!

The scaling trick works for constant-drag vegetation ($m = 1$) and Manning resistance ($m = 5/3$), but not for exponential-drag vegetation.

Just a thought - when working with distinct channels and large cells, perhaps the microchannel topography should be considerably different. A trapezoidal channel could be represented by nested wedges, representing bottom slope, side slope, and overbank.

10/25/02 Advective flux revisited.

SAS

I realized recently that it will be inconvenient to calculate advective fluxes using gradients of state variables, as I had outlined earlier. When simultaneously doing water and sediment flux there is no problem. The difficulty arises when I try to time-average the water fluxes.

As the largest water pulse moves downstream, maximum flux follows it, so maximum flux does not occur at the same time for all cells. This implies that there is no head configuration that reproduces maximum flux for all cells.

One approach is to store head values independently for each cell (4 head values per node) to represent peak-flow configuration, and cumulative flux for each cell centroid. Peak-flow cell K would need to be recalculated for effective-steady-state parameters and transport simulations.

Another approach is to store flux values perpendicular to each cell face at the face centroid and the cumulative storm flux. Fluxes vary linearly along coordinates, thus integration is straightforward. The centroids are only important for anisotropic diffusion, where

$$\mathbf{q}_x(\xi,\eta) = -K_{xx}\xi_{,x}(\mathbf{v}_{u2} + \mathbf{v}_{u4}\eta)\cdot\mathbf{h} - K_{xy}\eta_{,y}(\mathbf{v}_{u3} + \mathbf{v}_{u4}\xi)\cdot\mathbf{h} \tag{16-368}$$

$$\mathbf{q}_y(\xi,\eta) = -K_{yx}\xi_{,x}(\mathbf{v}_{u2} + \mathbf{v}_{u4}\eta)\cdot\mathbf{h} - K_{yy}\eta_{,y}(\mathbf{v}_{u3} + \mathbf{v}_{u4}\xi)\cdot\mathbf{h} \tag{16-369}$$

These can be rewritten for control volume edges as

$$\mathbf{q}_x(0,\eta) = \mathbf{q}_x(0,-1) + w_y[\mathbf{q}_x(0,1) - \mathbf{q}_x(0,-1)] \tag{16-370}$$

$$\mathbf{q}_y(\xi,0) = \mathbf{q}_y(-1,0) + w_x[\mathbf{q}_y(1,0) - \mathbf{q}_y(-1,0)] \tag{16-371}$$

$$w_y = (\eta+1)/2 \tag{16-372}$$

$$w_x = (\xi+1)/2 \tag{16-373}$$

The benefit comes in when doing advection of a linearly interpolated concentration in the form

$$u = (\mathbf{v}_{u1} + \mathbf{v}_{u2}\xi + \mathbf{v}_{u3}\eta + \mathbf{v}_{u4}\xi\eta)\cdot\mathbf{u} \tag{16-374}$$

The result is

$$u\mathbf{q}_x|_{0,\eta} = [(\mathbf{v}_{u1} + \mathbf{v}_{u3}\eta)\cdot\mathbf{u}]\mathbf{q}_x(0,\eta) \tag{16-375}$$

$$u\mathbf{q}_y|_{\xi,0} = [(\mathbf{v}_{u1} + \mathbf{v}_{u2}\xi)\cdot\mathbf{u}]\mathbf{q}_y(\xi,0) \tag{16-376}$$

and integrals are quadratic rather than linear.

Thinking further, it would be simpler to store $\mathbf{q}_x(0,0)$, $\mathbf{q}_y(0,0)$, $\mathrm{d}\mathbf{q}_x/\mathrm{d}\eta$, and $\mathrm{d}\mathbf{q}_y/\mathrm{d}\xi$, where

$$\frac{\mathrm{d}\mathbf{q}_x(\xi,\eta)}{\mathrm{d}\eta} = \mathbf{q}_{x,\eta} = -K_{xx}\xi_{,x}\mathbf{v}_{u4}\cdot\mathbf{h} \tag{16-377}$$

$$\frac{\mathrm{d}\mathbf{q}_y(\xi,\eta)}{\mathrm{d}\xi} = \mathbf{q}_{y,\xi} = -K_{yy}\eta_{,y}\mathbf{v}_{u4}\cdot\mathbf{h} \tag{16-378}$$

These can be rewritten for control volume edges as

$$\mathbf{q}_x(0,\eta) = \mathbf{q}_x(0,0) + \eta\mathbf{q}_{x,\eta} = \mathbf{q}_{x0} + \eta\mathbf{q}_{x,\eta} \tag{16-379}$$

$$\mathbf{q}_y(\xi,0) = \mathbf{q}_y(0,0) + \xi\mathbf{q}_{y,\xi} = \mathbf{q}_{y0} + \xi\mathbf{q}_{y,\xi} \tag{16-380}$$

where $\mathbf{q}_{x0} = \mathbf{q}_x(0,0)$ and $\mathbf{q}_{y0} = \mathbf{q}_y(0,0)$. The concentration integral is then

$$u\mathbf{q}_x|_{0,\eta} = [(\mathbf{v}_{u1} + \mathbf{v}_{u3}\eta)\cdot\mathbf{u}][\mathbf{q}_{x0} + \eta\mathbf{q}_{x,\eta}] \tag{16-381}$$

$$u\mathbf{q}_y|_{\xi,0} = [(\mathbf{v}_{u1} + \mathbf{v}_{u2}\xi)\cdot\mathbf{u}][\mathbf{q}_{y0} + \mathbf{q}_{y,\xi}] \tag{16-382}$$

Rewriting,

$$u\mathbf{q}_x|_{0,\eta} = (\mathbf{a}_{x1} + \mathbf{a}_{x2}\eta + \mathbf{a}_{x3}\eta^2)\cdot\mathbf{u} \tag{16-383}$$

$$u\mathbf{q}_y|_{\xi,0} = (\mathbf{a}_{y1} + \mathbf{a}_{y2}\xi + \mathbf{a}_{y3}\xi^2)\cdot\mathbf{u} \tag{16-384}$$

where

$$\mathbf{a}_{x1} = \mathbf{q}_{x0}\mathbf{v}_{u1} \tag{16-385}$$

$$\mathbf{a}_{x2} = \mathbf{q}_{x0}\mathbf{v}_{u3} + \mathbf{q}_{x,\eta}\mathbf{v}_{u1} \tag{16-386}$$

$$\mathbf{a}_{x3} = \mathbf{q}_{x,\eta}\mathbf{v}_{u3} \tag{16-387}$$

$$\mathbf{a}_{y1} = \mathbf{q}_{y0}\mathbf{v}_{u1} \tag{16-388}$$

$$\mathbf{a}_{y2} = \mathbf{q}_{y0}\mathbf{v}_{u2} + \mathbf{q}_{y,\xi}\mathbf{v}_{u1} \tag{16-389}$$

$$\mathbf{a}_{y3} = \mathbf{q}_{y,\xi}\mathbf{v}_{u2} \tag{16-390}$$

The following line integrals are needed:

$$\begin{aligned}\int_{\xi_0}^{\xi_1} [u\mathbf{q}_x]_{\eta=0} x_{,\xi}\,\mathrm{d}\xi &= \int_{\xi_0}^{\xi_1} [(\mathbf{a}_{y1} + \mathbf{a}_{y2}\xi + \mathbf{a}_{y3}\xi^2)\cdot\mathbf{u}] x_{,\xi}\,\mathrm{d}\xi \\ &= x_{,\xi}\left(\mathbf{a}_{y1}\langle\xi\rangle + \mathbf{a}_{y2}\langle\xi^2\rangle + \mathbf{a}_{y3}\langle\xi^3\rangle\right)\cdot\mathbf{u} \\ &= (\mathbf{q}_{y0}\mathbf{I}_{afx1} + \mathbf{q}_{y,\xi}\mathbf{I}_{afx2})\cdot\mathbf{u}\end{aligned} \tag{16-391}$$

$$\begin{aligned}\int_{\eta_0}^{\eta_1} [u\mathbf{q}_y]_{\xi=0} y_{,\eta}\,\mathrm{d}\eta &= \int_{\eta_0}^{\eta_1} [(\mathbf{a}_{x1} + \mathbf{a}_{x2}\eta + \mathbf{a}_{x3}\eta^2)\cdot\mathbf{u}] y_{,\eta}\,\mathrm{d}\eta \\ &= y_{,\eta}\left(\mathbf{a}_{x1}\langle\eta\rangle + \mathbf{a}_{x2}\langle\eta^2\rangle + \mathbf{a}_{x3}\langle\eta^3\rangle\right)\cdot\mathbf{u} \\ &= (\mathbf{q}_{x0}\mathbf{I}_{afy1} + \mathbf{q}_{x,\eta}\mathbf{I}_{afy2})\cdot\mathbf{u}\end{aligned} \tag{16-392}$$

where the invariant integrals are

$$\mathbf{I}_{afx1} = x_{,\xi}(\mathbf{v}_{u1}\langle\xi\rangle + \mathbf{v}_{u3}\langle\xi^2\rangle) \tag{16-393}$$

$$\mathbf{I}_{afx2} = x_{,\xi}(\mathbf{v}_{u1}\langle\xi^2\rangle + \mathbf{v}_{u3}\langle\xi^3\rangle) \tag{16-394}$$

$$\mathbf{I}_{afy1} = y_{,\eta}(\mathbf{v}_{u1}\langle\eta\rangle + \mathbf{v}_{u2}\langle\eta^2\rangle) \tag{16-395}$$

$$\mathbf{I}_{afy2} = y_{,\eta}(\mathbf{v}_{u1}\langle\eta^2\rangle + \mathbf{v}_{u2}\langle\eta^3\rangle) \tag{16-396}$$

As before, the invariant integrals are different for each segment.

References

Ackers, P. and W. R. White. 1973. Sediment Transport: New Approach and Analysis. *Journal of the Hydraulics Division, American Society of Civil Engineers 99*(HY11), 2041–2060.

Beaumont, C., P. Fullsack, and J. Hamilton. 1992. Erosional control of active compressional orogens. In K. R. McClay (Ed.), *Thrust Tectonics*, London, pp. 1–18. Chapman & Hall.

Bird, R. B., W. E. Stewart, and E. N. Lightfoot. 1960. *Transport Phenomena.* New York, NY: John Wiley & Sons.

Campbell, G. S. 1977. *An Introduction to Environmental Biophysics.* New York: Springer-Verlag.

Chien, N. and Z. Wan. 1998. *Mechanics of Sediment Transport.* Reston, VA: ASCE Press.

Defina, A. 2000. Two-dimensional shallow flow equations for partially dry areas. *Water Resources Research 36*(11), 3251–3264.

Einstein, H. A. 1950. *The bedload function for sediment transportation in open channel flows.* Technical Bulletin 1026, United States Department of Agriculture.

Fair, G. M. and J. C. Geyer. 1954. *Water Supply and Wastewater Disposal.* New York, NY: John Wiley & Sons.

Fernandez, J. A., J. B. Case, C. A. Givens, and B. C. Carney. 1994. *A Strategy to Seal Exploratory Boreholes in Unsaturated Tuff.* SAND93-1184, Sandia National Laboratories, Albuquerque, NM.

Flanagan, D. C. and M. A. Nearing. 1995. *USDA - Water Erosion Prediction Project Hillslope Profile and Watershed Model Documentation.* NSERL Report No. 10, United States Department of Agriculture, Agricultural Research Service, West Lafayette, IN.

Julien, P. Y. 1995. *Erosion and Sedimentation.* Cambridge, England: Cambridge University Press.

Kilinc, M. and E. V. Richardson. 1973. *Mechanics of Soil Erosion From Overland Flow Generated by Simulated Rainfall.* Hydrology Paper 63, Colorado State University, Fort Collins, CO.

Meyer, L. D. and W. H. Wischmeier. 1969. Mathematical Simulation of the Process of Soil Erosion by Water. *Transactions of the American Society of Agricultural Engineers 12*(6), 754–762.

Scott, R. B. and J. Bonk. 1984. *Preliminary Geologic Map (1:12,000 scale) of Yucca Mountain, Nye County, Nevada, with Geologic Cross Sections.* Open-File Report 84-494, United States Geological Survey, Denver, CO.

Stothoff, S. A. and A. C. Bagtzoglou. 1996. Subregional Hydrogeologic Flow and Transport Processes. In B. Sagar (Ed.), *NRC High-Level Radioactive Waste Research at CNWRA, July–December 1995*, Volume CNWRA 95-02S, San Antonio, TX, pp. 9–1–9–20. Center for Nuclear Waste Regulatory Analyses.

Sudicky, E. A. 1989. The Laplace Transform Galerkin Technique: A Time-Continuous Finite Element Theory and Application to Mass Transport in Groundwater. *Water Resources Research 25*(8), 1833–1846.

Woolhiser, D. A., R. E. Smith, and D. C. Goodrich. 1990. *KINEROS, A Kinematic Runoff and Erosion Model: Documentation and User Manual.* ARS-77, United States Department of Agriculture, Agricultural Research Service.

Yalin, Y. S. 1963. An Expression for Bed-Load Transportation. *Journal of the Hydraulics Division, American Society of Civil Engineers 89*(HY3), 221–250.

Yang, C. T. 1973. Incipient Motion and Sediment Transport. *Journal of the Hydraulics Division, American Society of Civil Engineers 99*(HY10), 1679–1704.

Zhang, X. and J. Ewen. 2000. Efficient method for simulating gravity-dominated water flow in unsaturated soils. *Water Resources Research 36*(9), 2777–2780.

17 Environ - Evaluation of Mass Balance Errors in PTC

Account Number: **20-7614-007**
Collaborators: **None**
Quoted Proposal: **In progress**
Directories: **$HOME2/WFO/Environ → $Environ**

Objective: Track down mass balance errors that occur in the contaminant transport portion of the 3D Princeton Transport Code (*PTC*).

PTC solves the saturated groundwater flow equation and contaminant transport with the resultant velocity field. I rewrote the code while at Princeton and Vermont, but did not change the solution algorithms. Environ is using the code extensively, and mass balance errors reported by the transport portion of the code are on the order of 10 percent. The flow portion of the code may exhibit mass balance errors for the first few time steps, which quickly decay to essentially zero.

The code involves a splitting scheme between the horizontal and the vertical, and experience suggests that the implementation of the splitting scheme is not correct for non-horizontal layers. In addition, mass balance errors may occur for horizontal elements (2D finite elements) that occur in portions of a velocity field where the field is changing direction.

12/20/95 Proposal.

Created first draft of the proposal in **$Environ/Proposal/massbal_prop.tex**.

4/22/96 Problem definition.

I have been given authorization by ENVIRON to proceed with work not to exceed $5000.00, which translates into something a little more than 40 of my hours. As agreed by ENVIRON, a set of problems will be provided, including:

1. 1D convection-dispersion with variable grid spacing, with both a Dirichlet boundary condition and a specified-flux boundary condition.
2. 1D convection-dispersion in a parallelepiped. Presumably the horizontal sweep will succeed;

the vertical slice may have problems. This problem will help identify if vertical slice errors are due only to variable layer thickness or also stem from tilted constant-thickness layers.

3. 1D convection-dispersion in a rectangle. The internal layer discretisation will consist of sine waves. This is a very good test to check on the success of the vertical slicing.

4. 2D convection-dispersion in a plane. One of the following problems will be produced. If time permits, both will be provided.

   (a) A gaussian hill plume in a rotational velocity field.

   (b) A variable velocity field consisting of three layers, a clay layer surrounded by two sand layers. A sand window in the clay layer, coupled with a pumping well in the bottom layer and an injection well in the top layer, will provide a strong S-shaped flow field.

The test problems will be run to verify that *PTC* accepts the input. ENVIRON will be provided with enough documentation for each input file to understand the modelled problem.

In order to generate the problems, *Matlab* files will be used to output *PTC* input files. All work will be done in ***$Environ/Verify***.

As the 2D finite element scheme is to be compared with the FE/FD splitting scheme, every effort must be turned to comparing as identical of a problem as possible in each case. Accordingly, the same number of nodes must be created each time, with the same nodal locations. The strategy will be to honor the restrictions inherent in the FE/FD splitting scheme with the 2D FE nodes. The following restrictions are honored:

- A scheme-independent set of boundaries and interfaces is generated.
- Identical node locations are used for the schemes.
- No nodes are on interface locations.
- Nodes are aligned vertically.
- The 2D FE scheme creates a band of averaged parameters along each interface to mimic the internal FD/FE procedure.

The *Matlab* files generated today include:

ptclayer.m Output of geometry-dependent parameters.

ptcprint.m Output of non-geometry-dependent parameters.

time_stamp.m Retrieval of time and date.

spr.m String print routine.

ptccmd.m Generic *PTC* command output routine.

4/24/96 Problem status.

Both horizontal and vertical schemes can now be generated. The **ptclayer.m** routine was augmented to handle boundary conditions as well, with new routines:

ptcbc.m Output of vertical-slice boundary conditions.

ptcsimwrt.m Output of simulation control parameters.

ptcnecmd.m Generic node/element command output routine.

The first test problem was created, a 1D problem with constant discretization. A number of file-creation bugs were eliminated based on this problem. The problem emphasized that there are some small differences in input structure; accordingly, I am using ENVIRON's own version for testing.

One potential *PTC* bug was identified. The dispersion coefficient is created using a longitudinal and a transverse dispersivity, and appropriate velocities. Rotating the 1D problem from vertical to horizontal switched the dispersivity used. In groundwater flow problems, it may make some sense to do this, but I think it might be better otherwise. At least mass balance is great for both horizontal and vertical problems. Upon discussion with Roger Page of ENVIRON, there was some modification to *PTC* that uses a transverse-vertical coefficient as well. Informal documentation on the modification was given to me.

References

18 Quick Looks

Account Number: **As noted**
Collaborators: **As noted**
Directories: **As noted**

Objective: Perform quick looks at technical questions that arise in brainstorming sessions and document the results. Each quick look should take a few hours to no more than a day.

1/18/96 Wetting of YM from dry state.

SAS

Bill Murphy has noted that there is an anomolous trend in the K/Ar ratio in zeolites obtained from YM, where as elevation increases roughly 1000 m the zeolites change from appearing 14 Ma to appearing 1 Ma in age. The elevation change is relative to the water table. In order to change the K/Ar ratio, it appears that relative humidity must be quite low, implying that the medium must be essentially dessicated as saturations must be almost zero before relative humidity is affected. In order to test the rates of water movement near dryout, a 1000-m uniform column of TSw was simulated in ***$BREATH2/VertImbib***, with initial conditions of 30 °C and saturation at 1 percent. A water table at the bottom was imposed, with no-flow conditions at the top. The top temperature was dropped 15 °C, while the bottom was held fixed; temperatures adjusted orders of magnitude faster than the moisture. The *breath* run file was generated by Matlab file **ingen_tm.m**.

Vapor density profiles at intervals of 0.1 Ma are shown in Figure 18-1a, while the corresponding saturation profile is shown in Figure 18-1b. The vapor density pulse reaches the top of the column after about 0.6 Ma. Interestingly, almost all of the transport is due to vapor diffusion; if vapor diffusion is shut off, the saturations only respond through capillary rise to a height of about 70 m after 1 Ma. The liquid in the TSw unit should be quite slow to respond relative to other units; however, vapor transport is efficient enough that it is unlikely that any part of YM will maintain near-zero relative humidities for more than 1 Ma, far below the time required for the K/Ar discrepancy to develop.

2/6/97 Plotting chlorine-36 along the ESF.

SAS

As a response to the request by reviewers that ^{36}Cl incidences be plotted spatially as an aid for readers of a Bill Murphy paper, I created a few *Matlab* routines in ***$HOME2/Matlab/Cl36Map***

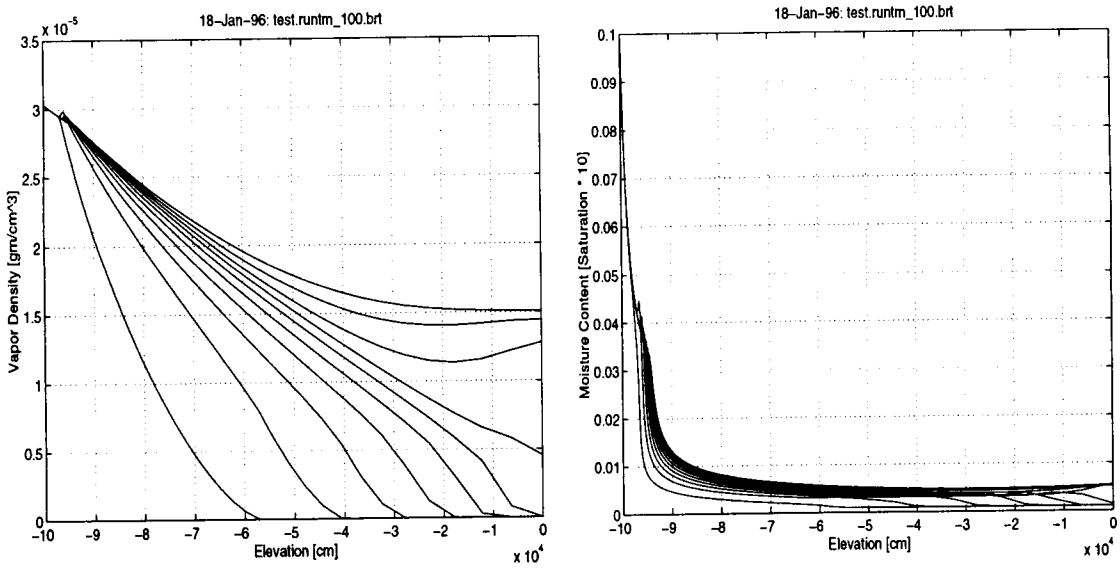

Figure 18-1: 1/18/96. Calculated (a) vapor density and (b) moisture content profiles every 0.1 Ma for imbibition from water table into dry TSw.

and used a digitized version of the ESF handed to me by Brent Henderson several months ago to translate stations to UTM coordinates. Bill had Art Ramos type values of ^{36}Cl from a paper by June Fabryka-Martin into an electronic file; the reported values apparently are not completely reliable so they will only be used in a general way and will be replaced when there is a reliable citation. Two types of symbol schemes can be used in **esflin2esfxys.m**: (i) only the subset falling into categories used by Bill are shown, and (ii) all values are shown with symbol area scaled by hit magnitude. A plot with the second type are shown in Figure 18-2.

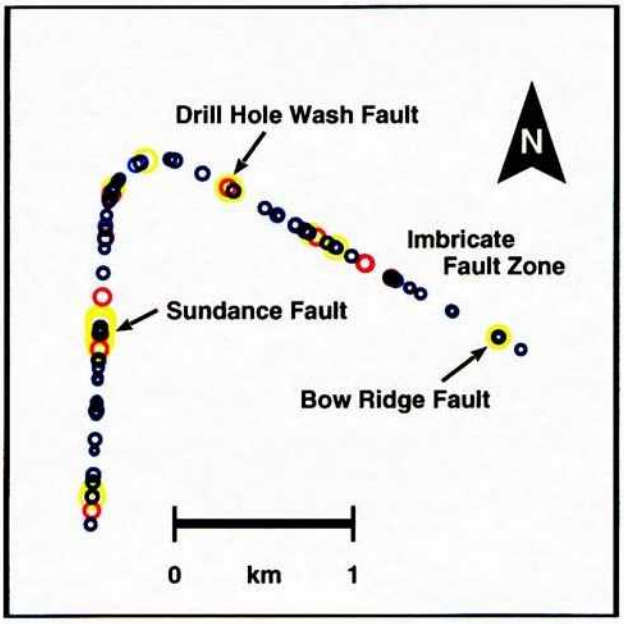

Figure 18-2: 2/6/97. Hits of ^{36}Cl plotted along trace of ESF.

References

Quarterly Information

Entries into Scientific NoteBook # 163 E for the period November 16, 1995, to December 30, 2002, have been made by Stuart Stothoff (SAS; December 30, 2002).

No original text entered into this Scientific Notebook has been removed (SAS; December 30, 2002).

I have reviewed this scientific notebook and find it in agreement with QAP-001. There is sufficient information regarding methods used for conducting tests, acquiring and analyzing data so that another qualified individual could repeat the activity.

E. C. Dr

4/2/2003

I have reviewed this scientific notebook and find it in agreement with QAP-001. There is sufficient information regarding methods used for conducting tests, acquiring and analyzing data so that another qualified individual could repeat the activity.

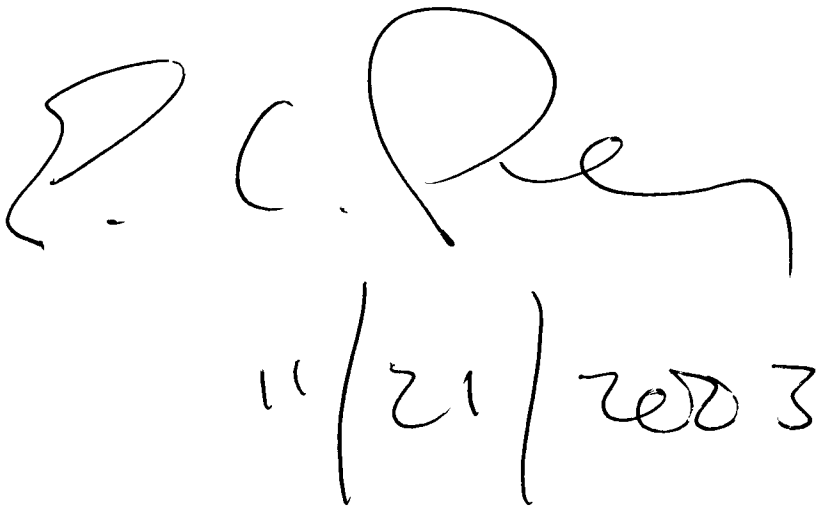

11/21/2023

5 Ambient Hydrology KTI – Major Report Soil Synthesis

Account Number: **20-5708-861**
Collaborators: **Randy Fedors**

Objective:

8/29/00 Input to Major Milestone.

SAS

Over a period of several months, I wrote up results and inferences in the form of sections of chapters intended to summarize major findings of the infiltration studies over the past few years. Most of the information represents synthesis work, thus it has not been documented along the way.

Substantially complete sections are included here, with the numbering scheme used in the original document. These sections represent the working document before formatting as a WordPerfect file and undergoing any CNWRA review.

Some of the figures are not included here. These figures are images based on digital elevation model (DEM) files, which have postscript files that are ponderous (4 to 10 Mb apiece) and make the electronic file untenably large. These figures were submitted to CNRWA as separate files. *Correction dated 9/3/03: These images are now included for completeness.* SAS

The soil-thickness section is included starting here. The original numbering started with section 3, subsection 1, and subsubsection 2.

5.1 ESTIMATING SOIL THICKNESS DISTRIBUTIONS

Soils in the Yucca Mountain (YM) area are composed of fine sands mixed with coarser rock shards and boulders, with the largest rock fragments decreasing in size from higher to lower elevations. At the highest elevations and on slopes steeper than the angle of repose, the mixture is essentially fine æolian sands distributed on and around outcrops and large boulders.

In some areas of YM, the bedrock may be fairly planar with minor irregularities. In many areas, however, the bedrock is somewhat irregular. For example, the Ghost Dance Fault exposure in Split Wash shows a strong stair-stepping behavior in the lower lithophysal unit of the TCw unit.

Individual steps may be 30 cm or greater. In the caprock, bedrock offsets can be at least 20 cm. Thus, assigning representative thicknesses and porosities is fraught with difficulty. Estimating infiltration is exacerbated by the nonlinear response of infiltration to colluvium thickness and porosity, so that using an areal average over a grid cell for both thickness and porosity, in order to estimate infiltration, does not necessarily yield estimates that are equivalent to the areal average of infiltration over the grid cell.

A detailed map of shallow soil thickness is not available and is difficult to measure, thus an alternative approach for estimating soil thickness was followed here. A mechanistic model combining colluvium and alluvium erosion and redistribution was created, using a DEM for the underlying elevation controls, in order to estimate soil thicknesses.

5.1.1 Soil-Balance Processes

Feedback cycles affecting soil thickness and texture are shown schematically in Figure 5-1. Climate drives the overall process. Effective moisture directly affects vegetation. Effective moisture also affects erosive power, weathering rates, and atmospheric dust sources. Feedback between vegetation and soil thickness and texture is also denoted.

In order to predict soil characteristics under present and future climatic conditions, these conceptual processes must be quantified in a series of mathematical formulas that can be linked in a computational model. The processes include

- Deposition and removal of fine particles through interactions with the atmosphere
- Transport of particles through overland flow (runoff, rainsplash)
- Transport of the bulk soil profile through creep and slump
- Modification of particles *in situ* through weathering processes
- Addition of particles from the bedrock

Each of these processes are discussed in this section, with simple mathematical representations proposed.

Atmospheric Interactions Dust is the primary source of fine particles under current climatic conditions. On a regional basis, dust arises from relatively local sources such as dry playas and is

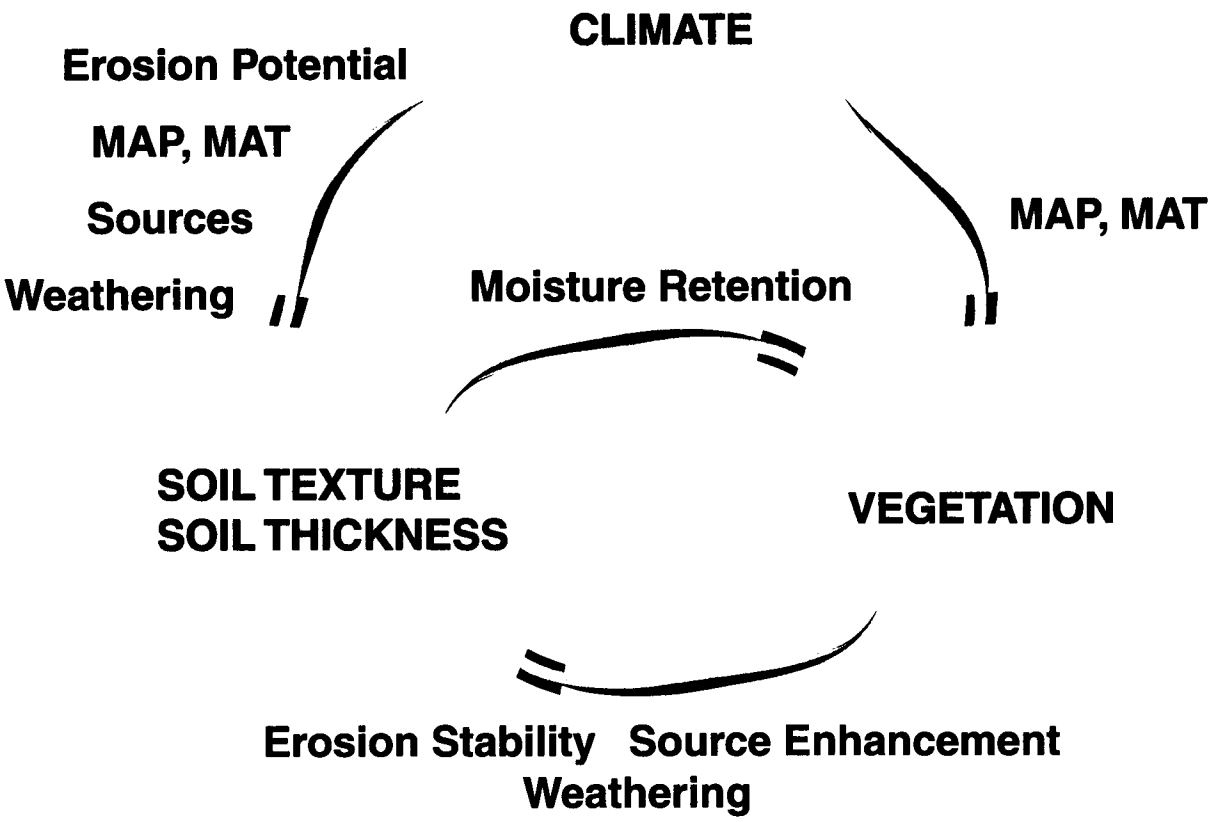

Figure 5-1: Conceptual representation of major influences on soil characteristics.

deposited over a much wider area. When deposition occurs near the source, changes in the local source may need to be considered over the period of interest. There appears to be no dominant dust source near YM, so that it is reasonable to consider regional changes in atmospheric dust concentrations and dust deposition rates.

Studies of present-day and paleo dust deposition rates have been performed in the YM region (Reheis et al., 1995), including sites at Fortymile Wash and Yucca Wash. Reheis et al. (1995) examined deposition rates for the last 15 ky in southern Nevada and California, estimating roughly 6, 3, and 2 gm/m^2/yr for silt, clay, and $CaCO_3$, respectively, for an accumulation rate of about 11 gm/m^2/yr. Extreme values for each category would yield bursts of no more than 65 gm/m^2/yr. At YM, sand is about 67 percent of the fine component of the soil, silt about 25 percent, and clay about 7 percent. The silt and clay fraction is 1/3 of the fine component of a typical YM soil, yielding total dust deposition rates of about 33 gm/m^2/yr. Assuming porosity is

0.4 and particle density is 2.5 gm/cm^3, soil thickness is gaining about 2.2 cm/ky.

The assumption that the deepest æolian soil found on Yucca Crest, roughly 50 cm thick, was deposited in the last 10 ky yields a maximum dust deposition rate on the order of 4 cm/ky for 20 percent rock fragments. More typical deposits are 20 to 30 cm, yielding dust deposition rates that bracket the regional average estimated by Reheis et al. (1995). As the washes are sheltered from the wind and have rougher surfaces, deposition rates in the washes would be expected to be larger than the exposed crest; however, wash hillslopes are far steeper than the relatively horizontal caprock and the dust is likely continuously lost due to far more erosive overland flow. As a first approximation, spatial variability of dust deposition is neglected in the computational model. The spatially uniform dust deposition rates in the model are constrained to have magnitudes consistent with estimates by Reheis et al. (1995).

Transport Through Overland Flow Transport of soil particles through overland flow moves particles from higher elevations to lower elevations via flowing water. For a given storm, the approach advocated by Flanagan and Nearing (1995) is straightforward. In this approach, sediment transport is modeled using equivalent steady-state water flows. Flanagan and Nearing (1995) obtains the equivalent steady state from transient simulations, using the maximum flux within each cell as the flux for the cell with an equivalent period of flux obtained by dividing cumulative discharge over the storm by the maximum flux. These equivalent steady fluxes are used for erosion and deposition calculations.

Erosion and deposition through overland flow can be calculated using a steady sediment-balance equation,

$$\nabla \cdot c_s \mathbf{q}_w - Q_{str} = 0 \tag{5-1}$$

where c_s is the concentration of the sediment in water and $\mathbf{q}_w$ is the flux of water. Following standard practices in the literature (*e.g.*, Woolhiser et al. (1990)), a simple kinetic rate law is used to characterize erosion and deposition,

$$Q_{str} = C_g(c_s - c_{eq}) \tag{5-2}$$

where c_{eq} is the equilibrium sediment concentration for a reach along a stream bed and C_g is an equilibrium constant.

Numerous equilibrium sediment concentration capacity relationships exist in the literature (*e.g.*, Yang (1973), Kilinc and Richardson (1973), Ackers and White (1973), Yalin (1963)). A particularly simple relationship is used herein (Meyer and Wischmeier, 1969), based on tractive

force:

$$c_{eq} = C_s \frac{v^4}{h}, \tag{5-3}$$

where C_s is a constant, v is water velocity, and h is hydraulic depth.

For erosion, C_g is a constant describing the erodibility of the alluvium or bedrock. For deposition ($c_s > c_{eq}$), C_g assumes that particles have fall velocities and drag characteristics similar to spheres (Fair and Geyer, 1954), and a coupled set of equations are used to calculate C_g:

$$v_s = \left[\frac{4}{3}\frac{\rho_s - \rho_f}{\rho_f}\frac{g d_s}{C_D}\right]^{1/2} \tag{5-4}$$

$$C_D = \frac{24}{Re} + \frac{3}{\sqrt{Re}} + 0.34 \tag{5-5}$$

$$Re = v_s d_s \rho_s / \mu \tag{5-6}$$

$$C_g = \frac{v_s}{h}\left(1 - \frac{c_{eq}}{c_s}\right) \tag{5-7}$$

where v_s is the particle settling velocity, g is the acceleration due to gravity, d_s is the particle diameter, C_D is the drag coefficient, Re is the Reynold's number, and μ is the fluid viscosity.

A water-balance equation is used to provide the flux of water used for sediment transport. In steady state, the water-balance equation is

$$\nabla \cdot \mathbf{q}_w + Q_{rain} = 0, \tag{5-8}$$

where Q_{rain} is the net rainfall - net infiltration. A standard practice in the literature is to use a kinematic-wave approximation for hydraulic flux in conjunction with the Manning hydraulic resistance law, so that (in metric units)

$$\mathbf{q}_w = \frac{S^{1/2} h^{5/3}}{n}, \tag{5-9}$$

where S is the slope and n is Manning's roughness coefficient. The kinematic-wave approach requires that each cell has an outlet.

Bulk Movement Gravity has a tendency to move soil masses downslope through creep and slump. Creep is slow bulk movement of the soil profile through accumulated small movements, while slump is catastrophic failure of the soil mass resulting in fast bulk movement. Creep is facilitated through processes that rearrange soil particles, such as freeze-thaw cycles, and is dependent on soil texture. Creep may occur through the entire soil profile; surficial processes such as rainsplash enhance creep near the ground surface. Slump is also dependent on soil texture, but generally

occurs when the soil column is extremely moist. Slump rarely occurs under present-day conditions at YM, although in 1984 a slow-moving localized intense summer rainstorm stripped 7040 m^3 of soil from Jake Ridge, about 6 km east of Yucca Crest. The recurrence rate of such incidences was calculated to be at least 500 yr to be consistent with existing soil profiles (TRW, 1998). Although slump is a more dramatic form of mass wasting, creep often occurs in the same environments and mediates the refilling of the slump reservoirs (Sidle et al., 1985).

The possibility for slumping or other slope failures is typically evaluated through comparing the shear strength S, or resistance to failure, with the forces oriented in the direction of failure. Shear strength of a soil column is (Sidle et al., 1985)

$$S = C' + \Delta C + (\sigma - u)\tan\phi' \tag{5-10}$$

where C' is effective soil cohesion (actual cohesion plus surface tension), ΔC is cohesion caused by root systems, ϕ' is effective angle of internal friction for the soil, σ is total normal stress, and u is pore water pressure. For an infinite-slope stability analysis (appropriate for soils that are shallow relative to slope length, such as is the case at YM),

$$u = M\rho_w g Z\cos^2\theta \tag{5-11}$$

$$\sigma = [\rho_b g Z + W_T]\cos^2\theta \tag{5-12}$$

$$\tau = [\rho_b g Z\cos\theta + W_T]\sin\theta \tag{5-13}$$

$$\rho_b = (1 - M)\rho_m + M\rho_{sat} \tag{5-14}$$

where τ is shear stress, M is the fraction of the soil profile that is saturated, Z is height above bedrock, ρ_w is water density, ρ_m is soil density at field moisture content (unsaturated), ρ_{sat} is saturated soil density, ρ_b is effective bulk soil density, W_T is the vegetative weight per unit area, and θ is the slope angle from horizontal. If $S > \tau$, theoretically the slope is stable to failure.

Cohesion, or bonding of soil particles, depends on soil composition. Selby (1993) discusses the strength of bonds in soils. Chemical bonds may occur through cementation (*e.g.*, precipitation of calcium carbonate), and can provide great strength to the system (10^4 to 10^5 kPa). Electrostatic bonds are restricted to clay particles, with soil strength of $< 10^3$ kPa. Apparent cohesion from capillary forces is most important in unsaturated silts and sands, with a strength of < 400 kPa. Apparent cohesion due to root networks typically falls in the range of 1 to 12 kPa (Selby, 1993).

Soil texture also affects soil shear strength through the effective friction angle ϕ'. The friction angle is 26 to 30° for pure quartz and many clay particles have friction angles about 13° (Selby, 1993). Heterogeneity, volume of voids, and particle size distribution has a greater effect on friction angle than minerology in soils, however (Selby, 1993). Uniform soils with large particles

(gravels) tend to have larger friction angles than uniform soils with finer particles, and the friction angle tends to increase as the particle-size distribution widens (Lambe and Whitman, 1969). Soils with angular particles also have greater friction angles, by a few degrees, than comparable soils with rounded particles (Lambe and Whitman, 1969). Particles tend to become rounded through working with water, thus æolian soils typical of YM tend to have angular particles. Typical friction angles for sands and sandy gravels are in the range of 30 to 40°.

For conditions at YM over a glacial cycle, cohesion under the saturated conditions leading to soil stability failure will probably be dominated by plant roots. Although cohesion within carbonate-precipitate zones would be far larger than any apparent cohesion due to root networks, carbonate precipitation on YM hillslopes and ridgetops primarily appears on and within bedrock, rather than with in the soil column. Carbonates are not apparent in cursory examinations of the soil columns at future-climate analog sites.

The factor of safety (S/τ) for slope stability under saturated conditions is presented in Figure 5-2 for several combinations of soil thickness and cohesion. It is assumed for all cases that the soil is saturated, porosity is 0.4, the friction angle is 35°, and particle density is 2.6 gm/cm^3. The cohesion provided by root networks is clearly important in maintaining slope stability for shallow soils, but is almost negligible for deeper soils.

Creep is often considered viscous film flow. For a viscous film on an incline (Bird et al., 1960),

$$v = \frac{\rho g b^2 \cos\beta}{2\mu}\left[1 - \left(\frac{x}{b}\right)^2\right], \tag{5-15}$$

$$\overline{v} = \frac{\rho g b^2 \cos\beta}{3\mu}, \tag{5-16}$$

$$q = \frac{\rho g b^3 \cos\beta}{3\mu}, \tag{5-17}$$

where v is velocity tangential to the incline [L/T], $\overline{v}$ is mean velocity tangential to the incline [L/T], q is volumetric flux tangential to the incline per unit width [L^3/LT], ρ is bulk density [M/L^3], g is acceleration due to gravity [L/T^2], b is thickness of the layer [L], μ is viscosity of the layer [M/LT], and x is distance below the top of the layer [L]. Typical viscosity values for earth materials are shown in Table 5-1.

Soils are often considered Bingham materials to estimate slope failure (deformation requires a yield stress to be exceeded before deformation occurs as a fluid with constant viscosity). The Bingham model neglects the response of soils to shear stresses below the yield stress, although slow creeping movements generally do occur at these lower stresses. Measured Bingham yield stress

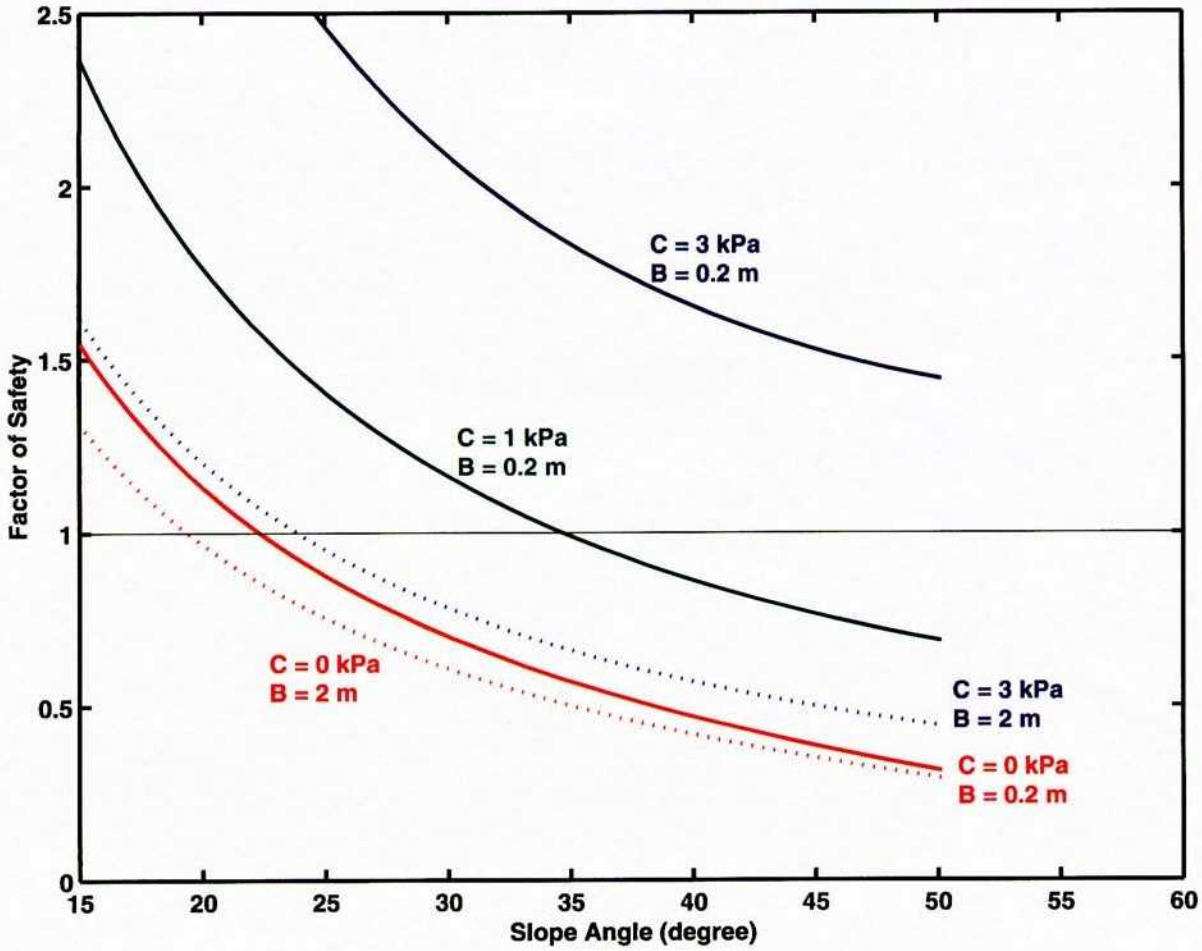

Figure 5-2: Factor of safety for slope failure for soils with thickness 0.2 and 2 m. Cohesions of 0 and 3 kPa are considered for both thicknesses; cohesion of 1 kPa is also shown for the thinner soil. For the thicker soil, plant-root cohesion has little effect on stability, but roots have a significant stabilizing influence for thinner soils.

Table 5-1: Dynamic viscosity (N s/m^2) for typical earth materials [after Selby (1993)].

Earth's mantle	10^{20}	Flowing lava	10^1 to 10^2
Shale	10^{16}	Debris flows	7.5×10^2
Evaporites	10^{13} to 10^{16}	Mudflows	2×10^2 to 6×10^2
Glacier ice	10^{12} to 10^{13}	Solifluction	10^2
Magma	10^2 to 10^3	Water at 20°C	10^{-3}

and viscosity are strongly dependent on moisture content and texture (Ghezzehei and Or, 2000), implying that yield strength and viscosity may both change by several orders of magnitude over the range of environmental conditions experienced in a typical decade.

Mechanical Weathering Weathering can be mechanical or chemical in nature. Mechanical processes tend to operate preferentially on larger particles, as the number of potential fracture planes is proportional to volume. On the other hand, chemical processes are most important on the surface of particles, thus are most important on small particles with large surface area to volume ratios.

Mechanical weathering arises when stresses in the rock are great enough to rupture the rock. Ruptures can occur along fracture planes or grain boundaries. The processes most commonly reported as causing mechanical weathering include expansion during freezing or salt crystallization, unloading after erosion, and expansion during thermal loads such as diurnal fluctuations or fire (Birkeland, 1999).

Relative freeze-thaw activity is amenable to quantification. For freeze-thaw cycling to be effective, liquid water must be present to freeze. Also, soil temperatures must cycle across the freezing point so that water can repeatedly freeze and melt. Neglecting the issue of water availability, the number of times the freezing point is crossed during a year becomes a measure of the relative importance of freeze-thaw activity on mechanical weathering.

The fraction of days with a freeze-thaw cycle can be calculated through Monte-Carlo simulation given the mean temperature, the variance of the daily average deviation from the mean, and the variance of the temperature range. If the two variance variables are assumed normal and correlated, realizations may generated by first sampling one and creating the the other from the first using

$$m_{Y|X} = m_Y + \rho\frac{\sigma_Y}{\sigma_X}(x - m_X) \tag{5-18}$$

$$\sigma^2_{Y|X} = (1 - \rho^2)\sigma^2_Y \tag{5-19}$$

where m represents the mean, σ^2 is the variance, and ρ is the correlation coefficient (Benjamin and Cornell, 1970).

The number of days with a freeze-thaw cycle is bell-shaped as a function of mean temperature, and is centered on 0°C with no correlation between the variance variables. With a positive correlation the peak is shifted below 0, while with a negative correlation the peak is shifted above 0. For reasonable inputs the shifts are only a degree or so. Halving the standard deviation for

daily temperature range halves the fraction of days with freeze-thaw cycles. Doubling the standard deviation for daily average deviation also halves peak, but doubles the spread of the curve and doubles the shift due to the correlation coefficient.

At a depth within the soil column, temperature perturbations decay, with effect of shrinking both standard deviations equally. The net effect would be to keep the same peak but decrease the spread of the curve.

The daily minimum and maximum temperatures for Beatty, NV, over the period from 1948 through 1994 (with several missing intervals), were used to estimate typical statistical parameters. The difference between maximum and minimum temperature varies slightly over the year, with the mean difference (all temperatures in Celsius) having the relationship $\overline{\Delta} = 18.3727 + 2.7465 \sin[\omega(J - 113.2405)]$, where $\overline{\Delta}$ is the mean difference and J is the Julian day of the year. The deviation from the mean is slightly skewed, with a mean of -0.5636 and a standard deviation of 4.

The seasonal mean temperature (the mean of maximum and minimum), $T = 15.5 + 10.8 \sin[\omega(J - 112)]$. A histogram of the deviation from the mean is less skewed than the corresponding temperature-difference case, with a mean of -0.182 and a standard deviation of 3.62. The correlation between daily-mean deviation and temperature-range deviation is 0.241. From this information, assuming normality for both distributions allows calculation of the number of freeze-thaw days and the fraction of time spent at various temperatures over the course of a year.

It is assumed that the decay of the temperature amplitude with depth can be applied to the standard deviations for daily temperature range and daily-mean deviation. Thus, both standard deviations are multiplied by $\exp(-z/D)$, where z is depth below the soil surface, $D = (2k_h/\omega C_h)^{1/2}$, and $\omega = 2\pi/24$ (representing a daily cycle). For typical soils, D for daily perturbations might be about 15 cm.

Typical cases are shown in Figure 5-3, using the standard deviations, correlation coefficient, amplitudes, and offsets determined using the Beatty data set and using 10^6 realizations for each day. Only mean annual temperature (MAT) and depth are varied. Note the peaks in Figure 5-3 correspond to the cases where the peak of either summer or winter has an expected temperature of 0 degree C. The decay of the amplitude of the annual cycle with depth is also considered, tending to bring the peaks towards 0 degree C. Also note that freeze-thaw cycles are rare and shallow (less than 10 cm) with a ground MAT equal to the atmospheric MAT at Desert Rock, NV (17.2 degree C). If soil temperatures were 5 degree C cooler, however, there might be an annual average of 15 freeze-thaw cycles at the ground surface and several cycles even 50 cm deep within the soil profile.

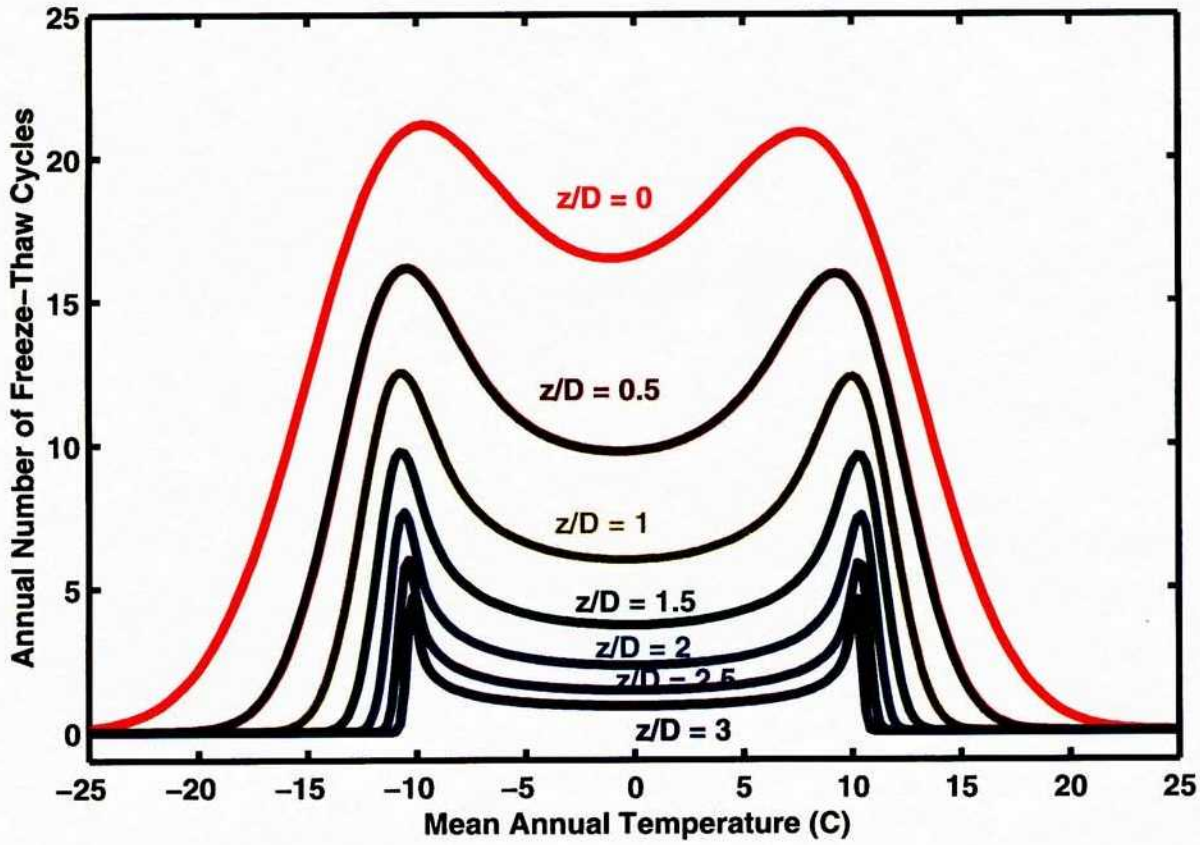

Figure 5-3: Mean number of freeze-thaw cycles as a function of MAT and dimensionless depth below ground surface.

Soil temperatures tend to be higher than air temperatures at YM; north-facing slopes are a few degrees warmer than air temperatures and south-facing slopes are at least four degrees warmer still. Even under glacial conditions it may be that south-facing YM slopes see minimal freeze-thaw activity. Under current conditions, higher elevations would be expected to exhibit significant freeze-thaw. Rainier Mesa, for example, reaches an elevation of roughly 2200 m, which is sufficiently cool that freeze-thaw should be particularly active.

Chemical Weathering Chemical weathering occurs when rocks and minerals are not in equilibrium with the near-surface water. Reactions occur to yield products that are more stable in near-surface environments. In some cases, minerals go into solution without precipitation of other substances. Otherwise, some or all of the ions released by weathering precipitate to form new compounds (*e.g.*, clay compounds), which can cause volume changes that stress the rock and pro-

mote mechanical weathering (Birkeland, 1999). Under present-day arid conditions and relatively coarse soils, chemical weathering is not a significant factor, thus is not considered in the computational model. Chemical weathering would be a more significant factor during wetter portions of the glacial cycle, thus simulations of soil genesis over a glacial cycle may not be able to neglect chemical weathering.

Bedrock Entrainment Bedrock chunks form a significant fraction of the soil column on YM hillslopes, with chunks ranging in size from gravel to tens of centimeters across. Bedrock fracture patterns are a primary determinant of the initial size of entrained chunks. Weathering processes active on soil particles are also active in the near-surface environment.

5.1.2 Computational Soil-Balance Model

For the purposes of landscape evolution, it is impractical to examine transport for every storm. Instead, a range of representative storms can be considered.

The model takes into account erosion and sediment transport due to water movement, as well as soil creep and passive degradation. In light of the uniformity of the æolian sands providing a primary source of particles, the model only accounts for one generic particle size, rather than considering a distribution of particle sizes. Extensions to the model are indicated to consider future conditions, when the soil has weathered into a broader particle distribution.

The model does not directly calculate erosion due to rain splash or long-range transport due to gravity (*i.e.*, boulders rolling downhill). In the current implementation, spatial variability in soil thicknesses arises solely from the variability in surface elevation; all erosion-balance parameters are assumed constant in space due to lack of field calibration data.

The current soil distribution on the ridges and hillslopes is relatively modern, with much of the Holocene soils stripped after the start of the current interglacial period. An important assumption in the modeling is that an equilibrium condition has been reached, at least for the ridges and hillslopes, and there is little remnant soil. An equilibrium condition has also been reached in the wash bottoms; however, alluvial fill and terraces represent a sequence of depositional events that cannot be considered with equilibrium modeling.

The classical approach to modeling colluvium redistribution, as exemplified in a DEM-based model presented by Dietrich et al. (1995), steps through time using a colluvium-diffusion equation.

The current approach, on the other hand, assumes steady-state equilibrium and considers overland sediment flow as well as creep. The soil-balance mathematical model generally follows Beaumont et al. (1992), with the overland flow and erosion models based upon work presented by Woolhiser et al. (1990).

Three equilibrium balance equations are solved to calculate the equilibrium thickness of soil over the YM region; (i) an overall soil mass balance, (ii) a sediment mass balance, and (iii) a hydraulic mass balance or overland-flow (stream) model. The overall mass balance for soil, the first equation, is

$$\nabla \cdot \mathbf{q}_{soil} + Q_{src} + \overline{Q_{str}} = 0, \tag{5-20}$$

where $\mathbf{q}_{soil}$ is the flux of soil, Q_{src} is the source of soil due to bedrock weathering and dust deposition, and $\overline{Q_{str}}$ is the time-averaged flux due to stream or other overland flow action. The erosion-balance model assumes that all processes are at equilibrium. Thus, the stream-flow model assumes that a representative spatially uniform rainfall rate is applied over the entire mountain, and the resulting equilibrium hydraulic flux distribution is used to calculate equilibrium sediment transport. As streamflow is actually highly episodic at YM, the equilibrium sediment-transport velocities and erosion/deposition rates must be adjusted to account for the time with no streamflow. Time averaged stream-action flux is approximated here by

$$\overline{Q_{str}} \approx F_{str} Q_{str}, \tag{5-21}$$

where F_{str} is the fraction of time stream flow occurs. The procedure is likely to under-represent the time average in headwater and overland-flow areas, and over-represent the time average in deep washes and downstream areas.

An improved approach to estimating the effects of overland flow would explicitly calculate the runoff from a series of storms using a model such as implemented in KINEROS (Woolhiser et al., 1990) or WEPP (Flanagan and Nearing, 1995). Runoff from each storm can be treated as an equivalent steady state flow. The maximum overland flow during the storm would provide the equivalent steady flow; the equivalent runoff period is obtained by dividing the total runoff during the storm by the maximum rate. This procedure provides a set of rates and equivalent periods for each grid cell.

Flux of soil, other than through sediment transport, is assumed to occur through viscous creep and is gravity-driven,

$$\mathbf{q}_{soil} = -\frac{\rho g b^3}{3\mu} \nabla Z, \tag{5-22}$$

where b is the thickness of soil, Z is the ground surface elevation, and K is a time-average viscosity (assumed spatially constant here). The soil-flux term is similar to the short-range transport model

used by Beaumont et al. (1992), except that here b is the variable to be determined and Z is constant, while in the Beaumont et al. (1992) application, Z is the variable to be determined and all other variables are assumed constant and lumped into one term.

The creep conductance depends on several factors. Creep is enhanced by moist conditions, particularly when enough dust is present to lubricate flows of larger particles. As root-length densities increase, however, creep is reduced. As the viscosity may vary by orders of magnitude, a time-averaged viscosity is used. In calculating a time-average set of properties, it is important to time-average the reciprocal of viscosity. If the reciprocal of viscosity is time-averaged, infrequent fast events such as slumping dominate creep transport; otherwise, such events are completely neglected.

A simple source term representing weathering is used here. It is assumed that soil protects the bedrock from physical weathering, and weathering decreases exponentially with soil thickness:

$$Q_{wea} = Q_0 \exp(-b/b_0) \tag{5-23}$$

where Q_0 is the source strength, and b_0 represents a weathering-protection soil thickness. The weathering model has two fitting parameters, Q_0 and b_0, which can be used to match observed soil thicknesses. Note that the number of freeze-thaw cycles in a year decays exponentially with depth below ground surface, consistent with the weathering source term. Particles generated from the bedrock are actually chunks of bedrock rather than grains typical of the fine portion of the soil; consideration of particle size distributions is beyond the scope of the work presented here.

The final equilibrium balance equation required to complete the soil-balance system is the water-balance equation,

$$\nabla \cdot \mathbf{q}_w + Q_{rain} = 0, \tag{5-24}$$

where Q_{rain} is the net rainfall. A standard practice in the literature is to use a kinematic-wave approximation for hydraulic flux in conjunction with the Manning hydraulic resistance law, so that (in metric units)

$$\mathbf{q}_w = \frac{S^{1/2} h^{5/3}}{n}, \tag{5-25}$$

where S is the slope and n is Manning's roughness coefficient.

Each of the three balance equations is solved using the same general finite-volume flow-routing approach. The DEM grid is discretized into square boxes, or nodes, with 1D connections to the nearest eight nodes. Taking advantage of the hyperbolic nature of the equations by assuming that upstream variables uniquely determine fluxes to downstream nodes, the nodes in the grid can be processed in order from highest to lowest elevation in one pass.

The water-balance equation is solved independently of the sediment- and soil-balance equations. In the water-balance equation, each node is processed using the algebraic equation,

$$A_i q_{rain} + \sum_{j=up} \frac{w_{ij} h_j^{5/3}}{n} \left(\frac{Z_j - Z_i}{\Delta_{ij}} \right)^{1/2} - \sum_{j=down} \frac{w_{ij} h_i^{5/3}}{n} \left(\frac{Z_i - Z_j}{\Delta_{ij}} \right)^{1/2} = 0, \qquad (5\text{-}26)$$

where node i is the node being processed, node j is a neighboring node, A_i is the area associated with node i, q_{rain} is the rainfall rate minus infiltration, w_{ij} is the width of the 1D connection between nodes i and j, and Δ_{ij} is the distance between nodes i and j. Summing over upstream nodes is denoted by $j = up$, and summing over downstream nodes is denoted by $j = down$. On a square grid with constant node spacing Δ, w_{ij} is $\Delta/2$ for nearest-neighbor connections and $\sqrt{2}\Delta/3$ for diagonal connections.

The sediment- and soil-balance equations are solved simultaneously, by requiring that each nodal soil thickness and sediment concentration is compatible with outflow from the node. The algebraic balance equations are:

$$\sum_{j=up} c_{sj} Q_{wij} - \sum_{j=down} c_{si} Q_{wij} + \frac{A_i}{8} \sum_{j=down} \overline{C_{gij}(c_{eqij} - c_{si})} = 0, \qquad (5\text{-}27)$$

$$\sum_{j=1}^{8} w_{ij} K_{ij} b_{up} \left(\frac{Z_j - Z_i}{\Delta_{ij}} \right) + A_i Q_0 \exp(-b_i/b_0) - \frac{A_i}{8} \sum_{j=down} \overline{C_{gij}(c_{eqij} - c_{si})} = 0, \qquad (5\text{-}28)$$

where b_{up} is the upstream soil thickness. Soil thicknesses are solved by bisection between a minimum thickness of 0 m and a maximum depth (arbitrarily assumed to be 20 m here). The equilibrium sediment concentration is found during each bisection step.

The flow-routing approach works well when there are no local minima in the domain, so that there is a route from every node to the boundary. A physical local minimum cannot exist at equilibrium unless there is a physical mechanism for removing soil (e.g., wind transport). Typically, however, local minima are artifacts of the DEM resolution, as elevations are only reported to the nearest meter. Also, narrow features such as upstream wash channels, which are on the order of a meter wide, cannot be resolved with the DEM grid. About 0.5 percent of the nodes in the DEM are local minima, almost all occurring in wash bottoms but a few occurring along ridgetops. For these minimum nodes, two preprocessing steps were performed to eliminate artificial local minima. First, a small amount of random noise (on the order of a millimeter) was added to each node, essentially eliminating flat spots. Second, nodes forming hollows were filled to create an outflow path. A number of passes were required to eliminate multinode basins.

There are a total of 11 adjustable parameters in the set of coupled balance equations. The 11 parameters, and values found to result in reasonable predictions of soil thicknesses, are shown in

Table 5-2: Adjustable parameters for creating soil-thickness distributions. Base, low, and high values refer to the base case value and values for sensitivity studies.

Name	Symbol	Base	Low	High
Net rainfall rate (cm/hr)	q_{rain}	1	0.2	5
Manning's roughness coefficient (–)	n	0.2	0.05	0.8
Particle diameter (mm)	d	1	0.1	10
Dust deposition rate (cm/ky)	Q_{dust}	2.2	0.733	6.6
Alluvium creep conductance (m/s)	K	10^{-11}	10^{-12}	10^{-10}
Alluvium weathering rate (m^3/m^2)	Q_0	10^{-13}	10^{-14}	10^{-12}
Alluvium weathering depth (cm)	b_0	1	0.33	3
Fraction of time in streamflow (min/100 yr)	F_{str}	300	60	1500
Kinetic coefficient for alluvium scour (s^{-1})	C_g	0.1	–	–
Kinetic coefficient for bedrock scour (s^{-1})	C_g	0.002	–	–
Traction coefficient for sediment equilibrium (s^{-1})	C_s	10^{-3}	–	–
Particle specific gravity (–)	S_s	2.5	–	–

Table 5-2. As F_{str}, K, and Q_0 control the relative importance of stream processes, soil diffusion, and weathering, these three parameters are not completely independent, so scaling the three parameters by the same constant does not modify the predicted soil distribution. The distributions of hydraulic depth, sediment concentration, and soil thickness shown in Figures 5-4 through 5-6, respectively, result from using the adjustable parameters in Table 5-2. A digitized outline of soil, as mapped by Scott and Bonk (1984), is shown in Figure 5-6 for reference. These distributions were generated by selecting representative parameters for the stream flow and sediment transport equations, then adjusting the soil parameters until the soil distribution was in reasonable agreement with the authors' observations of soil thicknesses in trenches and other representative locations in the YM area.

The soil distribution illustrated in Figure 5-6 is quite plausibly rendered, on the whole. The model predicts average thicknesses that are somewhat too large along crestlines and somewhat too shallow near the bottom of some of the side slopes, in part due to not imposing different weathering rates for the Tiva Canyon caprock and the lower Tiva Canyon Member. Headwaters of washes implausibly predict mixtures of deep soil and bare rock, due to the mismatch in resolution between the DEM and the wash channels; however, as the area with bare rock tends to be smaller than the grid size, this mixture does represent the infiltration distribution to some extent.

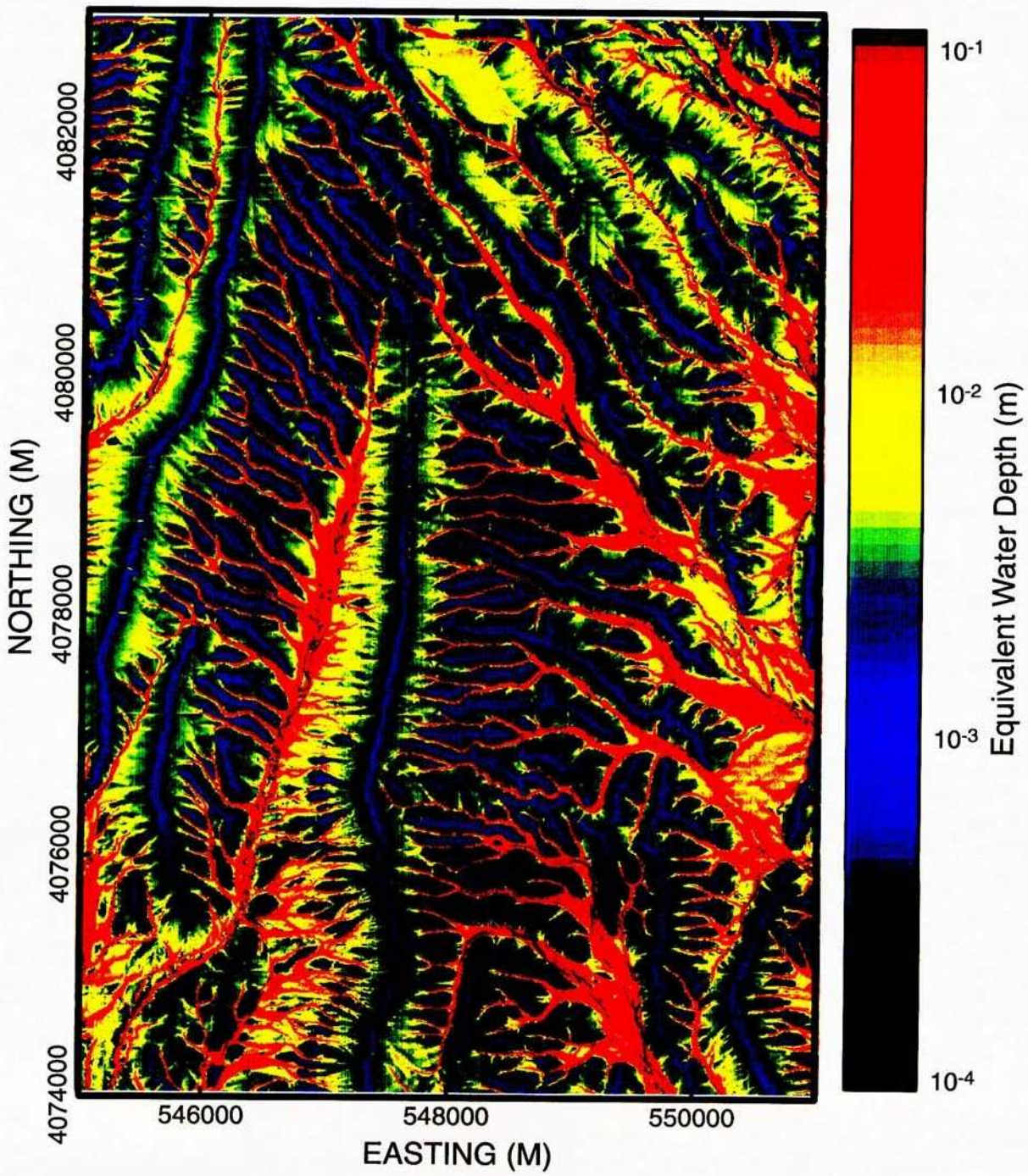

Figure 5-4: Water depth for the equivalent steady state storm using the parameters in Table 5-2.

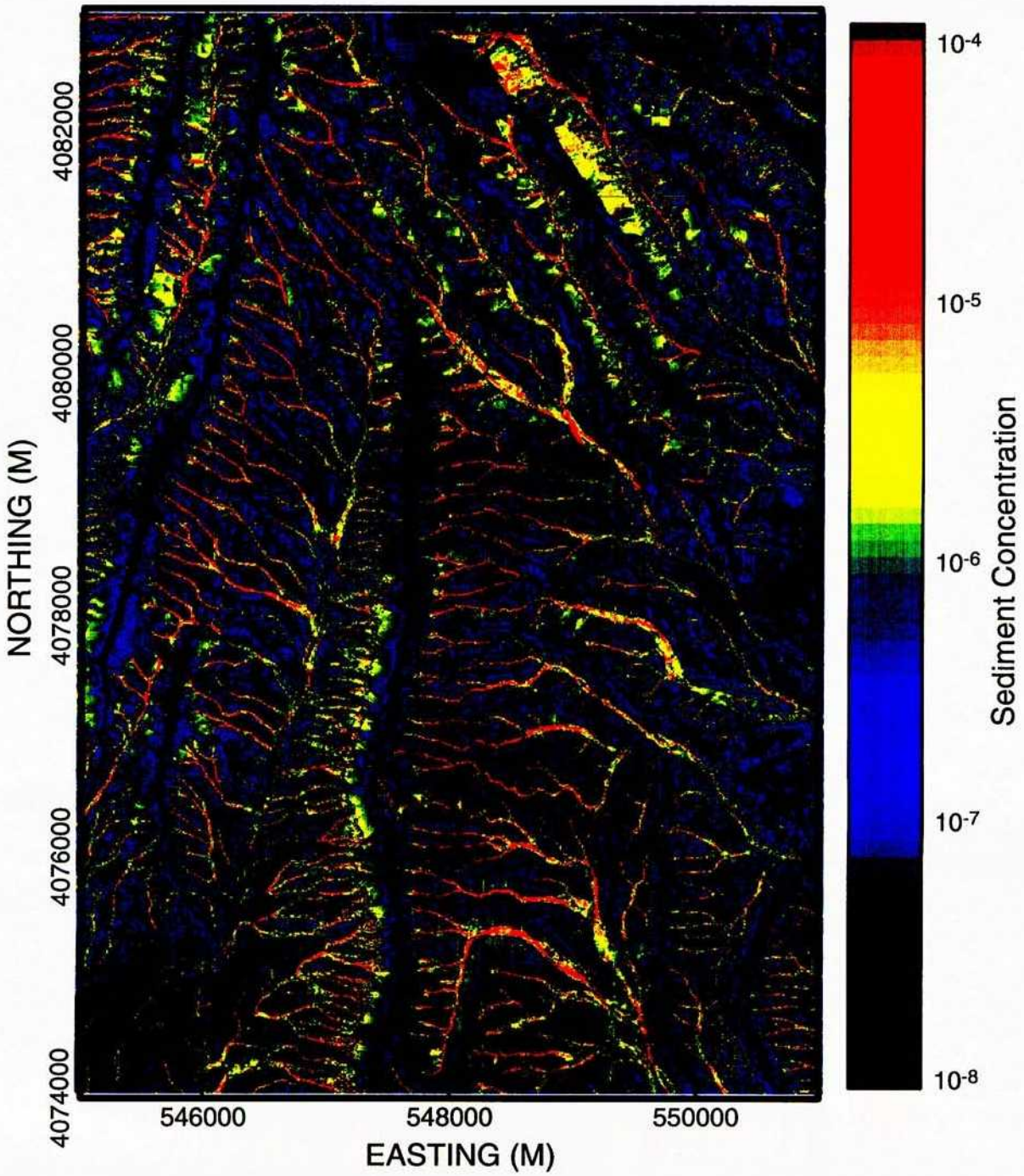

Figure 5-5: Sediment concentration for the equivalent steady state storm using the parameters in Table 5-2.

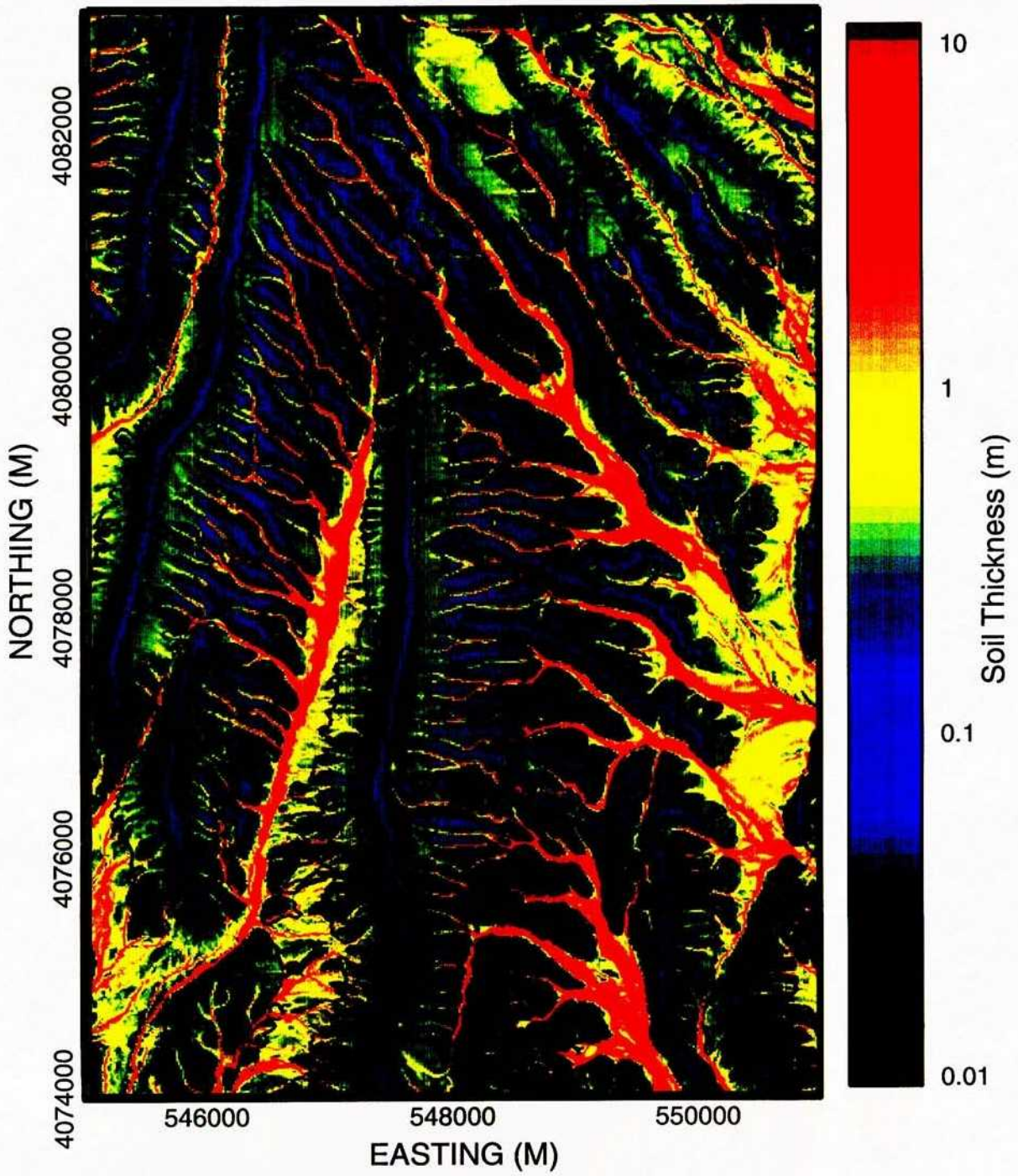

Figure 5-6: Alluvium thickness for the equilibrium system using the parameters in Table 5-2.

The biggest discrepancy between model predictions and the field observations is within the mapped soil outline, as evidenced by predictions of very shallow and very deep soil in adjacent pixels. The root of this discrepancy lies in the inherent dynamism of sediment transport processes in the deeper soil. Surface elevations vary over time as incised channels move around within deep soil, and it is unreasonable to expect that predictions based on equilibrium physics will behave properly when presented with a snapshot of such highly dynamic topography. The difficulty is only exacerbated by the 1-m vertical resolution of the DEM in the relatively horizontal wash bottoms.

Within the mapped soil outline, therefore, a post-processing step is performed to provide more realistic soil thicknesses. A power-law relationship of soil thickness to surface slope was determined by regression,

$$\ln(b) = a_1 + a_2 \ln(s) \tag{5-29}$$

where s is the slope, in degrees, of the ground surface interpolated from the nearest four grid points in the DEM. Depth of soil cover is obtained from geologic logs and sources such as Fernandez et al. (1994) and Flint and Flint (1995). Boreholes with reported covers less than 1 m or slopes greater than 25 degrees are not used. The boreholes can be grouped conveniently into two groups: 28 alluvium boreholes, which lie in alluvium or colluvium but not within an active wash channel; and 9 channel boreholes, where the channel boreholes lie within active wash channels. Regressed coefficients are significantly different for the two groups. For the alluvium boreholes, a_1 and a_2 are found to be 4.31 and -1.09, respectively, with a coefficient of determination of 0.69. For the channel boreholes, a_1 and a_2 are found to be 2.88 and -0.29, respectively, with a coefficient of determination of 0.66. Observations and corresponding regression lines are shown in Figure 5-7.

Wherever the slope is less than 10 degrees within the Scott and Bonk (1984) soil outline, the soil thicknesses were calculated using Equation 11-36; otherwise, the soil-routing model predictions are used. The effect of performing the post-processing is shown in Figure 5-8; this is the base-case soil distribution that will be used to estimate the spatial distribution of mean annual infiltration (MAI) at YM.

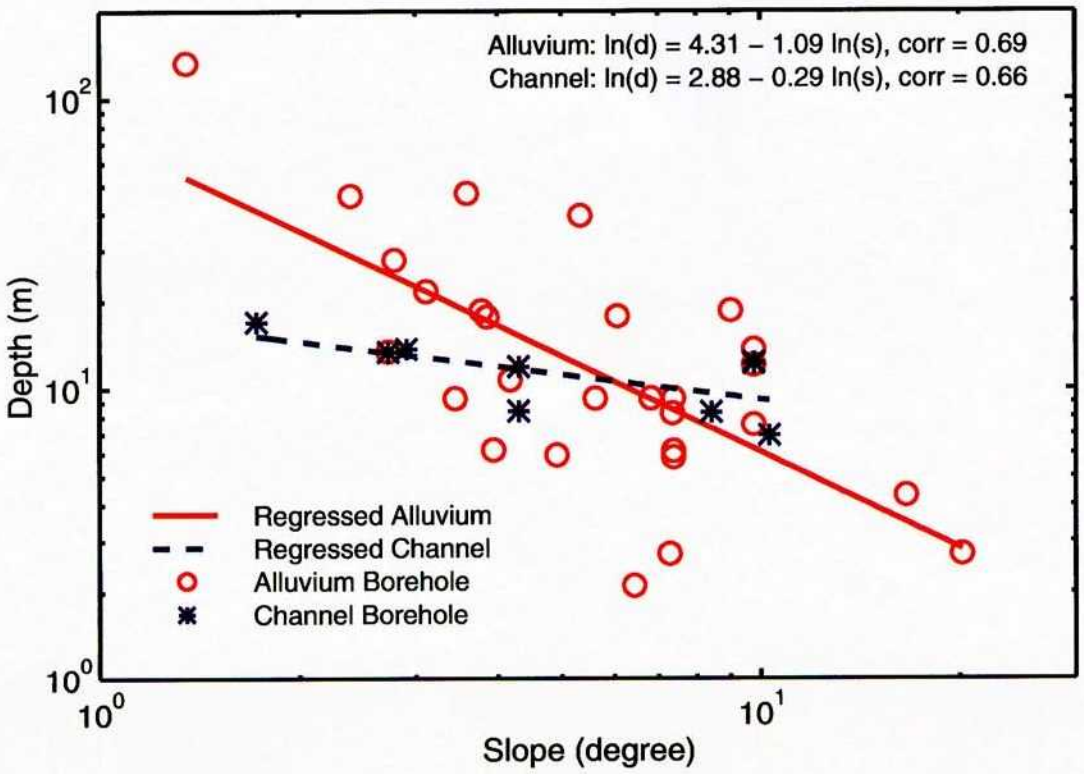

Figure 5-7: Comparison of regression equation for soil thickness with observations for both deep alluvium and channels.

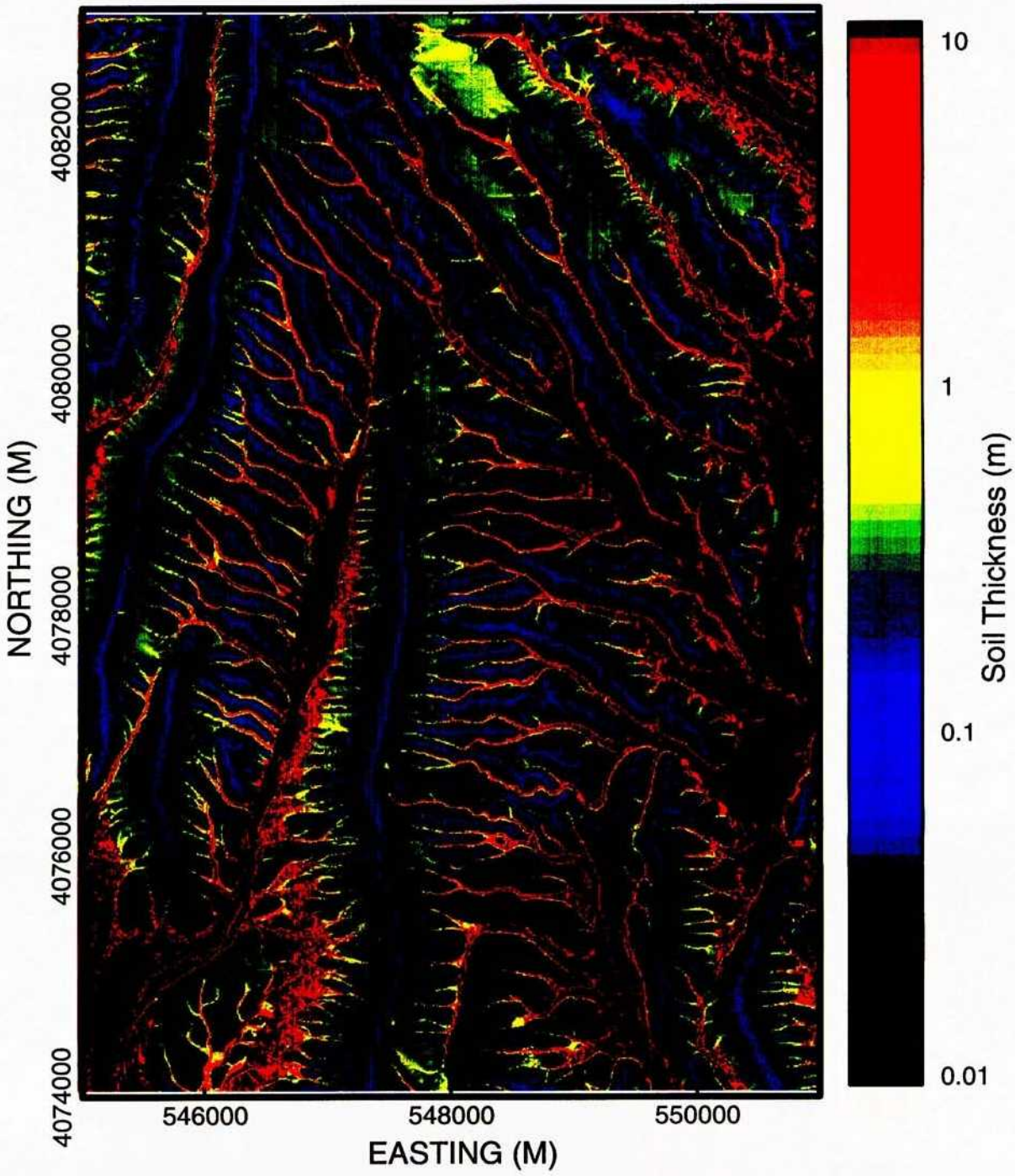

Figure 5-8: Alluvium thickness for the equilibrium system incorporating the deep alluvium regression equation.

5.1.3 Sensitivity to Input Parameters

The calculated distribution of soil thickness depends on the input parameters in a nonlinear way. Several of the most important factors are examined in this section to evaluate sensitivity of the soil thickness distribution to the parameters as well as to evaluate the appropriate range for the parameters. The Split Wash watershed is used as a basis for comparing different simulations, as field work has provided a feel for appropriate soil thickness distributions in this watershed and the scale is fine enough to see subtle differences between distributions. In addition, watershed simulations have been performed on Split Wash (Woolhiser and Fedors, 2000); the soil-thickness distribution used in the simulations was based on earlier results using the computational methods presented here.

The base United States Geological Survey (USGS) DEM used to describe the YM area is at a resolution of 30 m on a side. Fine features such as first-order channels (*e.g.*, roughly a meter wide) cannot be resolved with such a coarse grid. A base computational grid, with grid centers at a 7.5-m interval in both the east-west and north-south directions and 1-ft elevation resolution, was extracted from 10-m contours. Refined grids were obtained by subdividing each grid cell into 4 and 16 subcells, using bilinear interpolation to project elevations into the subcells. The finest grid cell is 1.875 m on a side, beginning to approach the resolution required to capture first-order channels (although the bedrock resolution is still at the 7.5-m scale). Most of the simulations use the single refinement.

Diffusive soil flux is estimated using

$$q = \frac{\rho K b^3}{\mu} \nabla(z_s) \tag{5-30}$$

where z_s is the elevation of the soil surface. The gradient of the soil surface is used to define the slope. The elevation DEM actually defines the top of the soil, but because of the possibility for inconsistencies such as local hollows it is more robust to use the DEM as the bedrock base and build soils above this base. The more-robust technique is used in all simulations reported here. Typically the soils are thin relative to the DEM elevation resolution, so it makes little difference whether the DEM describes the soil surface or bedrock surface. Channels may have sufficiently thick soil that the difference in elevations is a significant source of error, however.

Since the soil surface is unknown *a priori*, iteration is necessary to update the downslope elevations. Each simulation shown here uses 30 iterations to estimate soil thickness, terminating early if mean change within an iteration, Δ, is less than 1 cm. Mean change after 30 iterations is

typically less than 5 cm. Mean change is calculated by

$$\Delta = \left[\frac{1}{N}\sum(b^{i+1} - b^i)^2\right]^{1/2} \tag{5-31}$$

where b^{i+1} and b^i represent soil thickness from two successive iterations and there are N grid cells in the domain.

In the first iteration, the soil thickness distribution calculated from the elevation DEM provides the first estimate of the thickness distribution. In subsequent iterations, large oscillations in soil thickness occur within channels due to the cubic dependence of flux on thickness (ridgetops and hillslopes converge quickly and are essentially unaffected by oscillations). Note that the computational oscillations reflect the dynamic nature of the physical system, as the channel may move around considerably within alluvium-filled wash bottoms, actively cutting, depositing, and changing slope. In order to reduce channel oscillations and speed convergence to an equilibrium, soil thicknesses are only updated by a fraction of the calculated increment for all iterations after the first. Updated thickness is calculated by

$$b^{i+1} = b^i + \alpha_b(b_*^{i+1} - b^i) \tag{5-32}$$

where b_*^{i+1} is the raw thickness calculated using the most recent soil distribution, b^{i+1} is the updated thickness used in subsequent calculations, and α_b is a weighting parameter (0.2 is used in calculations).

The first set of simulations demonstrates the effect of grid refinement. Each simulation uses the same base physical parameters shown in Table 5-2, which provide soil distributions that are reasonably close to observed distributions. The three grids have cell dimensions of 7.5, 3.75, and 1.875 m. The resulting soil-thickness distributions are shown in Figure 5-9, with color coding according to the soil thickness. The identical soil-thickness distributions, color-coded according to the base-10 logarithm of the soil thickness, is shown in Figure 5-10. These two plotting schemes provide complementary information.

Overall soil-thickness patterns are preserved under grid refinement, but features such as channels are thinner and wash bottoms tend to have shallower soils. Features (both physical and nonphysical) can be observed with the finer grids that are less visible in the coarse grid. Herringbone patterns appearing in the broad flat areas on Yucca Crest, for example, may be a nonphysical relic of the original DEM grid. The sharp crest of the west flank of YM also may exhibit stair-stepping due to gridding. Speckling (adjacent patterns of shallow and deep soils) occurs when diffusive processes are small relative to advective processes, such as on steep slopes, and is partially due to amplification of DEM errors.

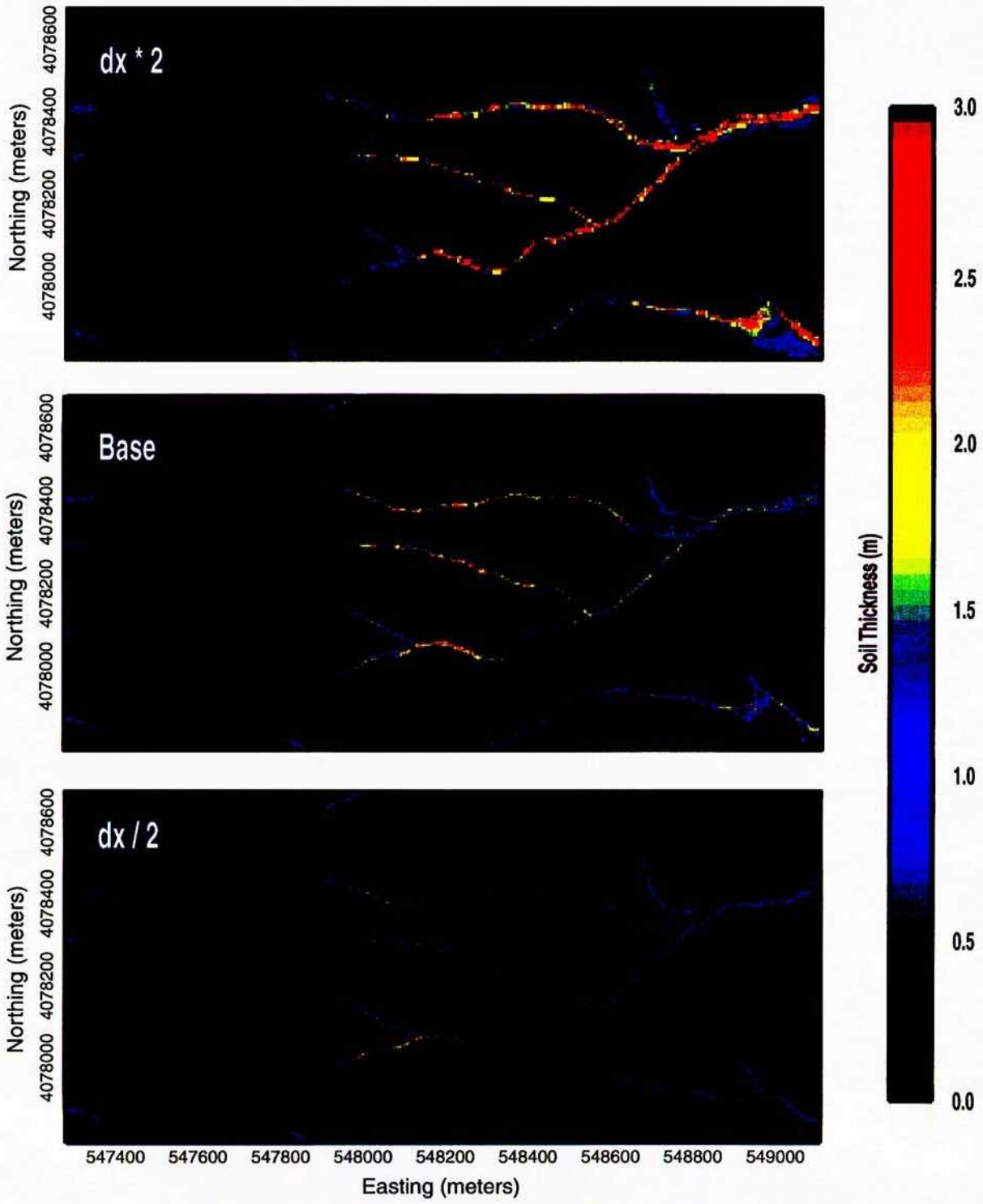

Figure 5-9: Soil thickness for the equilibrium system in Split Wash for the same bedrock grid but 3 different computational grid resolutions. Soil thicknesses are shown in a linear scale.

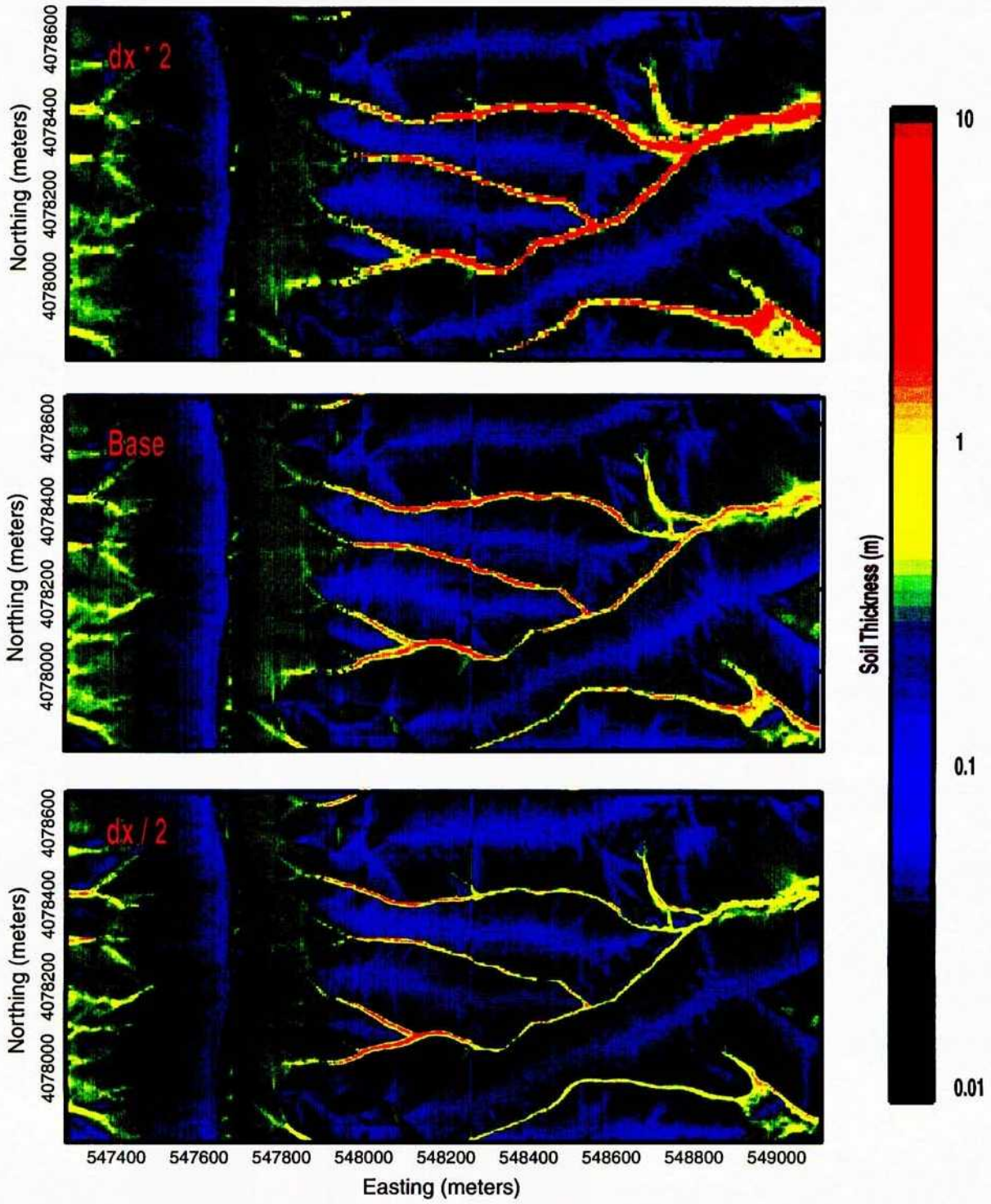

Figure 5-10: Soil thickness for the equilibrium system in Split Wash for the same bedrock grid but 3 different computational grid resolutions. Soil thicknesses are shown in a logarithmic scale.

The impact of different physical constants are shown in a sequence of figures. Each constant is investigated through a sensitivity study, multiplying and dividing the constant by the same factor while holding all other constants at the base value shown in Table 5-2. The grid has 3.75 m sides for all simulations.

Effective soil conductivity mediates the relative importance of creep. When conductivity is increased (viscosity is decreased), soil thicknesses decrease. In order to maintain the same flux, a factor of 8 change in effective soil conductivity should affect soil thickness by about a factor of 2, consistent with the results shown in Figure 5-11.

The base case scenario is not dominated by overland flow, but increases in effective-storm strength (Figure 5-12) or reductions in Manning's n (Figure 5-13) move the system towards a more erosive situation. Portions of the hillslopes are stripped in the more-erosive scenario for both parameters. On the other hand, the less-erosive scenario is relatively similar to the base case for both parameters. Interestingly, the fraction of time that overland flow occurs (Figure 5-14) has a much reduced impact on soil-thickness distributions. The effective soil particle dimension (Figure 5-15) also has little impact.

Dust is far more significant of a source material in the base case than the bedrock. Changing the dust strength by a factor of three has a noticeable impact on distributions (Figure 5-16), while changing the bedrock source strength only affects the shallow soils on ridgetops (not shown). The variability of dust deposition rates over the last glacial cycle implied by the Reheis et al. (1995) data implies that, all else being equal, equilibrium hillslope and ridgetop soil thicknesses may have varied by a significant amount over that period.

5.1.4 Future Conditions

Under wetter and cooler conditions expected for future segments of the glacial cycle, analog sites at higher elevations suggest that vegetation will be larger, have more extensive root systems, and crowns will cover a larger fraction of the ground surface. Observations at several analog sites suggest that the equilibrium system will feature deeper soils and later, long after the onset of cooler conditions, finer textures.

Under these conditions, several factors affecting soil processes will be at least slightly different than at present. The root system will provide cohesion to the soil mass, which will act to decrease the creep conductance (increase viscosity). As the soil texture becomes finer over time, the friction angle decreases, which would tend to increase conductance somewhat. Greater pre-

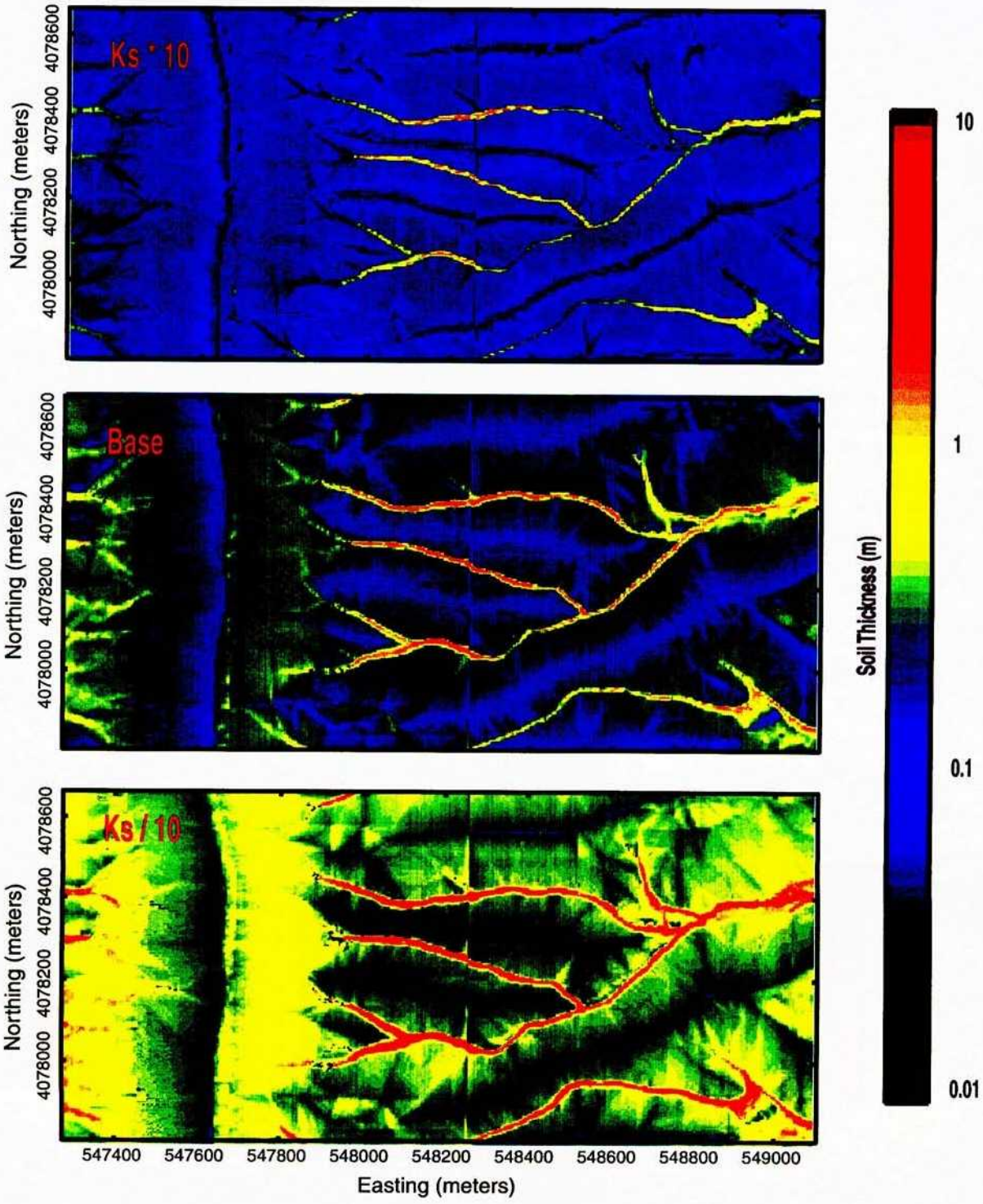

Figure 5-11: Soil thickness for the equilibrium system in Split Wash for 3 different soil creep conductivities (or viscosities). Soil thicknesses are shown in a logarithmic scale.

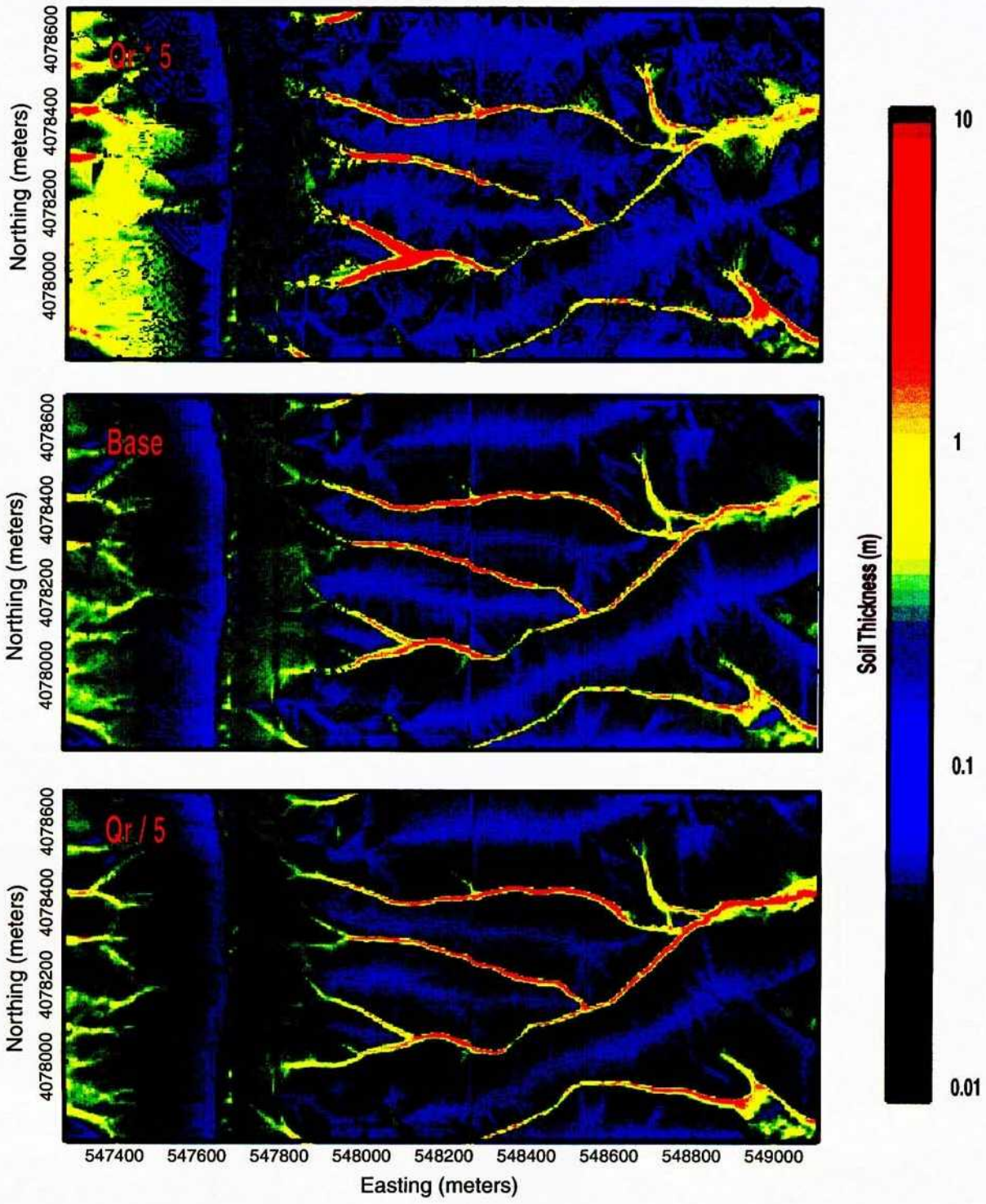

Figure 5-12: Soil thickness for the equilibrium system in Split Wash for 3 different effective rainfall rates. Soil thicknesses are shown in a logarithmic scale.

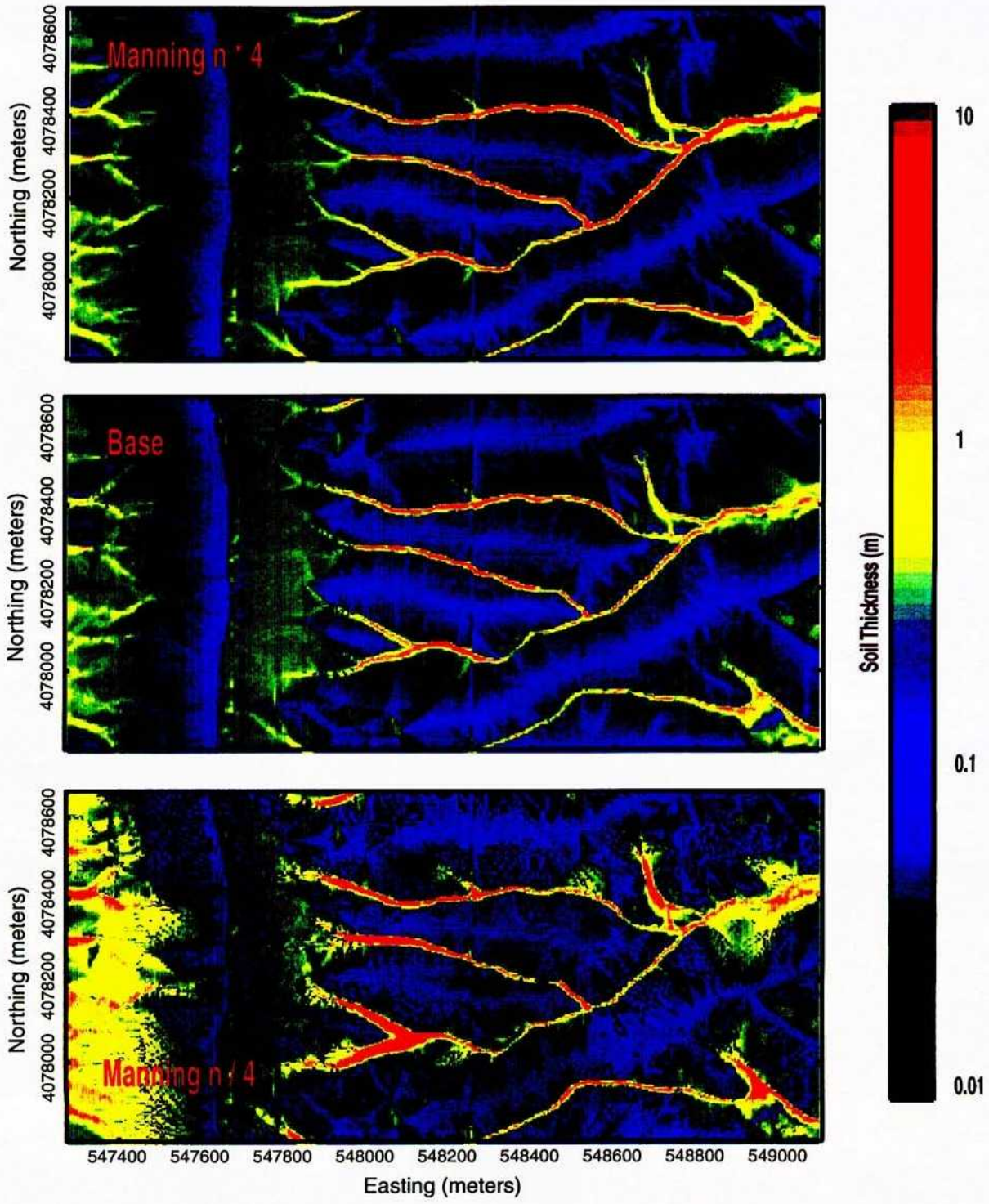

Figure 5-13: Soil thickness for the equilibrium system in Split Wash for 3 different Manning's n. Soil thicknesses are shown in a logarithmic scale.

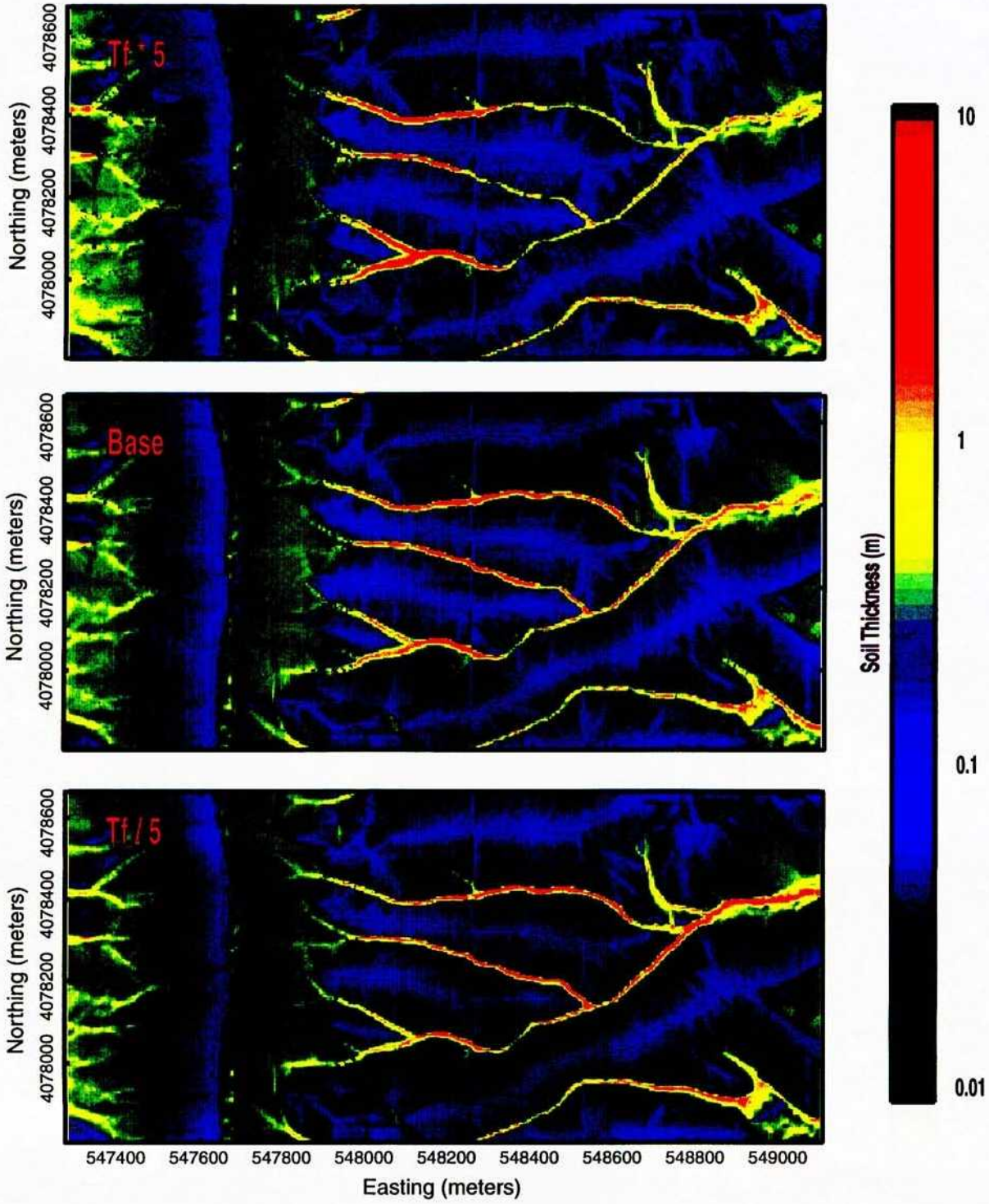

Figure 5-14: Soil thickness for the equilibrium system in Split Wash for 3 different effective streamflow periods (fraction of time streamflow is active). Soil thicknesses are shown in a logarithmic scale.

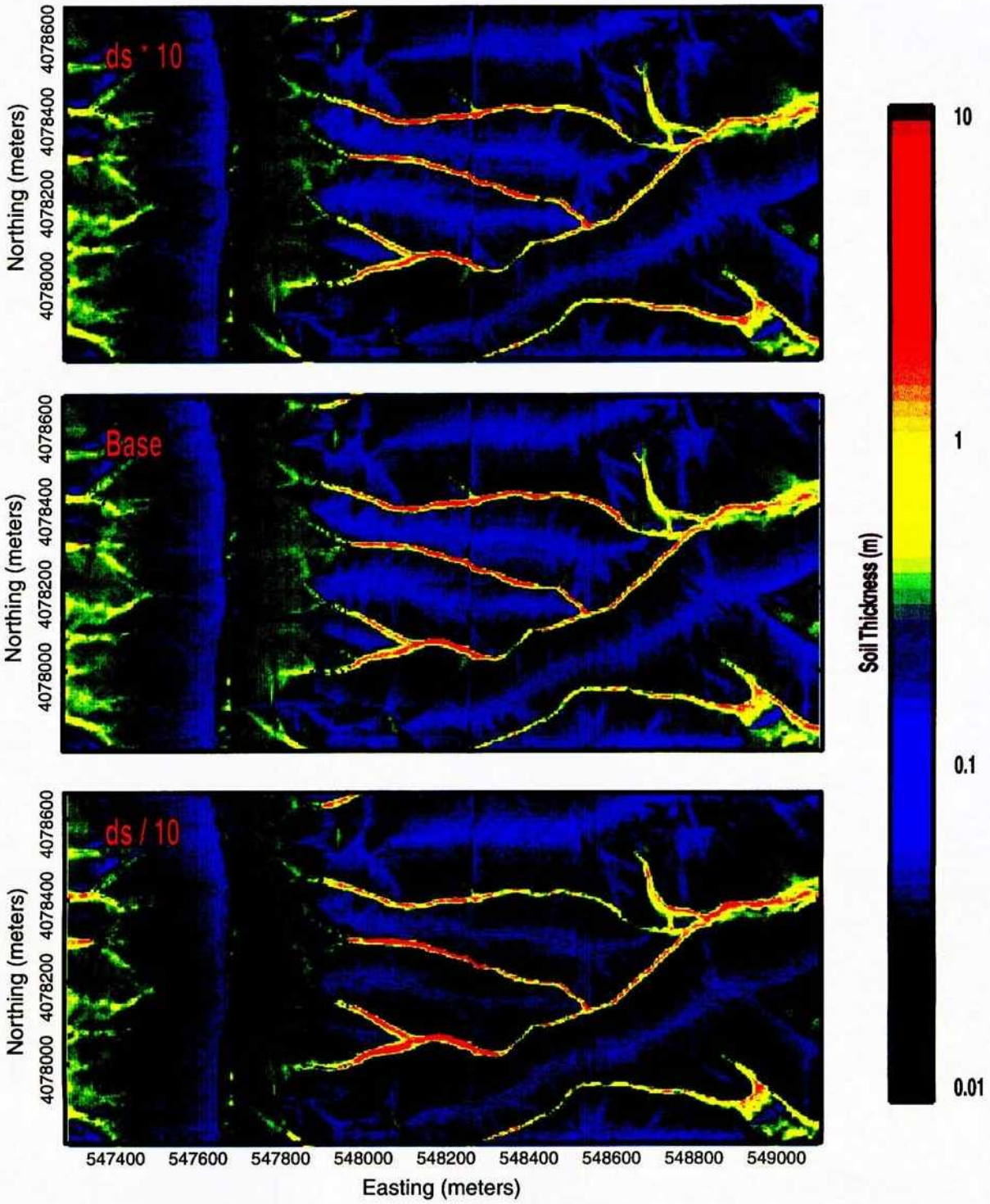

Figure 5-15: Soil thickness for the equilibrium system in Split Wash for 3 different soil particle diameters. Soil thicknesses are shown in a logarithmic scale.

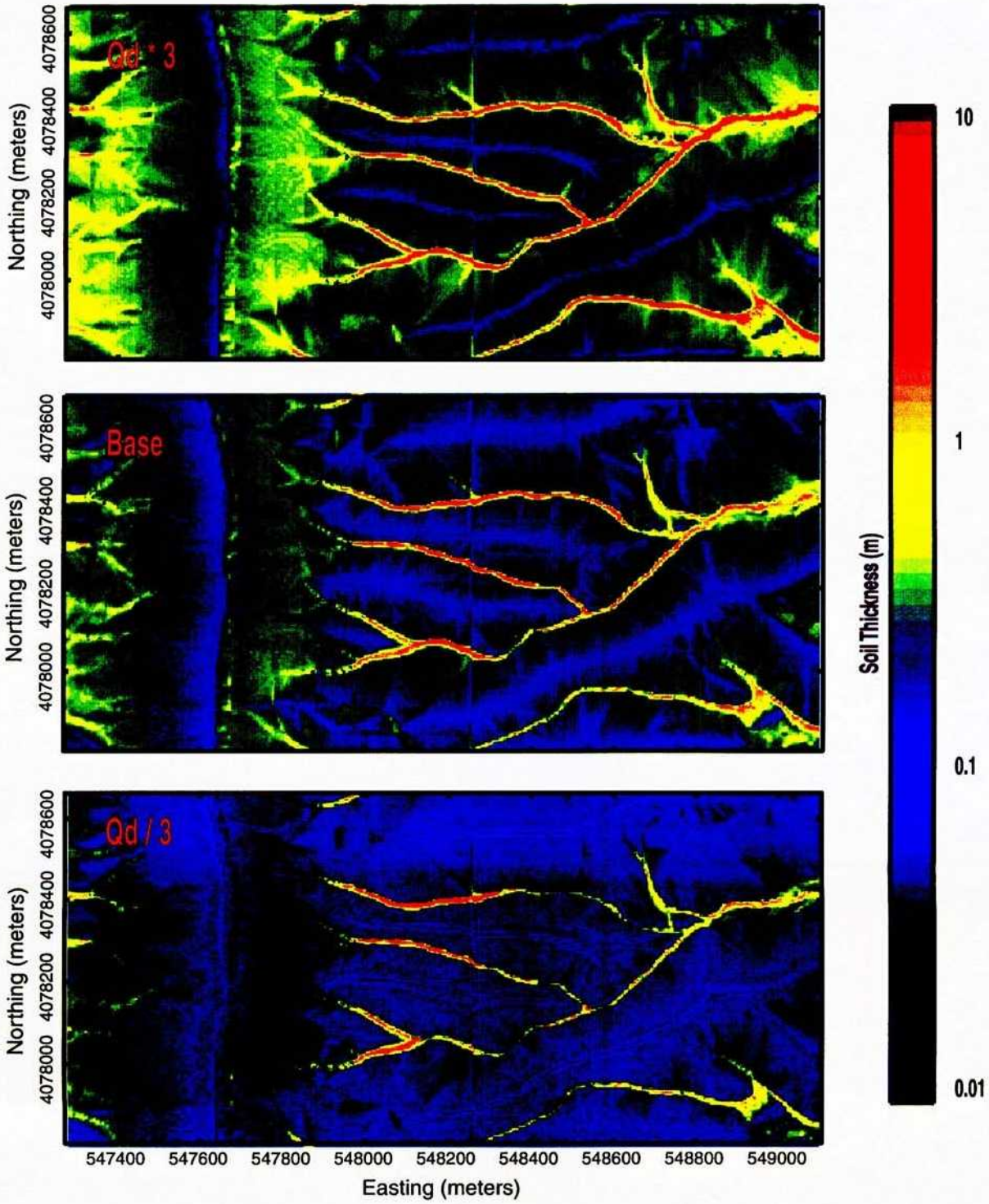

Figure 5-16: Soil thickness for the equilibrium system in Split Wash for 3 different dust deposition rates. Soil thicknesses are shown in a logarithmic scale.

cipitation will occur and storms will be more severe, but the increased crown cover will protect a greater area from erosion from rainsplash and these factors may offset. Atmospheric dust concentrations will likely be reduced as dust sources such as dry playas become wetter, but increased vegetation densities may enhance dust trapping and conditions will be more conducive to bedrock entrainment. All of these factors respond to changes in climatic conditions at different rates, so that the relative importance of each factor may be different for the various segments of a glacial cycle.

Based on the sensitivity studies of model inputs and considerations of possible changes to the input parameters, the most straightforward method for adjusting soil thickness distributions is by changing the soil creep conductance (or soil viscosity). Soil thickness is quite sensitive to conductance, while conductance of earth materials may vary by many orders of magnitude. An order of magnitude increase in viscosity will change soil thicknesses from the present thickness distribution to roughly the distribution observed in Phinney Canyon at an elevation of about 2200 m. Given the limitations of the modeling effort, simply adjusting viscosity provides a reasonable method for generating soil-thickness coverages that can be used to examine the impact on MAI.

References

Ackers, P. and W. R. White. 1973. Sediment Transport: New Approach and Analysis. *Journal of the Hydraulics Division, American Society of Civil Engineers 99*(HY11), 2041–2060.

Beaumont, C., P. Fullsack, and J. Hamilton. 1992. Erosional control of active compressional orogens. In K. R. McClay (Ed.), *Thrust Tectonics*, London, pp. 1–18. Chapman & Hall.

Benjamin, J. R. and C. A. Cornell. 1970. *Probability, Statistics, and Decision for Civil Engineers.* New York, NY: McGraw-Hill.

Bird, R. B., W. E. Stewart, and E. N. Lightfoot. 1960. *Transport Phenomena.* New York, NY: John Wiley & Sons.

Birkeland, P. W. 1999. *Soils and Geomorphology.* Oxford, England: Oxford University Press.

Dietrich, W. E., R. Reiss, M.-L. Hsu, and D. R. Montgomery. 1995. A Process-based Model for Colluvial Soil Depth and Shallow Landsliding Using Digital Elevation Data. In J. D. Kalma and M. Sivapalan (Eds.), *Scale Issues in Hydrological Modelling*, Advances in Hydrological Processes, pp. 141–158. Chichester, England: John Wiley & Sons.

Fair, G. M. and J. C. Geyer. 1954. *Water Supply and Wastewater Disposal.* New York, NY: John Wiley & Sons.

Fernandez, J. A., J. B. Case, C. A. Givens, and B. C. Carney. 1994. *A Strategy to Seal Exploratory Boreholes in Unsaturated Tuff.* SAND93-1184, Sandia National Laboratories, Albuquerque, NM.

Flanagan, D. C. and M. A. Nearing. 1995. *USDA – Water Erosion Prediction Project Hillslope Profile and Watershed Model Documentation.* NSERL Report No. 10, United States Department of Agriculture, Agricultural Research Service, West Lafayette, IN.

Flint, L. E. and A. L. Flint. 1995. *Shallow Infiltration Processes at Yucca Mountain, Nevada–Neutron Logging Data 1984-93.* Water-Resources Investigations Report 95-4035, United States Geological Survey, Denver, CO.

Ghezzehei, T. A. and D. Or. 2000. Dynamics of soil aggregate coalescence governed by capillary and rheological processes. *Water Resources Research 36*(2), 367–379.

Kilinc, M. and E. V. Richardson. 1973. *Mechanics of Soil Erosion From Overland Flow Generated by Simulated Rainfall.* Hydrology Paper 63, Colorado State University, Fort Collins, CO.

Lambe, T. W. and R. V. Whitman. 1969. *Soil Mechanics.* New York, NY: John Wiley & Sons.

Meyer, L. D. and W. H. Wischmeier. 1969. Mathematical Simulation of the Process of Soil Erosion by Water. *Transactions of the American Society of Agricultural Engineers 12*(6), 754–762.

Reheis, M. C., J. C. Goodmacher, J. W. Harden, L. D. McFadden, T. K. Rockwell, R. R. Shroba, J. M. Sowers, and E. M. Taylor. 1995. Quaternary soils and dust deposition in southern Nevada and California. *GSA Bulletin 107*(9), 1003–1022.

Scott, R. B. and J. Bonk. 1984. *Preliminary Geologic Map (1:12,000 scale) of Yucca Mountain, Nye County, Nevada, with Geologic Cross Sections.* Open-File Report 84-494, United States Geological Survey, Denver, CO.

Selby, M. J. 1993. *Hillslope Materials and Processes* (Second ed.). Oxford, England: Oxford University Press.

Sidle, R. C., A. J. Pearce, and C. L. O'Laughlin. 1985. *Hillslope Stability and Land Use.* Geophysical Monograph 42. Washington, DC: American Geophysical Union.

TRW. 1998. *Yucca Mountain Site Description.* B00000000-01717-5700-00019 REV 00, TRW Environmental Safety Systems Inc., Las Vegas, NV.

Woolhiser, D. A. and R. W. Fedors. 2000. *Upper Split Wash Modeling in Support of Shallow Infiltration Estimates.* Letter Report, Center for Nuclear Waste Regulatory Analyses, San Antonio, TX.

Woolhiser, D. A., R. E. Smith, and D. C. Goodrich. 1990. *KINEROS, A Kinematic Runoff and Erosion Model: Documentation and User Manual.* ARS-77, United States Department of Agriculture, Agricultural Research Service.

Yalin, Y. S. 1963. An Expression for Bed-Load Transportation. *Journal of the Hydraulics Division, American Society of Civil Engineers 89*(HY3), 221–250.

Yang, C. T. 1973. Incipient Motion and Sediment Transport. *Journal of the Hydraulics Division, American Society of Civil Engineers 99*(HY10), 1679–1704.

SCIENTIFIC NOTEBOOK

by

Stuart A. Stothoff

Southwest Research Institute
Center for Nuclear Waste Regulatory Analyses
San Antonio, Texas

September 4, 2003

Initial Entries

Scientific NoteBook: # 163 E

Issued to: S. A. Stothoff

Issue Date: Tuesday, November 16, 1993

By agreement with the CNWRA QA this NoteBook is to be printed at approximate quarterly intervals. This computerized Scientific NoteBook is intended to address the criteria of CNWRA QAP–001.

The scientific notebook number was changed from 163 to 163 E on October 4, 2000, to conform to changed CNWRA nomenclature. No entries were modified in the changeover.

Table 0-1: Computing Equipment

Machine Name	Type	OS	Location	Current
dimension	Dell Dimension	Windows 98	desk	yes
inspiron	Dell Inspiron	Windows 98	desk	yes
latitude	Dell Latitude	Windows 95	desk	yes
sierra.cnwra.swri.edu	Sun SPARC 20	Solaris	desk	yes
sisyphus.cnwra.swri.edu	Sun SPARC 20	SUNOS 4.1.3_U1	network	no
dopey.cnwra.swri.edu	Sun SPARC 10	SUNOS 4.1.3_U1	network	no
performer.cnwra.swri.edu	SGI Onyx	IRIX 5.3	network	no
yosemite.cnwra.swri.edu	SGI Onyx	IRIX 5.3	network	no
bemore.cnwra.swri.edu	SGI Onyx	IRIX 6.2	network	no
redwood.cnwra.swri.edu	SGI Indy	IRIX 6.2	network	no
bigbend.cnwra.swri.edu	Sun Ultra-2	SUNOS 5.5.1	network	no
scratchy1.cnwra.swri.edu	Sun Ultra-2	SUNOS 5.5.1	network	no
hornet.cnwra.swri.edu	Sun Ultra-2	SUNOS 5.5.1	network	no

Contents

List of Figures

List of Tables

6 Ambient Hydrology KTI – Major Report Bedrock Synthesis

Account Number: **20-5708-861**
Collaborators: **Randy Fedors**

Objective:

8/29/00 Input to Major Milestone.

Over a period of several months, I wrote up results and inferences in the form of sections of chapters intended to summarize major findings of the infiltration studies over the past few years. Most of the information represents synthesis work, thus it has not been documented along the way. Substantially complete sections are included here, with the numbering scheme used in the original document. These sections represent the working document before formatting as a WordPerfect file and undergoing any CNWRA review.

The bedrock section is included starting here. The original numbering started with section 3, subsection 2, and subsubsection 1.

6.1 BEDROCK HYDRAULIC PROPERTIES

Hydraulic properties of the bedrock units are important in estimating mean annual infiltration (MAI) above the repository block, which is typically characterized by shallow soil above bedrock. Department of Energy (DOE) estimates of Yucca Mountain (YM) hydraulic properties are primarily based upon (i) core-sample data (Flint and Flint, 1990; Flint et al., 1996b; Flint, 1998) and (ii) inversion of mountain-scale simulations (Bodvarsson and Bandurraga, 1996; Bodvarsson et al., 1997). For infiltration estimates, the scale of interest is intermediate between these two extremes. Typical one-dimensional (1D) simulations providing inputs for Performance Assessment (PA) exercises conceptually represent grid cells that are roughly 1 to 30 meters on a side. Core samples with K_{sat} measurements are 5 cm in length and 2.5 cm in diameter; moisture-retention properties are measured on subsamples that are 1 cm in length and 2.5 cm in diameter. The inversion process for mountain-scale properties assumes homogeneous material properties for each geologic unit; the influence of local variability in properties is lost through averaging. Rock properties at the infiltration scale are better estimated through formal upscaling of core sample data. Accordingly, the data

set of core samples used by Flint (1998) was acquired and used to provide independent estimates of bedrock properties.

Flint (1998) used a strategy of classifying the core samples into microfractured, zeolitic, and vitric/crystallized categories. The estimates of hydraulically important matrix properties (saturated hydraulic conductivity, K_{sat}, and retention properties) are expensive and time-consuming to measure, thus these properties were correlated to properties that were easier to measure (*e.g.*, porosity). Bedrock properties were estimated independently for each category. One difficulty with the strategy of splitting into categories is that alteration is not easily assessed and there are differing degrees of alteration.

The microfractured category has samples from vitrophyres assigned to it (*i.e.*, Ttrv1 and Ttrv3 from the Topopah Spring Tuff). The microfractured category reportedly includes the TC and PV3 hydrogeologic units. In addition, one sample each from the crystallized and welded Ttrn, Ttpul, and Ttpln units is assigned to the microfractured category due to visible microfractures.

The altered category includes all lithostratigraphic units below the vitric/zeolitic boundary (BT1, CHZ, BT, PP4, PP3, PP2, PP1, BF3, and BF2) plus the CMW (an altered portion at the base of the Tiva Canyon formation). As Flint (1998) notes, there are crystallized and vitric units within the "altered" category, but the assignment was done for simplicity in developing predictive equations.

The vitric/crystallized category includes everything left over after the other categories are considered.

An alternative approach is used here that uses the measured properties of all the core measurements without explicit regard to alteration in order to provide regressions for mean properties in terms of properties measured for all samples. Further, the statistical properties of the core samples are used in Monte-Carlo analysis to estimate the mean of the underlying statistical distributions, rather than the mean of the sampled cores.

6.1.1 Analysis procedure

The analysis approach consists of several components. Linear and nonlinear regression analysis is used to relate under-sampled parameters (K_{sat} and retention properties) to parameters sampled for every core, with estimates of the uncertainty in the regression parameters. The statistical distribution of the well-sampled parameters is obtained, including estimates of the uncertainty in

the parameters. The most-likely value of the under-sampled parameters is obtained through Monte-Carlo simulation based on the expected value for the uncertain statistical descriptions. Finally, the uncertainty in the under-sampled parameters is obtained through two nested levels of Monte-Carlo simulation: (i) simulations of the statistical parameters, and (ii) simulations of the distributions based on the sampled statistical parameters. The mathematical basis for this approach is presented in this section.

Linear regression procedure Regression analysis is commonly used when two or more variables have a linear relationship subject to random components (Mason et al., 1989). A general statement of the linear relationship is

$$y_i = \beta_0 + \sum_j^N \beta_j x_{ji} + e_i \tag{6-1}$$

where y_i is the ith observation of the response variable, x_{ji} is the ith observation of predictor variable j, β_0 is the actual intercept of the relationship, β_j is the actual slope of the relationship for predictor variable j, e_i is a random error component, and there are N predictor variables.

The fitted regression model provides $\hat{y}$, an estimate of y

$$\hat{y} = b_0 + \sum_j^N b_j x_j \tag{6-2}$$

where the b values are estimators for the corresponding β values.

Denoting the residual between predicted and observed values for y_i as r_i, the sum of squared residuals, SSE, is

$$\text{SSE} = \sum r_i^2 = \sum \left(y_i - b_0 - \sum_j^N b_j x_{ji} \right)^2 \tag{6-3}$$

Least-squares analysis obtains values for the b values that minimize SSE. In matrix form, the multiple linear regression model can be written

$$\mathbf{y} = \mathbf{X}\beta + \mathbf{e} \tag{6-4}$$

$$\mathbf{X} = \begin{bmatrix} 1 & x_{11} & x_{12} & \cdots & x_{1N} \\ 1 & x_{21} & x_{22} & \cdots & x_{2N} \\ \vdots & \vdots & \vdots & & \vdots \\ 1 & x_{i1} & x_{i2} & \cdots & x_{iN} \\ \vdots & \vdots & \vdots & & \vdots \\ 1 & x_{n1} & x_{n2} & \cdots & x_{nN} \end{bmatrix} \tag{6-5}$$

where $\mathbf{y}$, β, and $\mathbf{e}$ are vectors corresponding to y_i, β_j, and e_i, respectively. The normal least-squares equations are written

$$\mathbf{X}^T\mathbf{y} = \mathbf{X}^T\mathbf{X}\mathbf{b} \tag{6-6}$$

yielding the least-squares estimators $\mathbf{b}$

$$\mathbf{b} = (\mathbf{X}^T\mathbf{X})^{-1}\mathbf{X}^T\mathbf{y} \tag{6-7}$$

where superscripts -1 and T represent a matrix inverse and a matrix transpose, respectively. The sample covariance values are (Lapin, 1983)

$$S^2_{Y\cdot 12} = \frac{\text{SSE}}{n-m}(\mathbf{X}^T\mathbf{X})^{-1} \tag{6-8}$$

where there are m coefficients being determined. The standard error for each regression coefficient β_j is the square root of the corresponding diagonal element in $S^2_{Y\cdot 12}$. The standard error is a measure of the uncertainty regarding β_j.

For one predictor variable (Benjamin and Cornell, 1970),

$$b_0 = \overline{y} - b_1\overline{x} \tag{6-9}$$

$$b_1 = S_{xy}/S_{xx} \tag{6-10}$$

$$S_{xy} = \frac{\sum(y_i - \overline{y})(x_i - \overline{x})}{n-1} \tag{6-11}$$

$$S_{xx} = \frac{\sum(x_i - \overline{x})^2}{n-1} \tag{6-12}$$

$$\overline{x} = \frac{\sum x_i}{n} \tag{6-13}$$

$$\sigma^2_{b0} = \frac{\sigma^2}{n}\left(1 + \frac{\overline{x}^2}{S^2_{xx}}\right) \tag{6-14}$$

$$\sigma^2_{b1} = \frac{\sigma^2}{nS^2_{xx}} \tag{6-15}$$

where an overbar denotes sample mean and σ^2 is variance about the regression line.

Nonlinear regression procedure When the functional form to be regressed is not easily expressible as a linear sum, nonlinear regression is necessary. For example, nonlinear regression is used to estimate retention parameters. In this case, the parameters b_k that provide a minimum to

$$\text{SSE} = \sum\left(y_i - f(b_k, x_{ji})\right)^2 \tag{6-16}$$

are sought. Unconstrained minimization by adjusting the b_k parameters is used to find the minimum SSE.

Inferences regarding the coefficients are evaluated similarly to inferences with linear regression, except that each x_{ij} entry in the $\mathbf{X}$ matrix is replaced with

$$w_{ir} = \frac{\partial f(x_{ij}, \beta_k)}{\partial \beta_r} \qquad r = 0, 1, \ldots, q \tag{6-17}$$

where the partial derivatives are evaluated using the nonlinear estimates $b_0, b_1, \ldots, b_q$ (Mason et al., 1989).

Censored samples Certain parameters are only observed within a certain range due to observation limitations. For example, K_{sat} is only observed at values above 5×10^{-12} m/s due to mechanical constraints. The observations at the limit of the range are censored, but represent valuable information. In such cases, the censored observations are used at the limiting value. This procedure biases the sample mean and reduces the sample variance relative to the actual underlying distribution; however, neglect of the censored values would bias the sample statistics to an even greater extent.

Realizations of undersampled parameters One goal of the core-sample analysis is to examine the equivalent bulk properties of the matrix using many realizations while accounting for the uncertainty and variability of the core sample properties. This is accomplished in the following steps

- Create a realization for the correlation matrix between the core-sample properties used to estimate the matrix properties of interest
- Generate the number of core-sample realizations corresponding to the scale of interest and estimate the equivalent matrix properties
- Repeat to build up an estimate of the variability and uncertainty in the equivalent matrix properties
- Regress a relationship describing the equivalent bulk matrix properties

Matrix properties of interest include porosity, K_{sat}, and retention properties.

Correlated matrix properties can be generated through the lag-0/lag-1 expression by Matalas (1967), simplified to the lag-0 expression

$$\delta = \mathbf{B}\epsilon \tag{6-18}$$

$$\mathbf{B}\mathbf{B}^T = \mathbf{C} \tag{6-19}$$

where δ is a vector of random deviations from zero, ϵ is a random impulse drawn from a normal distribution with zero mean and unit variance, and the **C** matrix is the covariance matrix for the variables.

Following a procedure suggested by Bras and Rodríguez-Iturbe (1993), the **B** matrix can be obtained from **C** by defining two matrices **P** and **E** such that

$$\mathbf{CP} = \mathbf{PE} \tag{6-20}$$

$$\mathbf{P}^T\mathbf{P} = \mathbf{P}\mathbf{P}^T = \mathbf{I} \tag{6-21}$$

where **E** is a diagonal matrix of eigenvalues and **I** is the identity matrix. The **B** matrix can be decomposed through

$$\mathbf{C} = \mathbf{P}\mathbf{E}\mathbf{P}^{-1} = \mathbf{B}\mathbf{B}^T \tag{6-22}$$

yielding

$$\mathbf{B} = \mathbf{P}\mathbf{E}^{1/2} \tag{6-23}$$

Realizations are recovered from the deviation variable δ by taking into account the mean,

$$\mathbf{v} = \delta + \mathbf{m} \tag{6-24}$$

where **v** is the vector of variables and **m** is the corresponding mean value. Realizations with one or more variables falling outside a bounding range are discarded and resampled, yielding a truncated distribution.

When a variable is normally or lognormally distributed, realizations of the variable are straightforwardly evaluated. When a variable is skewed but not lognormal, an approximation is adopted that maps the variable into a normal distribution through the cumulative density function (CDF). A CDF is constructed based on the sample parameters, with corresponding probability values mapped to the CDF for a standardized normal distribution. For example, the value of the sample-distribution variable with a CDF of 0.5 is mapped to the normal-distribution CDF value of 0.5, with a standardized variable of 0. Estimates of covariances are made using the transformed variable. Realizations of the transformed variable are inverted to the original distribution using the same approach. This procedure preserves the mean and covariance of the transformed variables, although there may be bias in untransformed variables.

Numerical experimentation suggests that the mean and covariance structure of both the raw and transformed variables are captured through this procedure even for skewed distributions, although many realizations (at least 10^5) are necessary to recover input statistics for the raw variables.

In the work reported here, each distribution is tabulated with 500 entries between 6 standard deviations above and below the mean. Cubic splines are used to interpolate between entries. Using table lookup is an approach that applies to quite general statistical distributions.

Uncertainty in sample descriptors Estimates of material properties are based on a limited number of core-sample observations. Although the expected value of sample descriptors (*e.g.*, mean, variance) is the same as the actual value of the underlying process (except in censored distributions), sample descriptors rarely match the expected value due to limited observation. Sample descriptors are themselves random variables, with distributions that are amenable to statistical description.

Uncertainty in the value of the sample mean is usually assumed to be normally distributed with mean μ and variance σ^2/n, where μ and σ^2 are the mean and variance of the underlying distribution and there are n observations (Benjamin and Cornell, 1970). Uncertainty about the sample mean relative to the actual mean is described using the Student t distribution,

$$t = \frac{\overline{X} - \mu}{s/n^{1/2}} \tag{6-25}$$

where $\overline{X}$ is the sample mean and s^2 is the sample variance. The Student t distribution reduces to the normal distribution when $n > 30$. Uncertainty about the true mean decays as the square root of the number of samples.

Assuming that the sample sizes are sufficiently large, realizations of the z statistic (zero-mean, unit variance normal distribution) are used to characterize the uncertainty of μ. Given z_i, a realization of z, the corresponding realization of μ is

$$m_i = \overline{X} - \frac{sz_i}{n^{1/2}} \tag{6-26}$$

and the realization of X is

$$X_i = \overline{X} - sz_i[n/(n-1)]^{1/2} \approx \overline{X} - sz_i \tag{6-27}$$

Sample variance is generally assumed to have a χ^2 distribution, where

$$\chi^2 = \frac{(n-1)s^2}{\sigma^2} \tag{6-28}$$

where $\mathrm{E}[\chi^2] = n - 1$ and $\mathrm{Var}[\chi^2] = 2(n-1)$. As with the sample mean, the normal distribution is used to approximate the χ^2 distribution when $n > 30$,

$$z = \frac{\chi^2 - (n-1)}{[2(n-1)]^{1/2}} \tag{6-29}$$

Uncertainty about the true variance decays as the square root of the number of samples. The estimate of σ^2 given a realization of z is

$$s_i^2 = \frac{(n-1)s^2}{n-1+[2(n-1)]^{1/2}z_i} \tag{6-30}$$

The correlation ρ between two random variables x and y is estimated using (Lapin, 1983)

$$r = \frac{s_{xy}}{s_x s_y} = \frac{\sum xy - (1/n)\sum x \sum y}{s_x s_y} \tag{6-31}$$

where r is the sample correlation coefficient. Transforming the distribution using Fisher's Z,

$$Z = \tanh^{-1} r = \frac{1}{2}\ln\left(\frac{1+r}{1-r}\right) \tag{6-32}$$

the expected value and standard error of Z are

$$\mu_Z = \frac{1}{2}\ln\left(\frac{1+\rho}{1-\rho}\right) \tag{6-33}$$

$$\sigma_Z = (n-3)^{-1/2} \tag{6-34}$$

Given a realization of Z, the corresponding value of ρ is

$$r_i = \tanh\left[\frac{1}{2}\ln\left(\frac{1+r}{1-r}\right) + \frac{Z_i}{(n-3)^{1/2}}\right] \tag{6-35}$$

Realizations from uncertain distributions The aim of the analysis is to generate many realizations of under-sampled parameters by using a regression equation together with many realizations of well-sampled parameters. For example, K_{sat} might be an under-sampled parameter that is estimated with a regression equation based on a well-sampled parameter such as porosity. Sources of uncertainty include characteration of the statistical properties of the well-sampled parameters and characterization of the regression parameters. The approach adopted here is to sample the uncertain statistical parameters and, for each sampling, use Monte-Carlo simulation given the parameters to estimate many realizations of the variable parameters using the approach in Section 6.1.1.

Uncertain statistical parameters are evaluated building upon the methods described in Sections 6.1.1 and 6.1.1. In order to generate realizations of well-sampled variables, realizations of the uncertain means and covariance matrix are required. In order to generate realizations of regression parameters, realizations are necessary only for the uncertain covariance matrix.

The method used to estimate the effects of uncertainty in the statistical parameters for the well-sampled variables is analogous to the sampling procedure for individual realizations. Transformed versions of the uncertain parameters are all approximated by normal distributions when

there are more than about 30 samples. The deviations of the parameters from the mean are described by

$$\delta = \mathbf{B}\epsilon \tag{6-36}$$

$$\mathbf{B}\mathbf{B}^T = \mathbf{C} \tag{6-37}$$

$$\mathbf{v} = \delta + \mathbf{m} \tag{6-38}$$

where all the variables are analogous to those in Section 6.1.1. Given a realization of the transform variables, the actual parameter is obtained through inversion. Note that $\mathbf{m}$ and $\mathbf{C}$ are uncertain while ϵ is sampled from a zero-mean, unit-variance normal distribution.

A realization of $\mathbf{C}$ is built by

- Sampling for the variances (diagonal elements in $\mathbf{C}$) to calculate the standard deviation
- Sampling for each pairwise correlation coefficient
- Multiplying each pairwise correlation coefficient with the corresponding standard deviations

The covariance matrix for 3 well-sampled variables, for example, is defined by

$$\mathbf{C} = \begin{bmatrix} s_1^2 & r_{12}s_1s_2 & r_{13}s_1s_3 \\ r_{12}s_1s_2 & s_2^2 & r_{23}s_2s_3 \\ r_{13}s_1s_3 & r_{23}s_2s_3 & s_3^2 \end{bmatrix} \tag{6-39}$$

where each s_i is a sampled standard deviation and each r_{ij} is a sampled correlation coefficient. It is assumed that uncertainties in the means, variances, and pairwise correlation coefficients are independent, thus are sampled from their respective distributions.

Note that if $\mathbf{C}_m$ represents the covariance matrix used to generate realizations of the mean, the covariance matrix $\mathbf{C}_x$ used to generate realizations of the actual variables is

$$\mathbf{C}_x = \mathbf{C}_m + N\mathbf{I}\mathbf{s}^2 \tag{6-40}$$

where $\mathbf{s}$ is the s_i vector and there are N observations. The additional term accounts for variability about the mean.

The procedure for the regression coefficients is completely analogous, except that $\mathbf{m}$ is obtained from the sample statistics rather than sampled.

6.1.2 Saturated hydraulic conductivity

A total of 589 K_{sat} measurements were made, of which 188 were less than 5×10^{-12} m/s (0.16 mm/yr). At first thought, the raw K_{sat} statistics would be best to use for estimating layer properties; however, as the numerous low-K_{sat} measurements are not considered in the statistics for the raw values, second thought suggests that it may be appropriate to use the far more numerous porosity samples to estimate properties.

Description of samples Although one can wish that the hydrogeologic layers would be relatively homogeneous within each layer, unfortunately the properties are not necessarily homogeneous. As can be seen in the section of borehole SD7 displayed in Figure 10 by Flint (1998), zeolites occur in samples from the CHV, CHZ, BT, PP4, PP2, and PP1 hydrogeologic layers, while zeolites are missing from samples in the BT1, CHV, PP3, PP2, and BF3 hydrogeologic layers. Flint (1998) suggest that the presence of alteration can be estimated by a significant change in porosity after drying at elevated temperatures. Two porosity measurements were obtained for each sample: (i) dried at a temperature of 60 °C and a relative humidity of 65 percent, and (ii) dried at 105 °C and an ambient relative humidity (< 20 percent). Flint (1998) suggests that if the two porosity measurements differ by 0.05, the sample is altered. Areas in SD7 with the 5-percent differential porosity but not having zeolites (in the form of clinoptilolite) are reported to have vapor-phase minerals tridymite and cristobalite, although elevated cristobalite without tridymite does not exhibit the differential porosity.

Other areas with the 5-percent differential are pointed out as occurring at the base of the Tiva Canyon Tuff, and are attributed to alteration to clay (such as smectite). It is pointed out that the extent of alteration appears to be related to the topographic location of the borehole. Boreholes in narrow upwash channels may receive more frequent runoff, hence infiltration maintains higher water contents. Flint (1998) implies that alteration to clay is due to wet conditions. Despite the presence of the differential, these altered high-porosity samples tend to also have high K_{sat}.

A method for discriminating between alteration to zeolites and alteration to clays is offered by Flint (1998) using measurements of particle density obtained in two ways: (i) calculated from bulk density and porosity, and (ii) directly measuring the volume of the solid particles using helium pycnometry. Approximately 180 samples from UZ16 (judging from Figure 11 by Flint (1998)) were analyzed using the two techniques. For zeolitic samples, the calculated particle density almost invariably was greater than the measured density, by an average of about 0.07 g/cm^3, and the measured particle density was always less than 2.5 g/cm^3. For nonwelded vitric samples, the

calculated particle density was less than the measured density when the calculated density was less than 2.35 g/cm^3 and gradually switches above that value; however, the zeolitic samples tend to have a larger differential. The nonwelded vitric samples tend to have somewhat larger particle densities than the zeolitic.

The welded crystallized samples had calculated particle densities uniformly > 2.45 g/cm^3, while the densely welded vitric samples had calculated particle densities uniformly < 2.45 g/cm^3. Three classes could be distinguished from these samples: (i) welded/crystallized, (ii) nonwelded vitric, and (iii) nonwelded zeolitic or densely welded vitric. Despite the usefulness of the technique, helium-pycnometric measurements did not appear to be made on the majority of YM samples.

The complete set of measured K_{sat} values in the database reported on by Flint (1998) are shown in Figure 6-1. Microstratigraphic zones are grouped into the nomenclature of Montazer and Wilson (1984) according to Table 1 of Flint (1998).

The samples Flint (1998) considered microfractured are the TC and PV3 units (denoted with small circles). Additional apparently microfractured samples are denoted with black asterisks. For consistency with Figure 12 of Flint (1998), the TC unit consists of only the Ttrv1 subzone in Figure 6-1, even though the Ttrn3 subzone appears to be classified as TC in Table 1 of Flint (1996).

The remaining samples are color-coded broadly by formation. Outlying samples are labeled according to unit. Classification into the BT1a and BT1 hydrogeologic units is not clear from Table 1 by Flint (1998); the one Tbt1 sample was placed into the BT1 hydrogeologic unit. As alteration is a key component of the property-classification scheme proposed by Flint (1998), any sample meeting the 5-percent porosity-change criterion is circled.

Based on Figure 6-1, it can be argued that five general categories exist for the samples:

- Microfractured, low (< 0.05) porosity
- Microfractured, high (> 0.05) porosity (a cluster of labeled samples)
- Zeolitic
- Vitric/crystallized
- Inexplicably high (> 0.5) porosity, low-permeability (a pair of samples, labeled BT2 and BT4)

Flint (1998) lumps the first two categories, and never presents data in the last category. The Flint

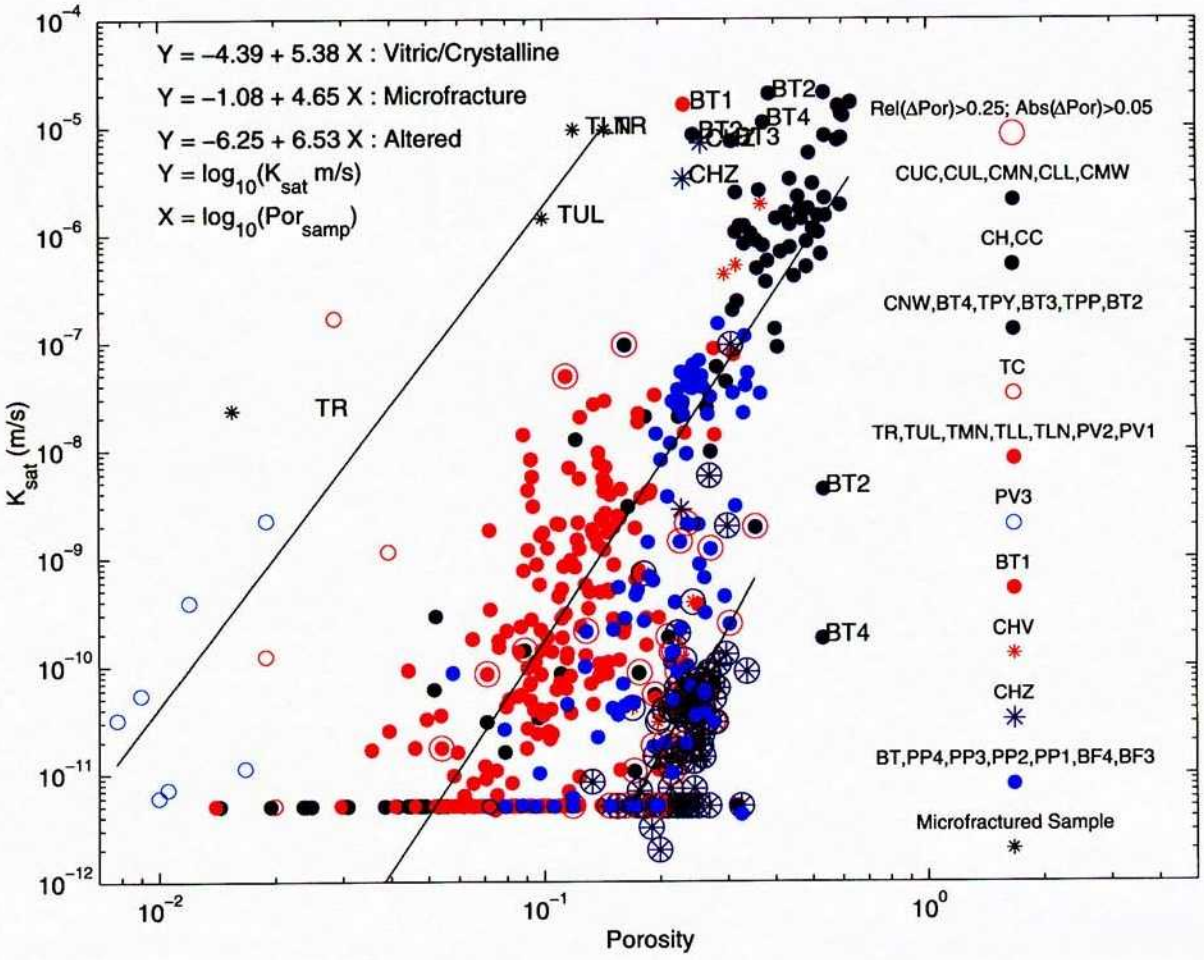

Figure 6-1: The complete set of measured K_{sat} values in the USGS database. Independently developed regression lines are shown for the samples in each of the 3 categories.

(1998) classification is broadly indicated in Figure 6-1 through regression lines for $\log_{10}(K_{sat})$ as a function of $\log_{10}(\varepsilon)$ (these regressions are not used elsewhere). It is not clear where the high-porosity microfractured category turns into the vitric/crystallized category; some of the high-permeability bedded-tuff samples may fall into the microfractured category due to handling difficulties. There is also a blurred boundary between the zeolitic and the vitric/crystallized categories; many of the "altered" samples in Figure 12 by Flint (1998) appear to fall squarely into the vitric/crystallized category.

Regression analysis A primary interest in finding relationships between easily measured core-sample properties and K_{sat} is in order to upscale the core-scale properties to the scale of more interest to infiltration modeling. There are a number of easily-measured properties obtained for each core sample, including:

- Bulk density (at 65 and 105 °C)
- Porosity (at 65 and 105 °C)
- Particle density (at 65 and 105 °C)
- Volumetric water content under field conditions
- Saturation under field conditions, both measured and corrected for evaporation

Some of the core samples have subsamples for which porosity and K_{sat} are measured. These subsamples provide the basis for estimating the relationship between easily measured core-sample properties and K_{sat}.

Prior to analysis, the data set of 4820 core samples was pruned of cores with missing measurements of volumetric water content or saturation, and samples with missing measurements of saturation corrected for evaporation had this value estimated by the uncorrected values. Cores with subsamples with measured K_{sat} were selected for further analysis.

The regression analysis seeks to find a relationship between a few easily measured properties and the subsample K_{sat} for all samples except for the microfractured samples. The primary emphasis is on characterizing the near-surface properties. Microfractured samples are a small minority of the total number of samples, the units have minimal outcrop area, and the relationships appear to be quite different from the matrix properties, thus apparently microfractured samples were removed from the regression analysis. The criterion for removal was that porosity was less than 0.05 or less than 0.2 and measured K_{sat} greater than 10^{-6}. The remaining 565 samples were used in the analysis.

All sets of 1-, 2-, and 3-parameter were exhaustively examined in the regression analysis. Linear and loglinear predictions for each of the parameters were tested, as well as calculated absolute and relative change in particle density, bulk density, and porosity. Samples with measured K_{sat} below the measurement limit (5×10^{-12} m/s) were included at the measurement limit.

A mean-square-error performance measure is used to make quantitative evaluations of the fit of the prediction to the measured data:

$$M = \frac{1}{N}\sum_{i=1}^{N}(Y_i - Y_{mi})^2 \tag{6-41}$$

where M is the performance measure, Y_i is the ith predicted value of $\log_{10}(K_{sat})$, and Y_{mi} is the ith measured value of $\log_{10}(K_{sat})$.

The USGS regression has 6 coefficients: two for the altered, three for the unaltered, and an exponent in the unaltered equation. For reference, performance measure M is 1.29 when using the K_{sat} values estimated by Flint (1998). Estimated K_{sat} values are thus deviate from the predicted values by a mean value of more than an order of magnitude.

The best single regression fit (1.39) occurs, rather surprisingly, for $\log_{10}$ corrected saturation. Saturation provides the single best predictor; all 4 values of M for the corrected and measured values (*i.e.*, linear and $\log_{10}$), are better than any other predictor and the best is comparable to the Flint (1998) estimate. For reference, M is 1.54 when using a linear regression on subsample porosity (1.77 for $\log_{10}$ regression).

A significant improvement occurs with one more variable. In this case, the best match occurs with corrected saturation (linear not logarithmic) and subsample porosity, with M dropping to 0.84. Considering three variables, the best match occurs with $\log_{10}$ of the subsample porosity, porosity at 65 °C, and volumetric water content at 105 °C, yielding an M value of 0.79. Clearly the parsimonious selection would use two variables, a saturation and a porosity, with a total of 3 coefficients. Note that there is not a tremendous difference between predictions using different types of porosity measurement or water content measurement. The difference between the USGS estimate and the 2-parameter estimate is $1.29 - 0.84 = 0.45$, which is a significant but not outstanding improvement. The explained variability (R^2) improves from 0.60 to 0.71, also a significant improvement.

The estimated K_{sat} using the best-fit 1-, 2-, and 3-parameter equations, as well as the USGS-estimated K_{sat}, are plotted as a function of the measured K_{sat} in Figure 6-2. The closer a point lies to the diagonal line, the better the fit. The best-fit regression equations are:

$$\log_{10}(K_{sat}) = -10.778 - 8.360\log_{10}(\theta_c) \tag{6-42}$$

$$= -7.778 - 4.184\theta_c + 7.568\varepsilon_{sample} \tag{6-43}$$

$$= -5.575 - 11.71VWC_{105} + 7.322\varepsilon_{65} + 4.317\log_{10}(\varepsilon_{sample}) \tag{6-44}$$

Table 6-1: Coefficients for $\log_{10}(K_{sat})$ 1-, 2-, and 3-parameter regressions, with associated sample covariance [decomposed into variance (S^2) and correlations]. Each correlation matrix is symmetric. Each regression is based on 535 samples.

Case	Variable	Coef	S^2	Correlation matrix			
1 Variable		-10.779	0.0041	1	1		
	$\log_{10}(\theta_c)$	-8.3601	0.0950		1		
2 Variables		-7.7779	0.0387	1	-0.9749	-0.9087	
	θ_c	-4.1840	0.0377		1	0.7930	
	ε_{sample}	7.5677	0.1413			1	
3 Variables		-5.5755	0.2022	1	-0.5816	-0.9717	0.9996
	VWC_{105}	-11.708	0.2489		1	0.3732	-0.5595
	ε_{65}	7.3221	0.5717			1	-0.9776
	$\log_{10}(\varepsilon_{sample})$	4.3171	0.1234				1

where a subscript of 65 denotes the measurement at 65 °C, a subscript of 105 denotes the measurement at 105 °C, a subscript of *sample* denotes the subsample measurement, θ_c is corrected saturation, ε is porosity, and VWC is volumetric water content. A table of the sample covariance matrix for these 3 regressions is presented in Table 6-1. Note that the coefficient variances increase markedly with the 3-variable regression, further suggesting that there is no reason to select a 3-parameter regression over the 2-parameter regression.

Bedrock properties examined in the regression equations are shown graphically in Figures 6-3 through 6-5, which are boreholes with samples having measured K_{sat}. Properties shown include: (i) porosity at 65 °C (shown both as a bar height and a color); (ii) saturation at 65 °C; (iii) particle-density difference (absolute density by bar height, relative density by color); (iv) measured subsample K_{sat} where available (large blue dots); (v) estimated K_{sat} (USGS are green dots, best 2-parameter regression are red dots); and (vi) formation identification. Blue denotes small values and red large in the color coding.

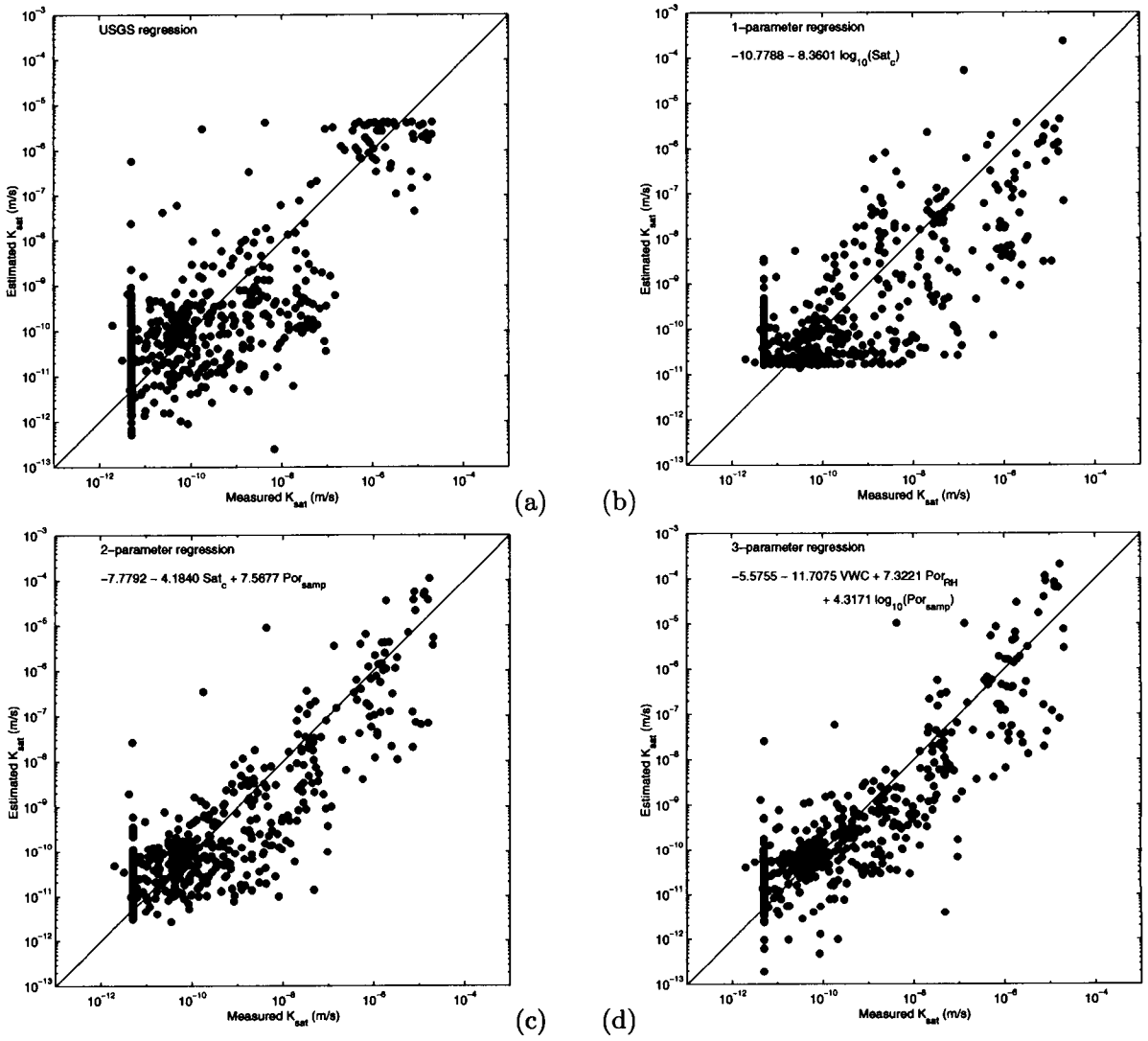

Figure 6-2: Best-estimate K_{sat} compared to measured K_{sat} using (a) the USGS estimate ($M = 1.29$, $R^2 = 0.597$), (b) the best 1-parameter regression ($M = 1.39$, $R^2 = 0.567$), (c) the best 2-parameter regression ($M = 0.84$, $R^2 = 0.738$), and (d) the best 3-parameter regression ($M = 0.79$, $R^2 = 0.754$).

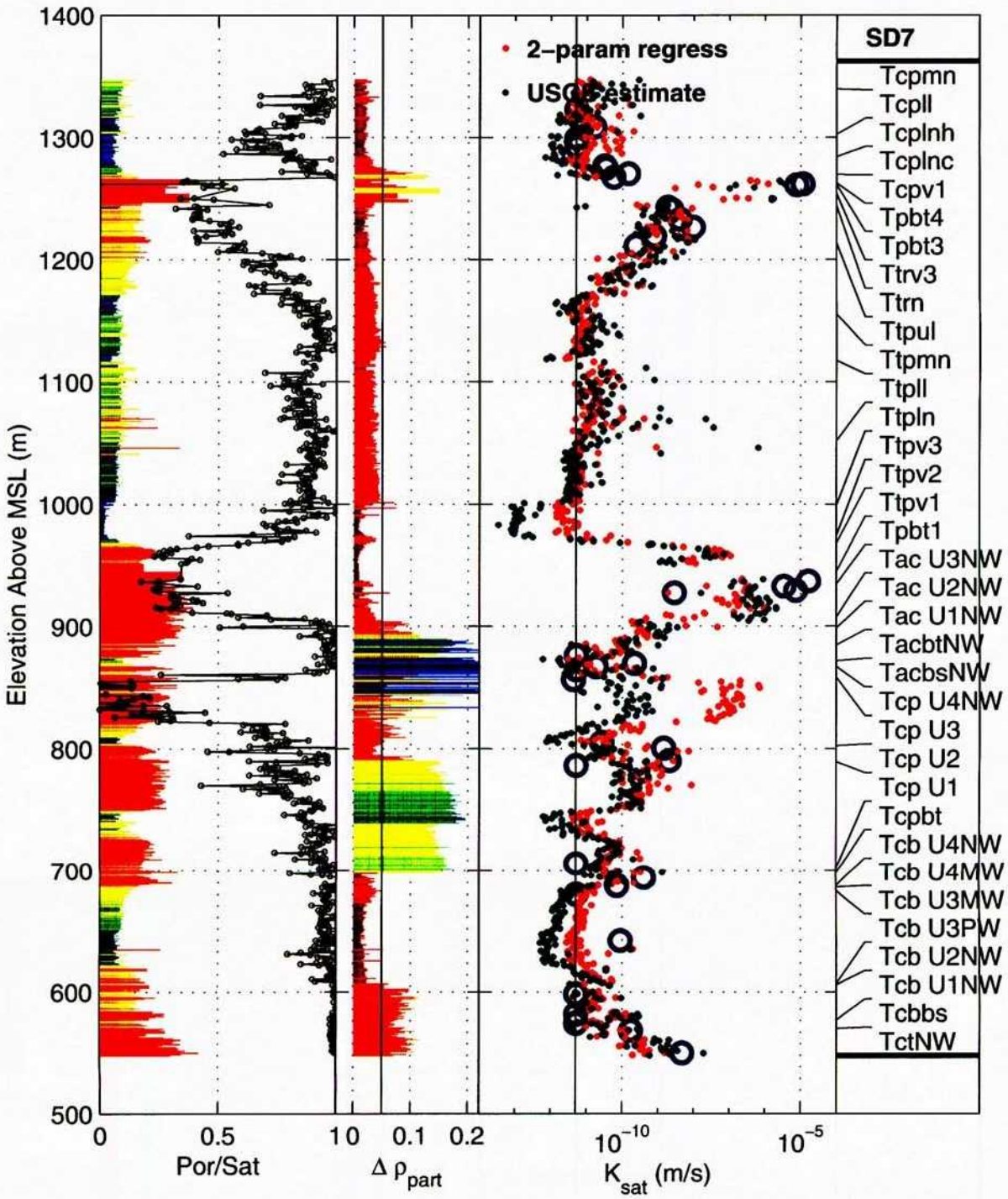

Figure 6-3: Porosity, saturation, change in particle density, and measured and estimated values for K_{sat} in borehole SD-7.

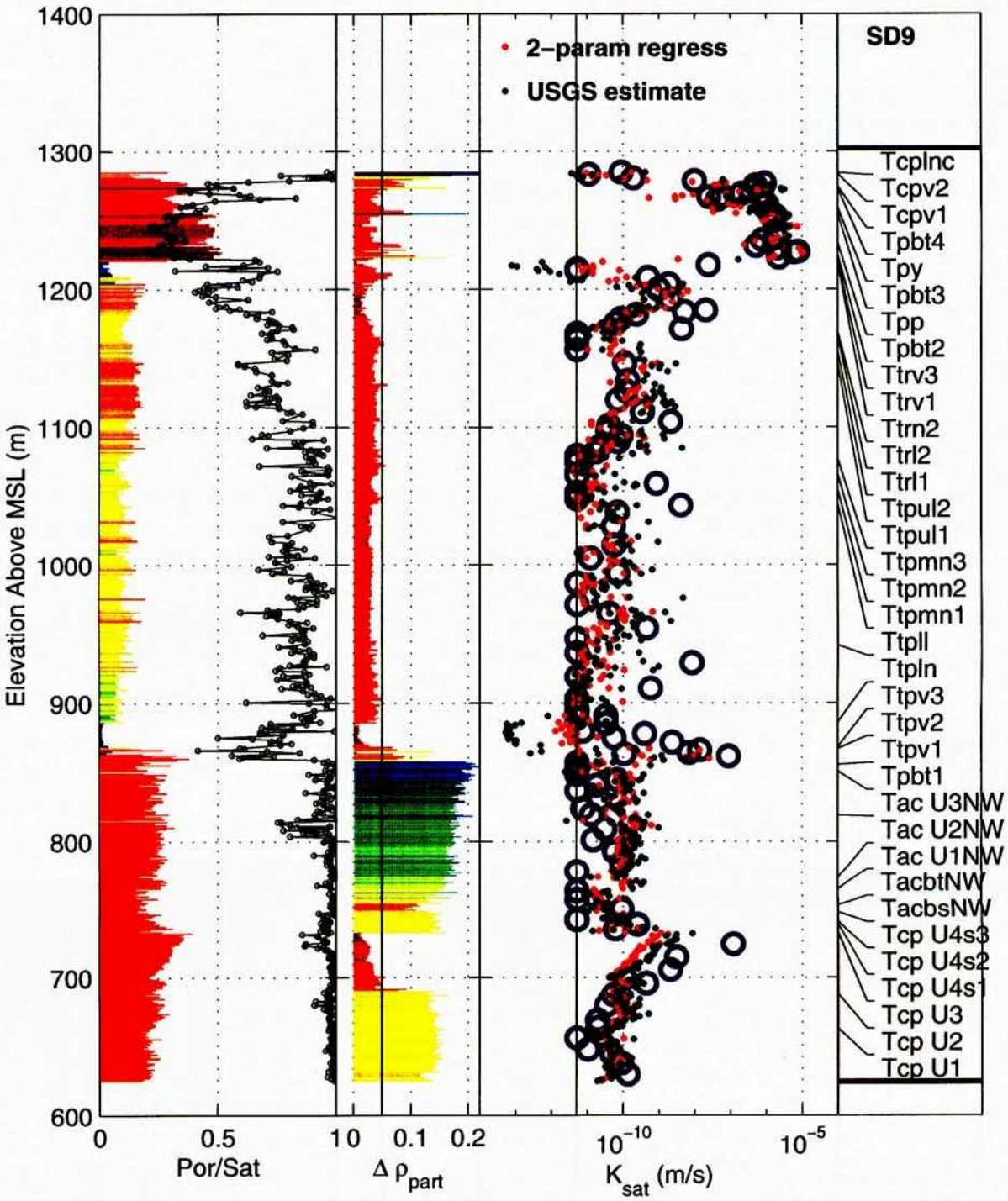

Figure 6-4: Porosity, saturation, change in particle density, and measured and estimated values for K_{sat} in borehole SD-9.

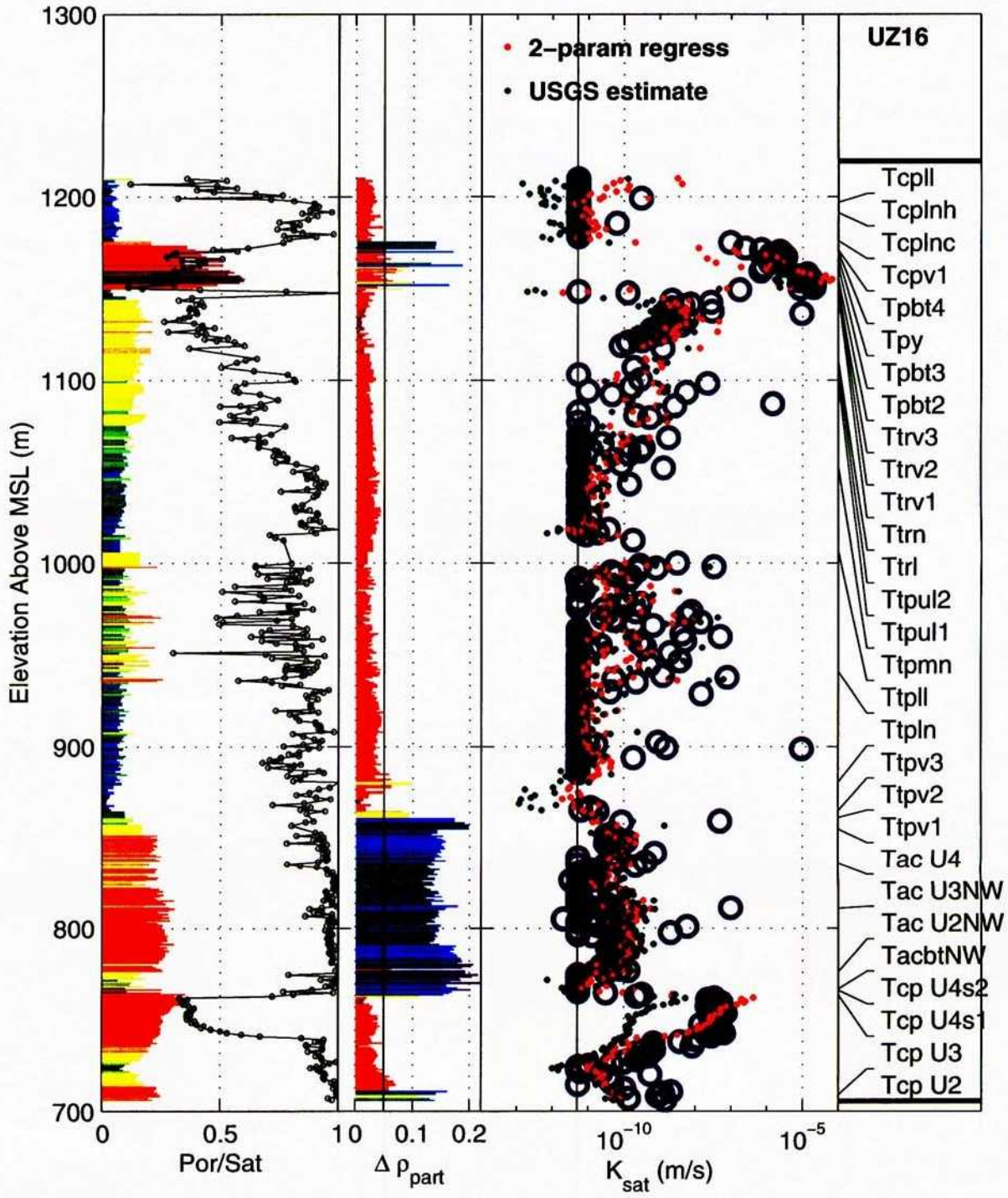

Figure 6-5: Porosity, saturation, change in particle density, and measured and estimated values for K_{sat} in borehole UZ-16.

Measured K_{sat} values are compared with estimates using the 2-parameter regression for representative units that have significant exposure areas in Figures 6-6 through 6-8. A location map on the left of the figures shows the location of the boreholes and the relative location of the unit within the formation. Observations from each borehole are color coded, with red denoting a southern borehole and blue denoting a northern borehole. Small circles denote western boreholes and large circles denote eastern boreholes. Estimated values of K_{sat} (K_e) are denoted by filled circles and measured values (K_m) by unfilled circles. Mean (μ), standard deviation (σ), and number of values (N) are indicated for the formation, with Y_e, Y_m, and $Y_e + Y_m$ denoting $\log_{10}(K_{sat})$ for estimated values, measured values, and the combined set of values.

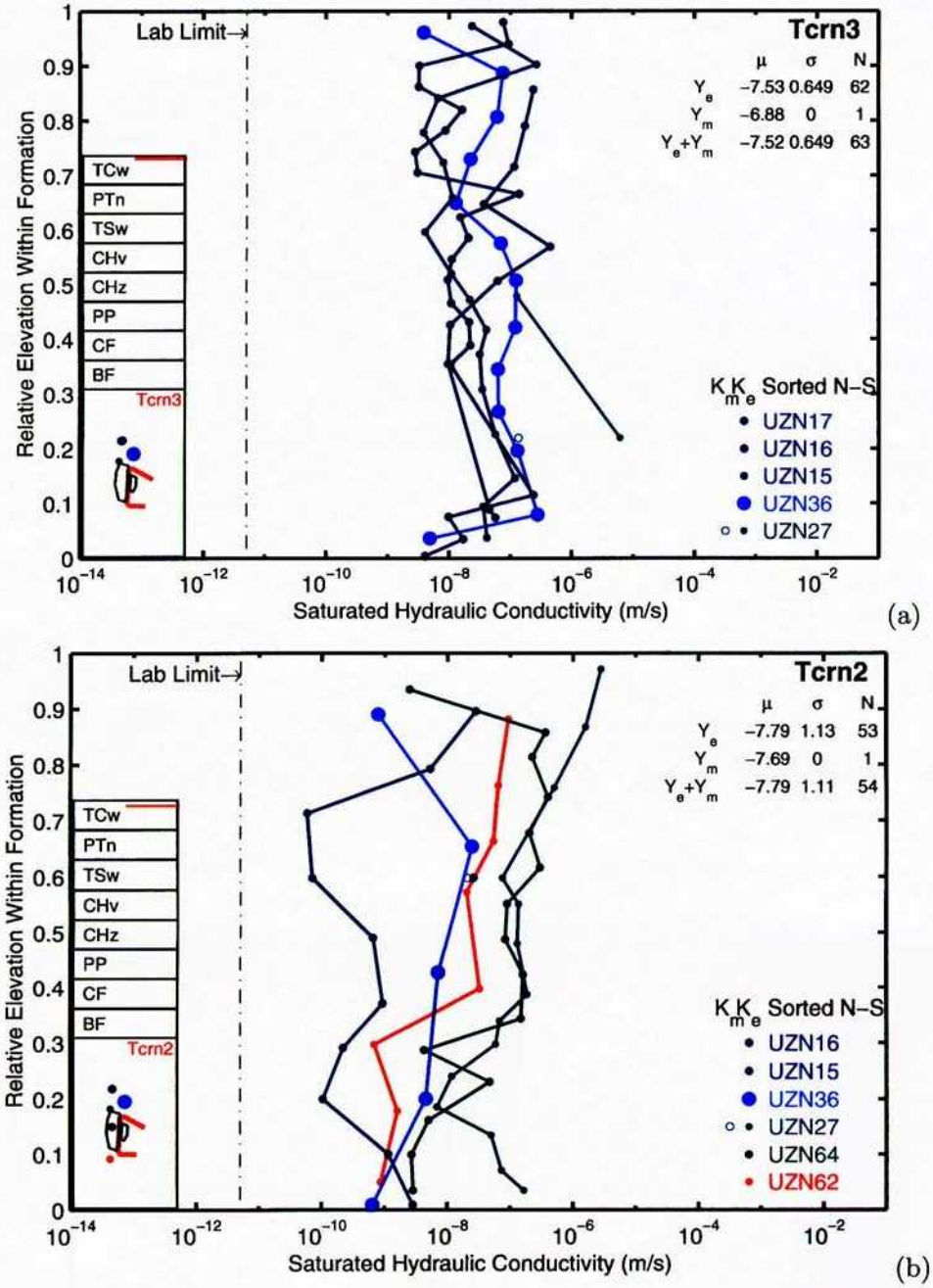

Figure 6-6: Measured and estimated values for K_{sat} in units (a) Tcrn3 and (b) Tcrn2. Estimated values are derived using the 2-parameter regression.

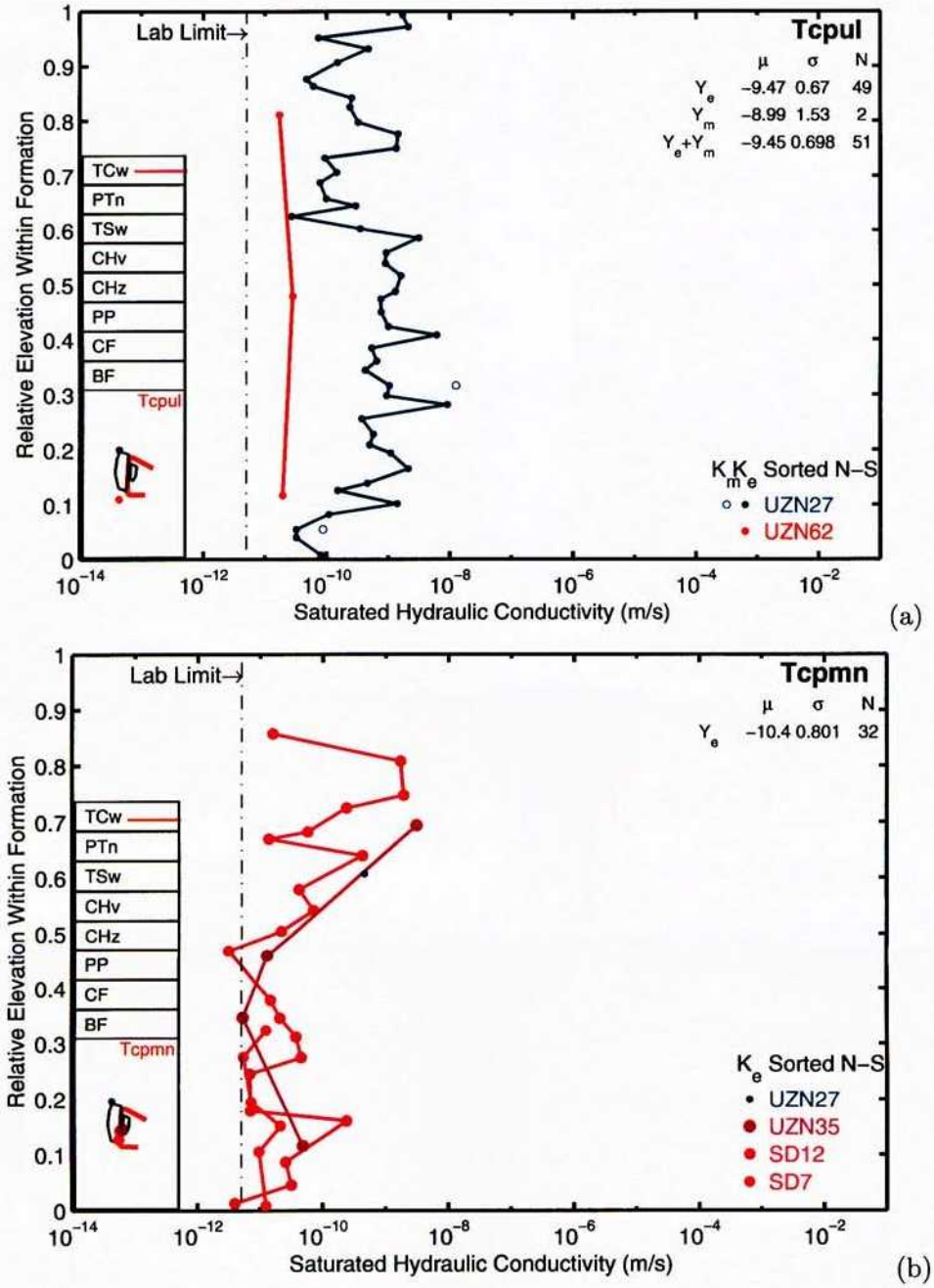

Figure 6-7: Measured and estimated values for K_{sat} in units (a) Tcpul and (b) Tcpmn. Estimated values are derived using the 2-parameter regression.

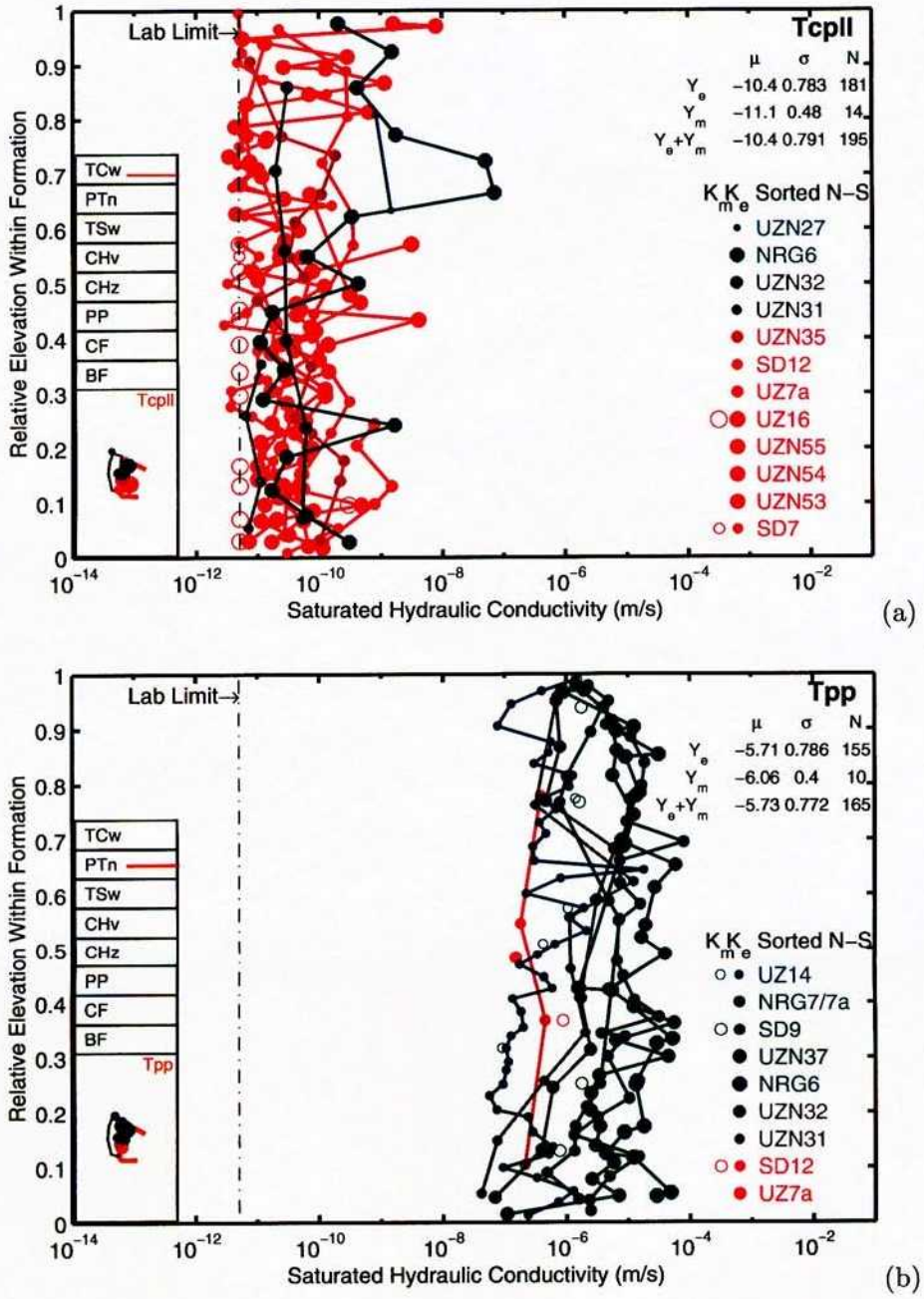

Figure 6-8: Measured and estimated values for K_{sat} in units (a) Tcpll and (b) Tpp. Estimated values are derived using the 2-parameter regression.

Units within the caprock are shown in Figure 6-6, units in the Tiva Ganyon formation below the caprock are shown in Figures 6-7 and 6-8a, and a unit in the Paintbrush Tuff nonwelded (PTn) is shown in Figure 6-8b. The values of K_{sat} for the moderately welded caprock unit are roughly midway between values for the nonwelded and densely welded units, with about 4 orders of magnitude range in estimated mean values.

Based on a complete set of figures for all units, there appears to be little in the way of systematic spatial variability in the material properties, either vertically or horizontally. Any systematic variability appears to be almost exclusively associated with the bedded nonwelded units. Units transitional from nonzeolitic to zeolitic also may have systematic variability.

Bedded units also tend to have larger nonsystematic variability. Table 6-2, which summarizes $\log_{10}(K_{sat})$ estimates for all of the units with core samples, exhibits larger variability with increasing permeability. Reduced variability in the low-permeability units is probably illusory due to censored and truncated saturation and porosity distributions and it may be reasonable to assume that all units have a standard deviation on the order of 1.2 to 1.5. The mean value for measured subsamples, estimates by Flint (1998), and estimates for the 2-parameter regression are all summarized in Table 6-2. An additional column denotes the aggregated hydrologic unit for each unit, discussed further in the next section.

Table 6-2: Measured and estimated values for $\log_{10}(K_{sat})$ in geologic units. The subsamples and Flint (1998) groups refer to K_{sat} measured and estimated by Flint (1998), while the 2-paramater group uses 10^5 realizations of corrected saturation and porosity. Columns denoted Unit and Form refer to the unit and equivalent hydrologic formation, respectively. Columns denoted N, m, m^*, $|\delta|$, and S denote number of observations, mean, corrected mean, absolute residual between corrected mean and estimated mean, and sample standard deviation, respectively.

		Subsamples			Flint (1998)			2-Parameter		
Unit	Form	N	m	m^*	N	m	$\|\delta\|$	m	$\|\delta\|$	S
Tcrn4	TCW	0	–	–	19	-10.50	–	-9.778	–	1.191
Tcplnc	TCW	17	-10.99	-10.62	272	-11.27	0.649	-10.63	0.004	1.024
Tcplnh	TCW	8	-11.30	-10.98	169	-11.74	0.758	-10.76	0.224	1.002
Tcrl1	TCW	0	–	–	9	-10.83	–	-10.32	–	1.183
Tcpul	TCW	2	-8.985	-8.700	49	-9.669	0.968	-9.456	0.756	1.075
Tcpll	TCW	14	-11.14	-11.21	181	-11.21	0.006	-10.32	0.882	1.126
Ttpul	TCW	1	-9.638	-10.18	135	-9.808	0.368	-9.633	0.543	1.197
Ttpul2	TCW	5	-10.69	-10.56	23	-9.737	0.824	-10.10	0.465	0.995
Ttpul1	TCW	40	-10.17	-10.01	227	-9.625	0.380	-9.926	0.079	1.130
Ttpll	TCW	65	-10.21	-10.17	451	-10.14	0.029	-10.24	0.065	1.081
Tcrn3	CUC	1	-6.876	-8.951	62	-6.865	2.086	-7.528	1.423	1.061
Tcrn2	CUC	1	-7.693	-8.380	53	-8.201	0.179	-7.836	0.544	1.365
Tcrn1	CUC	1	-7.690	-7.811	17	-8.352	0.541	-8.232	0.421	1.521
Ttrn	TC	38	-8.903	-8.937	450	-9.653	0.715	-8.861	0.077	1.124
Ttrn2	TC	13	-9.255	-9.091	40	-10.28	1.191	-9.760	0.670	1.191
Ttrl	TC	1	-9.740	-9.463	31	-9.148	0.314	-8.937	0.526	1.027
Ttrl2	TC	1	-11.30	-10.75	11	-9.795	0.951	-9.729	1.017	1.047
Ttrl1	TC	3	-10.85	-10.42	28	-9.441	0.980	-9.594	0.828	1.107
Tcrl2	TC	0	–	–	5	-9.662	–	-9.418	–	1.069
Tcpmn	TMN	0	–	–	32	-10.79	–	-10.38	–	1.102
Ttpmn	TMN	34	-11.08	-10.84	204	-10.89	0.049	-10.63	0.218	1.004
Ttpmn3	TMN	1	-11.30	-11.14	23	-10.90	0.239	-10.97	0.172	0.908
Ttpmn2	TMN	2	-10.19	-9.715	20	-9.998	0.283	-10.73	1.017	0.878
Ttpmn1	TMN	2	-11.30	-10.97	19	-10.86	0.110	-10.90	0.065	0.926
Tpp	BTA	10	-6.058	-5.756	155	-5.438	0.318	-5.723	0.033	1.150
Tbt2	BTA	10	-5.539	-6.358	85	-5.530	0.828	-5.778	0.580	1.256
Tbt4	BTB	3	-6.784	-6.957	20	-6.299	0.658	-6.922	0.035	1.742
Tbt3	BTB	8	-6.405	-6.208	55	-6.064	0.144	-7.122	0.914	1.287
Tpy	BTC	12	-6.803	-7.271	85	-6.955	0.316	-7.990	0.719	1.614
Ttrv3	TRV	8	-5.503	-6.068	62	-5.574	0.494	-5.611	0.456	1.275
Ttrv2	TRV	1	-5.074	-5.661	25	-7.425	1.763	-7.676	2.015	1.621
Ttrv1	TRV	4	-9.233	-8.560	17	-11.90	3.335	-10.18	1.619	1.225
Tcpv2	TPV	0	–	–	54	-9.403	–	-9.810	–	1.285
Tcpv1	TPV	10	-7.741	-6.890	76	-6.728	0.162	-7.790	0.901	1.648

The estimates for the 2-parameter regression shown in Table 6-2 are constructed through Monte-Carlo analysis with 10^5 saturation and porosity realizations. Following the procedures outlined in Section 6.1.1, both parameters are converted into sample distributions. It is assumed that each sample distribution is normal or a Type I largest-value or smallest-value distribution (Benjamin and Cornell, 1970)

$$f_Y(y) = \alpha \exp\left[\alpha(u-y) - e^{\alpha(u-y)}\right] \quad \text{Largest value} \tag{6-45}$$

$$f_Y(y) = \alpha \exp\left[\alpha(y-u) - e^{\alpha(y-u)}\right] \quad \text{Smallest value} \tag{6-46}$$

depending on the skew

$$\gamma = \frac{\sum(X-\overline{X})^3}{\sigma^3} \tag{6-47}$$

The Type I distributions have a skew of 1.1396 or -1.1396 for the largest- and smallest-value cases, respectively, while a normal distribution has zero skew. When the skew in the sample distribution is in the range $-1.1396 < 2\gamma < 1.1396$, the distribution is assumed normal; otherwise, the corresponding extreme-value distribution is used. Note that the Type I distributions are selected for convenience (the shape of the distribution is reasonable) rather than for any particular theoretical reason.

The sample distributions are transformed into normal distributions through the CDF. The covariance structure of the transformed distributions is used to generate 10^5 realizations, which are each inverted into saturation and porosity realizations. As the underlying distributions are unbounded, samples with a saturation or porosity out of the physical range are resampled. The valid realizations are used to estimate $\log_{10}(K_{sat})$ with the regression equations, including random variation about the regression equation. Thus, the resulting estimates of $\log_{10}(K_{sat})$ represent the predictions of the regression equation given the sample saturation and porosity statistics. Note that mean $\log_{10}(K_{sat})$ for a layer may vary in the third or fourth decimal place between different sets of 10^5 realizations.

Subsample sets used to measure K_{sat} typically had different mean porosity and saturation than the sets from the larger cores, which implies that the subsamples may represent biased samples. A corrected mean $\log_{10}(K_{sat})$ value is reported for the subsamples, using the deviation between mean porosity and saturation to calculate the predicted difference based on the regression equation. Deviations between the corrected $\log_{10}(K_{sat})$ estimate and both the Flint (1998) and 2-parameter regression are also reported. In most cases there is relatively little correction; however, certain units with few samples do have significant correction. The mean absolute correction is 0.42, while the maximum absolute correction (for a layer with one K_{sat} subsample) is 2.07.

Residual deviations between corrected $\log_{10}(K_{sat})$ and regressed values provide an estimate of the explanatory power of the approach. The residual deviation δ between the layer means is

$$\delta = m_Y - \hat{m_Y} \tag{6-48}$$

where m_Y is the corrected layerwise mean $\log_{10}(K_{sat})$ and $\hat{m_Y}$ is the mean of the generated $\log_{10}(K_{sat})$ values. The δ value is reported for each layer for both the Flint (1998) and 2-parameter regressions. The mean δ is 0.677 and 0.418 for the Flint (1998) and 2-parameter estimates, respectively. The 2-parameter estimate provides an improvement of about 38 percent based on this measure.

A graphical comparison of predictions for several units are shown in Figures 6-9 through 6-11, representing typical skewed and symmetric cases, with the figures representing a sequence of relatively good, medium, and poor fits. In each figure, each pairwise combination of saturation, porosity, and K_{sat} is shown. All measured subsample values are shown, as well as values estimated by Flint (1998). Only 1 sampled value in 20 is shown, however, for clarity. Mean values are denoted for each data distribution.

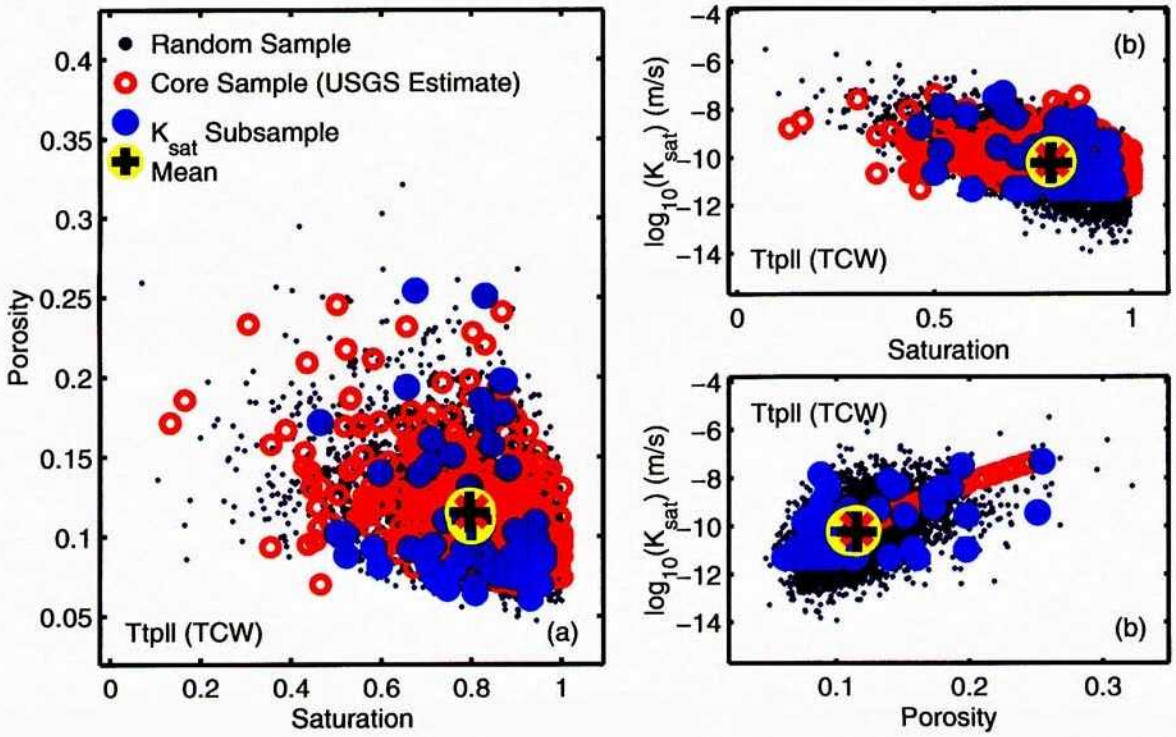

Figure 6-9: Measured and estimated values for pairwise combinations of porosity, saturation, and K_{sat} in unit Ttpll. Only 1 in 20 random samples are shown. Measured K_{sat} is not corrected for subsample deviations in saturation and porosity.

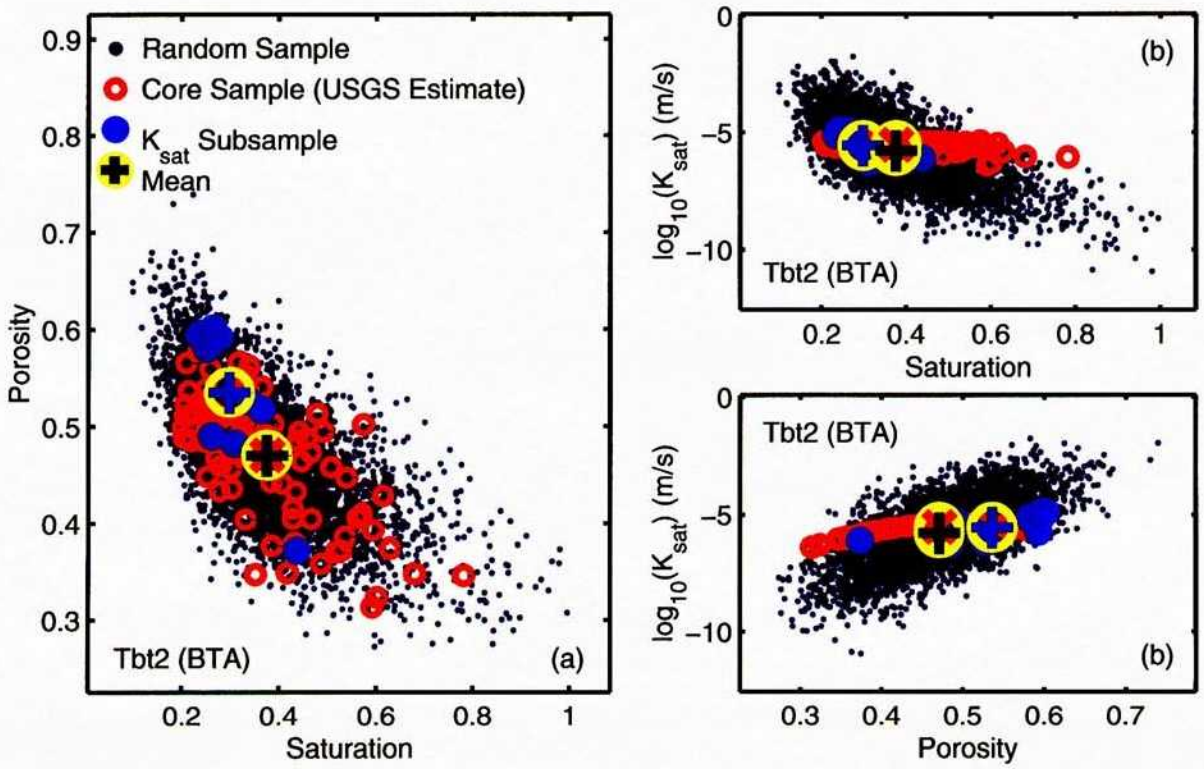

Figure 6-10: Measured and estimated values for pairwise combinations of porosity, saturation, and K_{sat} in unit Tbt2. Only 1 in 20 random samples are shown. Measured K_{sat} is not corrected for subsample deviations in saturation and porosity.

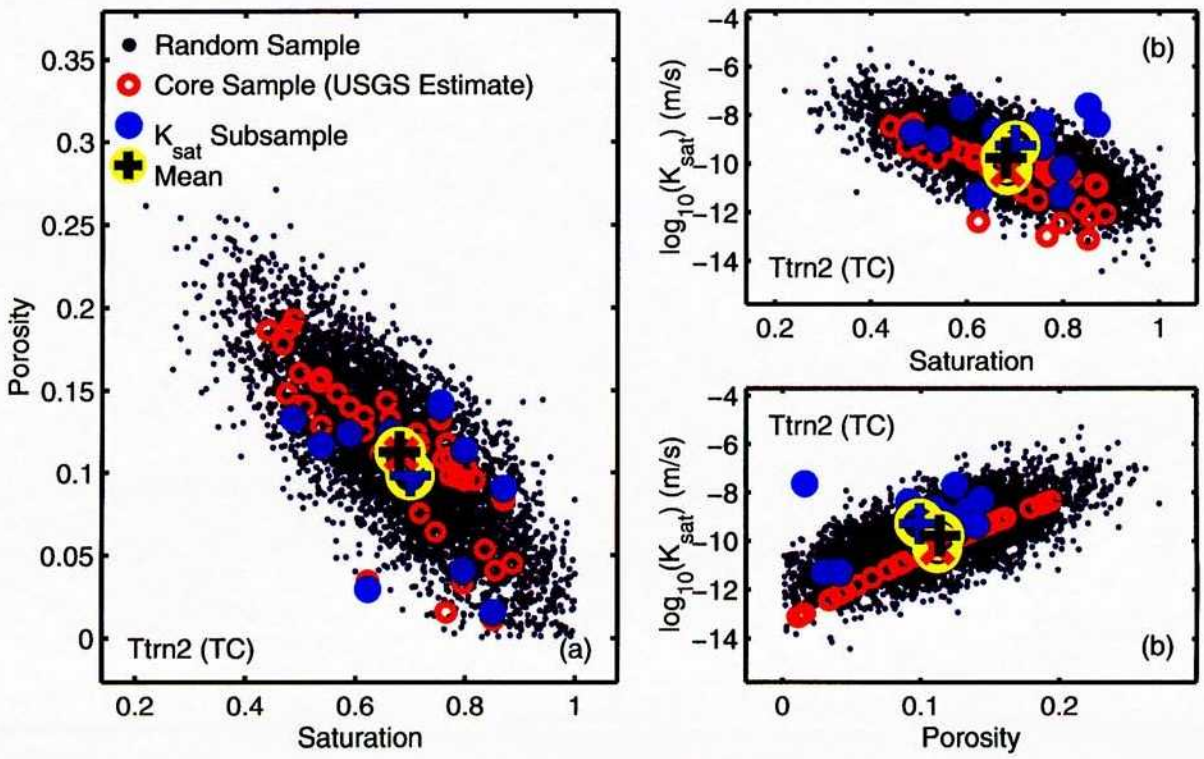

Figure 6-11: Measured and estimated values for pairwise combinations of porosity, saturation, and K_{sat} in unit Ttrn2. Only 1 in 20 random samples are shown. Measured K_{sat} is not corrected for subsample deviations in saturation and porosity.

Aggregation of units Many of the units within the various formations can be grouped based on similar matrix hydraulic properties. Flint et al. (1996a) performed one such aggregation using the properties estimated by Flint (1998), also performing a conversion from the bedrock units defined by Scott and Bonk (1984) and the more recent units defined by Day et al. (1998). The aggregation suggested by Flint et al. (1996a) is presented in Table 6-3, as well as a somewhat revised independent aggregation using the 2-parameter estimate for $\log_{10}(K_{sat})$. The independent aggregation is based on estimated mean $\log_{10}(K_{sat})$, with the primary requirement that means within a group are within an order of magnitude of one another. Seven equivalent hydrologic formations, labeled TCW, CUC, TC, TMN, BTA, BTB, and BTB, are aggregated by considering mean K_{sat} of the subunits. An additional two formations, TRV and TPV, are constructed to match map units with significantly different properties in the merged subunits. Subunits defining the equivalent formations are shown in Table 6-4. In cases where a mapped unit is not sampled, the corresponding aggregate formation is guided by assignments performed by Flint et al. (1996a). These units generally crop out outside of the repository footprint.

As a practical matter, a bedrock matrix can be considered essentially impermeable for infiltration when the matrix K_{sat} is less than about 1 mm/yr [$\log_{10}(K_{sat}) < -10.5$], where K_{sat} is in m/s. A bedrock unit with such a low permeability would need to be completely saturated all year to transmit 1 mm/yr, which is unlikely at YM. Certainly a significant soil covering would be necessary to protect the bedrock from evapotranspiration (ET). Fractures are the primary possible source for infiltration to penetrate low-permeability bedrock. Fracturing is vastly greater in the middle nonlithophysal unit of the Tiva Canyon welded (TCw) (Tcpmn) than in the adjoining units. Accordingly, middle nonlithophysal units are handled separately from the adjacent units despite having similar matrix K_{sat}.

The mean K_{sat} for the aggregated units can be estimated from the pooled samples in the same way that properties were calculated for the individual subunits in the previous section. The statistics defining the aggregated units are calculated using the pooled samples without attempting to compensate for the effect of different numbers of samples in each subunit (*i.e.*, it is tacitly assumed that the relative frequency each unit is sampled does not bias the representativeness of the aggregated unit). The properties for the aggregated units are shown in Table 6-5. The mean absolute layerwise residual after subsample correction is 0.374 and 0.306 for the Flint (1998) and 2-parameter estimates, respectively. It can be concluded that the estimation procedure with the 2-parameter method provides almost 20 percent smaller residual on a layerwide basis. This improvement is less than for the subunits, presumably because variability arising from small sample sets is reduced due to aggregation.

Table 6-3: Comparison of bedrock map units used by Day *et al.* (1998) (denoted Dea98) with corresponding Scott and Bonk (1984) units (denoted SB84) according to Flint *et al.* (1996) and independently derived equivalent hydrologic units. Equivalent units used to assign hydraulic properties are shown in parentheses. Y is $\log_{10}(K_{sat})$.

	Flint et al. (1996)			Independent		
Dea98 Unit	SB84 Unit	Subunit Y	Formation Y	Formation	Subunit Y	Formation Y
Qtac	Qtac			Qtac		
Qtc	Qtc			Qtc		
Tmr	(cnw)		-6.3	(TPV)		-7.8
Tmrw	(tmn)		-10.5	(TMN)		-10.6
Tpkl	(tcw)		-10.2	(TCW)		-10.2
Tpkt	(bt3)		-6.3	(BTB)		-7.1
Tcu	(tcw)		-10.2	(TCW)		-10.2
Tcrv	(tc)		-8.8	(TRV)		-6.7
Tcrn4	tc	-10.5	-8.8	TCW	-9.8	-10.2
Tcrn3	cuc	-6.9	-7.4	CUC	-7.5	-7.7
Tcrn2	cuc	-8.2	-7.4	CUC	-7.8	-7.7
Tcrn1	cuc	-8.4	-7.4	CUC	-8.2	-7.7
Tcpul	cul	-9.7	-7.9	TCW	-9.5	-10.6
Tcpun	(tcw)		-10.2	(TMN)		-10.6
Tcpum	(tcw)		-10.2	(TCW)		-10.2
Tcpmn	tcw	-10.8	-10.2	TMN	-10.4	-10.6
Tcpll	tcw	-11.2	-10.2	TCW	-10.3	-10.2
Tcpln	tcw		-10.2	TCW	-10.2	-10.2
Tcplnc	tcw	-11.3	-10.2	TCW	-10.6	-10.2
Tcpv	tcw	-6.7, -9.4	-10.2	TPV	-7.8, -9.8	-8.4
Tbt5	(bt4)		-5.4	(BTB)		-7.1
Tpy	bt3	-7.0	-6.3	BTC	-8.0	-8.0
Tpp	tpp	-5.4	-6.1	BTA	-5.7	-5.7
Tbt2	bt2	-5.5	-5.4	BTA	-5.8	-5.7
Tppw	(tcw)		-10.2	(TCW)		-10.2
Tpu	(tpp)		-6.1	(TCW)		-10.2
Ttrv	tc	-5.1, -5.5, -9.2	-8.8	TRV	-5.6, -7.7, -10.2	-6.7
Ttrn3	tc	-9.7	-8.8	TC	-8.9	-8.9
Ttrn2	tr	-9.3	-8.8	TC	-9.8	-8.9
Ttpul	tul	-9.8	-9.7	TCW	-9.6, -9.9, -10.1	-10.2
Ttpmn	tmn	-10.0, -10.9, -10.9	-10.5	TMN	-10.6, -10.7, -11.0	-10.6
Ttpll	tll	-10.1	-9.6	TCW	-10.2	-10.2
Ttpmnl	tmn	-10.9	-10.5	TMN	-10.9	-10.6
Ttr	(tc)		-8.8	(TRV)		-6.7
Ttrl	tc	-9.1, -9.4, -9.8	-8.8	TC	-8.9, -9.4, -9.6	-8.9

Table 6-4: Stratigraphic units in Flint (1998) database used to define independently derived equivalent hydrologic formations.

Equivalent Formation	Subunits Defining Equivalent Formation Properties
TCW	Tcrn4, Tcplnc, Tcplnh, Tcrl1, Tcpul, Tcpll, Ttpul, Ttpul2, Ttpul1, Ttpll
CUC	Tcrn3, Tcrn2, Tcrn1
TC	Ttrn, Ttrn2, Ttrl, Ttrl2, Ttrl1, Tcrl2
TMN	Tcpmn, Ttpmn, Ttpmn3, Ttpmn2, Ttpmn1
BTA	Tpp, Tbt2
BTB	Tbt4, Tbt3
BTC	Tpy
TRV	Ttrv3, Ttrv2, Ttrv1
TPV	Tcpv2, Tcpv1

Table 6-5: Measured and estimated values for $\log_{10}(K_{sat})$ in equivalent hydrologic formations. The subsamples and Flint (1998) groups refer to K_{sat} measured and estimated by Flint (1998), while the 2-paramater group uses 10^5 realizations of corrected saturation and porosity. Columns denoted N, m, m^*, $|\delta|$, and S denote number of observations, mean, corrected mean, absolute residual between corrected mean and estimated mean, and sample standard deviation, respectively.

	Subsamples			Flint (1998)			2-Parameter		
Unit	N	m	m^*	N	m	$\|\delta\|$	m	$\|\delta\|$	S
TCW	152	-10.42	-10.34	1535	-10.53	0.185	-10.24	0.104	1.144
CUC	3	-7.420	-8.270	132	-7.593	0.677	-7.733	0.537	1.300
TC	56	-9.146	-8.954	565	-9.662	0.708	-8.942	0.011	1.170
TMN	39	-11.05	-10.80	298	-10.82	0.020	-10.64	0.163	0.999
BTA	20	-5.798	-6.046	240	-5.470	0.576	-5.746	0.301	1.191
BTB	11	-6.508	-6.413	75	-6.127	0.286	-7.089	0.676	1.468
BTC	12	-6.803	-7.271	85	-6.955	0.316	-7.973	0.701	1.608
TRV	13	-6.618	-6.452	104	-7.052	0.600	-6.715	0.263	1.922
TPV	10	-7.741	-7.839	130	-7.839	0.000	-8.400	0.561	1.668

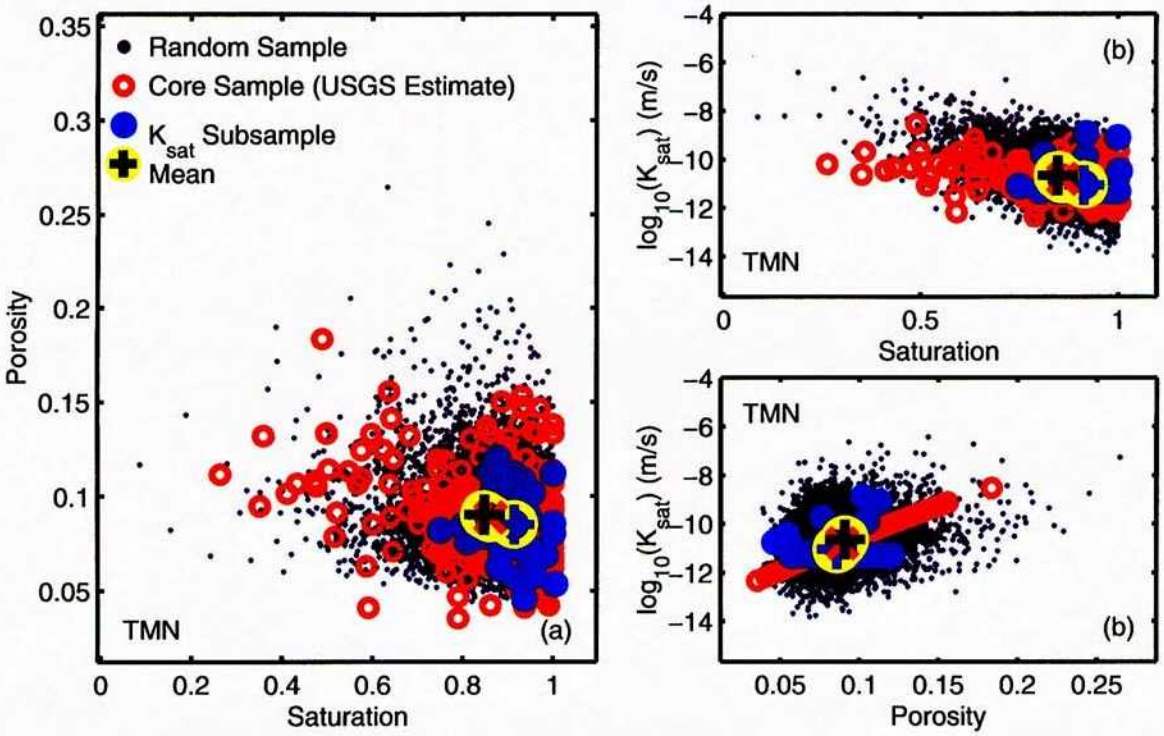

Figure 6-12: Measured and estimated values for pairwise combinations of porosity, saturation, and K_{sat} in equivalent hydrologic unit TMN. Only 1 in 20 random samples are shown. Measured K_{sat} is not corrected for subsample deviations in saturation and porosity.

A graphical comparison of predictions for two equivalent hydrologic formations are shown in Figures 6-12 and 6-13, representing the best and worst fits of the formations with at least 10 subsample measurements. These figures are exactly analogous to the unit plots.

6.1.3 Retention properties

Published retention measurements are available for core samples obtained from outcrops (Flint et al., 1996b). The procedure Flint et al. (1996b) followed was to use RETC for the data of each core sample individually, obtaining van Genuchten α and m, then regressing these sample values into a global relationship. The alternative approach followed here is to estimate the retention properties by obtaining the parameters that best match all retention curves considered simultaneously.

Each retention curve is assumed to be governed by a van Genuchten relationship in the form

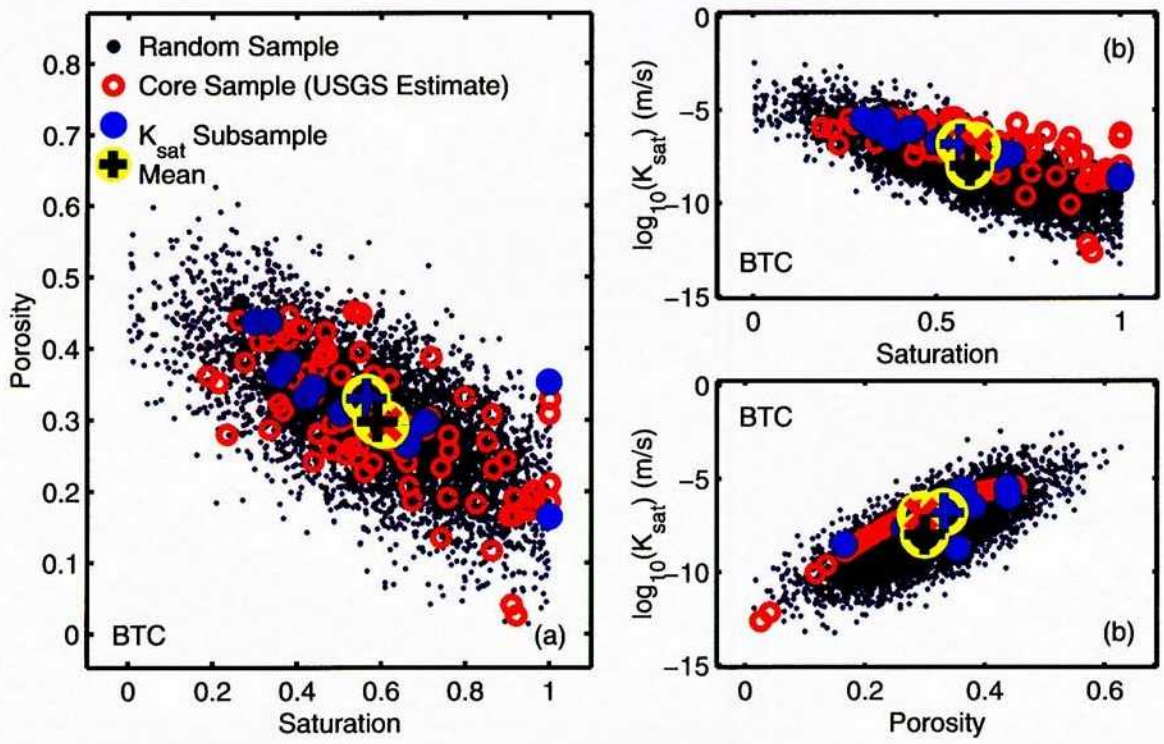

Figure 6-13: Measured and estimated values for pairwise combinations of porosity, saturation, and K_{sat} in equivalent hydrologic unit BTC. Only 1 in 20 random samples are shown. Measured K_{sat} is not corrected for subsample deviations in saturation and porosity.

(van Genuchten, 1980)

$$\theta_e = [1 + (\alpha|h|)^n]^{-m} \tag{6-49}$$

$$= [1 + (P_c/P_0)^n]^{-m} \tag{6-50}$$

where h is pressure head, P_c is capillary pressure ($P_c = -h\rho g$), θ_e is effective saturation [$\theta_e = (VWC - VWC_r)/(\varepsilon - VWC_r)$], α, n and m are fitting parameters (usually $m = 1 - 1/n$), P_0 is $1/\rho g\alpha$, VWC is volumetric water content, ε is porosity, and VWC_r is residual water content. In most of the sample retention plots presented by Flint et al. (1996b), it appears that VWC_r is essentially zero, thus it is assumed in the following that VWC_r is 0. Note that the retention curve is associated with a curve describing unsaturated hydraulic conductivity in the form

$$K(P_c) = K_{sat}\theta_e^{1/2}\left[1 - \left(1 - \theta_e^{1/m}\right)^m\right]^2 \tag{6-51}$$

The objective function M is minimized using unconstrained minimization, where

$$M = \frac{1}{N - N_c} \sum_{i=1}^{N} [\log_{10}(P_{mi}) - \log_{10}(P_{ei})]^2 \tag{6-52}$$

$$\log_{10}(P_{0i}) = a_0 + a_1 V_{1i} + a_2 V_{2i} \tag{6-53}$$

$$m_i = b_0 + b_1 V_{3i} + b_2 V_{4i} \tag{6-54}$$

where M is the objective function, N is number of observations, N_c is number of determined coefficients, P_m is measured capillary pressure, P_e is estimated capillary pressure, V_{ji} are the variables being regressed against, and a_j, b_j are the regression constants. Note that the regression is linear in P_0 and nonlinear in m.

Flint et al. (1996b) report pairs of VWC and capillary pressure (P_c) in their Appendix II. Data from two subsamples (TS47s, CH60s) were discarded, as properties (*e.g.*, porosity) for the parent core samples were either not determined or were not reported in the electronic data set. Several VWC/P_c pairs had only one of the pair reported, or had a zero value for VWC; these pairs were also discarded.

Although porosity and saturated VWC should be identical, the measured porosity of some core samples was not consistent with the VWC reported at a P_c of 0.01 bar [note that Flint et al. (1996b) assume full saturation at 0.01 bar]. Accordingly, for the purposes of regression, effective saturation was calculated by multiplying all VWC values for a sample by $0.999/VWC_0$, where VWC_0 is VWC at 0.01 bar; also, the porosity for each subsample was assumed to be VWC_0. Because of this inconsistency, the core-sample value for the difference between porosity at 65 and 105 °C was used as a candidate regression parameter, but not either porosity value individually. VWC_0 is the surrogate for porosity used in the regression.

All combinations of 1-parameter and 2-parameter fits for both P_0 and m were exhaustively checked for the best value of M. The 8 candidate regression variables included VWC_0, bulk density at both 65 and 105 °C, particle density at both 65 and 105 °C, and change in porosity, bulk density, and particle density between 65 and 105 °C. Unfortunately saturation was not measured for these cores, as it was the most useful measurement in the borehole-data set. However, saturation in outcrop samples is strongly affected by surface conditions not seen by the borehole set, so it would be difficult to relate saturation measurements between the two data sets.

The optimal fit provided by the best set and the worst set of parameters was not greatly different, differing by only about one-third, and all optimal fits were on the order of 10 (mean error for a measured/estimated P_0 pair is about one order of magnitude). A spot check for several

combinations of parameters suggests that worse fits would be obtained for P_0 rather than $\log_{10}(P_0)$ and for $\log_{10}(m)$ rather than m.

The similarity between estimates of fit to the retention data can be partially explained by correlation between parameters and partially due to noisy measurements. One would expect that little additional explanatory power is achieved when a highly correlated parameter is added and absolute values of correlation coefficients between VWC_0 and other parameters range between 0.46 and 0.92. It appears that the overall fit is best when VWC, ρ_b, and ρ_p are all used, while ρ_b and ρ_p are measured at different temperatures. The Δ parameters have relatively low explanatory power, consistent with the K_{sat} regressions.

Noisy measurements are due to inherent limitations in the measurement techniques in these welded tuffs. At high VWC, VWC is easy and P is difficult to measure (P is reported in quanta of 1.4 bar, with many repetitions of low values). At low VWC, VWC is difficult and P is easy to measure, (VWC is reported in quanta of 0.001, with many repetitions of low values). Simultaneous fitting of all retention curves may help to reduce the impact of noise by providing many more data points considered for each regression coefficient.

The best overall fit (0.200) only has 2 measured variables (both variables are used in each of the two regression equations); however, there is little loss in explanatory power when m is regressed to only 1 variable. The best 2-variable model with 5 coefficients is:

$$P_0 = a_1 + b_{11}\rho_p^{105} + b_{12}\,VWC_0 \tag{6-55}$$

$$m = a_2 + b_{21}\,VWC_0 \tag{6-56}$$

The best-fit coefficients and associated sample covariance matrix for the 2-variable model are reported in Table 6-6. For this set of coefficients, R^2 is 0.865 and M is 0.203. Note that regressed van Genuchten m coefficients are relatively certain and m only varies in the range of roughly 0.3 to 0.36. For comparison, the best M is 0.290 if the same regression variable is used for both P_0 and m (4 coefficients determined).

The procedure for obtaining regression equations for P_0 and m does not readily allow estimates of the residual error in P_0 and m about the regression equations. Residual error is estimated by independently estimating the retention properties for each curve.

Table 6-6: Coefficients for selected retention-parameter regression, with associated sample covariance [decomposed into variance (S^2) and correlations]. The correlation matrix is symmetric. Each regression is based on 394 observations.

Parameter	Variable	Coef	S^2	Correlation matrix				
P_0		-12.512	0.7781	1	-1	-0.9740	-0.1345	-0.4679
	ρ_p^{105}	-3.8063	0.1214		1	0.9717	0.1440	0.4594
	VWC_0	-4.5142	0.06924			1	-0.0896	0.6527
m		0.3024	0.00012				1	-0.8128
	VWC_0	0.1158	0.00194					1

6.1.4 Aggregate matrix properties

The bulk matrix properties that affect infiltration are at the scale of a few square meters. However, measurements of the matrix properties are made at the much smaller core-sample scale (*e.g.*, 5 to 25 cm^3). Unfortunately, simply averaging the core sample properties may not provide the appropriate bulk properties, as the variability of properties at the smaller scale can affect the larger scale. The problem of estimating bulk properties is exacerberated under unsaturated conditions, as hydraulic conductivity is dependent on pressure; under dry conditions, fine material may be more conductive than coarse material and under wet conditions the converse is true.

DOE approach Flint (1998) adopted the approach of using an arithmetic average for most properties (*e.g.*, porosity, bulk density, and water content) and a geometric average for K_{sat} and water potential. Retention properties were not identified by Flint (1998), but presumably geometric averaging for P_0 and arithmetic averaging for van Genuchten m or n would be suggested. Averaging is performed for the samples within a particular layer.

Flint (1998) discusses the use of power-law averages to estimate bulk K_{sat}. A power-law average for K_{sat} is

$$K_{sw} = \left[\frac{1}{N} \sum_{i=1}^{N} f_i K_i^w \right]^{1/w} \tag{6-57}$$

where N is the number of samples, f_i is a weight for each sample, and w is an empirical coefficient.

A harmonic mean is obtained by setting w to -1 and f_i to 1, while an arithmetic mean is obtained by setting w to 1 and f_i to 1. The estimated value of K_{sw} increases as w increases. In

the extreme of harmonic averaging, the extreme low values of K_i dominate the average, while at the other extreme of arithmetic averaging the extreme high values of K_i dominate. Accordingly, estimation of harmonic and arithmetic means requires many realizations for robust statistics. Note that the case where w is 0 corresponds to the geometric mean

$$K_{sg} = \exp\left[\frac{1}{N}\sum_{i=1}^{N} f_i \log(K_i)\right] \tag{6-58}$$

For saturated vertical percolation, perfectly horizontal or perfectly vertical homogeneous stratified layers would require that the f_i values represent relative layer thickness ($f_i = b_i / \sum b_j$, where b represents layer thickness). Flint (1998) cites work by McKenna and Rautman (1996) suggesting that the dips of the units at YM are consistent with $w = -0.4$, based on linearized (saturated) conditions. When the medium has unstructured heterogeneity, often the geometric mean is used (essentially equivalent to $w = 0$).

Independent approach The reasonableness of the bulk matrix properties obtained through averaging is assessed using an independently derived approach. The conceptual model is of a series of parallel vertical columns with periodic unimpeded horizontal flow. Each column consists of a stack of core-scale realizations. Each row in a column consists of 1 or more core-scale realizations, with multiple samples in a row accounting for local lateral flow. The approximation of periodic unimpeded horizontal flow represents flow occurring along stratigraphic layers, depositional layers, and subhorizontal fractures. The approach becomes more appropriate as the medium becomes more anisotropic, either in the horizontal (short vertical stacks) or in the vertical (long vertical stacks). Core-scale realizations are generated using the methods in the previous sections.

The independent approach seeks to derive equivalent bulk properties that preserve both areal-average steady gravity-drainage flux and areal-average steady velocity over a range of capillary pressure. Simultaneously meeting the pair of requirements allows unique equivalent K_{sat}, porosity, and retention properties to be found; porosity cannot be determined if the velocity requirement is neglected.

The procedure for generating equivalent bulk properties is

- Select discrete values of capillary pressure over a wide range
- Determine the corresponding bulk average flux and velocity for each capillary pressure

- Estimate bulk properties corresponding to the bulk average flux and velocity using unconstrained minimization

A detailed description of this procedure follows.

In steady gravity drainage, flux is equivalent to unsaturated conductivity, which is a function of capillary pressure. With the assumption that capillary pressure is equal throughout the column, unsaturated conductivity can be determined in each sample. The equivalent conductivity for the column is determined through harmonic averaging. The bulk conductivity (hence flux) across all columns is obtained by arithmetic averaging. Thus,

$$K(P_c) = \frac{1}{N_c} \sum_{i}^{N_c} \left[\frac{1}{N_r} \sum_{j}^{N_r} K_{ij}^{-1}(P_c) \right]^{-1} \tag{6-59}$$

where $K(P_c)$ is the bulk unsaturated hydraulic conductivity as a function of capillary pressure P_c and N_c and N_r are the number of columns and rows, respectively. Each of the K_{ij} values are the arithmetic average of the number of samples in each row of the column.

An actual column would exhibit local perturbations in capillary pressure to maintain continuity in the face of changing properties. The assumption of a single capillary pressure throughout the column neglects these local perturbations, which are expected to be secondary to the conceptual model assumptions of parallel columns with periodic unimpeded horizontal flow.

Average velocity in a column composed of N segments is the length of the column divided by travel time through the column. Column-average velocity, $\bar{v}$, is estimated by

$$\bar{v} = \frac{1}{T} \sum_{i=1}^{N} b_i \tag{6-60}$$

$$T = \sum_{i=1}^{N} \frac{b_i}{v_i} \tag{6-61}$$

$$v_i = \frac{K_i}{\varepsilon_i \theta_i} \tag{6-62}$$

where T is travel time, b is length of segment, v is average velocity, K is unsaturated conductivity, ε is porosity, and θ is saturation. When each segment of the column is the same length, $\bar{v}$ is the harmonic average of v.

Just as flux through each column is different, velocity is different in each column. The arithmetic mean of average velocity in all of the columns may not be the most relevant mean,

particularly when transport is concerned. Only a few columns may contribute most of the flux and the velocity in these columns is far more important for transport. A flux-weighted average velocity provides a method for capturing the dominant columns, with an overall average velocity, $\bar{V}$, of

$$\bar{V} = \frac{\sum_i^{N_c} \bar{q}_i \bar{v}_i}{\sum_i^{N_c} \bar{q}_i} \tag{6-63}$$

where $\bar{q}_i$ is column-average flux and $\bar{v}_i$ is column-average velocity.

Once the response of bulk flux and bulk velocity to changing capillary pressure is obtained, unconstrained minimization allows equivalent properties to be determined. The objective function for minimization is

$$u = \left[\sum_{i=1}^{N} w_i [(\bar{Y}_{qi} - Y_{qi})^2 + (\bar{Y}_{vi} - Y_{vi})^2] \right]^{1/2} \tag{6-64}$$

where $\bar{Y}_q$ and $\bar{Y}_v$ represent the logarithm of bulk flux and velocity estimated using the average of core-scale realizations, Y_q and Y_v represent the logarithm of bulk flux and velocity estimated using the bulk parameters, and w_i is a weighting function.

Even though each of the parameters are constrained, transformed variables can be used to allow unconstrained minimization algorithms. The logarithms of both K_{sat} and P_0 are used as the transform variable. Both van Genuchten m and porosity (both of which must lie between 0 and 1) are transformed using

$$Y = \frac{1}{2} \log \left(\frac{X}{1 - X} \right) \tag{6-65}$$

where Y is the transformed variable and X is the original variable.

The weighting function w_i can be set to 1. However, the portion of the curve near 50 mm/yr was slightly emphasized in the matching procedure using the function

$$w_i = \exp[-|\bar{Y}_{qi} - \log(50)|/8], \tag{6-66}$$

where Q is in units of (mm/yr). Decay away from the target flux is relatively gentle.

Example results The independent approach for estimating bulk matrix properties generally predicts that bulk matrix properties are somewhat different than properties obtained through simple averaging, although K_{sat}, P_0, and m are reasonably close to estimated values. The independent approach tends to yield higher K_{sat} than the geometric mean, and the retention properties tend to be representative of a wider pore-size distribution than obtained from a geometric mean (P_0 is larger and m is smaller than the core-scale means). Strikingly, bulk porosity can be much smaller than the average core-sample porosity, at least half to several orders of magnitude smaller.

A simple example based on the TCW equivalent hydrologic formation, representing most of the outcrop area above the repository footprint, demonstrates this procedure. The independent approach was used to generate bulk properties. All regression equations were assumed certain with the best estimate from the samples. The mean, variance, and covariance for porosity, saturation, and bulk density was assumed to be same as the sample properties. A total of 2^{20} core-scale samples were generated for these properties. Using the regression equations, estimates of K_{sat}, porosity, P_0, and m were obtained for each realization, with variability about the regression equation explicitly incorporated for K_{sat}. The regression equation for P_0 and m provides an estimate of the mean values; the variability of P_0 about the mean was assumed equal to the variability of P_c about the regressed retention relation and the variability of m was assumed negligible.

The computed mean K_{sat} for several combinations of column height and number of samples per each row are shown in Figure 6-14a. For comparison, the mean K_{sat} corresponding to the power-law approach is shown using the right-hand axis. The w corresponding to a particular averaging scheme is determined by finding the same mean K_{sat}.

In general, as local lateral flow increases the bulk K_{sat} also increases. When each column has a cross section of only 4 to 8 cores, the corresponding w is greater than 0 (bulk K_{sat} is more conductive than the geometric mean). This result is in contrast to the suggestion that $w = -0.4$ is appropriate for YM. Bulk K_{sat} may be more than an order of magnitude larger than suggested by the power-law average with $w = -0.4$, perhaps in the range of 0.4 to 0.6 instead.

The results of using a power-law average for the remaining 3 factors are shown in Figures 6-14 and 6-15. For this example, bulk K_{sat} and P_0 obtained through the independent approach have roughly the same w. On the other hand, van Genuchten m and porosity do not match with any power-law expression. The m and P_0 parameters change simultaneously consistent with a change in texture (*e.g.*, both may change to indicate a wider pore-size distribution), although neither parameter changes dramatically. The most striking impact is on porosity; as the ability for lateral redistribution increases, porosity dramatically decreases. Only a few columns contribute the bulk of the flow, while most pore space is not within a significant flow path.

Effect of spatially variable statistical parameters The example shown in Figures 6-14 and 6-15 assumes that adjacent core-scale realizations are uncorrelated, but in actuality local correlation may exist. Istok et al. (1994) examined the variability of the welded-to-nonwelded transition in the shardy base of the TCw unit, with core samples obtained from 26 vertical transects along 1.3 km of the west flank of YM in Solitario Canyon (SC). The vertical transects had horizontal

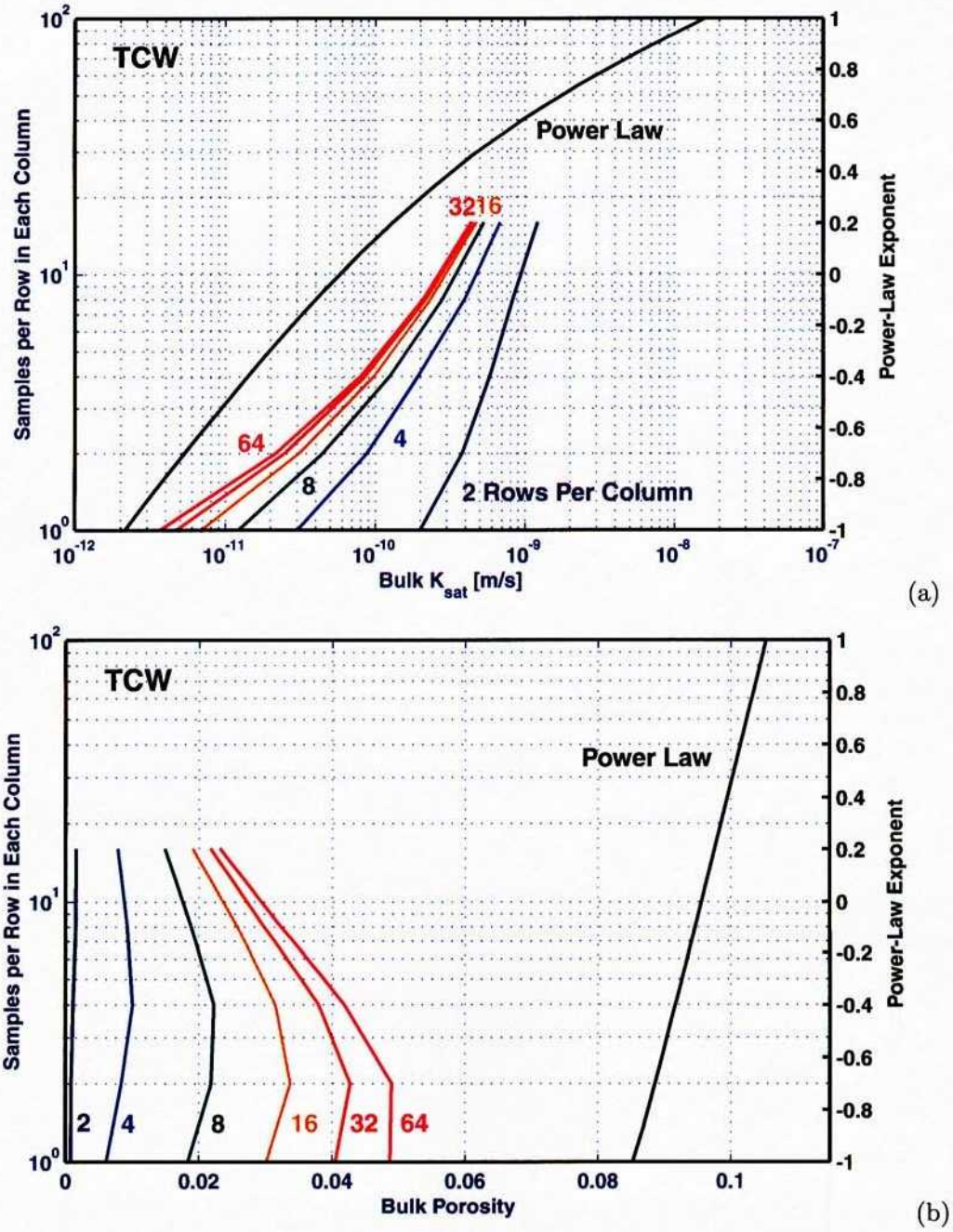

Figure 6-14: Bulk properties for the TCW equivalent hydrologic unit for 2^{20} realizations. Column-based and power-law averaging approaches are compared for (a) K_{sat} and (b) porosity. Numbers adjacent to the curves denote the number of rows in each column.

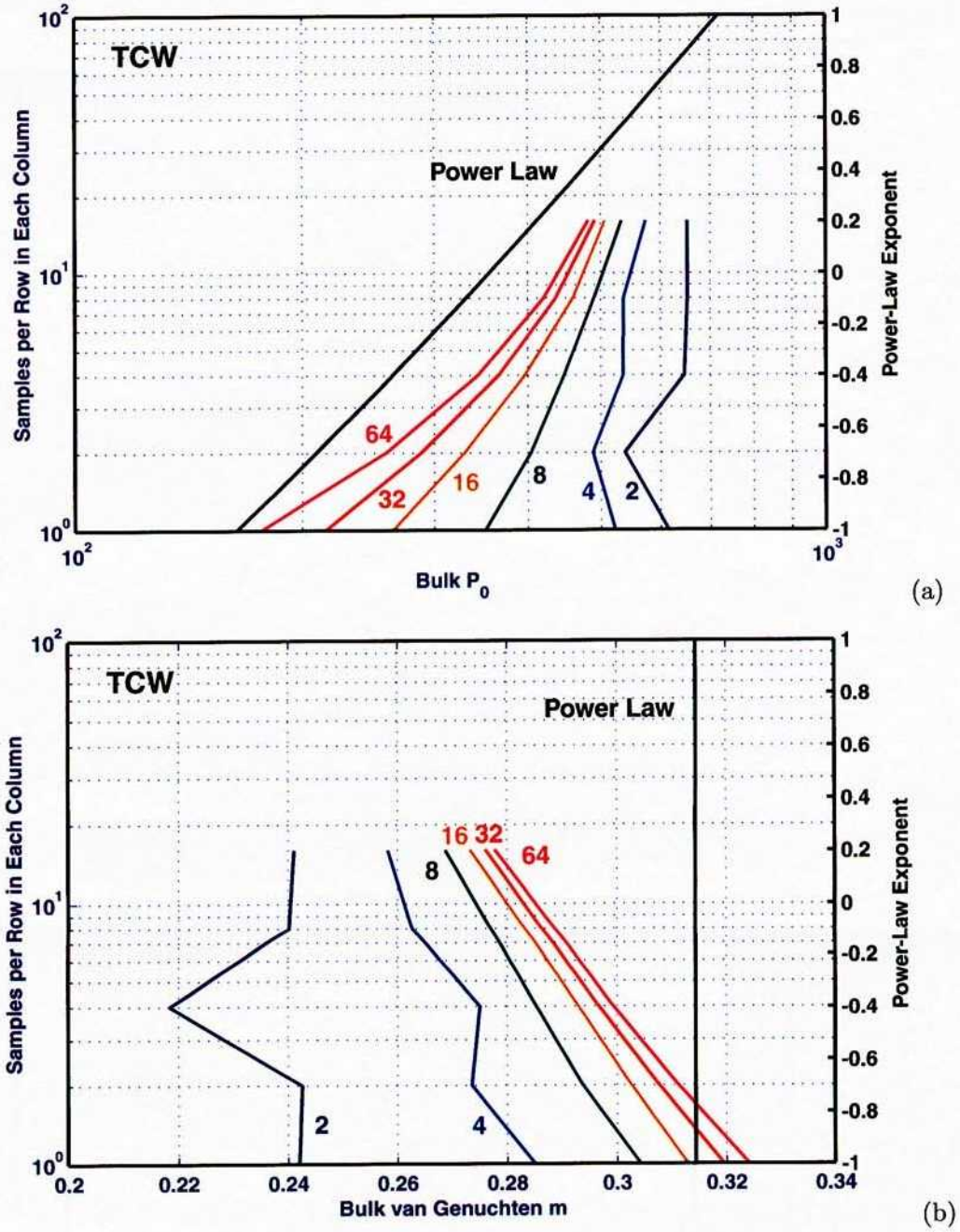

Figure 6-15: Bulk properties for the TCW equivalent hydrologic unit for 2^{20} realizations. Column-based and power-law averaging approaches are compared for (a) P_0 and (b) van Genuchten m. Numbers adjacent to the curves denote the number of rows in each column.

spacing between 19 and 200 m and vertical spacing between 0.15 and 2.9 m, with total stratigraphic thickness of 30 to 40 m. The analysis grouped the cores into relative stratigraphic coordinates (*i.e.*, fraction of distance between bottom and top of the stratigraphic sequence). Strong vertical trends were observed, based on cooling history, and a regression equation was fit for both porosity and $\log_{10}(K_{sat})$. Little or no horizontal trending was observed within the 1.3 km zone (other outcrop and borehole samples north and east of the sample zone varied from the vertical profile, which was attributed to different emplacement environments due to distance from the source). Deviations from the vertical regression curve were fit with a pure nugget (no local correlation), as were deviations from the horizontal, suggesting that correlation may be negligible even for separations as little as 3 sample-lengths apart.

Based on the results of Istok et al. (1994), it is probably reasonable to assume that properties of adjacent core samples are independent given the deterministic trend in properties based on emplacement history. The deterministic trend in properties is usually not known, however, providing a source of uncertainty that may be handled as long-range correlation with much longer length scales in the horizontal. Accordingly, overall variability can be partitioned into long-range correlation and a nugget of pure variability. The example assumes that all variability is due to the nugget effect. Correlation reduces variability, which reduces the difference between harmonic and arithmetic means. However, horizontal correlation enhances lateral movement, which allows water greater latitude to find a pathway around local barriers and drives the mean towards the arithmetic-average endpoint.

In the equivalent hydrologic units, horizontal correlation is probably least important in the welded units and most important in the nonwelded units. Low horizontal correlation implies relatively long columns, while high horizontal correlation implies relatively short columns. However, longer columns have more of a chance to explore local heterogeneity and thus the number of realizations per row should be greater than in cases with short columns. Accordingly, a fairly wide range of properties have relatively similar bulk K_{sat} and P_0. The van Genuchten m parameter does systematically vary to some extent, but long-and-wide columns yield similar m as short-and-narrow columns. Bulk porosity systematically varies with column length and width to a greater extent, but again there is some compensating response as columns move from slender to stout.

In summary, it is reasonable to assume that the effects of core-scale heterogeneity, given known statistical properties, may be bounded in this example with averaging columns on the order of 16 to 64 cores in height and 4 to 16 in cross section. These averaging schemes correspond to a power-law average for K_{sat} and P_0 of w between 0 and 0.6 (typically the same factor for both properties) and a reduction in bulk porosity by a factor of 5 to 10 relative to the arithmetic mean.

The van Genuchten m parameter is reduced as P_0 increases, consistent with a wider pore-size distribution. Similar results are obtained for the other equivalent hydrologic units. By implication, bedrock matrix properties used to date in modeling infiltration may be somewhat misrepresented, particularly K_{sat} and porosity.

Effect of uncertain statistical parameters The statistical description of the core-sample hydraulic properties is based on core samples. Because of the limited (albeit large) number of samples, there is uncertainty regarding the actual statistical description. The uncertainty in bulk hydraulic properties resulting from the limited number of core samples can be formally assessed with the assumption that the core samples are randomly selected from the population of potential core samples across the entire region. The calculated bulk properties thus represent the equivalent formation as a whole.

A first-order sensitivity of each bulk hydraulic property to each statistical parameter is assessed by perturbing each statistical parameter, one at a time, and calculating the corresponding change in each hydraulic property. The resulting sensitivity, S_{ij}, is

$$S_{ij} = \frac{\partial H_i}{\partial Z_j} \tag{6-67}$$

where H_i represents hydraulic property i and Z_j represents the normalized deviation of statistical parameter j. The mechanisms for sampling from an uncertain statistical distribution are developed in Section 6.1.1. A pair of evaluations are used to assess sensitivity to each particular statistical parameter j by setting Z_j to -4 and 4, respectively, and calculating H_i for both values. The range in Z_j encompasses 4 standard deviations on either side of the mean value, an extremely large range.

There are 17 coefficients with sensitivities assessed. These coefficients include

- 3 coefficients for the K_{sat} regression equation (a_{10}, a_{11}, a_{12})
- 3 coefficients for the P_0 regression equation (a_{20}, a_{22}, a_{23})
- 2 coefficients for the m regression equation (a_{30}, a_{33})
- 3 means for well-sampled properties (m_1, m_2, m_3)
- 3 variances for well-sampled properties (v_1, v_2, v_3)
- 3 correlation coefficients between well-sampled properties (r_{12}, r_{13}, r_{23})

The a_{ij} coefficients are regression coefficients for under-sampled property i for well-sampled property j (the $j = 0$ case is the regression constant). Under-sampled parameters 1, 2, and 3 are K_{sat}, P_0, and m, respectively, while well-sampled parameters 1, 2, and 3 are θ_c, ε, and ρ_p^{105}, respectively.

The base values and sensitivities are summarized for each aggregate formation in Figures 6-16 and 6-17. Each evaluation uses 2^{20} realizations. Averages with three representative power-law weights are shown (-1, 0, and 1, corresponding to harmonic, geometric, and arithmetic averages). Bulk hydraulic properties are assessed using all combinations of 4, 16, and 64 rows and 4, 16, and 64 samples per row. Minimum, mean, and maximum bulk properties for the 9 combinations are shown. In the figures, these six values are clustered in the same sequence (-1, 0, 1 power-law averages; minimum, mean, maximum bulk property) for each equivalent formation.

Variability across the set of 17 coefficients (35 realizations, including the base unperturbed realization) is represented in the figures by a 5-point sequence for each bulk property averaging scheme. The median value is denoted with a dot, while lines connect the maximum value with the 75th quartile and the minimum value with the 25th quartile. Note that in almost every case the 25th and 75th quartiles are essentially indistinguishable from the median, indicating that there is little sensitivity to almost every statistical parameter.

Each 5-point sequence is color-coded according to the source of the sensitivity with the largest absolute value. Three color codes denote coefficients in the regression equations used for K_{sat}, P_0, and m. The remaining three denote (i) a mean for a well-sampled parameter, (ii) a variance for a well-sampled parameter, and (iii) a correlation between well-sampled parameters. In most cases, most or all of the 6 averages for a value have the same source for the largest sensitivity, and usually all but one or two sensitivities are insignificant.

There are several significant inferences that can be drawn based on these sensitivity results. It is important to note that the statistical parameters are quite well estimated in general, at least for equivalent formations. There is usually minimal change in bulk properties even when the "true" statistical parameters are four standard deviations from the estimated parameters; extreme excursions in the plots only occur for one parameter. The TCW, TC, and TMN equivalent formations are particularly well determined; the remaining formations have fewer samples and thus are less well determined. Individual units from the formations generally have few samples, usually fewer than any of the equivalent formations, thus most individual units have properties less certain than any of the equivalent formations. For example, only 12 of 34 units have more than 75 core samples, while all equivalent formations have at least 75 samples.

Sensitivities are usually roughly comparable for different averaging schemes, even when the

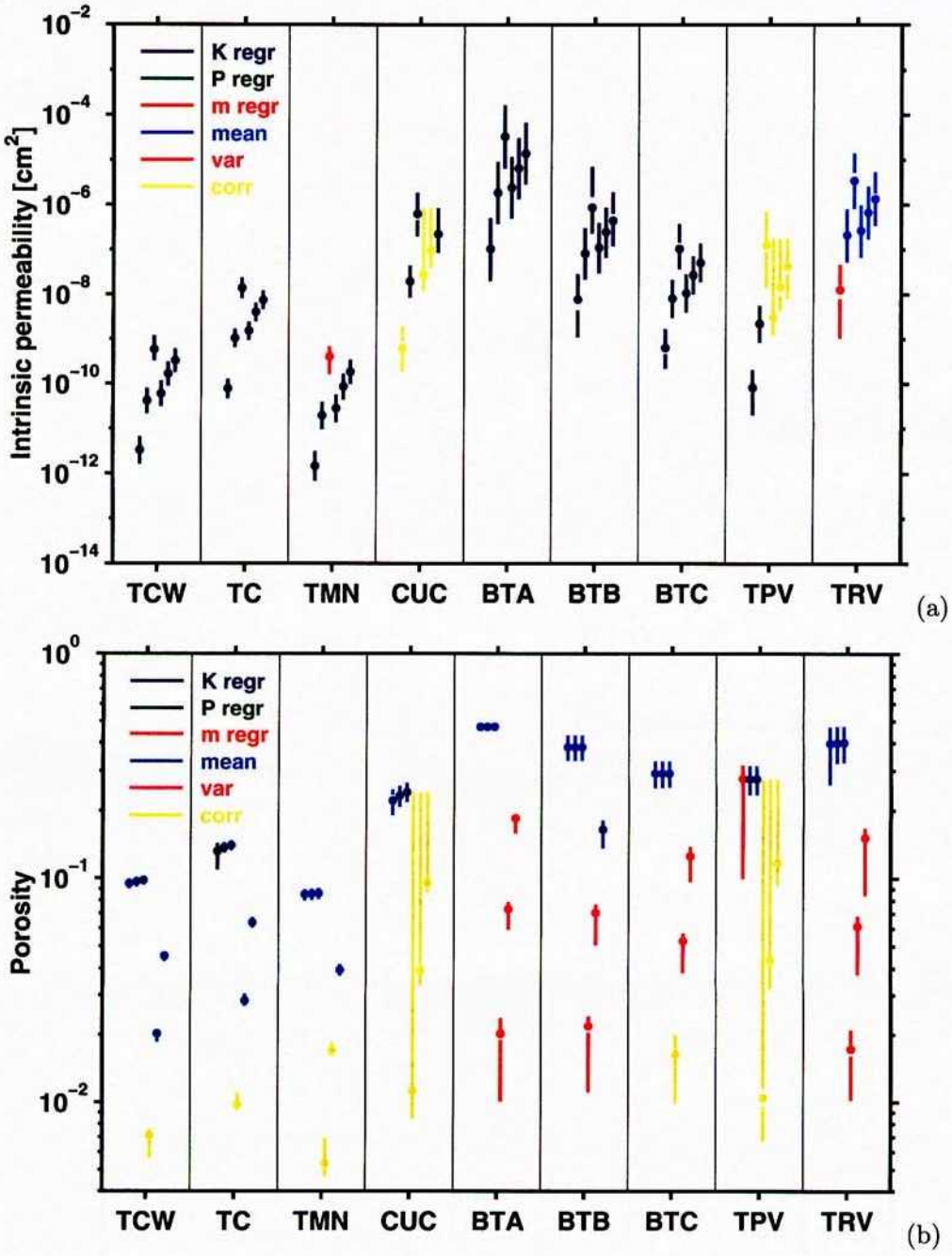

Figure 6-16: Estimates of (a) bulk intrinsic permeability and (b) bulk porosity for 9 equivalent formations using 6 measures (in the sequence of -1, 0, and 1 power-law average, and minimum, mean, and maximum equivalent bulk estimate). The 0, 25, 50, 75, and 100 quartiles are indicated for each measure using a 5-point plot, while the source of the sensitivity with largest absolute value is coded by color.

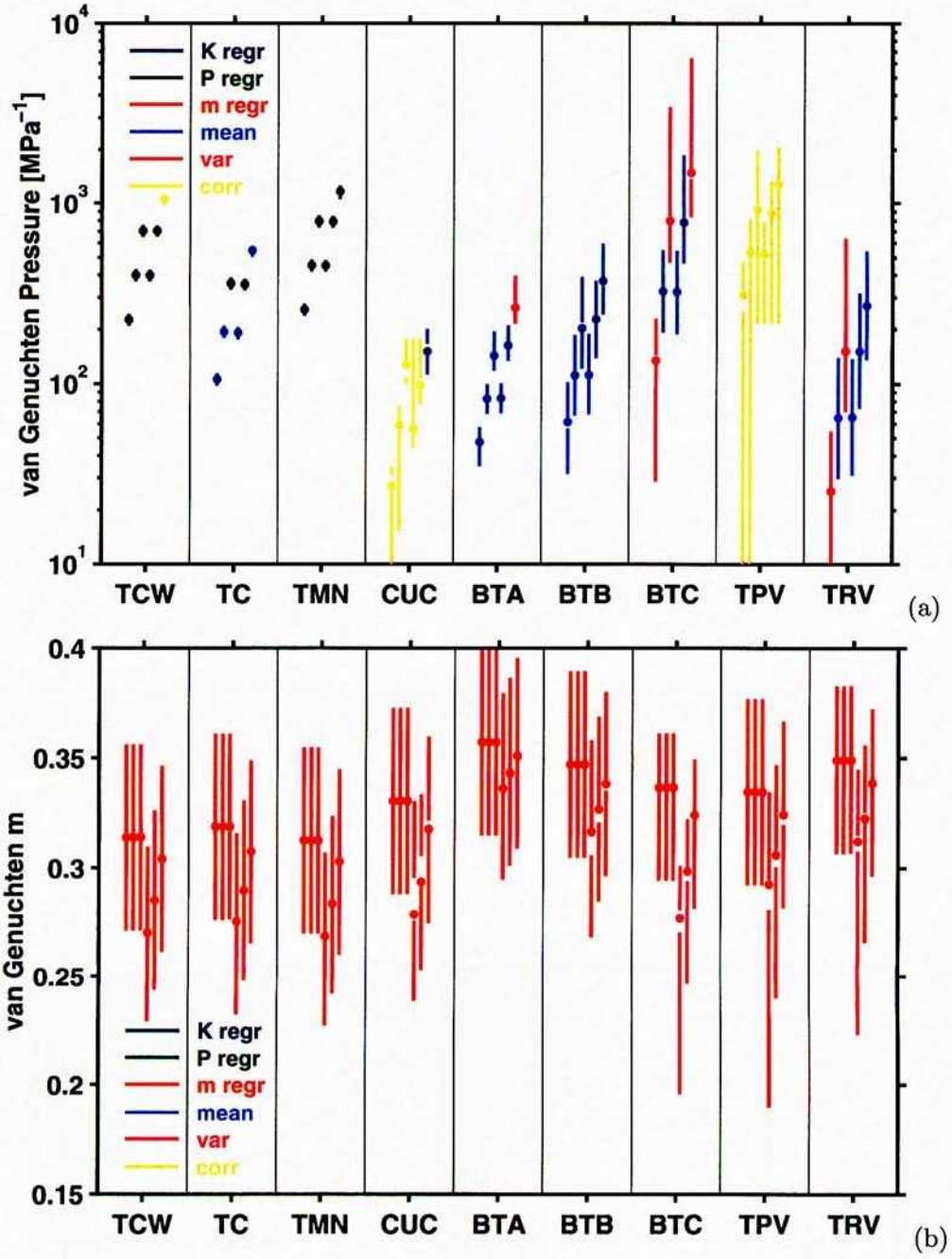

Figure 6-17: Estimates of bulk van Genuchten (a) P_0 and (b) m for 9 equivalent formations using 6 measures (in the sequence of -1, 0, and 1 power-law average, and minimum, mean, and maximum equivalent bulk estimate). The 0, 25, 50, 75, and 100 quartiles are indicated for each measure using a 5-point plot, while the source of the sensitivity with largest absolute value is coded by color.

mean for the averaging scheme is far different. In the less well-determined formations, uncertainty in the well-sampled parameter statistics is generally more important than the regression uncertainty except for m (which has few samples to determine the regression parameters).

It is also important to note that there can be far more uncertainty associated with the averaging scheme than with the number of samples. For example, the range in K_{sat} between different averaging schemes in the TCW equivalent formation is more than two orders of magnitude, while the range for an averaging scheme is about half an order of magnitude. Uncertainty due to averaging scheme is, for each formation, about ± 1 order of magnitude for bulk K_{sat}; about ± 0.5 order of magnitude for bulk P_0; about ± 0.03 for bulk m; and about ± 0.6 order of magnitude for bulk porosity. The averaging scheme used to estimate equivalent bulk properties has a particularly dramatic impact on uncertainty in bulk porosity, which would otherwise be considered quite well known.

The statistical parameters responsible for the uncertainty are ranked in Tables 6-7 through 6-10. The effect of uncertainty is evaluated for each of the 6 averaging approaches and 9 formations, for a total of 54 possible ranks. The most important parameters to capture are those that cause the largest swings in the bulk properties. These parameters are characterized in two ways: (i) whether the response to perturbation exceeds a threshold value, and (ii) the frequency that the response is large in relative rank. Note that if perturbing a statistical parameter frequently causes a large relative response (high rank) but rarely has a large absolute response (low exceedance frequency) the importance of accounting for uncertainty in that parameter is low. Further, it is a sign that the importance of accounting for uncertainty is low for essentially all statistical parameters in at least a few formations.

Uncertainty in the regression coefficient for saturation in the K_{sat} regression equation is the highest-ranking parameter in about half of the cases and dominates the exceedance rankings. Statistical descriptions of the well-sampled parameters accounts for almost all of the remaining high-rank parameters. For formations where there are many core samples to determine the statistics of the well-sampled parameters, other regression-coefficient uncertainty is relatively important but overall uncertainty is low.

For porosity and P_0, the statistics of the well-sampled parameters are most important, particularly the correlation and variance values. Interestingly, saturation statistics are high in the P_0 ranking even though P_0 does not use saturation in the regression equation; this is due to the linking of saturation, K_{sat}, and P_0 when determining equivalent bulk properties. The m parameter, on the other hand, is by far the most sensitive to the regression coefficients describing m.

Table 6-7: Relative ranking of the effect of statistical coefficients on uncertainty of bulk $\log_{10}$ permeability. The first two ranking columns indicate the frequency of large responses to perturbations in the coefficient, while the last three columns indicate how often the coefficient has the 1st, 2nd, or 3rd largest effect. Entries in the first column have ΔH_i greater than the exceedance threshold for $\Delta Z_j = 8$, while entries in the second column have ΔS_i between the two exceedance thresholds.

	Exceedance Threshold		Rank Frequency		
Coefficient	1.25	0.75	1	2	3
a_{11}	6	21	28	14	3
m_1	0	9	5	8	8
m_2	0	6	0	15	19
v_2	0	5	1	6	6
r_{12}	1	3	4	2	4
r_{13}	1	3	2	3	3
r_{23}	0	2	1	1	0
v_3	0	1	1	0	0
v_1	0	1	0	0	1
a_{12}	0	0	12	5	6
a_{20}	0	0	0	0	4
Total	8	51	54	54	54

These results consistently suggest that the regression coefficients are relatively well known (with the possible exception of m). The results also suggest that uncertainty is low in the three equivalent formations with the most core samples (TCW, TC, and TMN) but is more significant in the remaining 6 equivalent formations with relatively fewer samples.

Summary of aggregate bedrock findings The DOE approach to estimating bedrock properties for the purposes of infiltration studies (but not for three-dimensional (3D) site-scale modeling) relies on averaging the properties of core samples obtained from each formation. Porosity is directly measured in the core samples, but the remaining hydraulic properties (which are more expensive to measure) are estimated indirectly using regression equations that link easily sampled properties to the hydraulic properties. Given a full set of core-sample estimates, unit- and formation-scale properties were obtained through power-law averaging.

In order to assess the DOE estimates, an independent set of bulk-property estimates were

Table 6-8: Relative ranking of the effect of statistical coefficients on uncertainty of bulk $\log_{10}$ porosity. The first two ranking columns indicate the frequency of large responses to perturbations in the coefficient, while the last three columns indicate how often the coefficient has the 1st, 2nd, or 3rd largest effect. Entries in the first column have ΔH_i greater than the exceedance threshold for $\Delta Z_j = 8$, while entries in the second column have ΔS_i between the two exceedance thresholds.

	Exceedance Threshold		Rank Frequency		
Coefficient	0.5	0.25	1	2	3
r_{12}	2	2	5	14	8
r_{13}	2	1	4	3	6
v_2	0	3	6	7	10
v_3	0	2	6	12	8
r_{23}	0	1	1	6	10
a_{30}	0	1	1	0	0
m_1	0	0	30	7	7
v_1	0	0	0	2	2
a_{10}	0	0	0	2	1
a_{12}	0	0	1	0	1
Total	4	10	54	54	54

obtained using alternative approaches that attempt to fully account for uncertainty and variability. Independent regression equations were developed linking easily sampled properties to the hydraulic properties of interest. Using the core-scale statistics to generate many core-sample realizations, the power-law averaging approach was compared with a technique that directly estimates the bulk properties from the core samples by matching bulk flux and velocity estimates. Recognizing that estimates of core-scale statistics are uncertain due to limited sampling, the effect of uncertain statistics was also assessed by a perturbation analysis.

The power-law and equivalent-bulk-property approaches match best for K_{sat}, with the equivalent-bulk-property estimates falling between geometric and arithmetic averaging. This is in contrast to the DOE conclusion that the appropriate scheme is between geometric and harmonic averaging. The equivalent-bulk-property estimates are 0.5 to 1.5 orders of magnitude larger than the power-law average using the suggested averaging weight.

The van Genuchten properties are more consistent between schemes, although the equivalent-bulk-property estimates may fall outside the power-law range. The equivalent bulk hydraulic prop-

Table 6-9: Relative ranking of the effect of statistical coefficients on uncertainty of bulk $\log_{10} P_0$. The first two ranking columns indicate the frequency of large responses to perturbations in the coefficient, while the last three columns indicate how often the coefficient has the 1st, 2nd, or 3rd largest effect. Entries in the first column have ΔH_i greater than the exceedance threshold for $\Delta Z_j = 8$, while entries in the second column have ΔS_i between the two exceedance thresholds.

	Exceedance Threshold		Rank Frequency		
Coefficient	1	0.5	1	2	3
v_3	2	4	5	4	4
m_1	0	6	15	24	12
r_{12}	2	3	6	1	0
r_{13}	1	1	6	0	2
r_{23}	0	1	0	0	2
m_3	0	0	8	17	24
a_{23}	0	0	13	5	4
v_1	0	0	1	1	2
v_2	0	0	0	2	1
a_{30}	0	0	0	0	2
Total	5	15	54	54	54

erties tend to describe a somewhat coarser medium than the power-law averages.

The big difference between schemes is in estimating porosity. The equivalent-bulk-property estimates of porosity tend to be 0.4 to 1.2 orders of magnitude smaller than the power-law averages. The implication is that flow is concentrated into relatively few paths within the bedrock while the bulk of the pore space contributes to water storage but not water movement. It makes little difference whether the "dead" storage is accounted for under steady conditions, but there may be implications for transient simulations near the ground surface where the rock may dry out.

A coarser medium with low effective porosity has mixed impacts on infiltration processes relative to a finer medium with high effective porosity. The coarse medium is more efficient in conducting water to depth under wet conditions, as the low porosity and high K_{sat} promote rapid drainage. On the other hand, there may be conditions under which the finer medium will accept water but the coarser medium is a capillary barrier.

Uncertainty in estimates, given an averaging scheme, is low for almost all statistical param-

Table 6-10: Relative ranking of the effect of statistical coefficients on uncertainty of bulk m. The first two ranking columns indicate the frequency of large responses to perturbations in the coefficient, while the last three columns indicate how often the coefficient has the 1st, 2nd, or 3rd largest effect. Entries in the first column have ΔH_i greater than the exceedance threshold for $\Delta Z_j = 8$, while entries in the second column have ΔS_i between the two exceedance thresholds.

	Exceedance Threshold		Rank Frequency		
Coefficient	0.08	0.04	1	2	3
a_{30}	40	14	42	8	2
a_{33}	3	31	9	43	2
v_3	2	3	3	1	5
v_2	0	2	0	1	3
r_{23}	0	2	0	1	2
r_{12}	0	1	0	0	2
m_1	0	0	0	0	33
r_{13}	0	0	0	0	4
Total	45	53	54	54	54

eters, particularly in the equivalent formations with many samples (*i.e.*, TCW, TC, TMN). The remaining formations have estimate uncertainty more comparable to averaging-scheme uncertainty due to the relatively few samples, but typically only one or two statistical parameters contribute essentially all of the uncertainty. If the analysis were to be extended to the level of individual units, estimate uncertainty would be larger than in any of the equivalent formations for about 2/3 of the units.

6.1.5 Fracture properties

Fracture properties affect estimates of MAI in two primary ways. Hydraulic properties of individual fractures determine flow rates for each fracture for particular moisture availability, while the areal average of fracture void space in the bedrock determines the areal average flow through the fractures. These properties have not been examined in detail, thus are subject to a great deal of uncertainty.

Near-surface fractures at YM are usually filled with either the fine component of the overlying soil or a mixture of calcium carbonate and siliceous materials. Based on field observation, the calcium carbonate/silicate fillings appear to be prevalent in systems with relatively fine and

infrequent fractures, such as the lithophysal units of the TCw. Soil fillings are more evident in units with relatively large-aperture fractures and fissures, such as caprock and nonlithophysal units of the TCw unit, although it is possible that carbonates appear at depth in fractures that have soil fillings near the soil/bedrock interface. Unfilled fractures are common in the nonwelded units of the PTn, although little evidence of flow through the fractures is evident Moyer et al. (1996). In welded tuff, however, unfilled fractures appear to be rare. Even apparently unfilled fractures in well-washed areas of welded tuff such as active bare-rock channels in Split Wash appear to have soil fill below the channel bottom, based on observations of drainage rates from ponded waters. Relative distributions of the different fillings in the near-surface environment has seen little or no quantification.

Observations suggest that the texture of soil fillings is similar to the overlying soil, thus it would be expected that the hydraulic properties of soil fillings are also similar to the overlying soil.

It is difficult to extract undisturbed samples of fracture fillings to perform analyses of the fill properties, thus the properties of carbonate and silicate fillings have not been examined in detail. A small number of fill samples analyzed by the United States Geological Survey (USGS) were obtained (personal communication, D. Hudson, 1997; DTN GS950308312210.002 "Preliminary Fault/Fracture Properties" and DTN: GS950708312211.003 "Updated Fracture/Fault Properties for Fast Pathways Model"). Analyzes were performed both perpendicular to the fracture plane and along the fracture plane. Saturated hydraulic conductivity for these samples are shown in Figure 6-18. The limited number of samples is suggestive that flow may be relatively easily conducted along the fractures and restrained from entering the matrix, although it is not clear that all samples represent the same type of fill material. Flint et al. (1996a) used 5×10^{-7} m/s for fracture-fill K_{sat} based on the arithmetic average of this data. Note that the model of Flint et al. (1996a) does not require retention properties for fracture materials.

Baumhardt and Lascano (1993) measured the hydraulic properties of a caliche layer near Lubbock, TX, finding that the vertical and horizontal means (using the logarithm) were 8.72×10^{-6} and 2.26×10^{-5} m/s, respectively. This set of properties are somewhat larger than the along-fracture properties measured by the USGS. Retention properties of the caliche layer were described with van Genuchten parameters $\alpha = 3.555$ kPa^{-1}and $n = 1.271$, which is consistent with a clay texture.

Based on the measured samples and the caliche data, fracture filling K_{sat} is likely between the arithmetic average and Baumhardt and Lascano (1993) values. At the higher end of the K_{sat} range, retention properties are likely similar to clay, but retention properties at the lower end of the K_{sat} range have not been determined. It is not clear how to incorporate the data on across-fracture

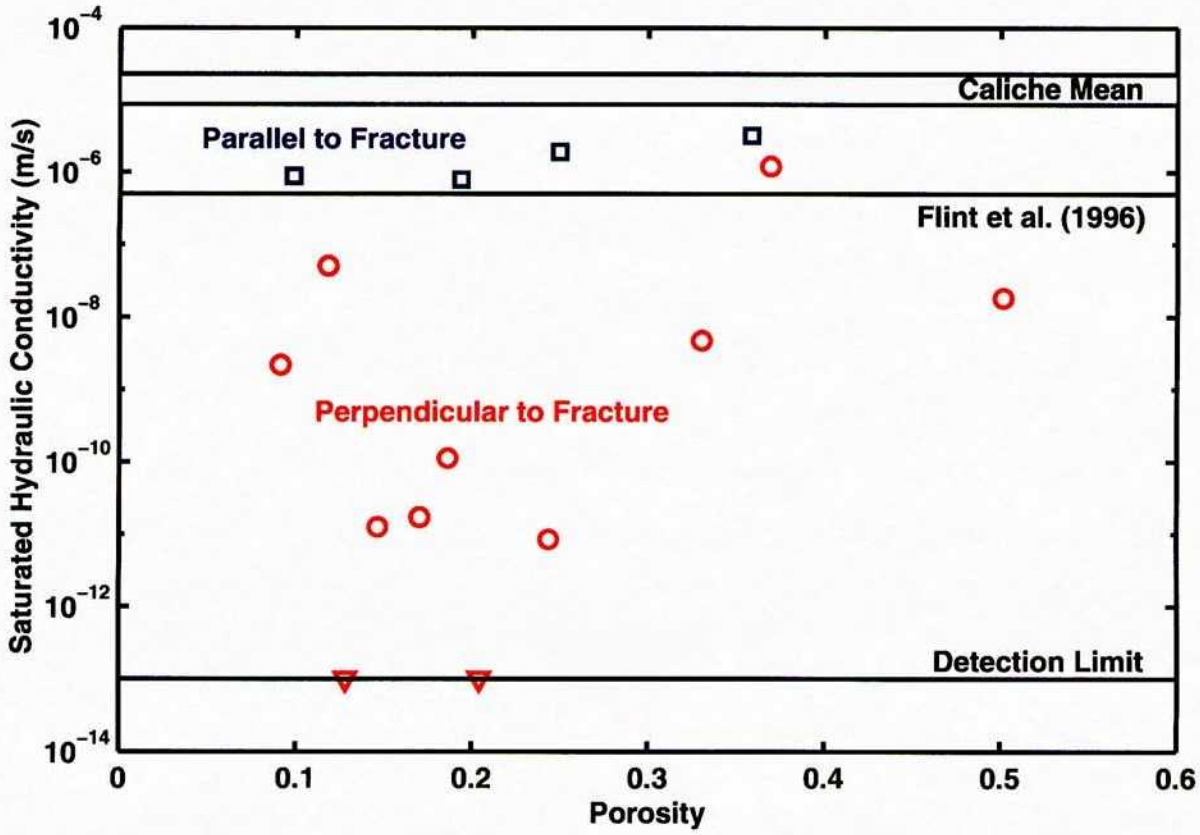

Figure 6-18: Saturated hydraulic conductivity for samples of fracture-fill material. Along-fracture conductivity is consistently greater than 10^{-6} m/s, while across-fracture conductivity may be many orders of magnitude smaller. The vertical and horizontal geometric mean of the Baumhardt and Lascano (1993) caliche data set are shown as a bar. The value used by Flint et al. (1996a) for modeling is the arithmetic average of the sample values.

K_{sat}. There is considerable uncertainty regarding this parameter, however, and it is not clear how to incorporate the data on across-fracture K_{sat}.

Some of the fractures may not be filled and at some depth into the bedrock fill material ceases to exist. Unfilled fractures are likely to have a narrow aperture, or else soil would enter them. Hydraulic properties of unfilled fractures have been examined using the parallel-plate assumption, which relates fracture K_{sat} to the cube of aperture. Obviously aperture is an important parameter to describe the fracture. Fracture retention properties are typically modeled as a very coarse material such as gravel. However, 1D simulations of infiltration that considered soil over unfilled fractures found that MAI is not sensitive to fracture properties, except when there are few fractures

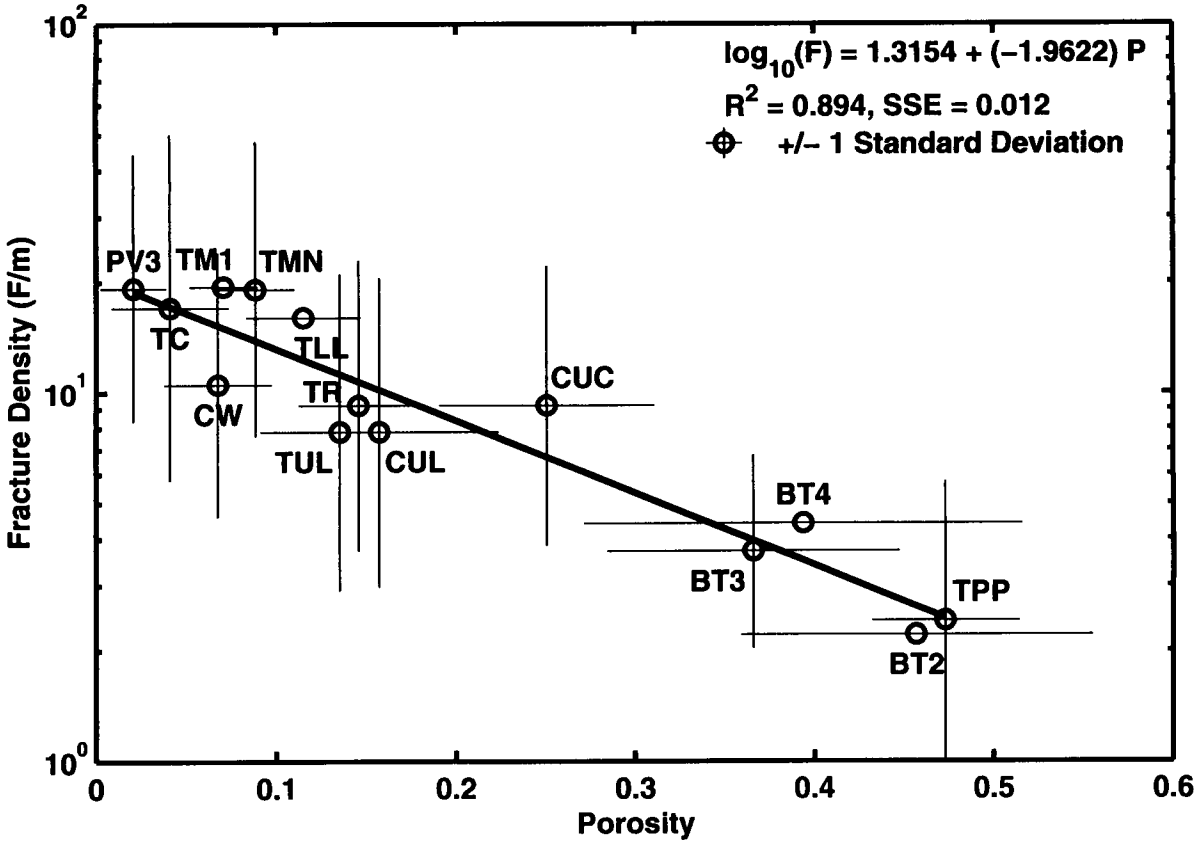

Figure 6-19: Approximate fracture density of hydrologic units compared to the matrix porosity. Uncertainty in porosity values is indicated by ±1 standard deviation in core-sample porosity. Note that lithophysal units tend to fall below the regression line, suggesting that relationship may be stronger if the pore space of the lithophysae is accounted for. Uncertainty in fracture density is unknown.

(Stothoff, 1997). The lack of sensitivity is because the capillary barrier effect that limits flow from the soil to the fracture unless the soil is essentially saturated is strong and the permeability of the fractures is large, thus drainage into fractures is controlled by the ability of the soil to deliver water to the fracture.

Flint et al. (1996a) estimate the fracture void space in the bedrock based on unattributed estimates of fracture density, in terms of fractures/m. A weighted average apportions the relative occurrences of filled and unfilled fractures in 3 aperture classes, although the weights are not presented. The relationship between matrix porosity and fracture density is shown in Figure 6-19, which uses the fracture densities reported by Flint et al. (1996a) and the porosity values for the

core samples reported by Flint (1998). Uncertainty in porosity values is shown as a spread of ± 1 standard deviation about the mean value for each unit.

Uncertainty in fracture density is not considered by Flint et al. (1996a), but Sonnenthal et al. (1997) examined typical fracture spacings in the Exploratory Studies Facility (ESF) for fractures with traces of at least 1 m. The spacing for these fractures is not the normal distance between the center of fractures, thus is only a rough measure of spacing. In most units, the coefficient of variation for fracture spacing appears to be on the order of 1 to 1.5, with the bedded tuffs having a coefficient of variation as small as 0.5. Clearly the distribution must be skewed (*e.g.*, lognormal), as a normal distribution with this coefficient of variation would have in many nonphysical negative observations. The mean fracture density is roughly an order of magnitude smaller than reported by Flint et al. (1996a), ranging from 0.30 to 2.09, thus the fracture sets considered by Flint et al. (1996a) likely also include fractures with much smaller trace lengths. Assuming that a lognormal distribution is appropriate, the linear mean and standard deviation of the fracture spacing provided in Table 7.7 by Sonnenthal et al. (1997) implies that the standard deviation of $\log_{10}$ fracture density is between 0.21 and 0.59, with a mean standard deviation of about 0.38. As a rough guide to uncertainty of fracture density, one-standard-deviation bounds are shown for $\log_{10}$ fracture density in Figure 6-19 wherever direct correspondence can be made between the ESF mapping and the Flint (1998) units.

Variability of the porosity and fracture density measurements shown in Figure 6-19 corresponds to local estimates. The variability of local estimates is larger than the variability of averages. In general, variance of a local average decreases as the reciprocal of the number of values averaged (Vanmarcke, 1984), or $\sigma_N = \sigma/N^{1/2}$, where σ is the standard deviation of the local estimate, σ_N is the standard deviation of the local average, and N is the number of values averaged. For example, the standard deviation of the average fracture density should decrease by an order of magnitude when fractures are considered 100 at a time. Assuming for the sake of argument that the scale of interest to infiltration processes is 1 to 4 m, the standard deviation of fracture density for units with an average fracture density of 2 m^{-1} drops to about 0.71 to 0.35, respectively, of the original value. If the average fracture density is 20 m^{-1}, the standard deviation drops to about 0.22 to 0.11 of the original value. Accordingly, at scales of interest to infiltration processes (*e.g.*, a few meters) the variability of fracture density in bedded tuffs is only somewhat reduced but for welded tuffs the variability is reduced by a factor of 5 to 10. Note that as a typical core sample is roughly 50 cm^3 in volume, there are 2×10^4 samples in a cubic meter of bedrock and the variability of average porosity in a cubic meter of bedrock is reduced to about 0.007 times the variability of core samples.

Independent estimates of fracture void space necessarily are qualitative for most units [,

except for the surveys based in the caprock]. Based on field impressions, the average fracture/fissure void space in TCw units is lowest in the lithophysal units, greater in the nonlithophysal units, and greatest in the caprock. The fracture densities presented by Flint et al. (1996a) are generally consistent with these observations.

Overall, there is a rather large uncertainty in fracture properties due to the paucity of site information. No attempt is made by DOE to account for the uncertainty in properties. Based on the preponderance of evidence that suggests deep penetration of wetting pulses through fast paths, it is clear that fractures form a significant pathway in the subsurface. Implications of this uncertainty are discussed in chapter 5.

References

Baumhardt, R. L. and R. J. Lascano. 1993. Physical and hydraulic properties of a calcic horizon. *Soil Science 155*(6), 368–375.

Benjamin, J. R. and C. A. Cornell. 1970. *Probability, Statistics, and Decision for Civil Engineers.* New York, NY: McGraw-Hill.

Bodvarsson, G. and T. M. Bandurraga (Eds.). 1996. *Development and Calibration of the Three-Dimensional Site-Scale Unsaturated Zone Model of Yucca Mountain, Nevada*, LBNL-39315, Berkeley, CA. Lawrence Berkeley Laboratory.

Bodvarsson, G. S., T. M. Bandurraga, and Y. S. Wu (Eds.). 1997. *The Site-Scale Unsaturated Zone Model of Yucca Mountain, Nevada, for the Viability Assessment*, LBNL-40376, Berkeley, CA. Lawrence Berkeley Laboratory.

Bras, R. L. and I. Rodríguez-Iturbe. 1993. *Random Functions and Hydrology.* New York, NY: Dover Publications, Inc.

Day, W. C., C. J. Potter, D. S. Sweetkind, and C. A. S. Juan. 1998. *Bedrock geologic map of the central block area, Yucca Mountain, Nye County, Nevada.* Miscellaneous Investigations Series I-2601, United States Geological Survey, Denver, CO.

Flint, A. L., J. A. Hevesi, and L. E. Flint. 1996a. *Conceptual and Numerical Model of Infiltration for the Yucca Mountain Area, Nevada.* Milestone 3GUI623M, Department of Energy, Las Vegas, NV.

Flint, L. E. 1996. *Matrix Properties of Hydrogeologic Units at Yucca Mountain, Nevada.* Milestone 3GUP604M, Department of Energy, Las Vegas, NV.

Flint, L. E. 1998. *Characterization of Hydrogeologic Units Using Matrix Properties at Yucca Mountain, Nevada.* Water-Resources Investigations Report 97-4243, United States Geological Survey, Denver, CO.

Flint, L. E. and A. L. Flint. 1990. *Preliminary Permeability and Water-Retention Data for Nonwelded and Bedded Tuff Samples, Yucca Mountain Area, Nye County, Nevada.* Open-File Report 90-569, United States Geological Survey, Denver, CO.

Flint, L. E., A. L. Flint, C. A. Rautman, and J. D. Istok. 1996b. *Physical and Hydrologic Properties of Rock Outcrop Samples at Yucca Mountain, Nevada.* Open-File Report 95-280, United States Geological Survey, Denver, CO.

Istok, J. D., C. A. Rautman, L. E. Flint, and A. L. Flint. 1994. Spatial Variability in Hydrologic Properties of a Volcanic Tuff. *Ground Water 32*(5), 751–760.

Lapin, L. 1983. *Probability and Statistics for Modern Engineering.* Boston, MA: PWS Publishers.

Mason, R. L., R. F. Gunst, and J. L. Hess. 1989. *Statistical Design & Analysis of Experiments With Applications to Engineering and Science.* New York, NY: John Wiley & Sons.

Matalas, N. C. 1967. Mathematical Assessment of Synthetic Hydrology. *Water Resources Research 3*(4), 937–945.

McKenna, S. A. and C. A. Rautman. 1996. *Scaling of Properties for Yucca Mountain– Literature Review and Numerical Experiments on Saturated Hydraulic Conductivity.* SAND95-2338, Sandia National Laboratories, Albuquerque, NM.

Montazer, P. and W. E. Wilson. 1984. *Conceptual Hydrologic Model of Flow in the Unsaturated Zone, Yucca Mountain, Nevada.* Open-File Report 84-4345, United States Geological Survey, Lakewood, CO.

Moyer, T. C., J. K. Geslin, and L. E. Flint. 1996. *Stratigraphic Relations and Hydrologic Properties of the Paintbrush Tuff Nonwelded (PTn) Hydrologic Unit, Yucca Mountain, Nevada.* Open-File Report 95-397, United States Geological Survey, Denver, CO.

Scott, R. B. and J. Bonk. 1984. *Preliminary Geologic Map (1:12,000 scale) of Yucca Mountain, Nye County, Nevada, with Geologic Cross Sections.* Open-File Report 84-494, United States Geological Survey, Denver, CO.

Sonnenthal, E. L., C. F. Ahlers, and G. Bodvarsson. 1997. Fracture and Fault Properties for the UZ Site-Scale Flow Model. See Bodvarsson et al. (1997), pp. 7–1–7–33.

Stothoff, S. A. 1997. Sensitivity of long-term bare soil infiltration simulations to hydraulic properties in an arid environment. *Water Resources Research 33*(4), 547–558.

van Genuchten, M. T. 1980. A Closed-form Equation for Predicting the Hydraulic Conductivity of Unsaturated Soils. *Soil Science Society of America Journal 44*, 892–898.

Vanmarcke, E. 1984. *Random Fields: Analysis and Synthesis.* Cambridge, MA: The MIT Press.

7 Ambient Hydrology KTI – Major Report Meteorology Synthesis

Account Number: **20-5708-861**
Collaborators: **Randy Fedors**

Objective:

8/29/00 Input to Major Milestone.

SAS

Over a period of several months, I wrote up results and inferences in the form of sections of chapters intended to summarize major findings of the infiltration studies over the past few years. Most of the information represents synthesis work, thus it has not been documented along the way. Substantially complete sections are included here, with the numbering scheme used in the original document. These sections represent the working document before formatting as a WordPerfect file and undergoing any CNWRA review.

Some of the figures are not included here. These figures are images based on digital elevation model (DEM) files, which have postscript files that are ponderous (4 to 10 Mb apiece) and make the electronic file untenably large. These figures were submitted to CNRWA as separate files.

The meteorology-synthesis section is included starting here. The original numbering started with section 3, subsection 3, and subsubsection 1.

7.1 METEOROLOGY

Meteorologic inputs have a direct influence on mean annual infiltration (MAI), as will be demonstrated in detail in Section ??. Meteorologic parameters affect the infiltration, runoff, and evapotranspiration (ET) components of a hydrologic balance. The precipitation rate directly affects the balance between infiltration into the rooting zone and runoff, while ET removes infiltrated waters before they can leave the rooting zone and become net infiltration. The meteorologic factors with the most direct influence on MAI are precipitation and temperature, with atmospheric vapor density, cloud cover, and windspeed each having a lesser impact. Each of the meteorologic factors affecting simulations that predict MAI are discussed in this section, both for present-day climatic conditions and for possible future climatic conditions.

Precipitation at Yucca Mountain (YM) is infrequent and episodic. Because precipitation is partitioned between runoff and infiltration based on precipitation rates relative to infiltration rates, it is important for simulations to estimate precipitation rates at a relatively short time scale (*e.g.*, minutes to an hour). Storm magnitudes and storm frequencies are both of interest. However, seasonal variation is also important, as precipitation in low-ET seasons is more effective for net infiltration than is precipitation in high-ET seasons. Over a glacial cycle, both magnitudes and seasonality of precipitation may change. In this section precipitation is examined to estimate precipitation rates at YM under present-day conditions based on regional patterns. Precipitation is known to vary with elevation; the regional patterns provide guidance for estimating the spatial distribution of precipitation at YM. The regional analysis also provides estimates of precipitation at future-climate analog sites, important for relating vegetation and soil observations to YM. Modification of precipitation patterns due to global influences is also examined, including the El Niño and Pacific Oscillation patterns.

The remaining meteorologic parameters affect ET, which is active over seasonal time scales rather than hourly time scales. Numerical experiments indicate that hourly variation in ET-affecting meteorological parameters may be important within a day after rainfall events only for certain shallow soils. In most cases, predicted MAI is essentially unchanged if seasonal-average parameters are used as input instead of hourly parameters, as long as precipitation is applied at hourly intervals in both cases. Thus, the emphasis here is on estimating ET-affecting meteorologic parameters on a seasonal basis, including air temperature, atmospheric vapor density, incident longwave and shortwave radiation, and windspeed. The spatial distribution of these factors is also examined.

7.1.1 Meteorologic sites and records

Meteorologic observations are only available at YM since the 1980s, from the onset of YM site characterization. The relatively short period of record is not sufficient to capture large precipitation events with long return periods, which may dominate MAI. The network of stations provide information on hourly variability spatial distributions of climatic parameters over the relatively short period that the stations have been operated.

Stations with record periods of more than 50 yr exist in the Nevada Test Site (NTS), with recorded daily precipitation totals and temperature extremes. Several of the NTS stations (particularly 4JA and Area 12) are used for Department of Energy (DOE) infiltration modeling (Flint et al., 1996).

The National Weather Service (NWS) maintains an extensive network of meteorological stations across the United States (US). Daily summaries of precipitation and temperature extremes are the most plentiful data type, available for numerous COOP stations. Hourly records are available for a fraction of these stations, with the closest station located at Desert Rock airport (Mercury, NV). Sites with longer hourly records are available at 5 Nevada cities (Elko, Ely, Las Vegas, Tonopah, and Winnemucca).

7.1.2 Analysis of historical records

Historical records of climatic parameters provide guidance on expected behavior at YM and future-climate analog sites. Particular values of interest include seasonal precipitation, storm magnitude and frequency, and seasonal temperature changes.

Daily precipitation and temperature-extreme records, from station inception through 1997, were obtained for the network of COOP stations in Arizona, California, Nevada, and Utah. These data are available on CD-ROM from the National Climatic Data Center (NCDC) web site (www.ncdc.noaa.gov). A reduced set of stations was obtained by restricting the analysis to include all NV stations, all UT stations west of longitude W 113°, all AZ stations west of longitude W 113° and north of latitude N 35°, and all CA stations east of longitude W 118.2° and north of latitude N 34.5° (north of the San Gabriel mountains and east of the crest of the southern Sierra Nevadas). All stations in Inyo and Mono counties were also explicitly included. The boundaries were selected to include stations in more-or-less the same climatic regime as YM under present or future conditions, with at least a 2-degree buffer on every side of YM. The Sierra Nevada and San Gabriel ranges make natural boundaries, while the northern and eastern boundaries are more diffuse. The set of stations was further reduced by eliminating stations with record lengths less than a cutoff value (*e.g.*, 5 yr for temperature). The stations used in subsequent analyses are shown in Figure 7-1 and are listed in Appendix B.

The overall region bounded by latitudes N 34° and N 42° and longitudes W 113° and W 120° was divided into thirds by both latitude and longitude to yield 9 subregions, facilitating comparisons of climate across the region. The subregions are indicated in Figure 7-1. Under the regional subdivision, YM (latitude N 36.83° and longitude W 116.5°) is almost midway between the central and mid-southern subdivisions. The eastern and northern subdivisions are useful for examining the effect of monsoonal and future glacial conditions.

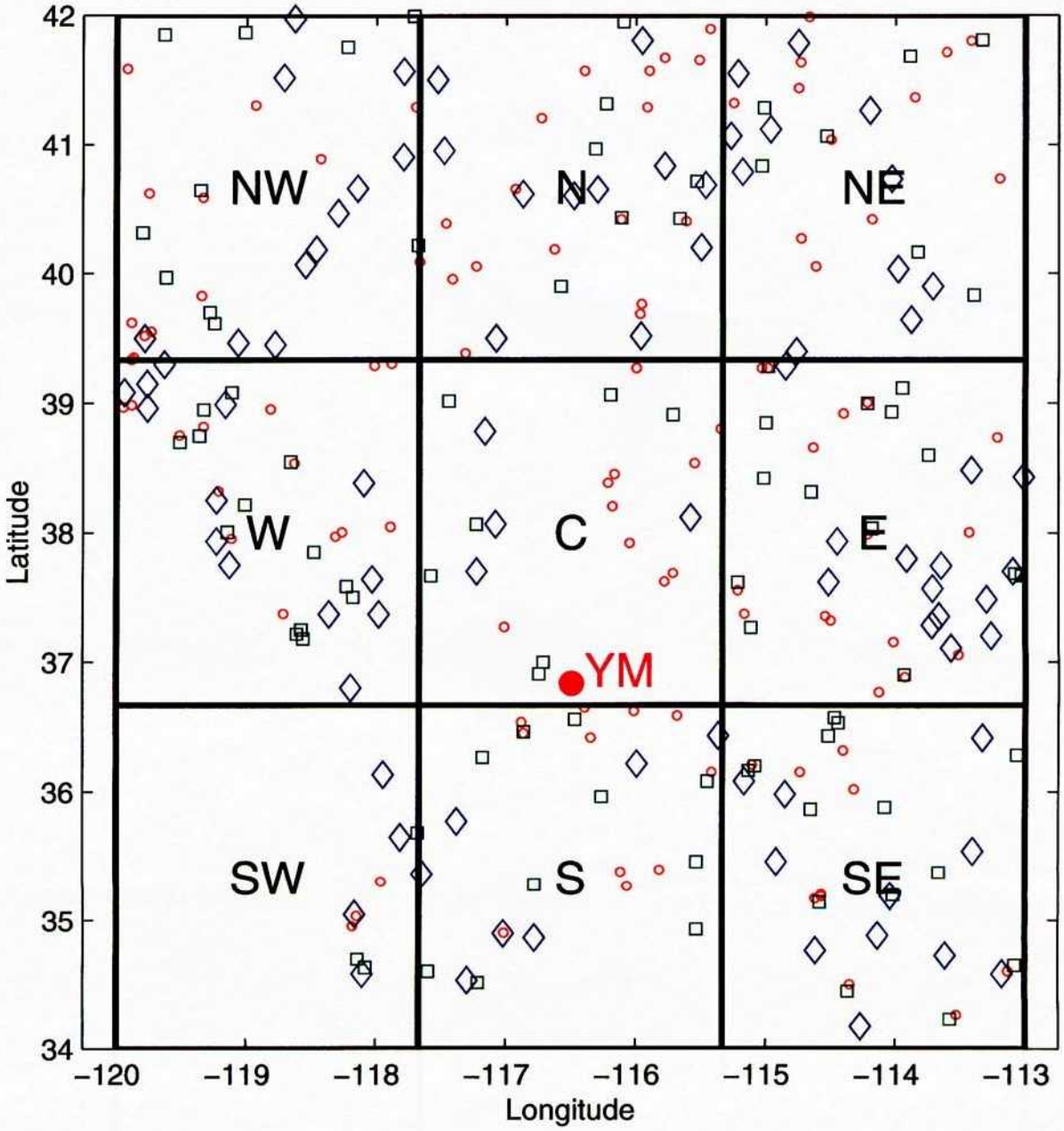

Figure 7-1: Locations of COOP and WBAN stations used in meteorological analyses. Red circles denote record lengths of 5 to 20 yr, green squares denote record lengths of 20 to 40 yr, and blue diamonds denote record lengths of greater than 40 yr. Regions used in subsequent analyses are shown for reference.

Seasonal variation of precipitation The predominant weather patterns in the southwestern U.S. change during the year (TRW, 1998). Northern Pacific cyclonic fronts are important November through April, arriving from the northwest. Eastern Pacific cyclonic fronts are important April through June, October, and November, arriving from the southwest. Gulf of California tropical storms are important in August and September, arriving from the south. And Gulf of Mexico monsoon storms are important in July and August, arriving from the southeast. The effects of these seasonal variations on precipitation is demonstrated using all COOP stations in the region with at least 40 yr of precipitation records.

Mean daily precipitation provides a measure of how much moisture is available for infiltration. Mean daily precipitation is shown with a linear scale in Figure 7-2 and a logarithmic scale in Figure 7-3. Mean daily precipitation as snow is shown in Figure 7-4. Mean daily precipitation for each Julian day of the year is obtained by averaging the precipitation for the same day in every year observations were made. As precipitation is episodic and infrequent, the statistics are quite noisy; accordingly, a moving average of 60 days is used to smooth the noise (the daily value is replaced by the average of the month prior and subsequent to the day). A similar averaging procedure is used for each of the figures in this section.

Elevation has a marked influence on precipitation, which can obscure the influence from the various weather patterns. Comparing Figure 7-2 with Figure 7-3 suggests that precipitation patterns are approximately exponentially distributed with elevation.

The records from the COOP stations tend to show influences from three major sources. Northern stations, dominated by the northern Pacific cyclonic fronts, tend to have a moderately dry summer, with roughly half of the precipitation as the remainder of the year. Southern stations, dominated by the eastern Pacific cyclonic fronts, tend to have much drier cyclonic contributions (roughly 1/10 of winter precipitation). Monsoon contributions strongly overprint the cyclonic signatures in the southeastern region, decreasing to the west and north.

The overall moisture availability patterns are only part of the picture. The typical storm size and frequency is also important; short intense storms have a different hydrologic impact than do extended low-amplitude storms. The overall patterns represented by seasonal mean daily precipitation are broken into frequency and magnitude components in the next series of figures.

The frequency that storms occur is indicated in Figure 7-5. A moving average of 60 days is used to smooth the curves. For each Julian day of the year, the number of wet days over the period of record is divided by the number of days with observations to obtain a daily frequency. For example, if there are 4 days with precipitation on Julian day 9 (*i.e.*, January 9) and 40 years with

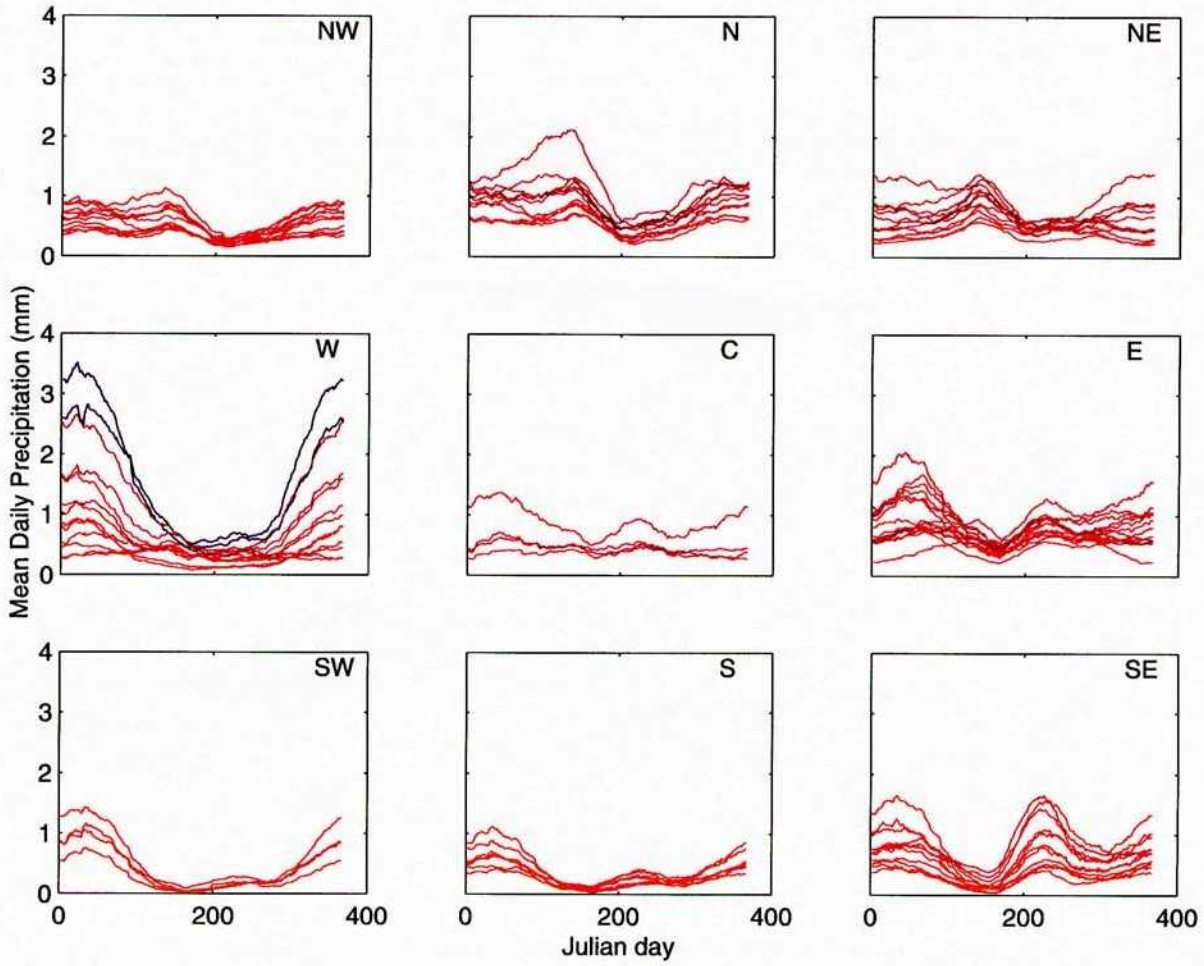

Figure 7-2: Mean daily precipitation for each COOP station with a record of at least 40 yr over the station's period of record. Smoothing used a 60-day window. Station elevation is denoted by color, with red for low elevations and blue for high elevations.

records on Julian day 9, the daily frequency is 0.1 and wet days occur, on average, every tenth day. Plotted on a logarithmic scale, clearly the frequency of wet days is strongly elevation dependent, but otherwise similar within a subregion.

The frequency curves show that the cyclonic component of precipitation has a similar relative frequency for all elevations, with relatively frequent storms in winter and relatively infrequent storms in summer. Increasing elevation increases the actual frequency of cyclonic storms but not the relative frequency (*i.e.*, winter storms may occur three times as frequently as summer storms in a particular region regardless of elevation). Latitude alters the relative distribution of cyclonic

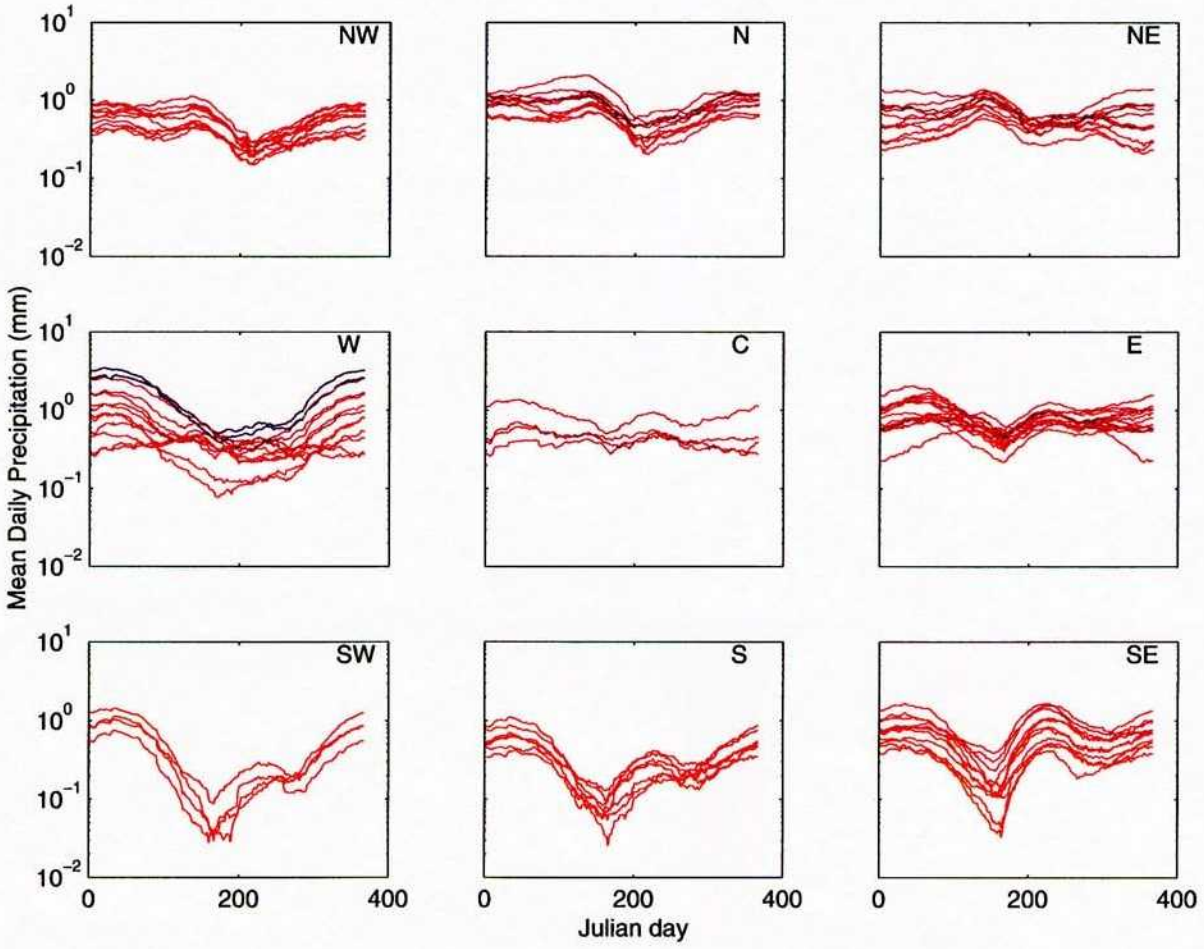

Figure 7-3: The same curves shown in Figure 7-2 plotted on a logarithmic scale.

storms between winter and summer, with winter storms 10 times as frequent as summer storms in the south and less than 3 times as frequent in the north.

The monsoonal component varies across the region of interest, with an evident signature in the southeast that decreases to the north and west and completely disappears in the NW subregion. The monsoonal component increases in frequency as elevation increases, consistent with evaporation losses during precipitation (virga). Although the overall frequency of storms at YM during the summer monsoon is less than during the winter, monsoonal storms may be as much as 2 to 3 times more frequent than cyclonic storms during the peak of the monsoonal period. In the southeast region, monsoon-peak summer storms can be more frequent than winter-peak storms at higher elevations.

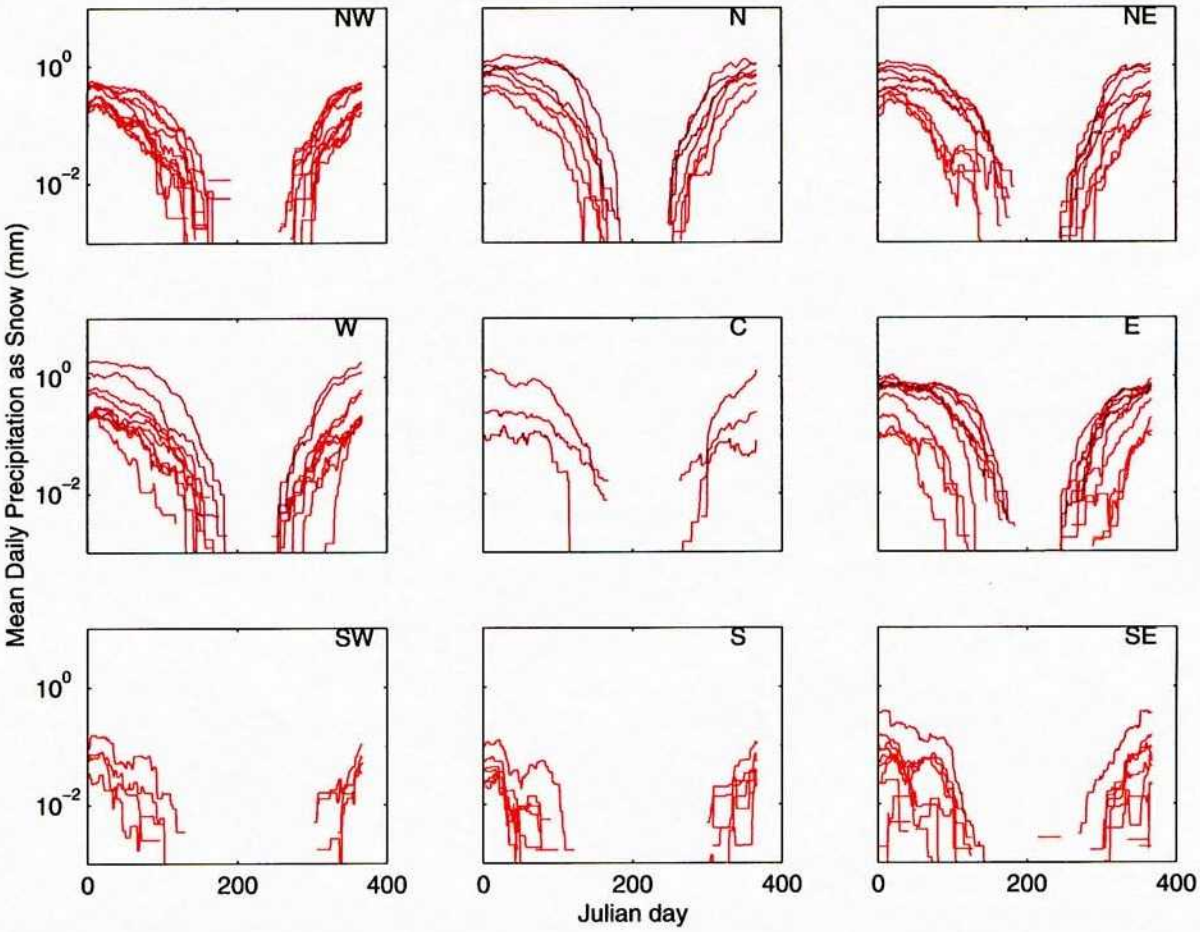

Figure 7-4: Mean daily precipitation as snow for each COOP station with a record of at least 40 yr over the station's period of record. Smoothing used a 30-day window. Station elevation is denoted by color, with red for low elevations and blue for high elevations.

The mean daily wet-day precipitation is shown in Figure 7-6. This measure indicates the seasonal change in typical total storm precipitation. In all regions, there is a tendency for increasing elevation to result in exponentially increasing wet-day precipitation as well as exponentially increasing frequency of wet days. The elevation dependence of wet-day frequency and wet-day precipitation appear to have a comparable influence on mean daily precipitation. Based on the daily patterns, it is likely that the increased wet-day precipitation is due to both longer storm duration and greater storm intensity with elevation, but this cannot be verified using the daily information.

As with the frequency data, there are clear patterns based on storm origin. Northern Pacific cyclonic storms tend to have daily wet-day precipitation totals that are relatively uniform across

the year. Somewhat greater wet-day precipitation (roughly 1.5 times greater) occurs in late spring and early autumn than during the remainder of the year. Eastern Pacific cyclonic storms tend to provide significantly greater precipitation (roughly 3 times greater) during the winter than during the summer. The transition between northern and eastern Pacific dominance is clearly seen in the W subregion, with a mixture of the NW and SW patterns. In the southeast, summer monsoonal precipitation can provide total storm precipitation equivalent to or slightly greater than the winter storms. Elevation appears to be less important than station location relative to storm tracks in determining the seasonal dependence of storm magnitude.

The overall precipitation patterns observed for northern stations, dry summers relative to the rest of the year, are primarily due to decreased storm frequency with storm magnitude having a smaller influence. The cyclonic component of southern stations is exaggerated relative to the northern stations, with much drier summers than winters. Winter storms are both relatively frequent and large in magnitude relative to summer cyclonic storms. In the northeastern region, a peak in precipitation occurs in late spring caused by relatively greater storm frequency and magnitude. The southern stations have a corresponding lull in both frequency and magnitude.

The monsoon signature dominates the cyclonic signature in the summers in the south and east, with increasing importance at higher elevations. In the southeast, monsoon storm frequency is greater than winter storm frequency at higher elevations; otherwise the winter frequencies are greater. Monsoonal storms tend to be comparable or larger than the winter storms. These tendencies are exaggerated for stations further east than considered here, such as Tucson, where the monsoon dominates annual precipitation.

Mean annual precipitation Mean annual precipitation (MAP) is an important overall descriptor of moisture availability, although seasonality and episodicity are also important. The spatial distribution of MAP is an important factor in estimating the spatial distribution of MAI. Using the regional set of COOP stations, an independent estimate predicting the regional variation of MAP is developed here.

Precipitation patterns vary considerably over the region, thus it is no surprise that MAP also varies considerably over the region. It is apparent from Figure 7-3 that, within an area with similar storm tracks, mean daily precipitation increases roughly exponentially with increasing elevation. Thus, consistent with the findings of Hevesi et al. (1992b), the logarithm of MAP may be better predicted than untransformed MAP.

Several schemes were investigated to predict mean annual $\log_{10}$ precipitation (MAlP) =

$\log_{10} MAP$, primarily involving polynomial interpolations based on elevation, latitude, longitude, and products of these factors. With sufficient high-order terms, more than 70 percent of the variability is explained. However, formulae using high-order polynomials are not transparent to analyze and it is computationally demanding to search the possible combinations. An alternative approach is adopted here that uses elevation, latitude, longitude, and a set of radial basis functions to predict MAlP. The basis functions provide local modification to the regional interpolation. The number of basis functions should be kept as small as possible so that the number of undetermined coefficients is much smaller than the number of observations.

The formula for interpolation using radial functions is written

$$\hat{Y} = a_o + a_z N_z + a_g N_g + a_t N_t + \sum_i a_i P_i(N_g, N_t) \tag{7-1}$$

$$N_z = z/1000 \tag{7-2}$$

$$N_t = (L_t - 34)/(42 - 34) \tag{7-3}$$

$$N_g = (L_g - 113)/(120 - 113) \tag{7-4}$$

$$P_i = \left[(N_g - N_{gi})^2 + (N_t - N_{ti})^2\right]^{1/2} \tag{7-5}$$

where $\hat{Y}$ is predicted MAlP, L_t is north latitude in decimal degrees, L_g is west longitude in decimal degrees, z is elevation in meters, the i subscripts denote the location of interpolation poles, and the a variables denote regression constants. Both radial and inverse-radial ($1/P_i$) basis functions were examined. Radial functions performed slightly better than inverse-radial functions and are defined when a pole is located over a COOP station. The interpolations from inverse-radial functions are not discussed further.

Two data sets are used in the regression results: all 171 COOP stations with at least 20 yr record length, and the 86 of these stations with at least 40 yr record length. For both sets, 4 regressions are presented: (i) elevation only; (ii) elevation, latitude, and longitude; (iii) elevation, latitude, longitude, and 9 poles located at the corners and half points ($N_g = 0, 1/2$, and 1; $N_t = 0, 1/2$, and 1); (iv) elevation, latitude, longitude, and 16 poles located at combinations of $N_g = 0, 1/3, 2/3$, and 1, and $N_t = 0, 1/3, 2/3$, and 1.

The results of the regressions are shown in Figures 7-7 and 7-8. The COOP stations are represented by filled circles, with the size of the circle proportional to record length. The color of the circle is red if the station is in the south and blue in the north. The color of the fill is yellow if the station is in the west and green in the east; stations near YM are red with yellow centers. Regression equations are included in the figures, as are the values of R^2 (fraction of variability explained by the regression).

Additional stations shown in the plots were not used in the regression and provide an independent check. The precipitation values for nine DOE met stations in the YM area over the period 1986 through 1997 (for 5 stations) or 1993 through 1997 (for 4 stations) are shown as crosses in the scatterplots. Note that this period was wetter than the long-term average, and the observated values are wetter than the regression predicts.

Stations within the NTS with MAP values reported by Hevesi et al. (1992b) are shown as squares in Figures 7-7 and 7-8. The record periods are between 16 and 25 yr for these stations.

Outside of the YM project, the United States Geological Survey (USGS) has operated a set of high-elevation precipitation gauges in southern and eastern Nevada. ¡reference from D. Groeneveld¿ The sites range from 7,760 through 10,650 ft in elevation. The observations were made by emptying the gauges twice a year, in October and in May. The record length is from 1984 through 1998 for some and 1986 through 1998 for the others. Note that it is difficult to measure snowfall, particularly with untended stations, and there is reason to believe that the actual snowfall may have been greater than measured. Further, the data may show local effects, as the data sets for the stations do not show increasing precipitation with elevation as would be expected. Nevertheless, the data provide a qualitative check on the high-altitude portion of the regression. The high-altitude observations are shown as diamonds in the plots.

The regression fits show increasingly good fits to the data as additional regression variables are added, as is expected. Using only elevation as a regression variable explains half of the variability in MAlP. With the maximum number of regression variables, almost 7/8 of the variability is explained; intermediate numbers of regression variables provide intermediate results.

The external data provides a useful check on the predictions. The high-altitude data straddle the regression predictions in all cases, supporting extrapolations above the high end of the elevation range. Interestingly, the observations from the NTS and DOE YM stations become increasingly larger than regression predictions as the number of regression variables increase, although the observations are within or on the edge of the scatter from the stations used for the regression. Regressions using only stations with at least 40 yr of data tend to predict slightly lower MAlPin the YM area than regressions using stations with at least 20 yr of data. Accordingly, NTS and YM observations are slightly better matched with the 20-yr regressions. Note that there are few COOP stations with 40-yr records near YM and the 20-yr regressions provide better spatial coverage. Accordingly, the 20-yr regressions may be preferable to the 40-yr regressions near YM.

The regression analysis equations can be reduced to a relationship solely dependent on elevation if the latitude and longitude are specified. Selecting a location centered on YM (N 36° 50'

Table 7-1: Regression equations for MAlP as a function of elevation in the form $\hat{Y} = a + bZ$, where $\hat{Y}$ is predicted MAlP and Z is in km.

a	b	R^2	N	Source
1.872	0.228	0.48	63	Southern NV (French, 1986)
1.902	0.271	0.76	12	NTS (French, 1986)
1.876	0.256	0.56	42	YM region (Hevesi et al., 1992b)
1.850	0.281	0.79	1531	Cokriged grids (Hevesi et al., 1992a)
1.875	0.280	–	–	YM region (Hevesi, 1999)
1.999	0.233	0.52	171	20-yr stations, elevation
1.947	0.270	0.49	86	40-yr stations, elevation
1.973	0.245	0.60	171	20-yr stations, elev/lat/long
1.917	0.293	0.56	86	40-yr stations, elev/lat/long
1.790	0.291	0.75	171	20-yr stations, elev/lat/long/4 poles
1.701	0.340	0.75	86	40-yr stations, elev/lat/long/4 poles
1.776	0.292	0.81	171	20-yr stations, elev/lat/long/9 poles
1.658	0.363	0.87	86	40-yr stations, elev/lat/long/9 poles
1.793	0.286	0.83	171	20-yr stations, elev/lat/long/16 poles
1.703	0.338	0.87	86	40-yr stations, elev/lat/long/16 poles

latitude, W 116° 30' longitude), the various relationships predicting MAlP are summarized in Table 7-1. The newer relationships are compared with the equations developed by French (1986) and Hevesi et al. (1992b) in Table ta:lPregYM and in Figure 7-9.

The equations all have generally similar coefficients and tend to form a band that observations lie within. The scatter between the points is illustrative of the difficulty in predicting MAP near YM; factors that are not controlled for clearly have a significant affect on MAP. Observed MAP may easily be 4/5 or 5/4 of predicted MAP. The uncertainty in MAP is often neglected, but can be formally taken into account. Formal analyses of the effects of this uncertainty on MAI, in Section ?? show that expected or areal-average MAI increases when the uncertainty is accounted for.

Temperature Temperature trends at the same COOP stations are shown in Figure 7-10. The temperature curves were not smoothed with a moving average. The seasonal patterns in mean daily temperature are quite consistent across the region, with elevation providing the primary difference

within a region.

The hourly readings from the NWS station at Desert Rock, NV, over the period of 1978 through 1994 (obtained from the NCDC repository) were used to estimate seasonal variation in mean temperature. The same procedure is used to estimate other atmospheric properties, reported in the next section. The hourly readings were averaged into an average daily temperature for each Julian day (a total of up to 384 readings for each Julian day). The annual cycle of the daily average temperature was well described with a sine wave,

$$v = \overline{v} + A\sin[\omega(J - t_0)] \tag{7-6}$$

where v is the variable being fit, J is Julian day, $\omega = \pi/180$ scales Julian day into radians, and $\overline{v}$, A, and t_0 are fitting parameters. The resulting fit to the seasonal pattern is shown in Figure 7-11. A similar annual pattern would be expected at YM, shifted up or down according to mean annual temperature (MAT) at the particular location of interest.

Predictive equations for the regional variation of annual-mean daily, maximum, and minimum temperatures were developed using the network of COOP stations. The 262 COOP stations with record lengths of at least 5 yr were used in the analysis. It is not necessary to have as long of a record length for temperature as it is for precipitation, since the same general patterns repeat from year to year.

The average of maximum and minumum temperature for each day is used to estimate the mean temperature for that day. All three temperatures are well predicted with two variables: elevation, and either latitude or mean annual solar flux on a horizontal plane external to the atmosphere at the latitude of the station. Solar flux, which drives heating, varies essentially linearly with latitude in the region. Only the relationships based on latitude are presented here for simplicity. The regression equations for both elevation-only and the two-variable relationships are shown in Table 7-2, as well as the regional elevation-dependent equations at the YM latitude and the regressions for the 9 DOE YM stations. The comparison between observed and predicted temperatures is shown in Figure 7-12.

The regression relationship explains 95 percent of variability in regional MAT. The maximum daily temperature is better predicted than the minimum daily temperature, with 97 percent of variability explained compared with 84 percent. The difference between maximum and minimum daily temperature is not dependent on elevation, latitude, or longitude. The poorer predictability for minimum daily temperature is probably due to local temperature inversions, in which cooler and denser air moves downslope through gravity drainage.

Table 7-2: Regression equations for mean annual daily, maximum, and minimum temperature as a function of elevation and normalized latitude in the form $\hat{Y} = a + bZ + cN_t$, where Y is predicted temperature in degrees Celsius, Z is in km, and N_t is latitude normalized between N 34° and N 42°. The 262 COOP stations with record length at least 5 yr were used. The 9 DOE YM stations provide site observations.

a	b	c	R^2	Description
23.18	-8.315		0.86	Regional daily temperature
24.30	-6.340	-6.861	0.95	Regional daily temperature
21.87	-6.340		0.95	Regional daily temperature at YM
21.20	-4.000		0.60	Observed YM daily temperature
31.98	-8.543		0.91	Regional maximum temperature
32.93	-6.856	-5.828	0.97	Regional maximum temperature
30.87	-6.856		0.95	Regional maximum temperature at YM
33.71	-9.506		0.93	Observed YM maximum temperature
14.38	-8.096		0.73	Regional minimum temperature
15.67	-5.824	-7.895	0.84	Regional minimum temperature
12.87	-5.824		0.84	Regional minimum temperature at YM
7.60	2.310		0.05	Observed YM minimum temperature

The DOE YM meteorological stations measured MAT that is reasonably close to the regional trend, although the somewhat less change with increasing elevation. Maximum and minimum daily temperatures are quite different than the regional trend and the change in temperature with elevation is quite different from the regional values. These trends are shown in Figure 7-13. Interestingly, the minimum daily temperature increases with elevation. These observations are presumably due to temperature inversions and advection from the warm flats to the nearby ridges.

Atmospheric and solar parameters Precipitation and temperature have the most significant effect on MAI of all atmospheric parameters. Changes in the remaining parameters modify rates of evapotranspiration, thereby modifying estimates of MAI that are primarily governed by MAP and MAT.

Evapotranspiration is ultimately controlled by two atmospheric parameters, vapor density (or relative humidity) and windspeed. Evapotranspiration requires a gradient in vapor density from the ground and leaves into the atmosphere. The gradient is partially controlled by atmospheric

vapor density and partially by soil moisture. Given a vapor density gradient, the actual vapor flux is also mediated by the atmospheric diffusivity, which is proportional to wind speed. Thus, drier and windier conditions would promote evapotranspiration and reduce MAI when soil moisture is not limiting.

The seasonal variation of atmospheric parameters measured at Desert Rock, NV, is estimated using the same procedure used to estimate the variation of mean daily temperature. The same period of record is used, 1978 through 1994. The seasonal variation of mean daily relative humidity and atmospheric vapor density are shown in Figure 7-14. Relative humidity variation is adequately described by a sine wave, although the monsoon in the late summer causes increased humidity that doesn't fit the sine wave. Using the mean relative humidity and temperature curves to predict vapor density results in some error, especially before and during the monsoon. Using relative humidity and temperature to estimate vapor density is subject to error from the exponential dependence of saturated vapor density on temperature. Note that the vapor density associated with cyclonic air masses is essentially constant through the year; changes in relative humidity and air temperature essentially counterbalance. A better fit to the vapor density patterns would be obtained by estimating relative humidity using a sinusoidal curve for the cyclonic air masses, adding a bell-shaped curve during the summer to account for the monsoon.

A regression equation based on regional values of mean annual vapor density (MAV) can be used to estimate the MAV distribution. Hourly values of vapor density were calculated from the hourly readings of temperature and relative humidity for the SAMSON stations used in the shortwave radiation calculations (except for the Washington, Idaho, and Oregon stations) and Desert Rock, NV. These were averaged to yield MAV for each station. The regression equation describing these values is

$$\hat{V} = 0.8019 - 0.0914Z \tag{7-7}$$

where $\hat{V}$ is $\log_{10}$(MAV) and MAV has units of gm/m^3. The equation explains 49 percent of the regional variability.

An additional several high-altitude vapor densities were estimated using the mean annual temperature and relative humidity for the 4 stations reported by McKinley and Oliver (1994) in the Kawich and Toiyabe Ranges, east and north of Tonopah, NV. The resulting regression equation is

$$\hat{V} = 0.817 - 0.1052Z \tag{7-8}$$

The revised equation explains 74 percent of the regional variability. The equations are essentially identical across YM elevations. The two relationships are shown in Figure 7-15.

The seasonal variation of wind speed and cloud cover is shown in Figure 7-16. Wind speed is described by a sine wave that is offset from the other parameters by about 120 days. The seasonality of wind speed is similar in the 9 DOE YM meteorological stations (TRW, 1998); however, local terrain has a significant impact on winds. For example, exposed stations have an annual average wind speed between 4.2 and 4.4 m/s, while the most sheltered station (in Coyote Wash) has annual average wind speed of 2.5 m/s.

Cloud cover is described by a sine wave that is roughly in phase with temperature and relative humidity. Cloud cover determines the relative magnitude of incoming longwave and shortwave radiation. Longwave radiation increases and shortwave radiation decreases with increasing cloud cover.

The steep north- and south-facing sides of YM ridges are exposed to significantly different shortwave radiation loads. Since the sun is always south of YM, south-facing slopes receive a stronger shortwave radiation load. Two factors are important in estimating the shortwave load: (a) ground orientation and (b) shadows from ridges. As shadowing is most significant early and late in the day, when shortwave fluxes are relatively small, ground orientation has the biggest effect on annual shortwave load in most locations.

The effect of ground orientation is shown in Figure 7-17, which provides the mean annual extraterrestrial solar flux for various orientations of a flat plane. A table of mean annual solar flux was built as a function of north-south and east-west ground orientation. Average instantaneous flux was calculated every fifteen minutes for a year to obtain mean annual flux. For typical YM slopes of 20° north and south, the south-facing slope has 2.25 times greater solar load over a year (450 W/m^2 compared to 200 W/m^2). The difference becomes larger as the slopes steepen.

Daily patterns Atmospheric variables tend to change over the day in characteristic patterns. These patterns are forced by solar radiation, thus have patterns that are governed by daylight hours. The hourly data from Desert Rock, NV, over the period of 1978 through 1994 provides a representative sequence of patterns. These observations were averaged into mean values for each hour of the day, providing a guide to the daily variation.

Radiation and cloud cover patterns over the day are shown in Figure 7-18. Sunrise and sunset are marked with the shortwave radiation curve. The slight rise in longwave radiation during the day is due to the typical increase in cloud cover during the afternoon.

Wind speed shows a clear solar forcing, with a lull near daybreak. Atmospheric vapor density

is relatively constant over the day, as is expected with no nearby open water. These patterns are shown in Figure 7-19. Because of the relatively constant vapor density, temperature and relative humidity have inverse patterns over the day, as can be seen in Figure 7-20.

It is likely that the cloud cover patterns at YM are essentially identical to Desert Rock, thus longwave and shortwave radiation patterns should also be essentially identical. The 9 DOE YM meteorologic stations (TRW, 1998) show that vapor density is well mixed during the day at YM; however, the different stations have different responses at night. Mean relative humidity varies between 19 and 23.4 percent at 4 p.m. but ranges between 31 and 48 percent at 4 a.m. The correlation between night-time relative humidity and both elevation and mean daily wind speed is quite low for the YM stations.

Wind speed may be better represented by the Desert Rock data in the flats and alluvial valleys than in the YM washes. Based on the abnormal temperature patterns across YM, gravity drainage likely occurs in the washes. Gravity drainage occurs once solar forcing ends, thus winds associated with gravity drainage would peak after sundown. Gravity drainage may also explain the lack of pattern in the relative humidity data.

Interannual variation Interannual cycles in ocean elevation and temperature can affect global weather patterns. For example, relationships between the Southern Oscillation Index (SOI) and western US precipitation and temperature have been documented (Redmond and Koch, 1991). The SOI represents the difference in mean sea level between Tahiti and Darwin, with an index less than -0.5 denoting an El Niño event and and an index greater than 0.5 denoting a La Nina event. A number of comparisons are available online at (http://www.wrcc.dri.edu/enso/enso.html). In general, the strongest relationships between SOI and climate have been found to be between between summer (June-November) SOI and winter (October-March) climate. Responses change across the western US, with El Niño events tending to generate wetter and slightly cooler conditions in the desert southwest and drier and warmer conditions in the Pacific Northwest (Redmond and Koch, 1991). The reverse is true for La Nina winters, with more reliable responses obtained for La Nina in the southwest. The dividing line between responses is roughly between San Francisco, CA, to Cheyenne, WY.

Relationships between winter precipitation and SOI are demonstrated in the scatterplots shown in Figure 7-21. Each of the COOP stations with record length of at least 40 yr are used in the analyses. Regional variation is indicated using the same 9 subregions as before. Each region is plotted independently. Within each plot, the color of the symbol is red in the south of the

subregion and blue in the north. In each figure, normalized winter precipitation is plotted against the mean preceeding-summer SOI. Normalized winter precipitation is obtained by dividing the winter precipitation for each station by the average winter precipitation over the period of record for the station. Total winter precipitation is the precipitation occurring in the months of October through March, inclusive. A wet year has a value of normalized precipitation greater than 1 and a dry year has a value less than 1. The figures were plotted using both linear and logarithmic scales for normalized winter precipitation; the logarithmic scale appeared to have a more linear and balanced distribution.

The set of points in each figure was regressed with SOI as the predictor variable. In the north, there is no predictive power, consistent with the dividing line between responses passing through the northern part of the region. Predictive power increases to the south and east, with R^2 between 24 and 31 percent in the SW, S, SE and W subregions; predictive power is 15 percent in the C subregion. Changing the record length considered to 20 yr has little effect on explanatory power.

7.1.3 Spatial distribution of present-day meteorological parameters

The primary method for estimating MAI in Nuclear Regulatory Commission (NRC) Performance Assessment (PA) activities uses the spatial distribution of hydrologic and meteorological parameters to estimate MAI in each cell of a DEM. The mean annual value for each of the parameters are used in abstracted relationships to predict MAI, with hourly variability accounted for in the abstraction process. Accordingly, the mean annual value for each of the meteorological parameters affecting MAI must be estimated for each cell. The procedure for distributing all of the mean annual values for each meteorological parameter is presented here.

Both MAP and MAT were shown to be strongly dependent on elevation within the YM region, although near YM the patterns are modified somewhat from the regional patterns. The elevation dependence of both MAP and MAT were examined through regression analyses. The regression equations are used to distribute mean MAP and MAT across the landscape, with the understanding that any particular location has associated uncertainty. Other parameters are not dependent on elevation, but are dependent on topography.

Mean annual precipitation Two 20-yr regression curves are suitable for bounding the predictions of MAP based on the comparison of site-specific observations with regression curves in Figure 7-9. The regional elevation-only curve suggests that conditions may be wetter than ob-

served, while the 9-pole curve suggests that conditions may be drier than observed. Averaging the two equations provides a reasonable best guess for local MAP distributions and is very close to the formula used by Hevesi (1999) to provide the most recent infiltration estimates for DOE. The predictive equations are

$$\hat{Y} = 1.999 + 0.233Z \qquad \text{Elevation only} \qquad (7\text{-}9)$$

$$\hat{Y} = 1.776 + 0.292Z \qquad \text{9 Poles} \qquad (7\text{-}10)$$

$$\hat{Y} = 1.888 + 0.263Z \qquad \text{Average} \qquad (7\text{-}11)$$

where $\hat{Y}$ is estimated $\log_{10}$(MAP) in mm/yr and Z is elevation (km). At elevation 1400 m, roughly midway between Yucca Crest (1480 m) and Coyote Wash (1280 m), the three equations predict 211, 153, and 180 mm/yr, respectively. At the same elevation, the relationship used by Hevesi (1999) predicts 185 mm/yr for MAP.

Mean annual temperature Two regression curves are used here as MAT distribution equations, the 2-variable regional daily temperature relationship and the observed YM daily temperature relationship. The predictive equations are

$$\hat{T} = 21.87 - 6.34Z \qquad \text{Regional trend} \qquad (7\text{-}12)$$

$$\hat{T} = 21.20 - 4.00Z \qquad \text{YM trend} \qquad (7\text{-}13)$$

where $\hat{T}$ is estimated MAT in degrees C. The two equations predict MAT at 1400 m elevation of 13 and 15.6°C, respectively, with a predicted difference in MAT from Yucca Crest to Coyote Wash of 1.27 and 0.8°C, respectively. Hevesi (1999) uses a slope of -9.8°C/km to distribute MAT, but centers the estimate at 1400 m elevation (approximately midway between elevation extremes above the repository). The higher slope results in a temperature difference of 1.96°C from Yucca Crest to Coyote Wash, which would slightly underestimate ET at the crest and overestimate ET in the washes relative to the other equations.

Mean annual vapor density Distributing MAV near YM is problematic due to the strong mixing during the day and variable behavior during the night that is not dependent on ground elevation. Although correlation of MAV with ground surface elevation is not strong, it does provide a basis for estimating the spatial distribution of MAV. Accordingly, the regression equation incorporating high-altitude data is used, so that MAV is distributed according to

$$\hat{V} = 0.817 - 0.1052Z \qquad (7\text{-}14)$$

where $\hat{V}$ is estimated MAV in g/m^3.

Mean annual windspeed Wind speed is not highly related to elevation. Instead, topography plays a dominant role, with YM washes sheltered from the prevailing winds. A heuristic model was developed to estimate mean annual windspeed (MAW) from topography using a DEM to describe the topography. The model is based on an index function describing whether a particular pixel is in a sheltered wash or is exposed to prevailing winds. The index function is based on local curvature and slope.

The index function is built up in steps. First, a set of index values are created for each pixel to describe slope (I_1), N-S slope (I_2), E-W slope (I_3), N-S curvature (I_4), and E-W curvature (I_5)

$$I_1 = \text{norm}\,(s) \tag{7-15}$$

$$I_2 = \text{norm}\left(\left|\frac{\partial Z}{\partial Y}\right|\right) \tag{7-16}$$

$$I_3 = \text{norm}\left(\left|\frac{\partial Z}{\partial X}\right|\right) \tag{7-17}$$

$$I_4 = \text{norm}\left(-\frac{\partial^2 Z}{\partial Y^2}\right) \tag{7-18}$$

$$I_5 = \text{norm}\left(\frac{\partial^2 Z}{\partial X^2}\right) \tag{7-19}$$

$$\text{norm}\,(x) = \frac{x - \min(x)}{\max(x) - \min(x)} \tag{7-20}$$

where X and Y are E-W and N-S coordinates and Z is elevation (all in the same units). These pixel index values are reset at threshold values to match wash characteristics. In the typical case developed here, I_2 is set to 1 if greater than 0.05 (significant ground slope) and I_3 and I_4 are set to 1 if greater than 0.6 (significant curvature).

Index values are then created for each pixel to describe wash intensity (I_w) and openness intensity (I_o)

$$I_w = \text{norm}\,(\text{smooth}\,[\max(I_2, I_4)(1 - I_1)]) \tag{7-21}$$

$$I_o = \text{norm}\,(\text{smooth}\,[1 + \text{norm}\,(I_1 + I_5) - I_w]) \tag{7-22}$$

where the smooth [] operator averages values from adjacent cells.

Surface-elevation-dependent MAW is created for the open areas, accounting for a certain amount of protection in alluvial valleys near YM

$$W_o = W_1 + \frac{Z - Z_1}{Z - Z_2}(W_2 - W_1) \tag{7-23}$$

where W_o is the alluvial valley MAW variation with elevation, Z_1 and Z_2 are reference elevations (1000 and 1500 m), and W_1 and W_2 are reference MAW (3.2 and 4.4 m/s).

Finally, the index values are combined with the MAW values to yield

$$W = W_o I_o + W_w(1 - I_o) \tag{7-24}$$

where W_w is the wash MAW (2.5 m/s). The reference values of MAW are based on Coyote Wash (2.5 m/s), Yucca Crest (4.4 m/s), and NTS-60 (3.4 m/s) (TRW, 1998).

The distribution of MAW using the index approach is shown in Figure 7-22.

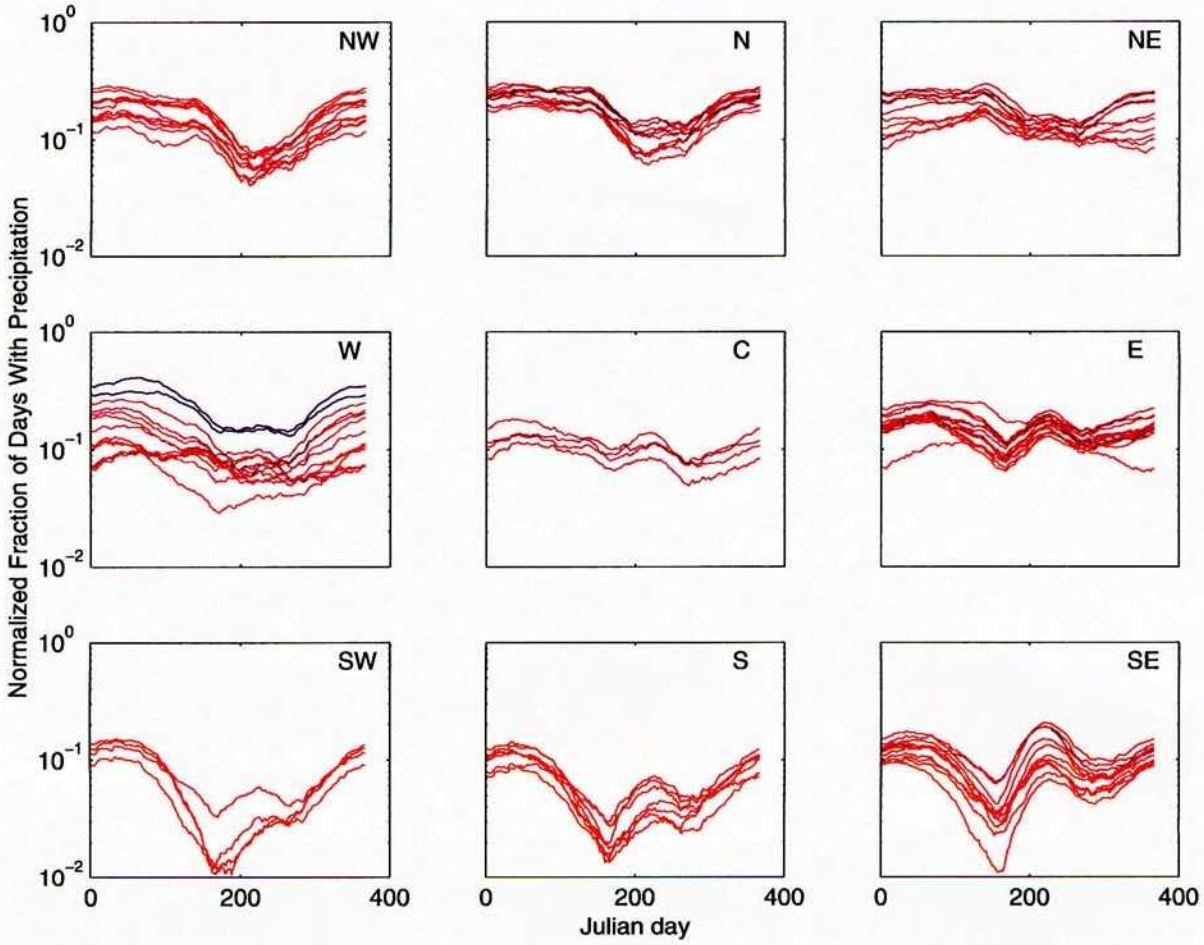

Figure 7-5: Fraction of days with precipitation for each COOP station with a record of at least 40 yr over the station's period of record. The reciprocal of this measure is mean number of days between days with precipitation. If every day with precipitation had only one storm and storms only occurred on one day, the reciprocal of this measure is equivalent to mean number of days between storms. Smoothing used a 60-day window. Station elevation is denoted by color, with red for low elevations and blue for high elevations.

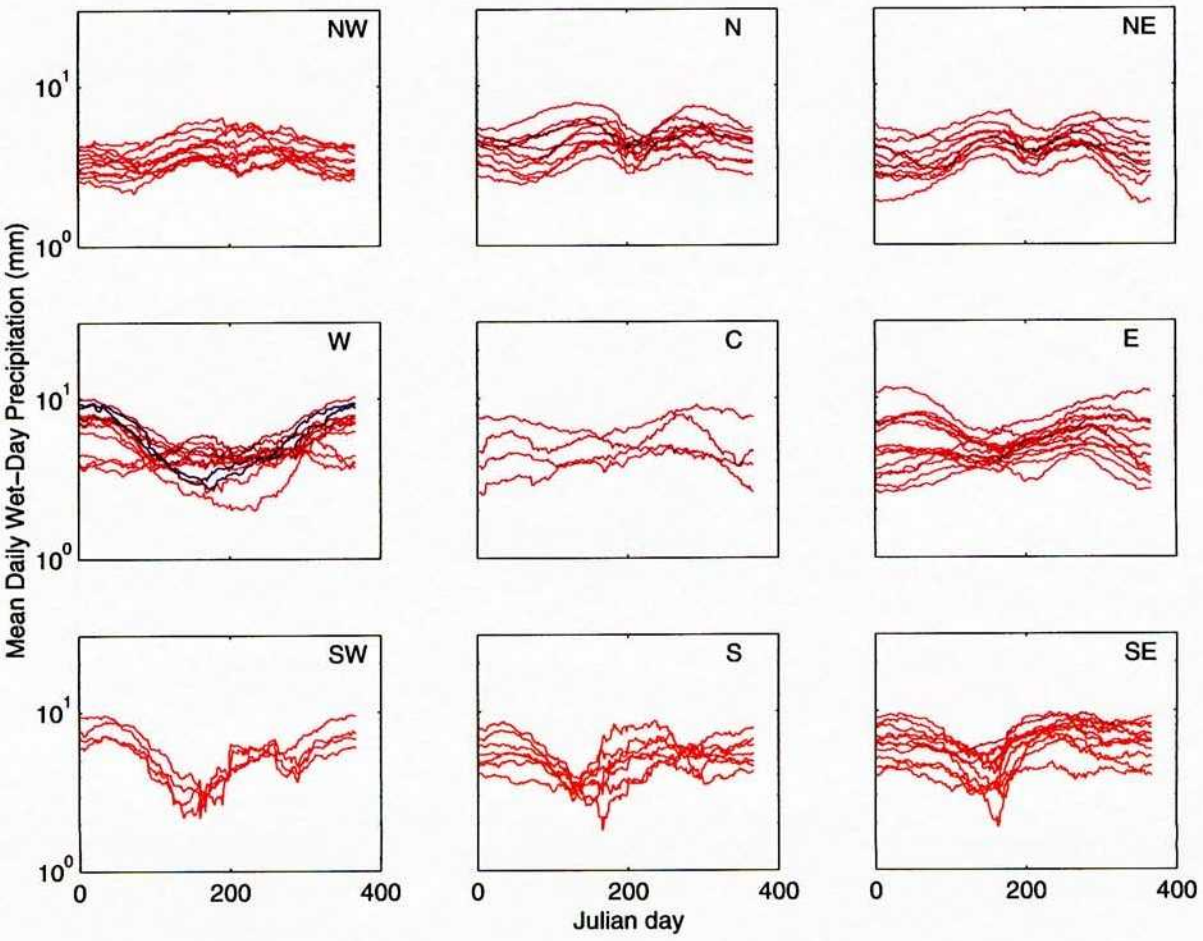

Figure 7-6: Mean daily precipitation on days with precipitation for each COOP station with a record of at least 40 yr over the station's period of record. If every day with precipitation had only one storm, this measure is equivalent to mean storm magnitude. Smoothing used a 60-day window. Station elevation is denoted by color, with red for low elevations and blue for high elevations.

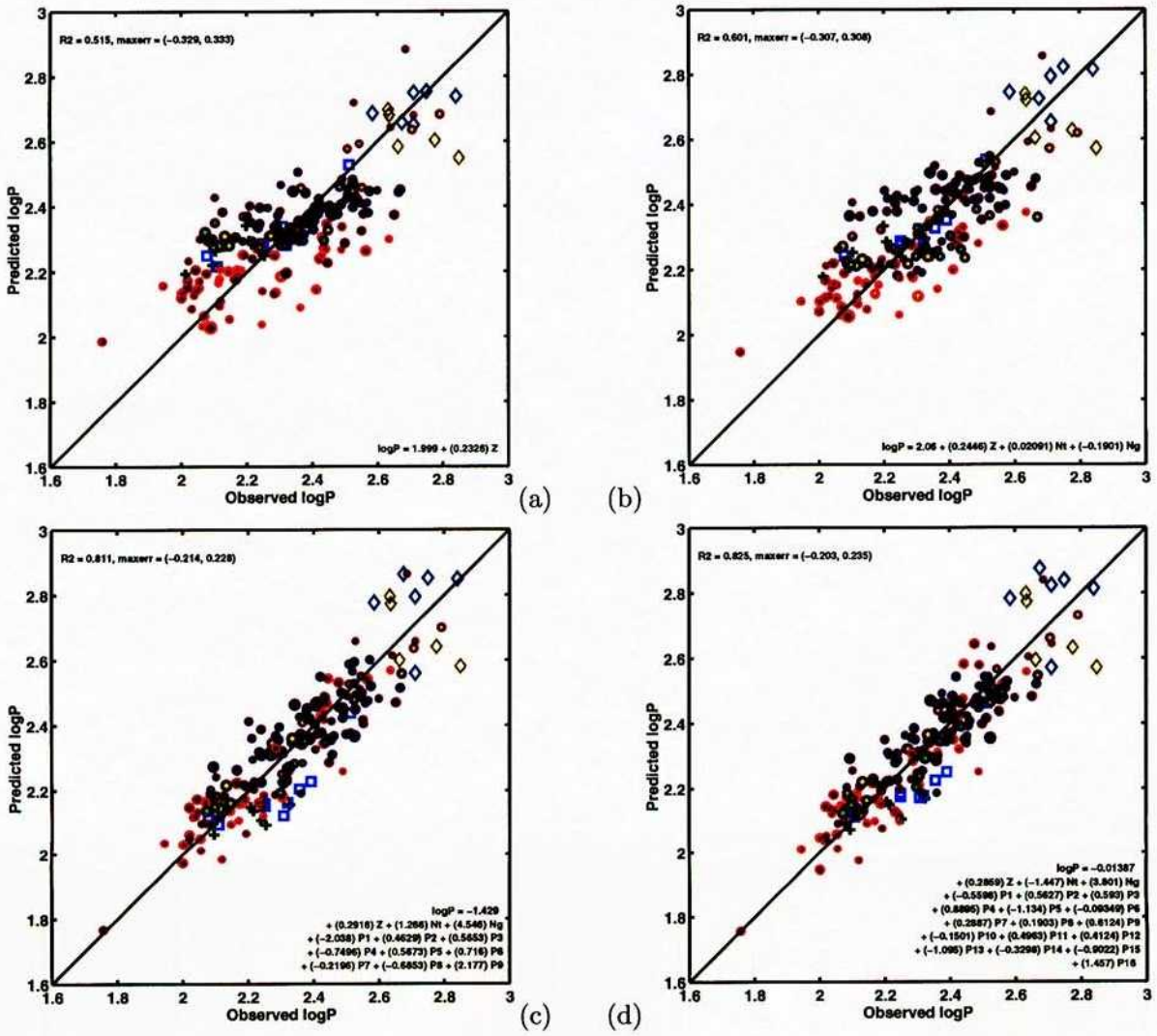

Figure 7-7: Predicted versus observed $\log_{10} MAP$ for all 171 stations with at least 20 yr of observations. Regressions use (a) elevation only; elevation, latitude, longitude, and (b) no poles; (c) 9 poles; and (d) 16 poles.

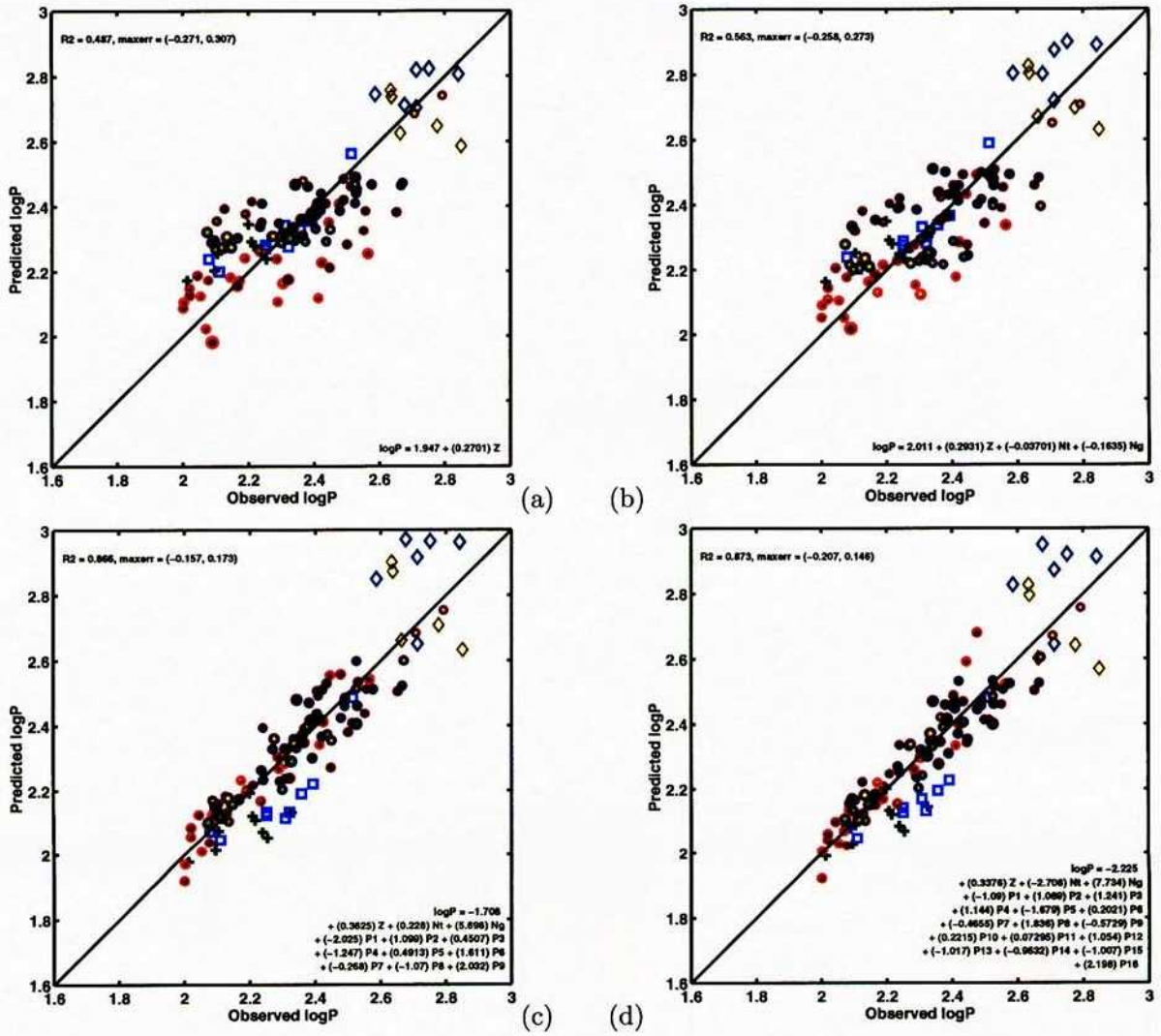

Figure 7-8: Predicted versus observed $\log_{10} MAP$ for all 86 stations with at least 40 yr of observations. Regressions use (a) elevation only; elevation, latitude, longitude, and (b) no poles; (c) 9 poles; and (d) 16 poles.

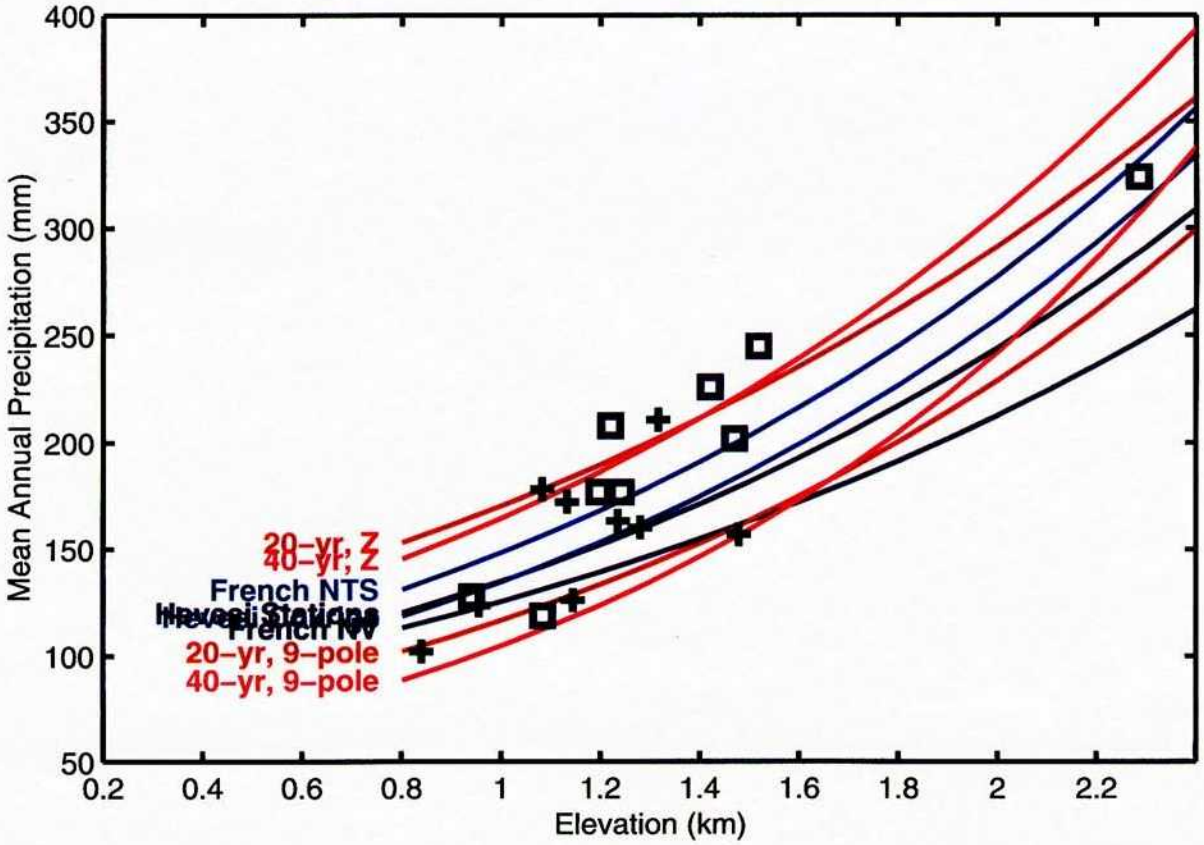

Figure 7-9: Comparison of regression equations for MAlP with observations at DOE YM stations (crosses) and NTS stations (squares).

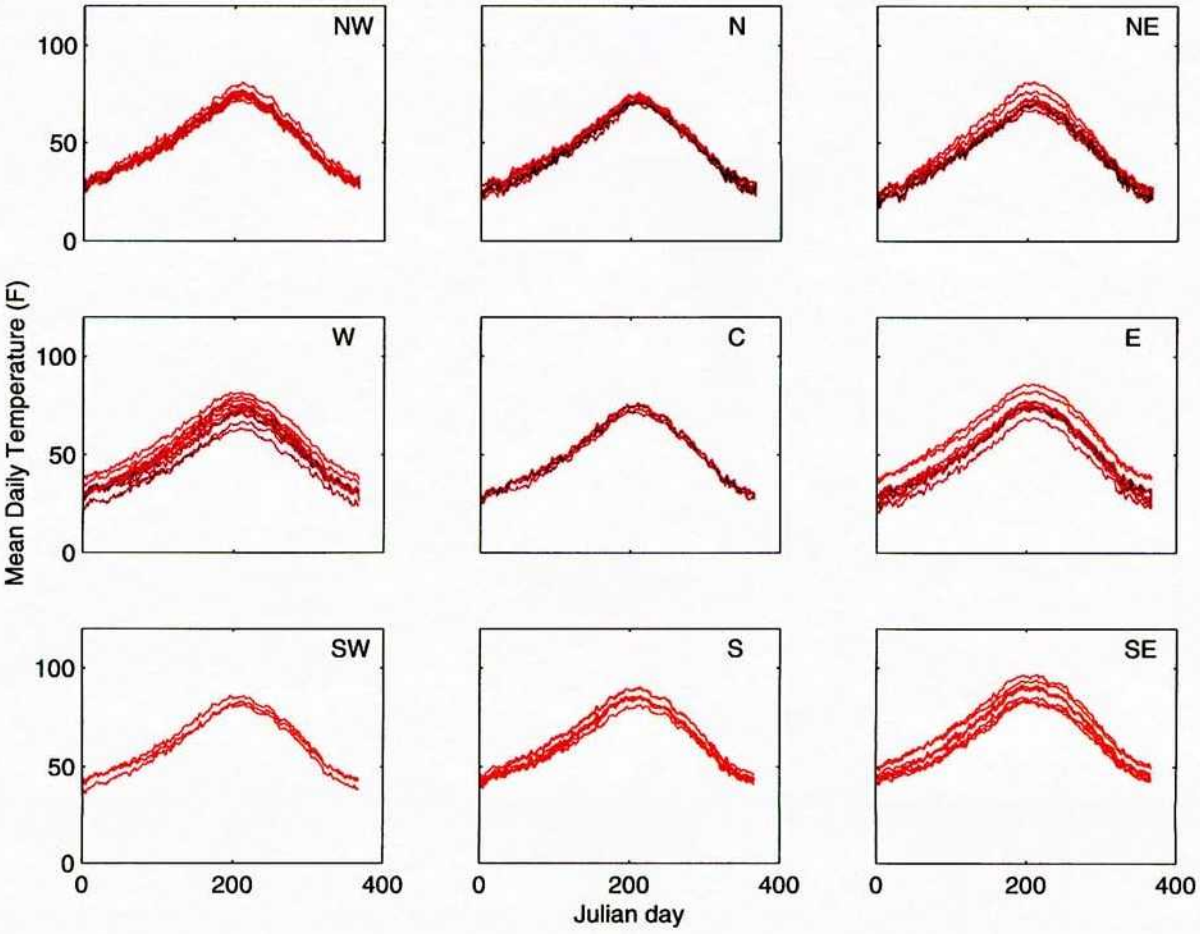

Figure 7-10: Mean daily temperature for each COOP station with a record of at least 40 yr over the station's period of record. No smoothing is used. Station elevation is denoted by color, with red for low elevations and blue for high elevations.

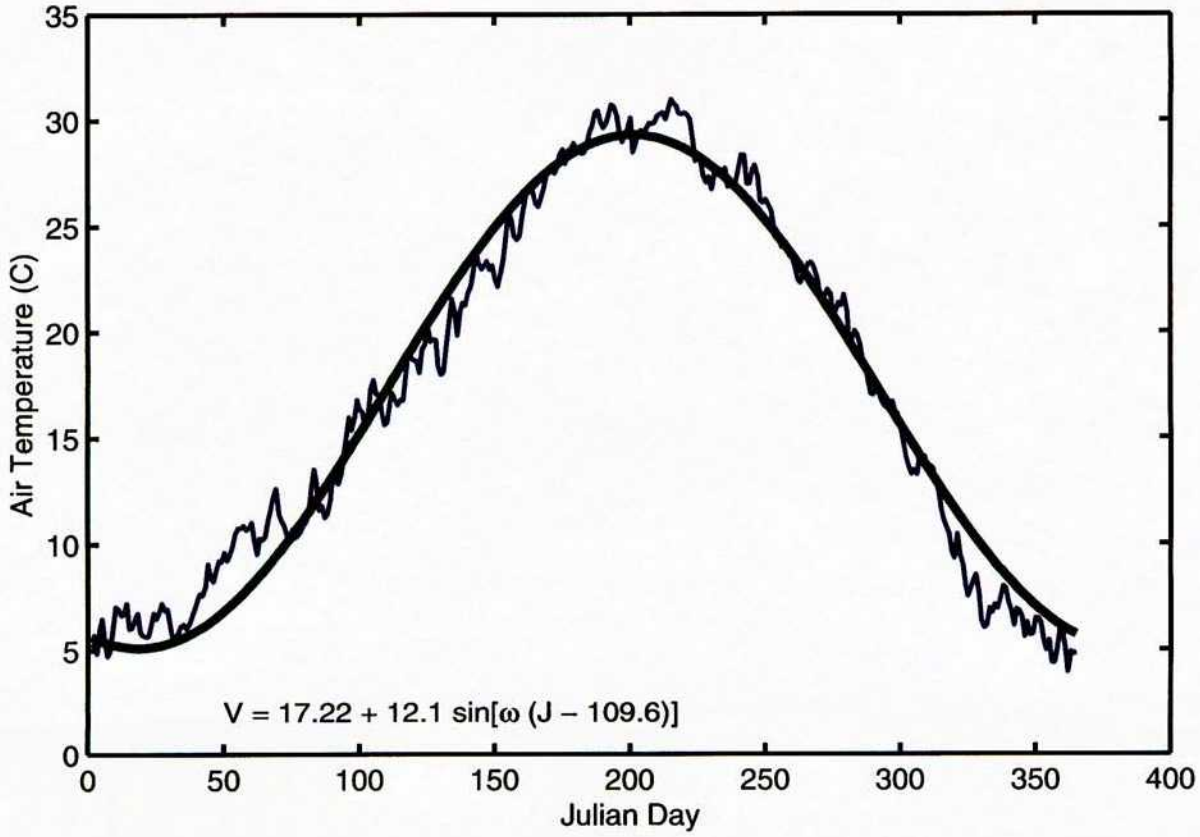

Figure 7-11: Seasonal variation of mean daily temperature at Desert Rock, NV.

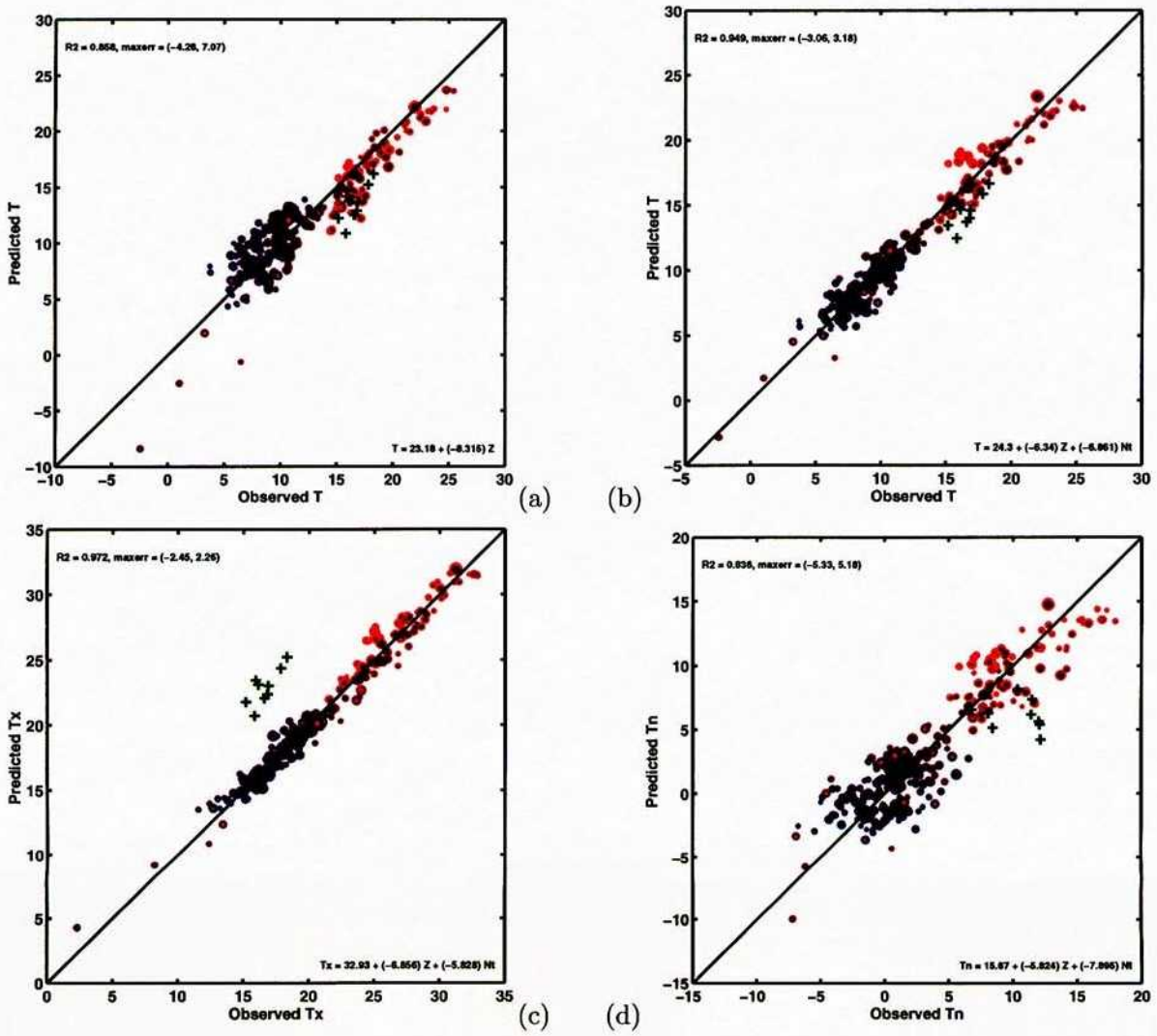

Figure 7-12: Predicted versus observed annual temperatures for all 262 stations with at least 5 yr of observations. Mean daily temperature predicted using (a) elevation only, and (b) elevation and normalized latitude; daily (c) maximum and (d) minimum temperature, predicted using elevation and normalized latitude. DOE YM meteorological stations indicated with crosses.

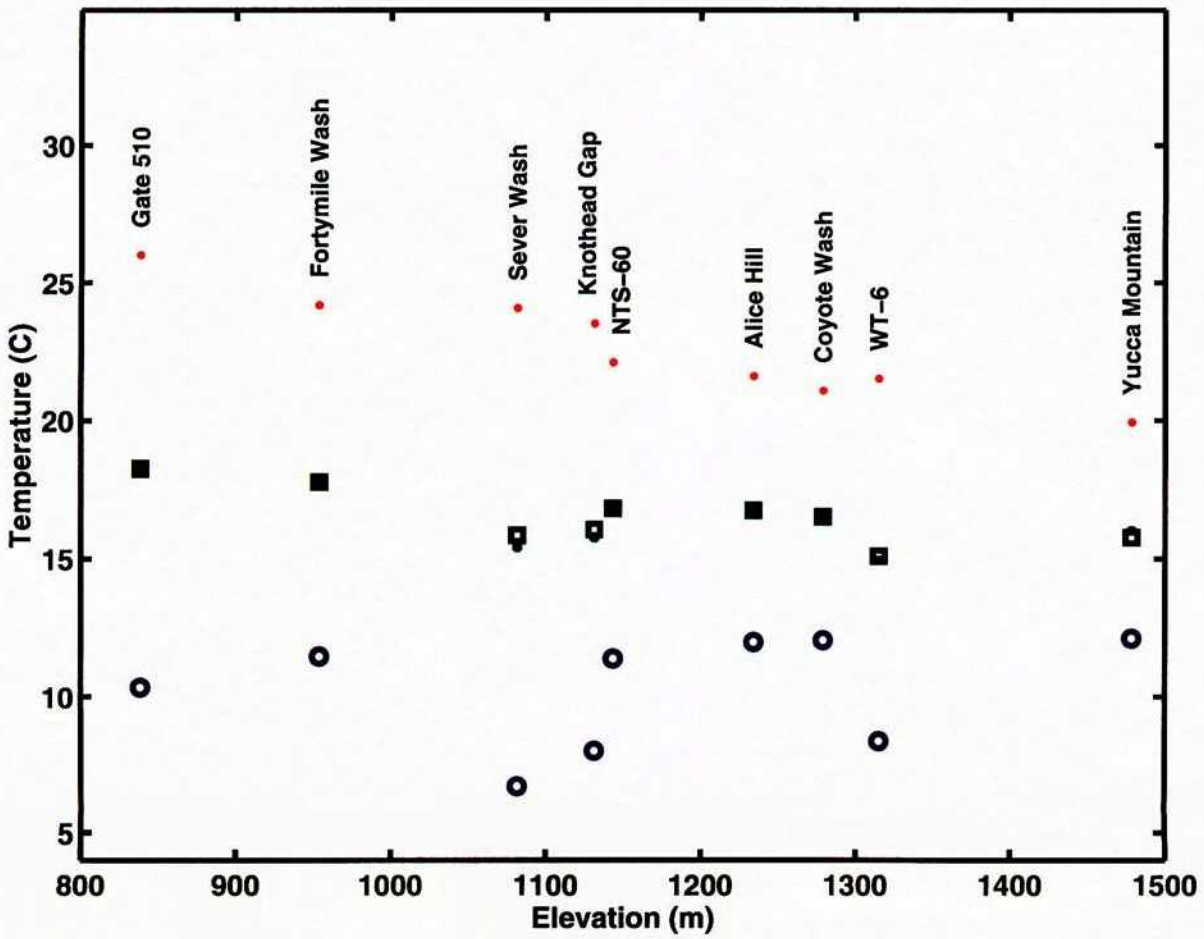

Figure 7-13: Observed mean annual maximum (dot), minimum (circle), and average (square) temperature at 9 DOE YM meteorologic stations. Crosses represent average of minimum and maximum temperatures.

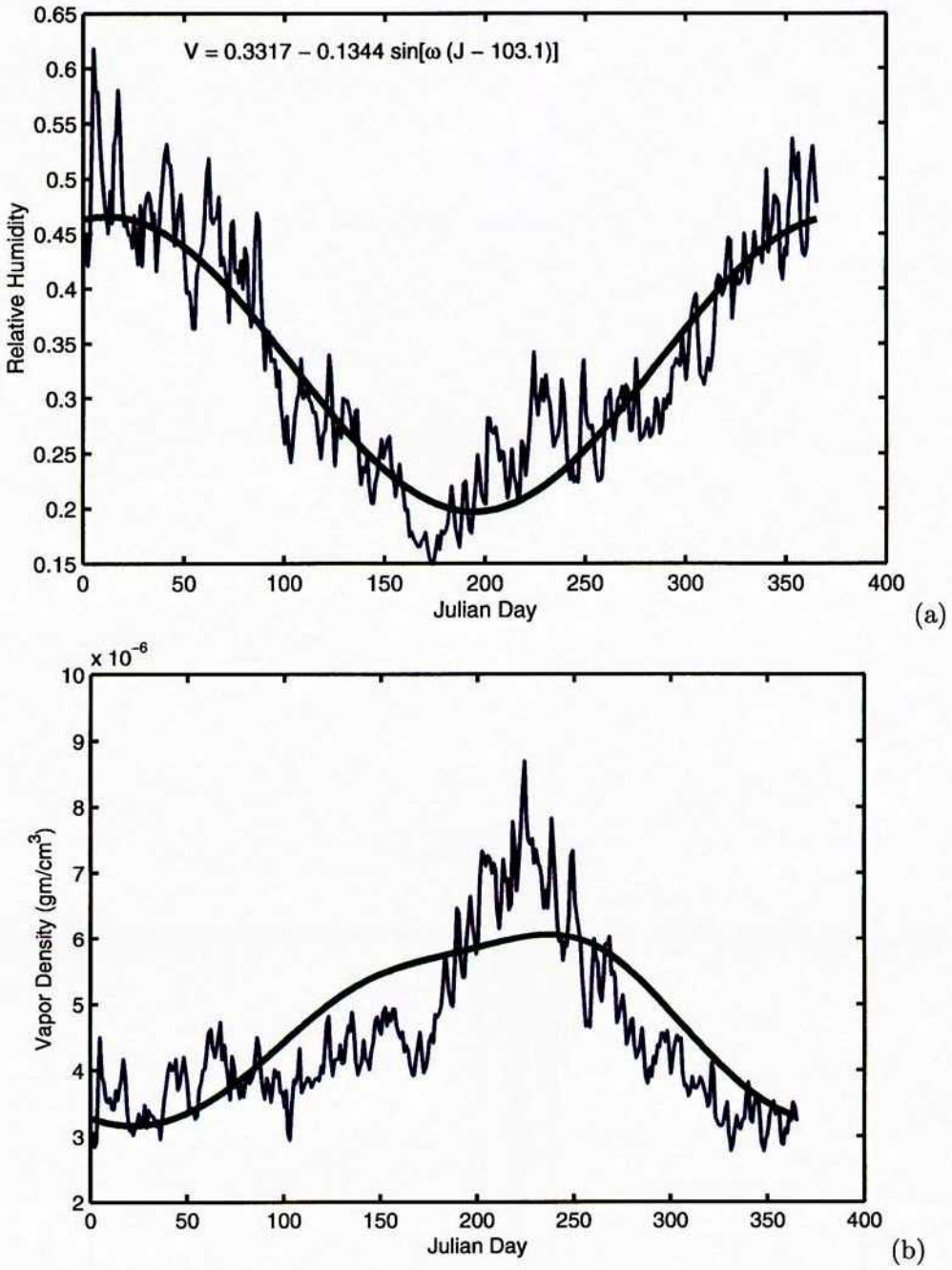

Figure 7-14: Seasonal variation of (a) mean daily relative humidity and (b) vapor density at Desert Rock, NV.

Figure 7-15: Regional dependence of MAV on elevation. *Correction dated 9/3/03: This figure was never created for the report being included.* SAS

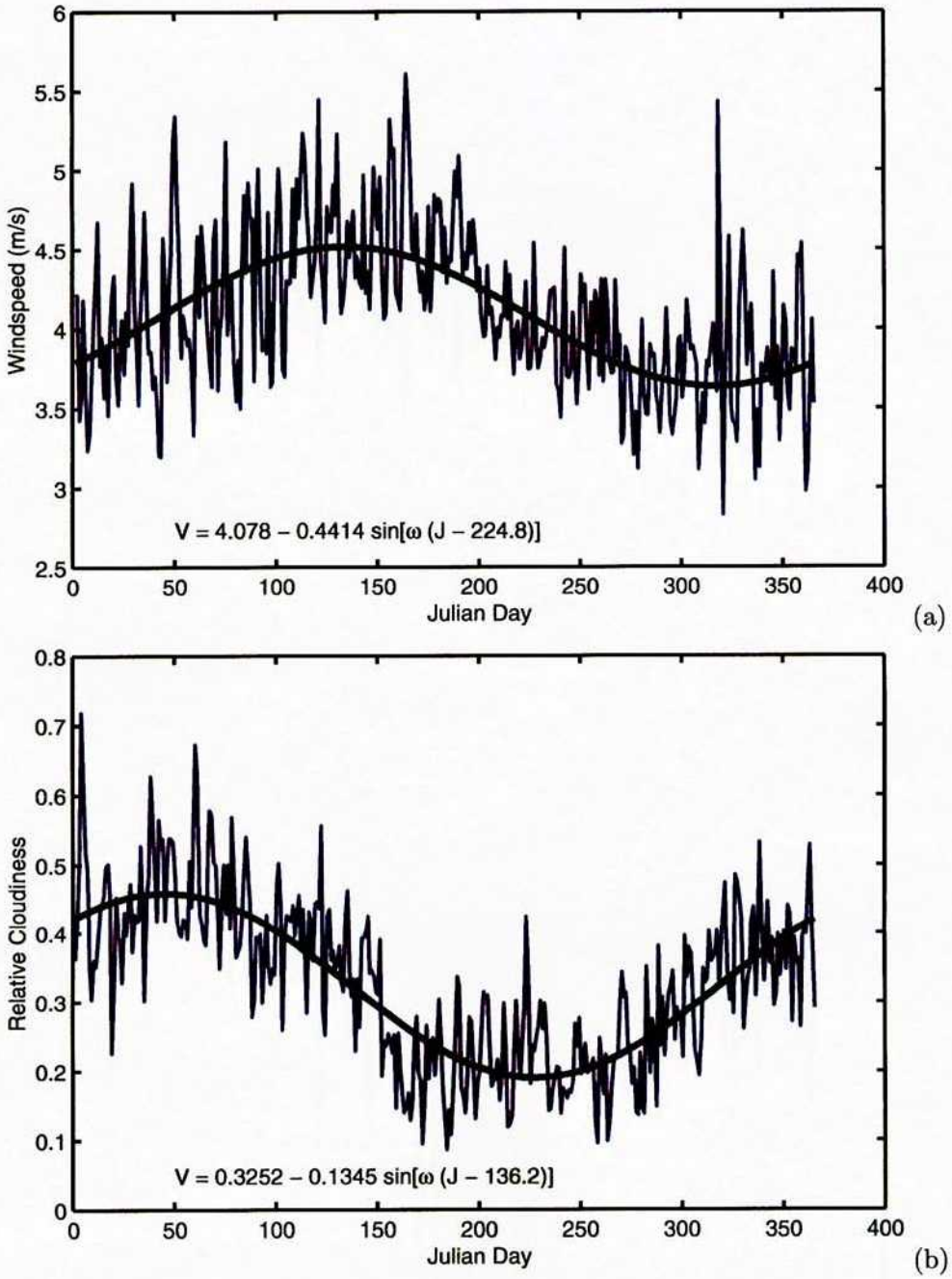

Figure 7-16: Seasonal variation of (a) wind speed and (b) cloud cover at Desert Rock, NV.

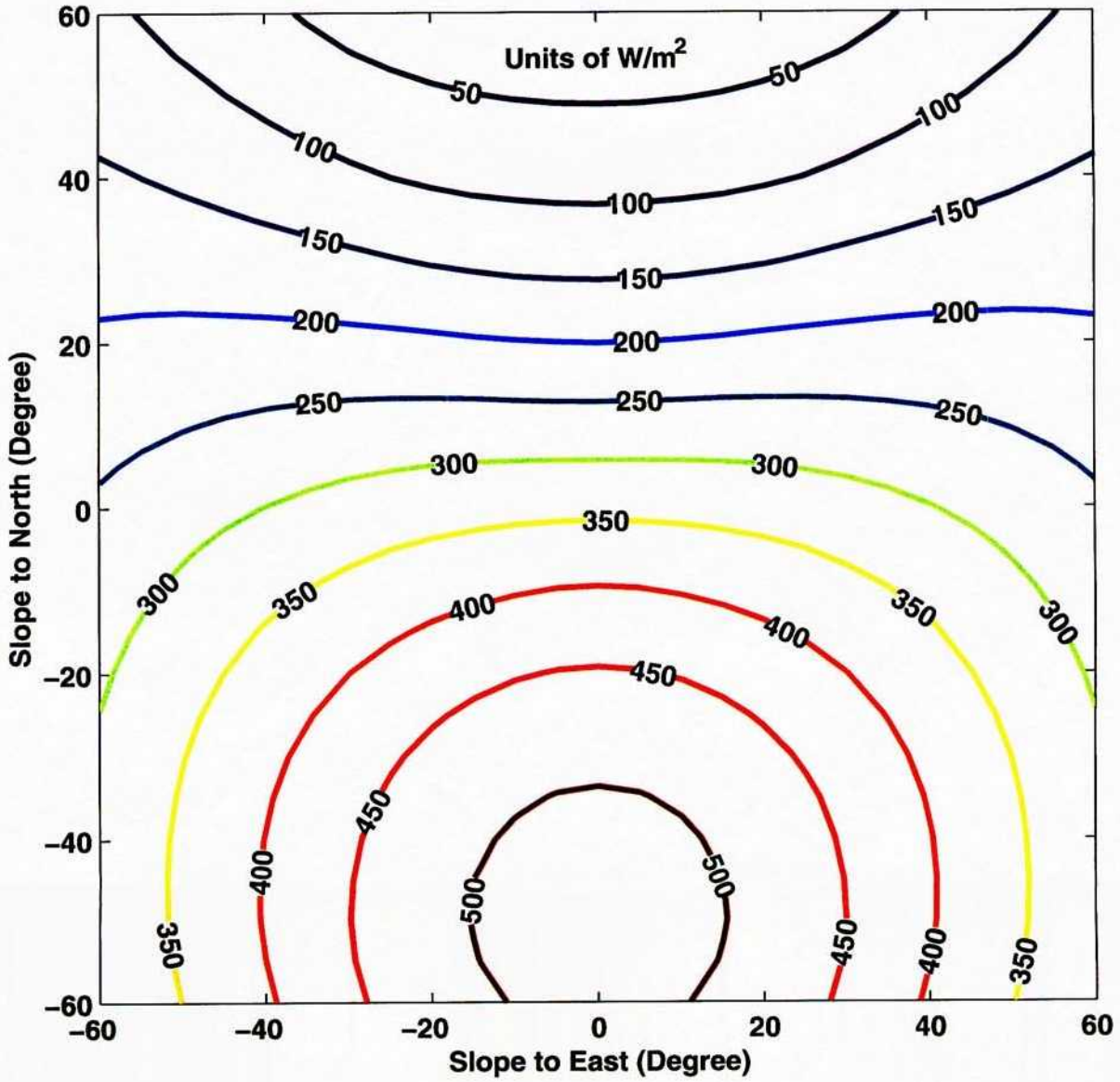

Figure 7-17: Mean annual extraterrestrial solar radiation flux on a flat plate at the latitude of YM as a function of orientation. Positive and negative slopes to the north represent north- and south-facing slopes, respectively. Similarly, positive and negative slopes to the east represent east- and west-facing slopes.

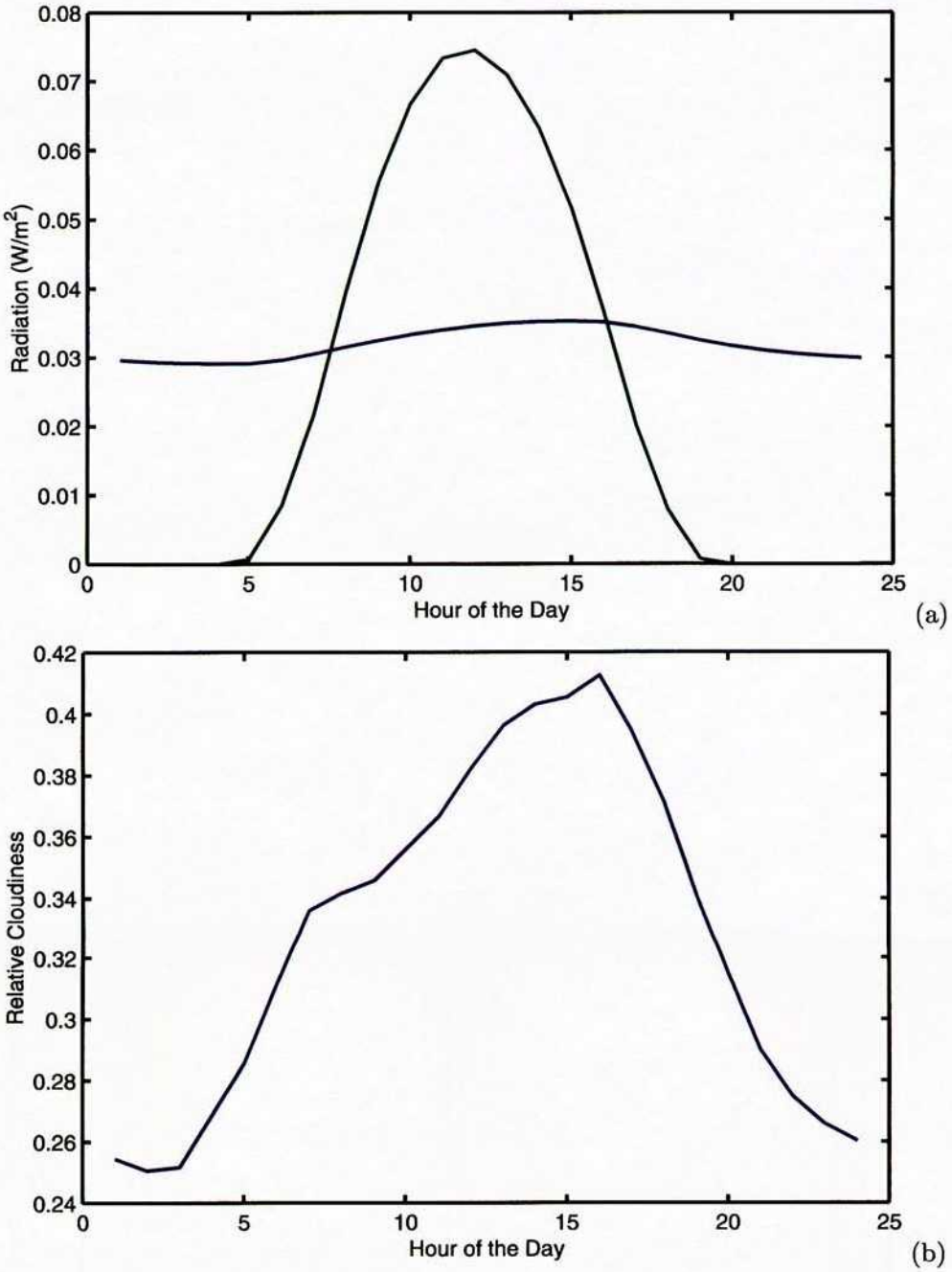

Figure 7-18: Mean hourly (a) longwave (blue) and shortwave radiation (green), and (b) cloud cover at Desert Rock, NV.

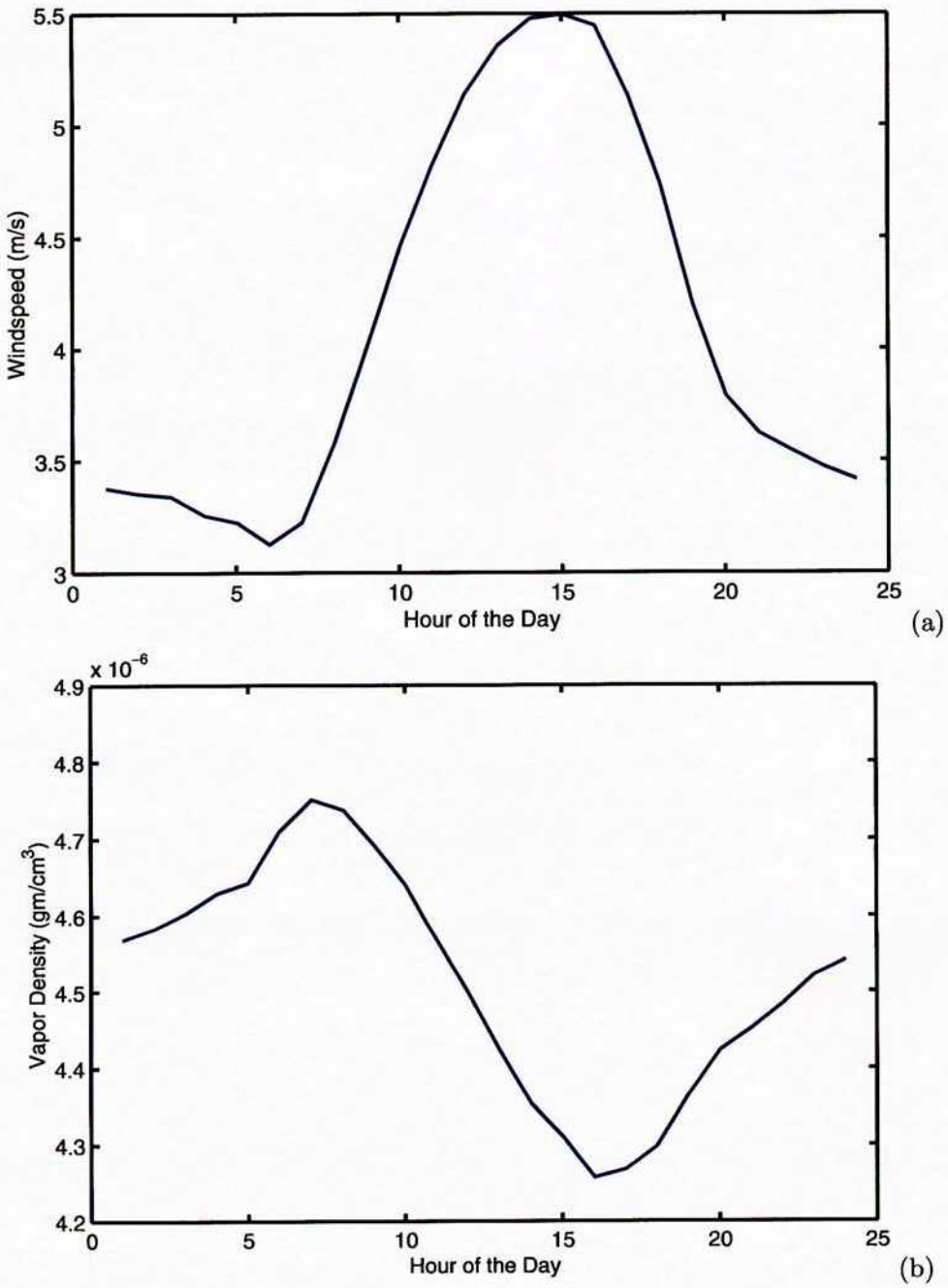

Figure 7-19: Mean hourly (a) wind speed and (b) vapor density at Desert Rock, NV.

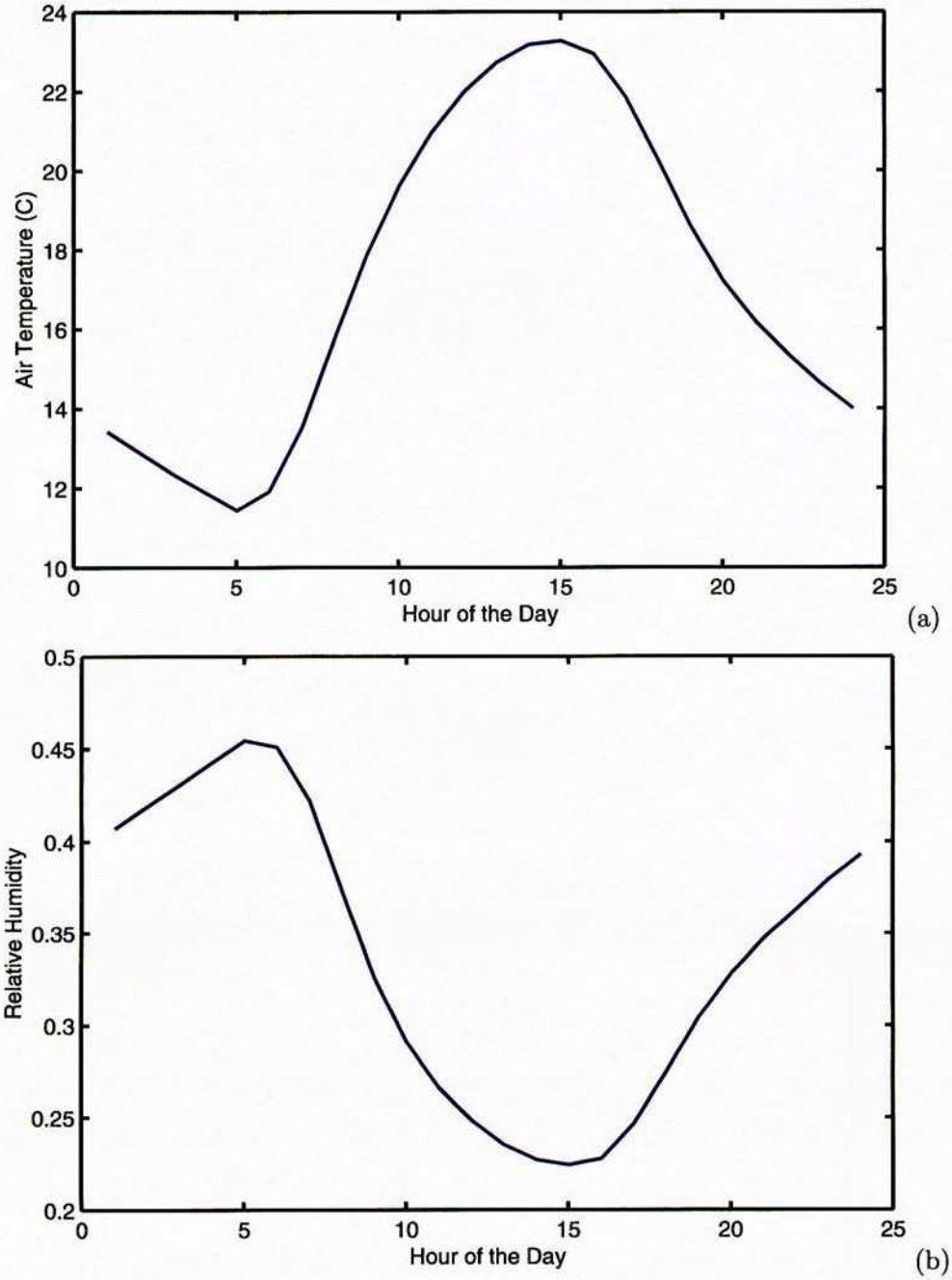

Figure 7-20: Mean hourly (a) temperature and (b) relative humidity at Desert Rock, NV.

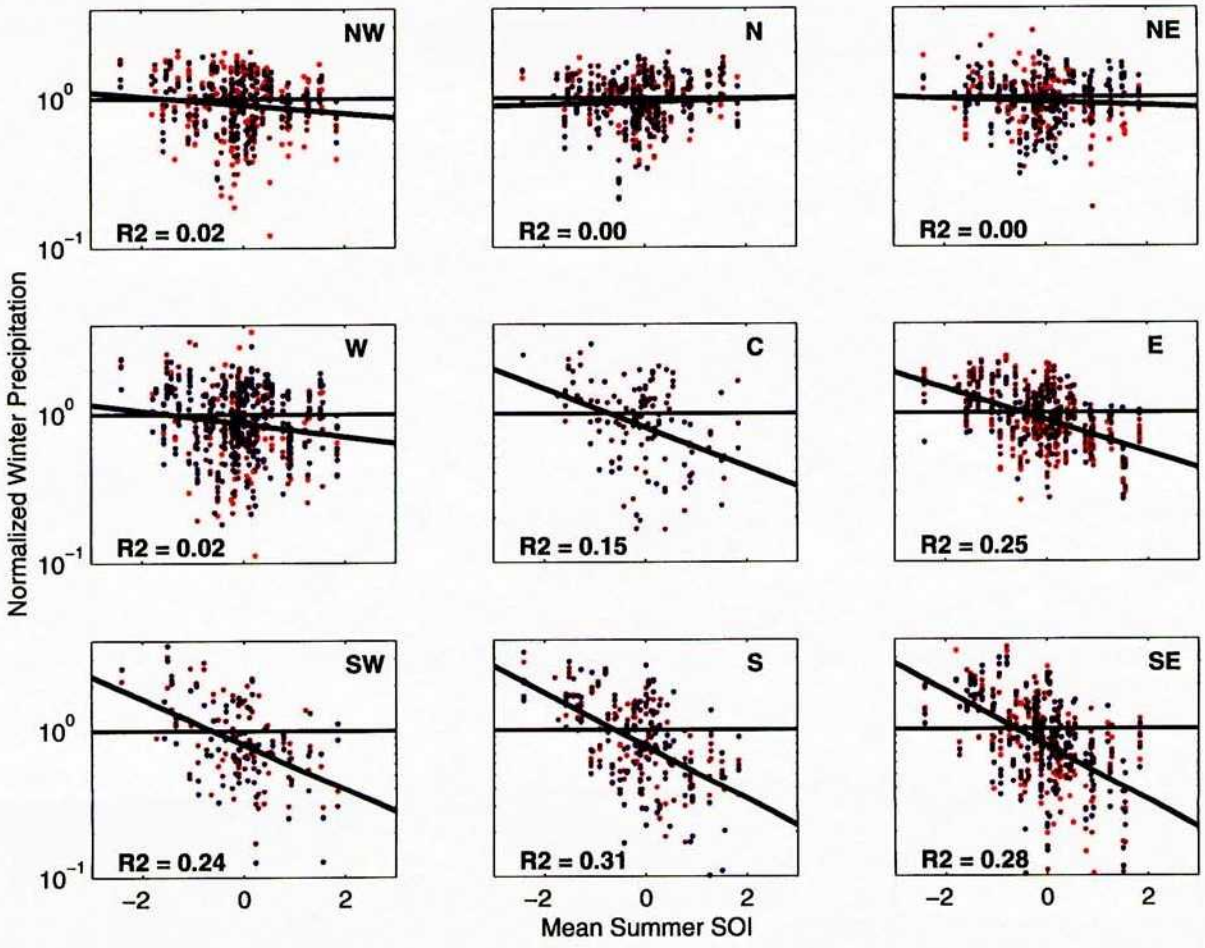

Figure 7-21: Normalized total winter precipitation versus the mean preceeding-summer SOI for 9 regional subdivisions.

Figure 7-22: Predicted MAW in the repository area at YM. *Correction dated 9/4/03: This figure was never created for the report being included.* SAS

Mean annual shortwave radiation The steep slopes of the YM washes ensure that topography dominates shortwave radiation. The dominant effect on mean annual shortwave radiation is due to ground orientation; shadows caused by the ridges are likely to have a secondary effect.

The table of mean annual extraterrestrial solar flux displayed in Figure 7-17 can be used to look up the annual flux given the ground surface orientation. Actual shortwave radiation reaching the ground surface is reduced by cloud cover. Although cloud cover is constantly changing, the impact on MAI is through ET, which can be calculated with reasonable accuracy using seasonal variation. Accordingly, two approaches are feasible for estimating mean annual incident shortwave radiation. The first approach uses daily and seasonal variation of cloud cover to directly calculate mean annual incident radiation. The simpler second approach, followed here, uses mean annual cloud cover to scale extraterrestrial shortwave radiation flux.

A simple relationship is used to estimate the transmission of shortwave radiation flux through cloud cover. Shortwave radiation transmission can be simply estimated through (Kimball, 1928)

$$\frac{R_s}{R_{sc}} = 1 - am_c \tag{7-25}$$

where R_s is shortwave radiation at the ground surface, R_{sc} is clear-sky shortwave radiation, a is a fitting constant, and m_c is the mean fractional cloud cover. The fitting constant is reported to be roughly 0.71. A slightly more complex relationship is reported by Black (1956) for average global conditions

$$\frac{R_s}{R_{sc}} = 0.803 - (0.340 + 0.458m_c)m_c \tag{7-26}$$

This relationship requires long-term average (*e.g.*, monthly) values for cloud cover.

A set of 239 WBAN stations across the US collected hourly meteorological readings over the period of 1961 through 1990. These readings include precipitation, temperature, relative humidity, cloud cover, and several measures of solar radiation. This data set, called Solar and Meteorological Surface Observation Network (SAMSON) is available from NCDC on 3 CD-ROMs (http://www.ncdc.noaa.gov). Readings from a subset of stations across the southwestern United States were examined to estimate the parameters in the two equations. The average ratio of ground to extraterrestrial radiation and average cloud cover during daylight hours were determined over the station period, from which a was estimated. The Black (1956) relationship was also evaluated with the same average parameters. Estimated parameters are shown in Table 7-3.

The Black (1956) relationship performs very well in estimating the mean shortwave radiation transmission with no calibration required. However, the relationship performs less well when the hourly values of cloud cover were used, underpredicting transmission by 81 to 89 percent. Simply

Table 7-3: Measured mean transmission of shortwave radiation and cloud cover, the estimated parameter for the Kimball (1928) equation, and the estimated mean transmission of shortwave radiation using the Black (1956) equation on hourly cloud cover and annual cloud cover. Measurements are at SAMSON stations over the period 1961 through 1990.

Station	WBAN ID	R_s/R_{sc}	m_c	a	Black (1956)	
					Hourly	Average
Flagstaff, AZ	03103	0.543	0.456	1.00	0.480	0.552
Phoenix, AZ	23183	0.570	0.333	1.29	0.569	0.639
Prescott, AZ	23184	0.557	0.407	1.09	0.517	0.589
Tucson, AZ	23160	0.571	0.375	1.14	0.537	0.611
Daggett, CA	23161	0.596	0.308	1.31	0.589	0.655
Alamosa, CO	23061	0.571	0.459	0.934	0.475	0.550
Grand Junction, CO	23066	0.535	0.508	0.915	0.441	0.512
Boise, ID	24131	0.495	0.553	0.914	0.394	0.475
Pocatello, ID	24156	0.486	0.585	0.877	0.375	0.447
Albuquerque, NM	23050	0.571	0.432	0.991	0.498	0.570
Tucumcari, NM	23048	0.537	0.453	1.02	0.488	0.555
Elko, NV	24121	0.509	0.525	0.935	0.423	0.498
Ely, NV	23154	0.532	0.518	0.903	0.433	0.504
Las Vegas, NV	23169	0.583	0.347	1.20	0.560	0.630
Reno, NV	23185	0.539	0.463	0.997	0.469	0.548
Tonopah, NV	23153	0.558	0.404	1.09	0.520	0.591
Winnemucca, NV	24128	0.519	0.512	0.941	0.428	0.509
Burns, OR	94185	0.497	0.546	0.922	0.394	0.481
Pendleton, OR	24155	0.472	0.599	0.881	0.359	0.435
Redmond, OR	24230	0.500	0.553	0.904	0.404	0.475
Cedar City, UT	93129	0.543	0.468	0.977	0.469	0.544
Salt Lake City, UT	24127	0.493	0.561	0.903	0.391	0.468
Spokane, WA	24157	0.459	0.635	0.851	0.331	0.402
Yakima, WA	24243	0.476	0.569	0.920	0.384	0.461

multiplying the relationship by about 1.15 would recover much of the predictive capability when using short-term cloud cover. The Kimball (1928) relationship is less useful, as the fitting coefficient is quite variable from station to station.

Typically 45 to 60 percent of extraterrestrial radiation is received at the ground surface across the western US, with Nevada stations receiving between 51 and 58 percent. Stations in Arizona, which has a monsoonal climate, are between 54 and 57 percent, while stations in Oregon, Washington, and Idaho are between 46 and 50 percent. If these locations are extrapolated to represent conditions during different portions of the glacial cycle, monsoonal conditions may see a slight increase in insolation while glacial conditions may see a slight decrease in insolation.

Mean annual longwave radiation Mean annual longwave radiation is primarily estimated from cloud cover and is assigned a uniform value for every pixel in the DEM.

References

Black, J. N. 1956. The distribution of solar radiation over the earth's surface. *Archiv. Meteorology Geophysics Bioklimatology B 7*, 165–189.

Flint, A. L., J. A. Hevesi, and L. E. Flint. 1996. *Conceptual and Numerical Model of Infiltration for the Yucca Mountain Area, Nevada.* Milestone 3GUI623M, Department of Energy, Las Vegas, NV.

French, R. H. 1986. *Daily, Seasonal, and Annual Precipitation at the Nevada Test Site, Nevada.* Publication no. 45042, Desert Research Institute, Reno, NV.

Hevesi, J. A. 1999. *Simulation of Net Infiltration for Modern and Potential Future Climates.* ANL-NBS-HS-000032, Department of Energy, Las Vegas, NV. Draft date 1/10/00.

Hevesi, J. A., A. L. Flint, and J. D. Istok. 1992a. Precipitation Estimation in Mountainous Terrain Using Multivariate Geostatistics. Part II: Isohyetal Maps. *Journal of Applied Meteorology 31*(7), 677–688.

Hevesi, J. A., J. D. Istok, and A. L. Flint. 1992b. Precipitation Estimation in Mountainous Terrain Using Multivariate Geostatistics. Part I: Structural Analysis. *Journal of Applied Meteorology 31*(7), 661–676.

Kimball, H. H. 1928. Amount of solar radiation that reaches the surface of the earth on the land and on the sea, and methods by which it is measured. *Monthly Weather Review 56*, 393–399.

McKinley, P. and T. Oliver. 1994. *Meteorological, Stream-Discharge, and Water-Quality Data for 1986 through 1991 from Two Small Basins in Central Nevada.* Open-File Report 93-651, United States Geological Survey, Denver, CO.

Redmond, K. T. and R. W. Koch. 1991. Surface Climate and Streamflow Variability in the Western United States and Their Relationship to Large-Scale Circulation Indices. *Water Resources Research 27*(9), 2381–2399.

TRW. 1998. *Yucca Mountain Site Description.* B00000000-01717-5700-00019 REV 00, TRW Environmental Safety Systems Inc., Las Vegas, NV.